Valorization of Lignocellulosic Materials: Designing, Synthesis, and Processing of Functional Polymer Nanocomposites

by

Mahesh Parit

A dissertation submitted to Graduate Faculty of
Auburn University
in partial fulfillment of the
requirements for the Degree of
Doctor of Philosophy

Auburn, Alabama
May 1, 2021

Keywords: Cellulose nanocrystals, Cellulose nanofibers, Kraft lignin, Polyvinyl alcohol, Polypyrrole

Approved by

Dr. Zhihua Jiang, Chair, Auburn Pulp and Paper Foundation Assistant Professor of Chemical Engineering and Director, Alabama Center for Paper and Bioresource Engineering
Dr. Alan David, John W. Brown Associate Professor of Chemical Engineering
Dr. Xinyu Zhang, Professor of Chemical Engineering
Dr. Maria Soledad Peresin, Assistant Professor, Forest Products Development Center, School of Forestry and Wildlife Sciences

ABSTRACT

The objective of this research is to valorize lignocellulosic materials obtained from kraft pulp and paper industry for functional applications through design, synthesis, and processing of their nanocomposites. The lignocellulosic nanomaterials that are mainly focused are cellulose nanocrystals (CNC), cellulose nanofibers (CNF), and kraft lignin (KL). Developing CNC, CNF, and KL based transparent and UV protection nanocomposite films and CNF based conducting nanocomposite films are two main aspects of functional applications in this research.

Simple, novel, and green approach is designed to produce transparent, homogeneous CNC-KL based UV protection films through optimal addition of electrolytes. First, the effect of electrolytes (NaOH, NaCl, CsCl, $CaCl_2$, $AlCl_3$) which varies in size, valency, and pH on CNC self-assembly, structural, optical, and mechanical properties was studied. The chiral nematic self-assembly of CNC could be tuned through addition of electrolytes. Nematic CNC films with maximum transparency and mechanical properties were prepared through optimized electrolyte addition. Further, CNC/KL nanocomposites were designed by incorporating the KL in NaOH containing CNC suspension and casting the mixture. NaOH facilitated uniform dispersion of KL in CNC film producing transparent, homogeneous, UV blocking nanocomposite films. To further improve the transparency of CNC/KL films, acetylation or oxidative peroxide bleaching treatment were applied to KL. The peroxide bleached KL obtained under optimized bleaching conditions resulted in improved transparency without significantly affecting its UV blocking properties. CNC nanocomposites using peroxide bleached KL showed superior performance in terms of UV blocking and transparency compared to 4-amino benzoic acid (4-ABA), a commercial organic UV absorbent and most of the lignin based transparent, UV blocking nanocomposites in literature. This work shows for the first time that CNC aqueous suspensions with and without containing lignin

could be tuned through the addition of electrolyte to produce transparent, homogenous films, providing a facile approach in engineering CNC/lignin transparent, UV-protection nanocomposite films.

To further expand the scope of the nanocellulose and KL, multifunctional nanocomposites were synthesized using KL, CNF, and polyvinyl alcohol (PVA). First, KL grafted CNF was produced via amidation reaction which was further treated with hydrogen peroxide bleaching treatment to reduce the lignin color. This modified nanofiber was introduced to aqueous PVA solution to cast nanocomposite films. Transparent, UV blocking PVA nanocomposites with high flexibility, mechanical strength, and thermal stability were obtained. Water vapor barrier properties of PVA were retained in these nanocomposites. Heat treatment of these nanocomposites rendered them water resistance and prevented lignin leaching. PVA and modified nanofiber nanocomposites also showed superior performance in terms of transparency and UV blocking properties compared to most lignin based transparent and UV blocking nanocomposites reported in literature.

Finally, a papermaking like method for the fast preparation of uniform cellulose nanopaper (CNP) was developed. This standardized method could also be used for comparing the CNF properties produced from different sources and processes. CNP produced using this method was developed as a flexible and biodegradable substrate for synthesizing the polypyrrole based conducting nanocomposite films with improved physical and electrical properties. A new approach based on *in-situ* CNP polymerization was developed. Physically cross linked PVA coated CNP (PVA-CNP) provided water stability, reduced porosity, and resulted in smooth deposition of PPy. As a result, PPy/PVA-CNP showed enhanced conductivity, dry and wet tensile strengths compared to widely used *in-situ* nanofiber polymerization approach in literature. The applicability of these

nanocomposite films in EMI shielding applications was shown. PPy/PVA-CNP exhibited higher shielding effectiveness (SE) compared to nanocomposites produced using *in-situ* nanofiber polymerization approach. These nanocomposites have applicability as an electromagnetic interference (EMI) shielding, and anti-static coating/packaging material for electronic devices.

In summary, this research established new routes to valorize the kraft pulping process derived lignocellulosic nanomaterials through their chemical modifications, synthesis, and processing into functional nanocomposites.

ACKNOWLEDGEMENTS

I would like to thank Dr. Zhihua Jiang for providing me opportunity to chase my curiosities within this research. I am also thankful to him for his constant encouragement and guidance towards achieving research goals. I would like to also thank my committee members and university reader for providing their precious time and feedback in the research. Acknowledgement and thanks are also extended to Haishun Du, and Dr. Xinyu Zhang for collaboration in the research and their help with regards to characterization and other critical discussions. I am thankful to Dr. Ilari Filpponen, Dr. Y.Y.Lee, Dr. Ramsis Farag, Dr. Burak Aksoy for their help in the research. I am also thankful to members of the Alabama Centre for Paper and Bioresource Engineering (AC-PABE) for their help and support in lab. I am thankful to my friends Vikrant Dev, Rajeshwar Chinnawar, Sagar Lonkar, Mehul Barde, Vinod Patil, and Yokesh Subramanian for their moral support and help during my stay at Auburn. Finally, I am very grateful to my parents and brother for their constant moral support and encouragement throughout my journey as graduate student to accomplish this milestone.

TABLE OF CONTENTS

ABSTRACT……ii

ACKNOWLEDGEMENTS……..……v

LIST OF FIGURES…….…….,,,..xi

LIST OF TABLES……..……xvi

LIST OF EQUATIONS……...……xvii

CHAPTER 1

INTRODUCTION…….……1

CHAPTER 2

BACKGROUND…….10

2.1 Cellulose nanocrystals……...….10

2.2 Cellulose nanofibers……..……...…..15

2.3 Lignin……...…..16

2.4 Lignocellulose processing……..18

2.4.1 Kraft Pulping……...……..18

2.4.2 Nanocellulose preparation……...…..19

2.4.2.1 Sulfuric acid hydrolysis……...……..19

2.4.2.2 TEMPO oxidation…….20

2.4.2.3 Microfluidization……..……22

2.4.3 Hydrogen peroxide bleaching……...……22

2.5 Polypyrrole…….25

CHAPTER 3

CELLULOSE NANOCRYSTAL FILMS- EFFECT OF ELECTROLYTE AND LIGNIN ADDITION ON SELF-ASSEMBLY, OPTICAL, AND MECHANICAL PROPERTIES……..…...29

3.1 Introduction……...……..……29

3.2 Experimental method…….……..31

3.2.1 Materials……..31

3.2.2 Methods……...…….31

3.2.2.1 Kraft lignin modification…….…....34

3.2.2.2 Film preparation…….…..32

3.2.2.3 Characterizations…….….33

3.3 Results and discussions……..…….….36

3.3.1 Structural and morphological characterization of CNC films……..…….…..36

3.3.2 Effect of electrolyte on CNC film optical properties……..…….....39

3.3.3 Theoretical estimation of CNC twist parameter……48

3.3.4 Effect of electrolyte on self-assembly of CNC……...…..51

3.3.4.1 Effect of electrolyte on CNC pitch…… ..……..51

3.3.4.2 Cross polarized optical microscopy of CNC films……..…….52

3.3.5 Effect of electrolyte on CNC crystallinity……..……..58

3.3.6 Cellulose nanocrystal-kraft lignin nanocomposite films…… ……62

3.3.7 UV blocking properties of cellulose nanocrystal-kraft lignin films…….64

3.3.8 Kraft lignin color reduction through acetylation and oxidative treatments……..67

3.3.9 Effect of electrolyte and lignin on CNC film mechanical properties……78

3.3.10 Effect of lignin on surface properties……81

3.3.11 Effect of lignin on CNC film thermal stability…….82

3.4 Conclusions……..83

CHAPTER 4

FLEXIBLE, TRANSPARENT, UV PROTECTING NANOCOMPOSITE FILMS BASED ON POLYVINYL ALCOHOL AND KRAFT LIGNIN GRAFTED CELLULOSE NANOFIBERS……..….86

4.1 Introduction……..86

4.2 Experimental method……...87

4.2.1 Materials……..87

4.2.2 TEMPO CNF Preparation……87

4.2.3 Amination of kraft lignin…….88

4.2.4 Synthesis of modified nanofibers……88

4.2.5 Hydrogen peroxide bleaching of modified nanofibers……89

4.2.6 Fabrication of PVA composites…….……..89

4.2.7 Characterizations……..89

4.3 Results and discussion…….91

4.3.1 Structural and morphological characterization……91

4.3.2 Thermal properties……...96

4.3.3 Mechanical properties……..99

4.3.4 Water vapor barrier properties……...101

4.3.5 Water resistance and lignin leaching test……...102

4.3.6 Optical properties……...104

4.4 Conclusions……107

CHAPTER 5

STANDARDIZATION OF PREPARATION PROCEDURE FOR UNIFORM CELLULOSE NANOPAPERS……109

5.1 Introduction……109

5.2 Experimental method……..111

5.2.1 Materials……...111

5.2.2 Fibrillation of CNF……...111

5.2.3 Nanopaper preparation……111

5.2.4 Characterizations……..112

5.2.5 Aspect ratio determination……...113

5.3 Results and discussion……..114

5.4 Conclusions……..121

CHAPTER 6

SYNTHESIS AND CHARACTERIZATION OF CELLULOSE NANOFIBER AND POLYPYRROLE BASED NANOCOMPOSITE FILMS WITH IMPROVED PHYSICAL AND ELECTRICAL PROPERTIES FOR ELECTROMAGNETIC SHIELDING APPLICATIONS……..…122

6.1 Introduction……122

6.2 Experimental method……123

6.2.1 Materials……123

6.2.2 Cellulose nanopaper preparation……..……..123

6.2.3 Synthesis of nanocomposite films……124

6.2.4 Characterizations……126

6.3 Results and discussions……..128

6.3.1 Morphology……128

6.3.2 FTIR spectroscopy……132

6.3.3 Conductivity……...135

6.3.4 Mechanical properties……137

6.3.5 Water resistance and surface wettability……142

6.3.6 EMI shielding properties of nanocomposite films ……..…….145

6.3.7 Thermal properties ……...…….149

6.4 Conclusions……151

CHAPTER 7

CONCLUSIONS AND FUTURE WORK……..….152

REFERENCES……157

***Key abbreviations**: CNC- Cellulose nanocrystals, CNF- Cellulose nanofibers, PPy- Polypyrrole, CNP-Cellulose nanopaper, KL-Kraft lignin, TEMPO* - 2,2,6,6-Tetramethylpiperidin-1-yl)oxyl, *TCNF-TEMPO cellulose nanofibers, TKL- Kraft lignin grafted TEMPO CNF*

LIST OF FIGURES

Fig. 2.1. Repeating single cellulose chain unit with 1-4 linkage and intra chain hydrogen bonding (dotted line), (b) Individual cellulose microfibril showing configuration of the crystalline and amorphous regions (c) cellulose nanocrystals with disordered amorphous regions dissolved in acid during hydrolysis……11

Fig. 2.2. Schematic illustration of particle orientation chiral nematic liquid crystals (left), left-handed chiral nematic phase (viewed from bottom) with hypothetical twisted layers (right)…….12

Fig. 2.3. Chiral nematic self-assembly of CNC rods in suspension and in casted film resulting in iridescence in the film…….12

Fig. 2.4. Twisted rod morphology of cellulose nanocrystal……13

Fig. 2.5. Lignin monomeric units……...16

Fig. 2.6. Sulfuric acid hydrolysis of cellulose to obtain CNC containing sulfate ester functionality……...20

Fig. 2.7. Mechanism of TEMPO oxidation of primary hydroxyl groups in cellulose to sodium carboxylate groups…….21

Fig.2.8. Proposed types of chromophores and leucochromophores in lignin……..24

Fig. 2.9. Proposed polymerization mechanism of pyrrole……..27

Fig. 3.1 (a) Dried CNC film, (b) and (c) SEM images of CNC film cross section……...37

Fig. 3.2. (a) Dried CNC film with electrolyte (NaOH), (b) and (c) Cross sectional SEM images of CNC (NaOH) films……38

Fig 3.3. Effect electrolyte concentration (a) CsCl, NaCl, NaOH (b) $CaCl_2$ and $AlCl_3$ on CNC particle size in 1.64 wt.% suspension……..40

Fig 3.4. Effect of electrolyte addition on zeta potential of CNC in 1.64 wt.% aqueous CNC suspension……..40

Fig.3.5. Transmission spectra of CNC films with various electrolyte concentrations (a) NaOH (b) NaCl (c) CsCl (d) $CaCl_2$ (e) $AlCl_3$……..44

Fig. 3.6. CNC films at various NaOH concentrations (a) 0.125 mmol/g (b) 0.25 mmol/g (c) 0.375 mmol/g (d) 0.5 mmol/g (e) 0.75 mmol/g (f) 0.875 mmol/g (g) 1.75 mmol/g (h) 2.5 mmol/g (i) 3.75 mmol/g…….....45

Fig.3.7. Images showing the transparency of the CNC films containing electrolytes (a) NaOH (b) NaCl (c) CsCl (d) $CaCl_2$ (e) $AlCl_3$ at 3 mmol/g concentration……46

Fig.3.8. Images showing the transparency of the CNC films containing electrolytes (a) CsCl (b) NaCl (c) NaOH at 1.5 mmol/g concentration……..46

Fig.3.9 CNC aqueous suspension phase diagram in presence of NaCl……...49

Fig.3.10. Calculated a) Effective diameter b) Ionic strength c) Debye length and d) Twist parameter for cellulose nanocrystals as a function of NaCl concentration……..49

Fig.3.11. Effect of electrolyte concentration on λ_{min} of CNC film……..51

Fig.3.12 Cross polarized optical microscopy images of CNC films containing various electrolytes at transition concentration. (First column – film position at 0° orientation to polarizer, Second column - film position at 45° orientation to polarizer)……53

Fig.3.13. (a) Dried dialyzed CNC film (b) Transmission spectra comparison of different CNC samples……...55

Fig. 3.14. Cross polarized reflected images of the dialyzed CNC films (First column – film position at 0° orientation to polarizer, Second column - film position at 45° orientation to polarizer)……56

Fig. 3.15. Schematic representation of CNC rods showing influence of dialysis and electrolyte addition on effective diameter……56

Fig.3.16. 5 wt.% aqueous samples of dialyzed CNC (left) and as received CNC (right)……..57

Fig.3.17. XRD plots for pure CNC films and CNC films containing 1.25 mmol/g of various electrolytes……59

Fig.3.18. Crystallinity of CNC films containing electrolytes at different concentrations…….59

Fig.3.19. Crystallinity of CNC film samples after treatment with electrolyte……60

Fig.3.20. Dialyzed and redispersed samples after treating with CsCl, NaCl, NaOH, $CaCl_2$ and $AlCl_3$ (from left to right)……60

Fig.3.21. Images of (a) Pure CNC film (b) CNC film with 0.875 mmol/g NaOH addition (c) CNC/KL (2 wt.%) (d) CNC/KL (2 wt.%) with 0.875 mmol/g NaOH addition……...61

Fig.3.22. Topographical AFM images of CNC/KL (10 wt.%) films using alkaline aqueous mixtures……..62

Fig. 3.23. Scanning electron microscopy images of the CNC/KL (10 wt.%) films…….63

Fig.3.24. Thickness of the nanocomposite films with various lignin concentrations……..65

Fig. 3.25. UV-vis transmission spectra of CNC and CNC/KL films with various lignin concentrations……65

Fig.3.26. UV-Vis transmittance of CNC and CNC/KL (10%) films before and after UV (254 nm) exposure for 2 hours. (UVT refers to UV Treated)…….65

Fig.3.27. Cross polarized reflected images of the CNC (0.875 mmol NaOH) and CNC/KL films (Column A – film position at 0° orientation to polarizer, Column B - film position at 45° orientation to polarizer)……66

Fig.3.28. FTIR spectra comparison of KL and Ac-KL…….68

Fig. 3.29. Kraft lignin samples before and after acetylation……..69

Fig.3.30. Transmission spectra showing the increase in transparency for 0.1 wt.% solution of KL and Ac-KL in dioxane/water (0.5/0.5 v/v) before and after peroxide bleaching…….69

Fig. 3.31. (a) CNC/KL (10 wt.%) and CNC/Ac-KL (10 wt.%) films (b) Transmission spectra of comparison for CNC/KL (10 wt.%) and CNC/Ac-KL (10 wt.%)……..70

Fig.3.32. FTIR spectra of KL and peroxide bleached KL samples…….71

Fig.3.33. 0.1 wt.% peroxide bleached samples (from left to right) KL, PBKL50, PBKL150, PBKL200 PBKL400, PBKL600, PBKL1000……72

Fig.3.34. Effect of H_2O_2/KL ratio on %T at 550 nm and %UV blocking at 400 nm of 0.1 wt.% bleached lignin solutions……73

Fig. 3.35. Transmission spectra of CNC, CNC/4-ABA, and CNC/lignin nanocomposite films (0.68 mmol/g NaCl added to films)…….74

Fig.3.36. Comparison of transparency and UV blocking at 400 nm CNC/PBKL150 with lignin based transparent nanocomposites in literature. Red dots correspond to this study……76

Fig.3.37. Scanning electron microscopy images of the CNC/lignin film cross sections showing the lignin dispersibility in 10 wt.% CNC/PBKL150 (a) and (b), 10 wt.% CNC/Ac-KL (c) and (d)…76

Fig.3.38. Stress vs strain% curve of CNC films containing various electrolytes (optimal concentration) and 10% KL……78

Fig.3.39. (a) Tensile strength and (b) Strain% of CNC films containing electrolytes with various concentrations……79

Fig.3.40. Contact angle measurements for CNC and CNC/lignin samples as a function of time……80

Fig.3.41. Thermogravimetric analysis for CNC and CNC/KL films (a) Weight % vs Temperature (b) Temperature derivative weight % vs Temperature……82

Fig.4.1. FTIR spectra of the (a) KL and AKL (b) TCNF and TKL……..93

Fig.4.2. Carboxyl content of nanofibers before and after KL grafting as estimated by conductometric titration…….....94

Fig.4.3. 0.1 wt.% suspensions of nanofibers (from right to left) TCNF, TKL, PBTKL100, PBTKL400……95

Fig 4.4. XRD plots for PVA and PVA/PBTKL400 nanocomposites……..96

Fig.4.5. SEM images cross sections of (a) and (b) PVA/PBTKL (5%), (c) and (d) PVA…….97

Fig.4.6. DSC thermograms for PVA and PVA nanocomposite samples showing (a) Glass transition and melting peaks (b) crystallization peaks……99

Fig.4.7. TGA plots for PVA and PVA nanocomposites (a) Weight% vs Temperature (b) Derivative weight % vs Temperature…….100

Fig.4.8. Stress vs (%) Strain plot of the PVA and PVA/PBTKL400 nanocomposite samples…101

Fig.4.9. Mechanical properties of PVA and PVA nanocomposites (a) Tensile strength (b) Elongation at break (c) Young's modulus and (d) Toughness……...102

Fig.4.10. WVTR and WVP of PVA and PVA/PBTKL400 samples…….103

Fig.4.11. Images showing water resistance and lignin leaching of (a) PVA/PBTKL400 (5wt.%), (c) PVA/PBAKL400 (5wt.%); Absorption spectra of aqueous sample containing (b) heat treated PVA/PBTKL400 (5 wt.%), (d) PVA/PBAKL400 (5 wt.%)…….105

Fig.4.12. Films samples of PVA and PVA nanocomposites (from right to left) PVA, PVA/PBTKL400 (5%), PVA/PBTKL100 (5%) and PVA/TKL (5%)……..106

Fig.4.13. Transmission spectra of PVA and PVA/PBTKL400 nanocomposite films……...107

Fig.4.14. Comparison of transparency and UV blocking at 400 nm of PVA nanocomposites with 5 wt.% and 10 wt.% concentrations of PBTKL400, PBTKL100 and TKL with lignin based transparent nanocomposites in literature. Red dots correspond to samples in this study……..108

Fig 5.1. Scanning election micrographs of nanofibers (a) and (c) CNF (b) and (d) CNF2P……..118

Fig 5.2. Distribution of nanofiber diameters (a) CNF (b) CNF2P…….118

Fig 5.3. Dried nanopapers using (a) unrestricted drying between nylon polyester fabrics and without drying rings (b) restricted drying between nylon polyester fabrics with drying rings…..123

Fig.6.1. CNP preparation using a standard sheet machine……126

Fig.6.2. Preparation methodologies of CNF-PPy based conducting nanocomposite films……..130

Fig.6.3. Surface morphology of the films (a) CNP (b) ISF……**.....**131

Fig.6.4. Scanning election micrographs of nanopaper samples: ISF (a,b,c), PPy/CNP (d,e,f), PPy/PVA-CNP (g,h,i)……..133

Fig.6.5. Images showing the flexibility of the PPy-CNF nanocomposite films. Row 1 (PPy/CNP), Row 2 (PPy/PVA-CNP), Row 3 (ISF). Broken portions of twisted ISF samples are marked by circle…….134

Fig.6.6. FTIR spectra of (a) heat treated and untreated PVA-CNP (b) CNP, PPy and CNF-PPy based nanocomposite films……..136

Fig.6.7. Images showing conductivity of (a) ISF (b) PPy/CNP (c) PPy/PVA-CNP (d) PPy/PVA-CNP (twisted) (e) PPy/PVA-CNP (bend)…….139

Fig.6.8. Stress vs Strain (%) plot for CNP using casting and standardized method……...140

Fig.6.9. Stress vs Strain (%) plot for (a) CNF and CNF-PPy nanocomposite films (b) wet CNF and CNF-PPy nanocomposite films……142

Fig.6.10. Comparison of the cellulose based conducting nanocomposite films based on their maximum reported conductivity and tensile strength……**...**143

Fig.6.11. Images showing water stability of the nanocomposite films before and after 7-day mixing……..144

Fig.6.12. (a) Electromagnetic shielding effectiveness plot for CNP and CNF-PPy composite films (b) Shielding effectiveness of the nanocomposite films at 10 GHz……...147

Fig.6.13. EMI shielding performance comparison for cellulose and conducting polymer based nanocomposite films……147

Fig.6.14. TGA curves of CNF, PPy and nanocomposite films…….150

Fig.6.15. Derivative weight loss plots for the CNF, PPy and nanocomposite samples……..…150

LIST OF TABLES

Table 3.1. Extinction coefficient values for various lignin samples…….....70

Table 3.2. Effect of H_2O_2 concentration on 0.1 wt.% lignin solution optical properties and extinction coefficient at 255 nm……73

Table 3.3. %UV A, %UV B, %UV blocking at 400 nm and %T at 400 nm for CNC and CNC nanocomposites……..75

Table 4.1. Lignin content in modified TCNF samples……...95

Table 4.2. % Crystallinity of PVA and PVA/PBTKL400 nanocomposites……96

Table 4.3. Thermal properties and crystallinity of PVA and PVA nanocomposite films……...98

Table 4.4. %UV blocking and %T of PVA and PVA nanocomposite films…….108

Table 5.1. Aspect ratio, average diameter, and average length of nanofibers calculated by fitting the linear term in equation 1……..117

Table 5.2. Mechanical and barrier properties of nanopapers (standard deviations are indicated in bracket)……120

Table 5.3. P values obtained from Tukey statistical test for comparison among different sample groups (0- CNF 7 litre, 1-CNF 1 litre, 2-CNF 2 litre, 3-CNF2P 1 litre, 4-CNF2P 2 litre)……..121

Table 6.1. Cellulose nanopaper and composite film's average weight and densities……133

Table 6.2. Conductivity and % PPy gain in nanocomposite films prepared using different methods……137

Table 6.3. Mechanical properties of CNF and CNF-PPy nanocomposite films……...142

Table 6.4. Water contact angle measurement of the films……...…145

Table 6.5. Comparison of EMI shielding effectiveness of conducting polymer and cellulose based nanocomposite films……148

LIST OF EQUATIONS

2.1. Bragg's law equation for crystalline materials……14

2.2. Bragg's law equation for CNC film……..…...14

2.3. Hydroperoxide ion formation reaction…….24

2.4. Hydrogen peroxide decomposition reaction in presence of metals……25

2.5. Hydrogen peroxide decomposition reaction in presence of metals…….….25

2.6. Hydrogen peroxide decomposition reaction in presence of metals……..…25

3.1. Beer Lambert's equation…….……33

3.2. Equation to calculate %UV A blocking……...34

3.3. Equation to calculate %UV B blocking……...34

3.4. Equation for crystallinity calculation……...36

3.5. Debye length according to SLO theory……47

3.6. Twist parameter according to SLO theory……...48

4.1. Equation to calculate %UV A blocking……...89

4.2. Equation to calculate %UV B blocking……...89

4.3. Equation for crystallinity calculation……...91

5.1. Equation for aspect ratio using sedimentation method……...116

6.1. Equation for conductivity using Ohm's law……...129

6.2. Equation for Skin Depth……148

CHAPTER 1

Introduction

The ever-increasing demand for petroleum derived materials, and associated problems with utilizing them, including climate change, environmental concerns, and depletion of petroleum resources, have led to the quest for biobased products [1]. Biomass derived materials are promising alternatives to the petroleum-based polymers due to their sustainability and biodegradability. The major structural components of trees and various plants — cellulose, lignin, and hemicellulose — are the most abundant naturally available biomass-based materials. Recently, there has been growing interest in the research on the utilization of lignocellulosic biomass to produce bio-based materials as renewable and cost-effective alternatives to existing petrochemical-based products. Various biodegradable polymers currently being used includes polylactic acid, polycaprolactone, poly(hydroxybutyrate), poly(3-hydroxybutyrate- co-hydroxyvalerate), poly(hydroxyalkanoates), cellulose, starch and lignin [2, 3]. Among these cellulose and lignin are two most abundantly available biobased polymers on earth. Nanocellulose is a nanomaterial derived from cellulose using various chemical and mechanical methods [4, 5]. Nanocellulose in the form of cellulose nanofibers (CNF) and cellulose nanocrystals (CNC) has interesting optical and mechanical properties. This research is focused on valorizing nanocellulose (CNC, CNF), and lignin through design, synthesis, and processing of their nanocomposites for multifunctional applications.

Nanocellulose (CNC, CNF) used in this research is either commercially available or prepared from paper mill sludge (PMS) which is a waste produced by pulp and paper industry in large volumes [6, 7]. Being a waste material, its cost of disposal is about $20-$50 per wet ton sludge [6]. Also, its disposal using landfills becomes more difficulties due to stringent environmental regulations, diminishing land availability, and public opposition in recent years [8].

PMS has high carbohydrate content and low or no lignin content, as well as well-dispersed structure andit is normally not necessary to apply a pre-treatment or purification process prior to the production of CNFs [9]. Therefore, this cheaply available waste is promising feedstock for producing nanocellulose. Kraft lignin (KL) used in this research represents a major byproduct of the pulp and paper industry, since an enormous amount of such material is produced annually. The kraft wood pulping process accounts for nearly 90% of the total chemical wood pulp production worldwide [10, 11]. This method generates lignin in the form of "black liquor", which is commonly used to generate energy in recovery boilers [12-14]. However, lignin can be transformed into more efficient and value-added utilization through various chemical modification strategies [15]. Currently, only about 100,000 tons of kraft lignin (KL) is valorized per year. For multifunctional nanocomposite applications the focus of this research is mainly based on developing (1) Nanocellulose (CNC and CNF) and KL based transparent and UV protection nanocomposite films (2) CNF based flexible, conducting nanocomposite films with improved conductivity and physical properties. These biobased functional nanocomposites have a large scope as barrier packaging materials in various consumer applications.

It is well known that UV radiation causes damage to human skin [16, 17] and organic materials like plastics, woods, or polymers, food materials, dyes, pigments, semiconductor and medical devices among others [18-26]. With increased application of UV light for industrial and commercial purposes, there are more chances of getting exposed to this harmful electromagnetic radiation. Therefore, there is a need to selectively control its harmful impact on human beings and sensitive materials and the development of polymer films that act as shields against UV radiation is an active and interesting field of research. In this context it would be highly desirable to design biodegradable, transparent nanocomposite films with high transparency, strength, and UV

absorption properties based on lignocellulosic materials. Nanocellulose possess desirable optical and mechanical properties for these applications. It can either be used as highly transparent matrix or as a reinforcing nanofiller for developing these nanocomposites. Lignin on the other hand is a natural UV absorber [27-29] and has several advantages over the commercially used organic and inorganic UV absorbers in terms of its biodegradability and processing ease. Organic absorbers are often toxic and degrade upon exposure to sunlight [30-32]. Inorganic UV blocking agents are mostly used in the form of nanoparticles and at higher loadings results in agglomeration reducing the transparency of the resultant polymer nanocomposite films [33-36].

First part of this research is focused on designing CNC and KL based transparent, UV protection films. CNC is promising material for producing biodegradable, high performance nanocomposite films [37-39] which have utility in optical [40, 41], biological [42, 43], medical [44] and electronic [45] applications. CNC has intriguing ability to self-assemble into chiral nematic liquid crystal phase with helical arrangement. CNC in dilute aqueous suspension has random orientation of rods; however, they self-assemble themselves into chiral nematic phase at higher concentration [46-49]. CNC films obtained by casting these aqueous CNC suspensions can retain their chiral nematic order resulting in iridescent film. This iridescence is caused by circular polarization of the incident light which reflect and transmit light of various colors [50]. Controlling this optical (ok) would facilitate their use in applications such as security papers, mirrorless lasing, and polarizing films [51-53]. The chiral nematic self-assembly of CNC in suspension and film can be affected or controlled by the addition of electrolytes, polymers or surfactants and application of high-energy sonication [54-58]. Despite several efforts to study the effect of electrolytes and alkali on the CNC suspension phase behaviour, there are limited studies reporting their effect on CNC film properties. In fact, only reported study in literature is by Reising et al [59] who has studied

the effect of pH in low pH range (3 to 7) on the self-assembly and mechanical properties of CNC film. There is lack of systematic study on effect of electrolytes with varying charge, size, and pH on CNC self-assembly, optical, and mechanical properties of CNC films. The first objective of this study is to understand the effect of electrolytes with different valences (monovalent, divalent, and trivalent), sizes, and pH on self-assembly, optical, and mechanical properties of CNC film. The electrolytes used in this study were NaOH, NaCl, CsCl, $CaCl_2$, and $AlCl_3$. The effect of the additions of these electrolytes on transparency and mechanical properties of CNC film was optimized. Second objective of this study is to design CNC and KL based transparent, UV protecting films. For this purpose, KL is incorporated to the optimized electrolyte containing CNC suspension to obtain transparent, UV blocking CNC/KL nanocomposite films. Further, to improve the visible light transparency of these nanocomposite films, KL color reduction was carried out by its chemical modifications using acetylation and hydrogen peroxide bleaching treatments. The optimized KL obtained from this treatment was compared with 4-amino benzoic acid (4-ABA), a commercial organic UV absorbent, by comparing the transparency and UV blocking properties of their CNC nanocomposites films.

To further improve scope of KL and nanocellulose based transparent, UV protection nanocomposite films in applications requiring high flexibility, strength, and water resistance; nanocomposites were fabricated by incorporating KL grafted CNF in polyvinyl alcohol (PVA) matrix. PVA is used as polymeric matrix for this purpose because it is biocompatible, economical, highly transparent over the whole visible spectrum and has good adhesion to hydrophilic surfaces and processability [60]. It has been widely used in applications where high transparency is desired such as for the fabrication of flexible optical devices and polarizing films, sunglasses, goggles, window glasses and transparent packaging [61-67]. Besides high transparency, PVA can also

provide good gas barrier properties which would be beneficial for certain food and electronic applications [68, 69]. Previous studies based on PVA-lignin films showed poor miscibility between the KL and PVA [70, 71]. Degree of dispersion of lignin in PVA matrix was improved by preparing lignin nanoparticles using self-assembly or application of high mechanical shear [72, 73]. Although some improvement in thermal stability was observed, transparency, water resistance, and mechanical strength of resultant films were poor. There were several attempts to incorporate multifunctional nanofiller to fabricate the PVA based transparent, UV blocking nanocomposites with improved thermal and mechanical properties. Sirvio et al. [74] synthesized UV absorbing CNC by grafting PABA using "click-type" reaction and incorporated this modified CNC in PVA. Zhang et al.[75] grafted CNC with cinnamate groups via esterification of surface hydroxyl groups with the cinnamoyl chloride and incorporated them in transparent matrices like PVA and polystyrene. Also, several studies reported lignin containing CNF produced from the various biomass resources to fabricate PVA based nanocomposite films [76-78]. Although these approaches resulted in flexible, transparent, UV blocking films with improved mechanical and thermal properties; without cheap and abundant feedstock, nanocellulose production on large scale can render this approach unfavourable. In this study, the objective was to synthesize modified CNF (TKL) using amidation of aminated kraft lignin (AKL) and TEMPO oxidized CNF (TCNF) and incorporate it into PVA to fabricate nanocomposite films. AKL and TCNF were in turn produced from KL and PMS via amination and TEMPO oxidation, respectively. Furthermore, TKL was treated using hydrogen peroxide to obtain PBTKL100 and PBTKL400 with reduced lignin color and improved the transparency of resultant PVA nanocomposites. So far there are no reports for developing transparent, UV blocking nanocomposites using lignin grafted nanocellulose. These nanocomposites were characterized for their morphological, thermal, mechanical, barrier and

optical properties. Water resistance and lignin leaching experiments of these nanocomposites were also carried out.

Second part of this research is focused on developing CNF based flexible, conducting nanocomposite films with improved conductivity and physical properties. These nanocomposite films have utility in electronic packaging applications. The rapid growth of electronic industry in a modern world has increased the dependence of our society on electronic devices and communication instruments. These devices require shielding enclosures for protecting them from the external electromagnetic interference (EMI) or to reduce their emitted electromagnetic radiations to the surrounding environment [79-81]. The incoming electromagnetic radiation can affect the device functionality and integrity, while the control over emitted radiations is required to comply with government standards [82]. Various conducting materials have been utilized for EMI shielding nanocomposite films such as metals [83, 84], carbon nanotubes [85], carbon black [86], carbon fibers [79], and graphene [87]. However, their utilization was hindered due to factors such as high cost, corrosion, requirement of higher loading, and resultant deterioration of mechanical properties at higher loading. Conducting polymers are interesting class of polymeric materials which can be used as an alternative material for EMI shielding due to their low cost, lightweight, corrosion resistance, ease of processing, and tunable conductivities [81]. Due to their electronic conductivity, conducting polymers can shield electromagnetic radiations predominantly through absorption [88]. However, conducting polymers are difficult to process unlike conventional thermoplastic and thermoset polymers using methods such as melt processing and solution casting [89]. It is insoluble in common solvents and it decomposes before reaching its melting temperature. Several attempts were carried out in order to improve the processability of conducting polymers via various flexible polymer matrices such as rubber [90], polyamides [91],

polyolefins [92], and polyesters [93]. Recently there has been increasing attention towards utilization of biobased nanocellulosic substrates for the preparation of conducting polymer based flexible conducting nanocomposites [89]. Among various nanocellulosic substrates, CNF is more promising due to its intrinsic flexibility and lower cost of production compared to cellulose nanocrystals (CNC) which are relatively expensive, rigid and form brittle films. CNF can act as biodegradable and flexible substrate which can interact with the conducting polymers through hydrogen bonding thereby improving their processability [94, 95]. This approach is more sustainable, renewable and reduces the dependence on the petroleum-based non-renewable resources.

For developing CNF based flexible and conducting nanocomposite films, PPy was chosen as conducting polymer. PPy is commonly utilized conducting polymer due to its high conductivity, good environmental stability, facile synthesis, and non-toxic nature. It has potential applicability in several areas such as antistatic materials, EMI shielding, biomedical devices, biosensing and electronic devices as a substitute for metallic conductors or semiconductors [96]. So far limited attempts have been made to develop PPy and CNF based flexible conducting films for EMI shielding applications. Wang et al. prepared hydrophobic bacterial cellulose-PPy based nanocomposite films with SE of -15 dB; however, the nanocomposite film thickness and mechanical properties are not reported [97]. Chen et al. prepared regenerated cellulose-PPy based nanocomposite films with conductivity of 0.08 S/cm, SE of -12.5 dB and tensile strength of 158 MPa [98]. However, in this study film thickness was not specifically mentioned and film processing was carried out using expensive ionic liquids.

Most studies for the preparation of PPy-CNF based composed films employed an *in-situ* nanofiber (ISF) approach; i.e., first synthesizing PPy coating on nanofiber surface followed by

film preparation using these nanofibers [88, 99-101]. Flexible nanocomposite films with tunable electrical conductivity could be obtained using this approach. Nevertheless, these nanocomposite films had poor mechanical strength compared to pure CNF film due to a reduction in their internanofiber hydrogen bonding and increase in the film porosity [98, 102]. Therefore, this research is focused on developing new approach to synthesize PPy-CNF based nanocomposite films with improved conductivity, mechanical strength, water resistance and EMI shielding. *In-situ* PPy polymerization was carried out on cellulose nanopaper (CNP) and PVA coated cellulose nanopaper (PVA-CNP). The CNP substrate used in synthesis of these nanocomposite films is prepared using the standardized papermaking-like process. This process of nanopaper preparation can facilitate scalable preparation of flexible conducting nanocomposite films compared to most of the casting-based approaches used for film preparation**.** The CNF-PPy nanocomposites synthesized using new approach were compared with the *in-situ* nanofiber based approach widely used in literature for their physical, electrical propertis. The simple, novel, low-cost and scalable approache to produce flexible conducting nanocomposite films used in this study have promising potential for developing flexible EMI shielding packaging materials for electronic devices.

The organization of this dissertation is as follows. Chapter 2 provides a review of background information relevant to this research. Chapter 3 describes the effect of electrolyte and lignin on self-assembly, optical, and mechanical properties of CNC films. Chapter 4 covers transparent, UV protecting nanocomposite films based on polyvinyl alcohol and kraft lignin grafted TEMPO cellulose nanofibers and Chapter 5 describes standardization of method of preparation of uniform cellulose nanopapers. Chapter 6 describes the polypyrrole and cellulose nanofiber-based nanocomposite films with improved physical and electrical properties for

electromagnetic shielding applications. Chapter 7 summarizes the conclusions and future work of this research.

CHAPTER 2

Background

2.1 Cellulose Nanocrystals

Cellulose is most abundant biopolymer available on earth with global production (and decomposition) of ~ 1.5×10^{12} tons per year which is comparable to main fossil and mineral reserves [103]. It is main macromolecular component of plant cell walls and can also be produced from the various organisms such as bacteria, fungi, algae, tunicates etc. Cellulose nanocrystals (CNC) are the anisotropic rigid crystals with a diameter between 4-25 nm and 100-1000 nm in length derived from acid hydrolysis of native cellulose. Cellulose is a linear homopolysaccharide consisting of D-glucopyranose units linked together by 1-4 linkages. Each monomer contains three hydroxyl groups which interacts through hydrogen bonding and controls its crystallinity and physical properties [104]. Cellulose microfibrils are the basic structural component of cellulose formed during the biosynthesis. The chains of poly-β-(1-4)-D-glucosyl residues aggregate to form a fibril which is a long threadlike bundle of molecules laterally stabilized by intermolecular hydrogen bonds [105-107]. Individual microfibril can be considered as linear chain of cellulose nanocrystals linked along the fibril axis by disordered amorphous domains [108].

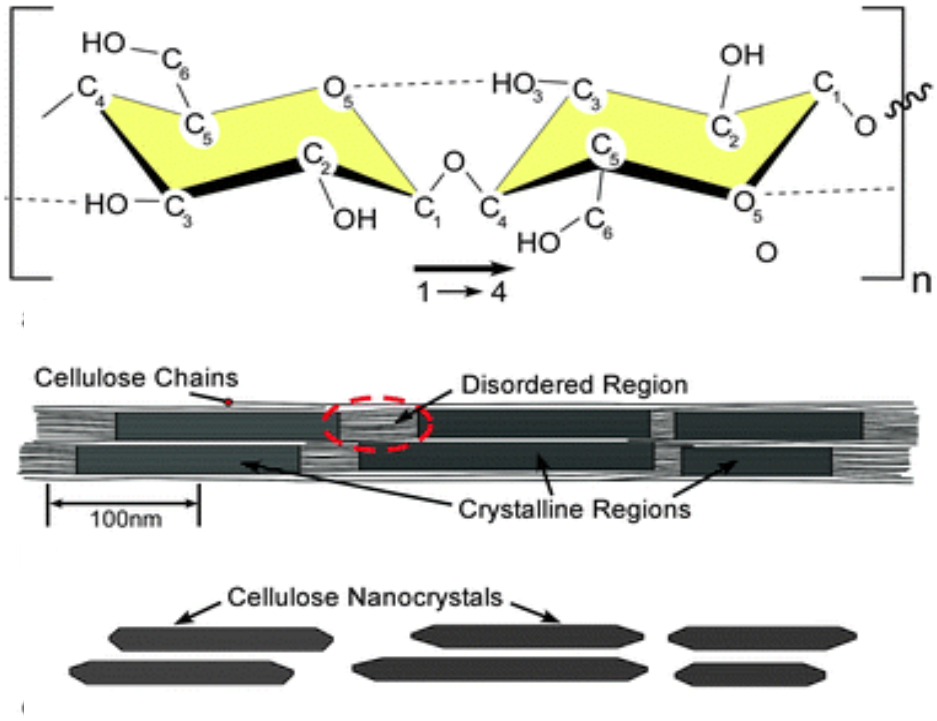

Fig.2.1. Repeating single cellulose chain unit with 1-4 linkage and intra chain hydrogen bonding (dotted line), (b) Individual cellulose microfibril showing configuration of the crystalline and amorphous regions (c) cellulose nanocrystals with disordered amorphous regions dissolved in acid during hydrolysis [37].

Sulfuric acid hydrolysis of cellulose fibers is widely used approach for producing CNC with sulfate esters functionality on the surface which gives stable aqueous suspensions due to electrostatic repulsion [109-111]. These nanocrystals exhibit liquid crystalline phase behaviour with increase in their concentration. In dilute dispersion CNC rods are randomly oriented forming an isotropic phase. At higher concentration, CNC assemble in chiral nematic manner to form cholesteric ordering with left-handedly rotating nematic layers along the perpendicular axis as shown in Fig.2.2 [112-114]. One full rotation (360^{o}) of these nematic layers is considered as a pitch length (P).

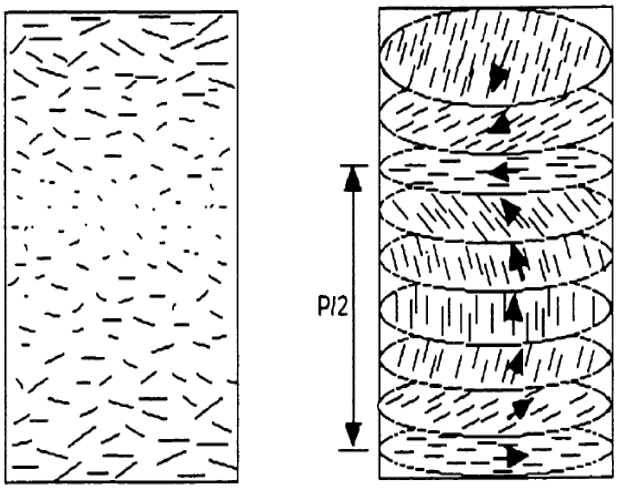

Fig.2.2. Schematic illustration of particle orientation chiral nematic liquid crystals (left), left-handed chiral nematic phase (viewed from bottom) with hypothetical twisted layers (right) [115].

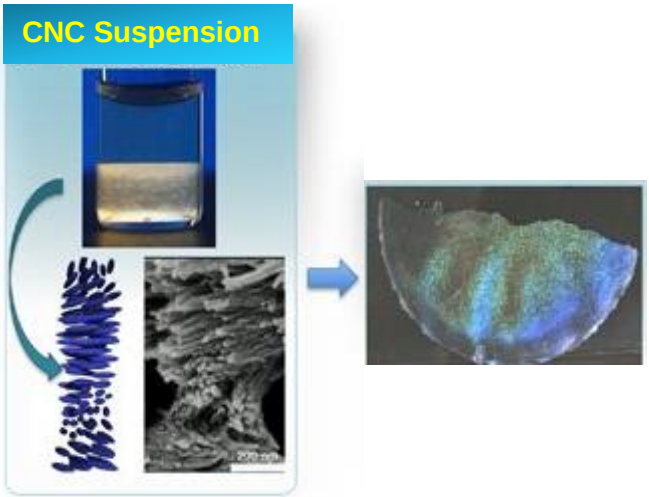

Fig.2.3. Chiral nematic self-assembly of CNC rods in suspension and in casted film resulting in iridescence in the film [50].

The chiral nematic self-assembly of CNC suspensions was first systematically studied by Revol, Gray, and co-workers [113-117]. Chiral nematically arranged CNC rods with pitch length

of the order of the wavelength of visible light reflect circularly polarised light of the same handedness as the chiral nematic phase. The wavelength of this selectively reflected light changes with viewing angle, leading to an iridescent appearance (Fig.2.3). The chiral nematic phase formation was observed only in sulfuric acid hydrolysed and phosphoric acid hydrolysed CNC but not for hydrochloric acid hydrolysed CNC [118]. Origin of chiral nematic ordering is attributed to surface charge on CNC; however, this reasoning is still debated. In some cases the twisted structure of nanocrystal rods is supposed to be responsible for their intrinsic chiral interaction [117, 119]. As shown in Fig.2.4, these screw-like rods can thread within each other giving tightly fitted cholesteric ordering. The physical twist in CNC rods can also impose a twist in electric double layer surrounding the rods.

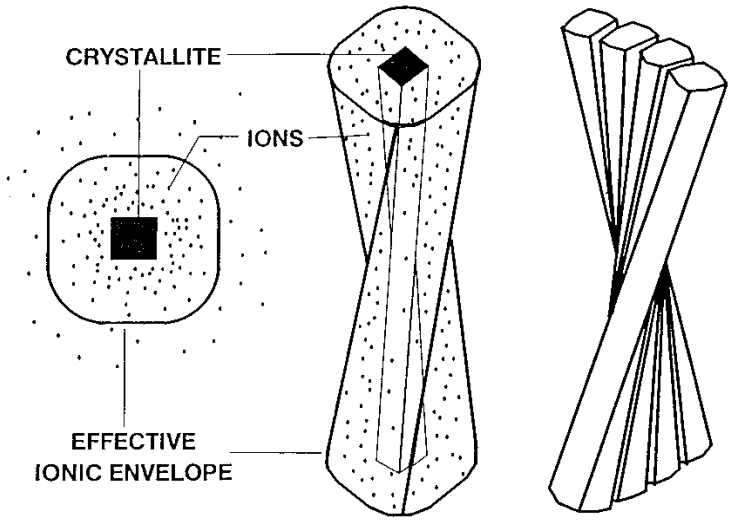

Fig.2.4. Twisted rod morphology of cellulose nanocrystal [117].

The self-assembled twisted layers of CNC rods in film resemble crystal lattices, which under certain circumstances result in Bragg's diffraction. The Bragg's diffraction happens when light of a wavelength comparable to successive crystallographic planes is scattered by different lattice planes that remain separated by the interplanar distance comparable to wavelength of light. Depending on the wavelength of the incident wave (λ), these scattered waves are able to interfere constructively according to Bragg's law

$$m\,\lambda = 2d\,\sin\theta \qquad 2.1$$

where m is a positive integer which ensures constructive interference (m= 1, 2…), d is the interparticle distance, and θ is the scattering angle. Using similar framework for CNC this equation is given as follows:

$$\lambda_{max} = n_{avg}\,P\,\sin\theta \qquad 2.2$$

In case of CNC film n_{avg} is the average refractive index of cellulose nanocrystals (1.562), P is the pitch of CNC, θ is the angle of the incident light. When the chiral nematic pitch is on the order of the wavelength of visible light, the iridescent visible colors are reflected. The reflection wavelength of CNC films can be tuned by modifying the CNC suspensions' ionic strength, sonication, surface charge density, and aspect ratio/length of the rods [55, 120, 121]. Also, absorption of water vapor and addition of polymer, surfactants can also alter the pitch and thereby the reflection wavelength [57, 122].

Due to intriguing mechanical and optical properties of CNC, focus on CNC based potential applications has drastically increased [50, 123-125]. CNC is promising biobased reinforcing nanomaterial for polymer nanocomposites mainly due to their inherent advantages including nanoscale dimension, high specific strength and stiffness, high surface area, ease of processing,

and cost effectiveness [126-129]. Interesting optical applications of CNC are due to its chiral nematic self-assembly. Controlling this optical behaviour would facilitate their use in applications such as security papers, mirrorless lasing, and polarizing films [51-53, 130]. Other interesting CNC applications includes sensors [131, 132] and supercapacitors [133].

2.2 Cellulose nanofibers

Cellulose nanofibers (CNF) are fascinating biomaterials due to their renewability, biodegradability, biocompatibility, and broad chemical modifying capacity. These materials are usually prepared from biomass derived lignocellulose fibers using mechanical disintegration processes such as homogenization [4, 134-136], microfluidization [137-140], grinding [4, 141], sonication [142-144], and cryocrushing in liquid nitrogen [145-147] with or without prior chemical or enzymatic pretreatment. These nanofibers are several micrometers long with an average diameter of 5-100 nm [137, 148, 149]. High aspect ratio and large number of interfibril hydrogen bonds contribute to their high strength and stiffness properties [148, 150-153]. They also possess interesting properties such as low coefficient of thermal expansion (CTE) and moisture adsorption; higher thermal stability, surface smoothness, barrier properties, and optical transparency [135, 148, 151, 152, 154-157]. Additionally, their low cost and ability to be surface functionalized makes them promising material for various large-scale applications [158, 159]. CNF can be processed into cellulose nanopaper which is 2D flat, foldable and strong film material of network forming nanofibers [160, 161]. There are several reports on the use of CNF in paper-like applications [148, 150, 151, 155, 162, 163]. These cellulose nanopapers have great potential for many new applications including transparent conductive films for electronics [157, 164-166], smart clothing [165], optically transparent electronic displays [160], membranes in fuel cells [167], tissue engineering [168] and liquid purification and filtration [169, 170]. Cellulose nanopapers are

excellent materials for optically transparent flexible electronic displays due to their low coefficient of thermal expansion [171] and minimum light scattering ability resulted from the nanometer sized fibers. High surface area, mechanical strength, low density and controlled permeability of CNF are crucial properties for the membrane applications [143].

2.3 Lignin

Lignin is an amorphous, polyphenolic branched structure formed from enzyme assisted dehydrogenative polymerization of the phenyl propanoid units [28]. It is the second most abundantly available biopolymer from the biomass resources, however, it is most underutilized material so far. Naturally, it is synthesized inside the plant cells enzymatically in presence of laccase and peroxidase. The polymerization of monolignol into lignin takes place from usually synapyl alcohol, coumaryl alcohol and coniferyl alcohol (Fig.2.5).

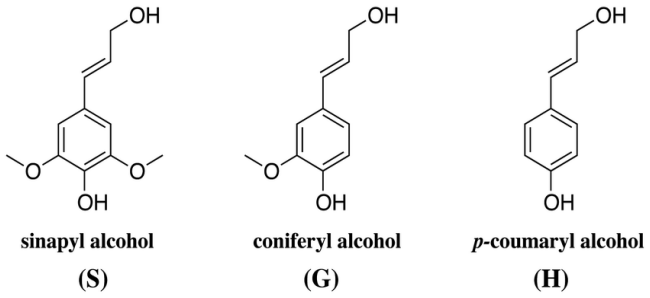

Fig.2.5. Lignin monomeric units [172].

Radicals generated in presence of the enzyme are combined to form ether (C-O) and carbon (C-C) linkages between the monolignols synthesizing supramolecular lignin structures of varying molecular weights. Naturally lignin occurs in conjunction with cellulose/hemicellulose through covalent bonding such as benzyl-ether, benzyl-ester, and phenyl-glycoside bonds, forming lignin–

carbohydrate complexes in plant cell walls. The lignin is separated from lignocellulosic materials using various separation methods. These methods and type of feedstock together influences the final structure of lignin.

In pulp and paper industries, KL is a main component of black liquor produced from the kraft process. It represents a major byproduct of the pulp and paper industry, since an enormous amount of such material is produced annually. The kraft wood pulping process accounts for nearly 85% of the total chemical wood pulp production in the United States [10]. During pulping process, the structure of KL changes significantly from its native structure. It has higher amounts of phenolic hydroxyl groups due the breakage of the β-aryl bonds while condensed C–C bonds in it increase with the duration of pulping time.

Over the last decade there has been great deal of progress in developing lignin into for thermoplastic polymeric materials. Lignin has been utilized through two major approaches, as a filler component for natural or synthetic polymers and as a copolymer used along with other natural or synthetic monomers. Lignin based polymer blends with petroleum-based polymers such as aliphatic polyesters (e.g., poly(Ɛ-caprolactone, poly(lactic acid))[173, 174], polyolefins (e.g., polyethylene, polypropylene)[175-180], poly(vinyl alcohol)[72, 73, 181], poly(ethylene oxide)[182, 183]. Most of the lignin based thermoplastic blends exhibited incompatibility between the polymeric matrix especially non-polar matrices like polyesters, polyolefins. Chemical modification of lignin need to be carried out wherever required for compatibilization [184, 185]. Although these modifications improve compatibility between the lignin and polymer matrix. They have limited impact towards significantly changing the properties of polymer. In another approach either unmodified or modified lignin was used for copolymerization with petroleum based

synthetic monomers or biobased monomers in order to obtain either fully or partially bio-based thermoplastic polymers [186-194].

2.4 Lignocellulose processing

2.4.1 Kraft pulping

Kraft pulping is widely used pulping process in pulp and paper industry producing about 163 million tons of pulp per year. Kraft pulping process accounts for 93% of the world's chemical pulp and 74% of the all pulp production [195, 196]. Popularity of this process is attributed mainly to recovery of inorganic chemicals and stronger pulp obtained after pulping.

In kraft process lignocellulose rich wood chips are cooked in an 'white liquor' which is an aqueous solution of sodium hydroxide (1 M NaOH) and sodium sulfide (0.25–0.75 M Na_2S) at temperatures of 165–175 ^oC for upto 2 hours [197]. In presence of hydroxide and hydrosulfide anions, lignin depolymerizes into smaller fragments that dissolve in the alkaline solution. The lignin removal process from fibers can be categorized mainly into three phases during the cooking process. The initial stage is extraction process where upto 15% of lignin is removed by cooking upto 150 ^oC. The second stage is a bulk delignification phse where most of the lignin (upto 60%) is removed which takes place from 150 ^oC to 180 ^oC and further cooking at 180 ^oC. The final stage removes up to 90% lignin by further cooking at 180 ^oC. Lignin removal rate is very slow at this stage, further cooking also causes degradation of carbohydrates in pulp.

Reaction occurring during the pulping are complex and not yet fully understood but essentially sulfide and hydroxyl ions promotes lignin fragmentation into soluble phenolate or carboxylate forms. In this process some carbohydrates and hemicellulose also degrades to some extent. In a typical cook to obtain bleachable grade pulp 80-90% of lignin, 80-90% of hemicellulose, 100% wood extractives and 10% cellulose are dissolved [198, 199]. However, the

residual lignin content in pulp fibers can be controlled by controlling the cooking conditions to obtain the any desired kappa number. Kappa number is a parameter which indicate the lignin content in fibers after cooking and lignin content can simply be obtained by multiplying kappa number by a factor of 0.15. H factor is used to control the extent of pulping and therefore lignin content, it is a variable which combines time and temperature. Delignification rate almost doubles with every 8°C increase cooking temperature. Therefore, lignin content of pulp fibers can be controlled by varying the time and temperature. For example, bleachable kraft softwood pulp of about 5% lignin can be obtained typically by cooking pulp for 1.5 h at 170°C. The same lignin content of in the pulp can also be obtained by cooking pulp at 178°C for 0.75 h or at 162°C for 3 h [200].

The residual liquor after cooking called 'black liquor' containing solubilized lignin is burned in recovery furnace to obtain an organic smelt of sodium carbonate and sodium sulfide. This smelt is dissolved in water to obtain 'green liquor' which is further reacted with quick lime (CaO) to convert Na_2CO_3 to NaOH in the process called 'recausticization' and regenerate the original white liquor [196].

2.4.2 Nanocellulose preparation

2.4.2.1 Sulfuric acid hydrolysis

Sulfuric acid hydrolysis is widely used method for the preparation of cellulose nanocrystals. This method was first developed by Ranby et al. [201] for producing CNC from wood and cotton fibers. CNC produced using this method can form stable aqueous dispersions due to electrostatic repulsion between the anionic sulfate ester groups on CNC surface introduced during hydrolysis [116]. Typical optimized conditions of hydrolysis uses 64 wt.% sulfuric acid, temperature of 45 ^{o}C, 25 to 45 min reaction time and acid to cellulose ratios of 8.75–17.5 mL/g [202]. Sulfate group

containing CNF can also be produced by using slightly milder acid hydrolysis conditions than optimal [203]. The cellulosic solid residue obtained in this process can be easily defibrillated using microfluidization and showed good dispersibility in aqueous medium.

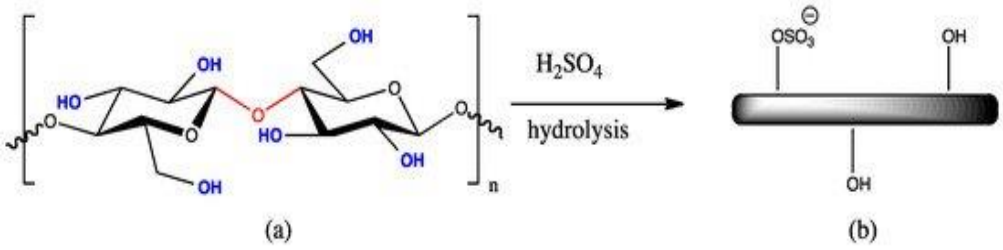

Fig.2.6. Sulfuric acid hydrolysis of cellulose to obtain CNC containing sulfate ester functionality [204].

2.4.2.2 TEMPO oxidation

TEMPO (2,2,6,6 -tetramethylpiperidine-1-oxyl radical) mediated oxidation is promising approach used to produce individualized water dispersible carboxylated CNF with high surface charge. TEMPO oxidation cellulosic material was first reported by Nooy et al [205-207], they were able to achieve position selective oxidation of C6-primary hydroxy groups to sodium C6-carboxylate groups with TEMPO/NaBr/NaClO system in water at pH 10. Several researchers have successfully employed this process for the preparation of carboxylated CNF from the cellulose fibers [208-211]. Recently TEMPO oxidation has also been used to produce the lignin containing CNF [212]. TEMPO is a water-soluble and stable nitroxyl radical, and commercially available for laboratory and industrial use. The proposed reaction mechanism of TEMPO-mediated oxidation of cellulose glucosyl unit is shown in Fig.2.7. Catalytic amounts of TEMPO and NaBr are used at room temperature in aqueous medium because of steric hindrance caused by the methyl groups present in TEMPO molecule. NaClO is used as primary oxidant for activating the the TEMPO oxidation

which converts primary hydroxyl groups of glucosyl unit to aldehyde groups and eventually to primary carboxyl groups. NaOH addition is carried out during the reaction to maintain the pH at 10, which neutralizes the carboxyl groups and form sodium carboxylate groups. For a given NaClO concentration the reaction is complete when there is no further consumption of NaOH, this process usually takes few hours.

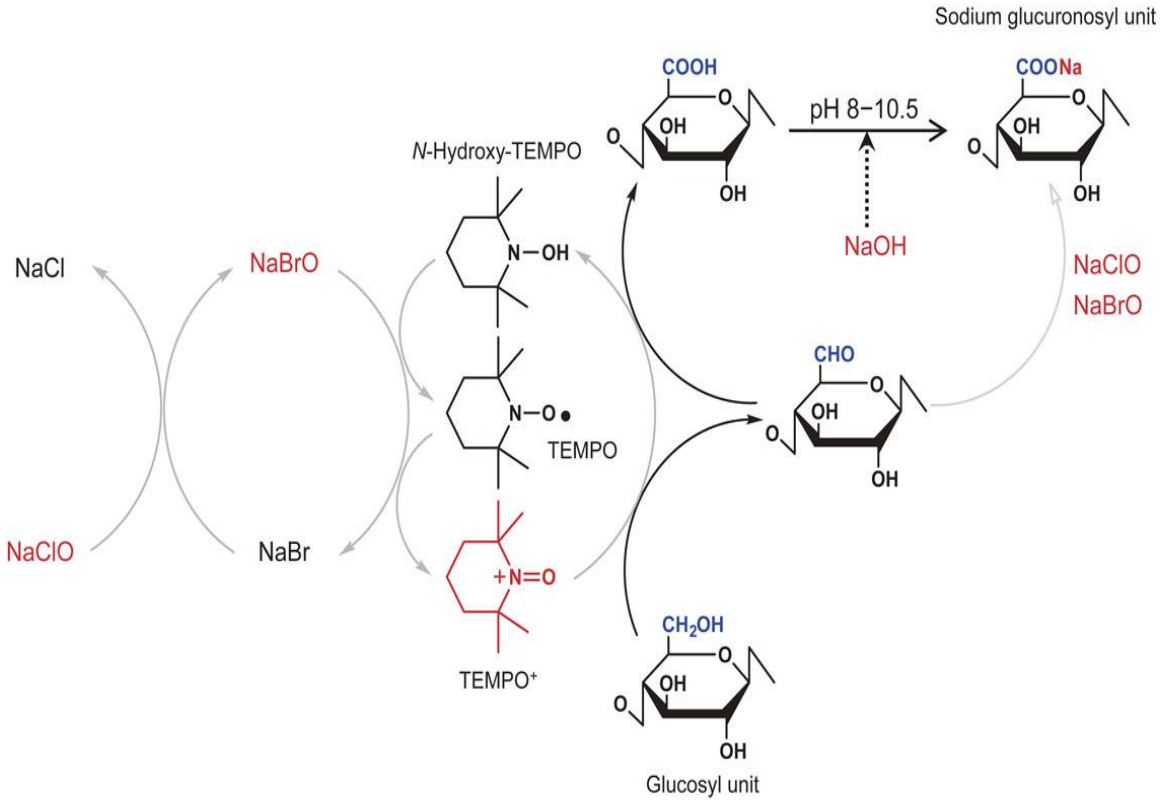

Fig.2.7. Mechanism of TEMPO oxidation of primary hydroxyl groups in cellulose to sodium carboxylate groups [213].

2.4.2.3 Microfluidization

Microfluidization is used to prepare CNF from pulp fibers pre-treated using mechanical or chemical treatments. Pulp fibers are passed through an interaction chamber with the help of intensifier pump at high pressures 30,000 psi (2068 bar) [214]. Fiber defibrillation takes place by

shear forces and impact against Z shaped channel walls and colliding streams. Diameters of these Z shaped channels typically ranges from 400 μm to 87 μm. Constant shear rate for defibrillation can be maintained by controlling the pump pressure during microfluidization.

Fiber pretreatments helps to reduce the energy consumption as well as clogging of the microfluidizer channel. Mechanical pretreatment reduces the fiber size using equipment's such as PFI mill, disk refiner and valley beater [105, 134, 135, 150, 215]. However, these methods can cause reduction in molecular weight and crystallinity of fibers along with increase in the energy consumption of nanocellulose preparation process. Chemical pretreatments such as acid hydrolysis [216, 217], oxidation [135, 212, 218], alkaline pretreatments [219]. Acid hydrolysis such as maleic, oxalic acid hydrolysis would remove the amorphous regions from the fibers and introduces the carboxylic functionality on fibers. Similarly, TEMPO-mediated oxidation can introduce the carboxyl functionality thereby improving the CNF individualization through electrostatic repulsion. In alkaline pretreatment, swelling of fibers would cause more uptake of water which hinders the hydrogen bonding between the fibers. These pretreated fibers would enable easy defibrillation of fibers with reduction in energy consumption during the microfluidization.

2.4.3 Hydrogen peroxide bleaching

Bleaching of pulp is traditionally carried out in pulp and paper industry to remove or brighten the residual lignin after cooking of wood chips. Lignin in its native form is slightly colored but it becomes dark in color during kraft pulping processes since it undergoes various chemical modifications. The bleaching processes are of various types, mainly they are lignin removing bleaching and lignin retaining bleaching. In lignin removing bleaching oxidants such as chlorine dioxide, oxygen and ozone are used Lignin retaining bleaching is accomplished with reducing

agents, such as dithionite, or oxidants, such as hydrogen peroxide with the removal of small amount of lignin.

The basic chromophoric units in lignin are carbonyl, ethylenic and aromatic structures. These structures as such do not impart color to the parent lignin structure, however, when they are part of lignin macromolecule, their absorption is altered by electronic and steric effects of substituent groups. Their absorption maxima can range from UV to visible spectrum of light thereby imparting the color of lignin. Some of the proposed chromophores in softwood kraft lignin includes coniferaldehyde- type structures, ortho- and para- quinoid units, quinone methide intermediates, metal-catechol complexes, stabilized free radicals (Fig.2.8). Additionally, leucochromophore structures can also contribute towards lignin color through chromophore formation. These structures are usually colorless, but they can be easily converted to chromophores through dehydration or dehydrogenation reactions as shown in Fig. 2.8.

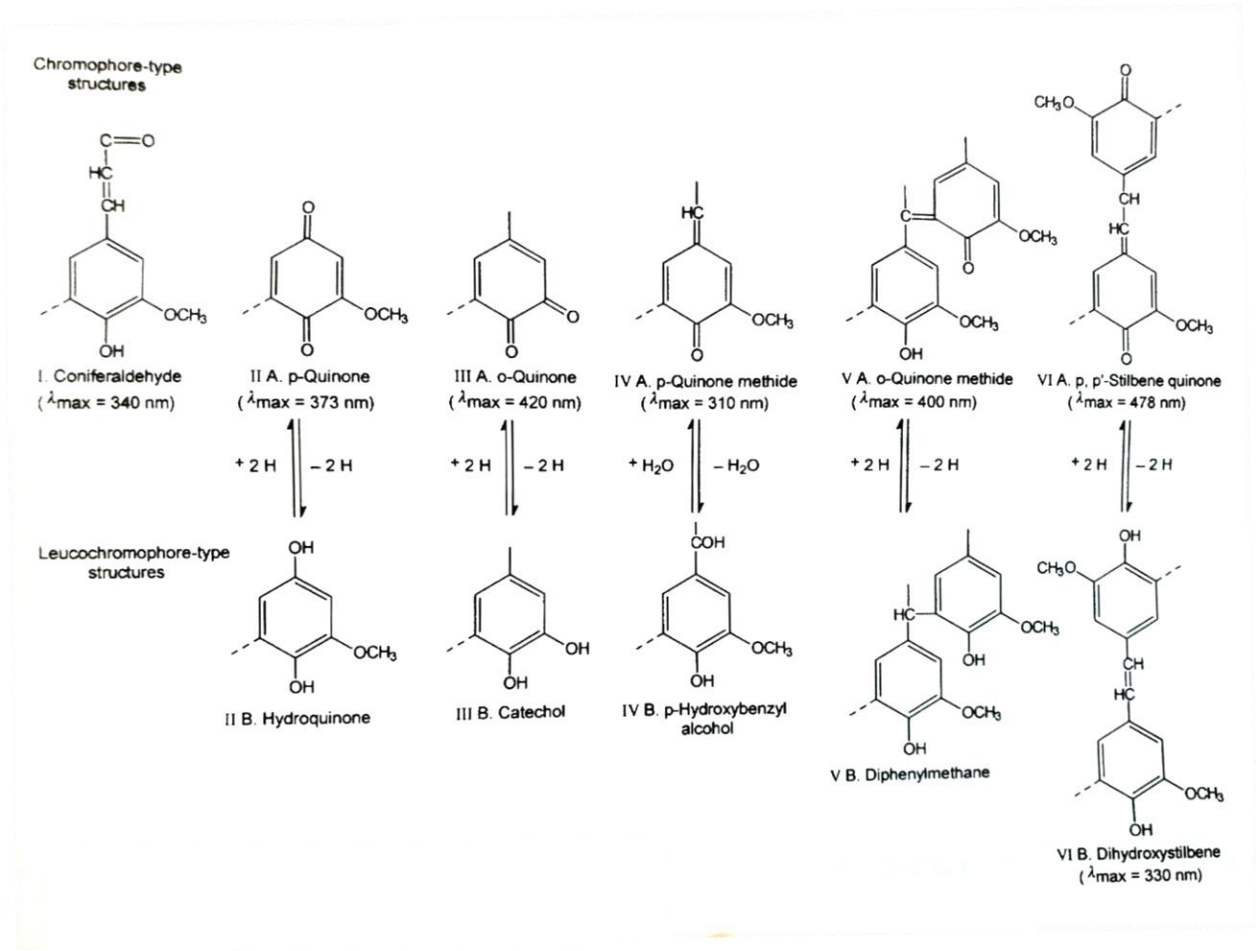

Fig.2.8. Proposed types of chromophores and leucochromophores in lignin [220].

The main reactive species in hydrogen peroxide bleaching is hydroperoxide ion (HOO^-) formed in alkaline conditions maintained by addition of NaOH (Equation 2.1). This hydroperoxide ion is highly reactive and stronger nucleophile than the hydroxide ion. The bleaching effect increases with increase in pH upto around 12 due to increase in hydroperoxide ion formation. Above pH 12 the bleaching effect is reduced mainly due to chromophore forming side reactions.

$$HOOH + HO^- \longleftrightarrow HOO^- + H_2O \qquad 2.3$$

H_2O_2 can also undergo decomposition during alkaline bleaching to release the oxygen usually results in foaming during the reaction. The transition metal impurities such as Cu, Mn and Fe in lignin or unbleached pulp are responsible for this decomposition [221, 222]. (Equation 2.4,2.5 and 2.6).

$$HOOH + M \longrightarrow M^+ + HO^- + HO^{\cdot} \quad 2.4$$

$$M^+ + HOO^- + HO^- \longrightarrow M + O_2^{-\cdot} + H_2O \quad 2.5$$

$$M^+ + O_2^{-\cdot} \longrightarrow O_2 + M \quad 2.6$$

It has been shown that these hydroperoxide ions and free radicals species generated during bleaching are involved in lignin color reduction through chromophore elimination reactions [223, 224].

2.5 Polypyrrole

Polypyrrole is an interesting conducting polymer due to its high conductivity, good environmental stability, ease of synthesis and non-toxic nature. It has applicability in several areas such as antistatic materials, EMI shielding, biomedical devices, various biosensing [225] and electrode materials for energy storage devices (electrochemical batteries and capacitors), electrocatalysts and biosensors, photo-luminescent materials, artificial muscles, gas sensors, anticorrosive coatings, electromagnetic shielding, materials for organic electronic devices etc. electronic devices as a substitute for metallic conductors or semiconductors. PPy has a conjugated bond structure, alternating single and double bonds, with one electron for each of the carbon atoms building up the π-electron system. The orbitals of the π-electrons overlap, leading to delocalization of the electrons along the polymer chain, which forms the basis for the electronic conductivity of the polymer [226]. However, due to the large gap between the (completely empty) conduction and

the (completely filled) valence bands, the polymer is an insulator in the reduced state. With oxidative doping, the conductivity of the polymer can be enhanced.

PPy is synthesized mainly through oxidative electrochemical or chemical polymerization of pyrrole using aqueous and non-aqueous solvents [227-229]. Electrochemical polymerization pyrrole is carried out oxidation of monomers on electrode forming a PPy film on its surface. While in chemical polymerization oxidation is carried out in presence of oxidants such as ferric chloride ($FeCl_3$), potassium persulfate ($K_2S_2O_8$)or hydrogen peroxide (H_2O_2) which synthesizes PPy in the form of powder [230]. The main advantages of chemical over electrochemical polymerization are that the polymer can be deposited on a variety of conductive or nonconductive substrates and bulk quantities of polymer can be produced for practical applications therefore it is preferred method from an industrial point of view [231]. The major disadvantages of chemical polymerization are that there is a limited choice of suitable oxidants and few available counterions, impurities are introduced with the oxidant, and it is difficult to control the oxidizing strength of the reaction solution which may cause chemical degradation during synthesis [232].

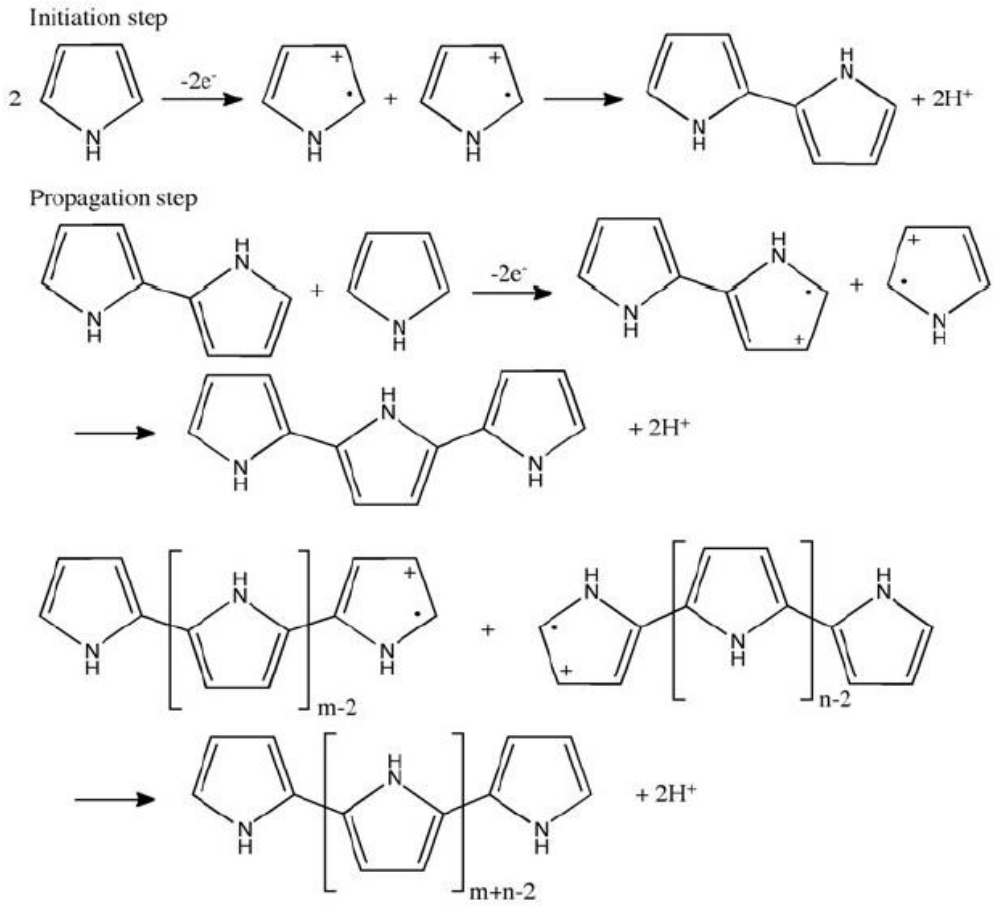

Fig.2.9. Proposed polymerization mechanism of pyrrole [228, 229].

It is considered that in first step, pyrrole monomers are oxidized to form radical cations. Further, two radical cations combine to form intermediate cation dimer releasing two protons and forming an uncharged dimer. In the next step, these dimers are immediately oxidized, as the greater conjugation makes it more easily oxidized than the monomer, and it undergoes coupling with a new radical monomer or oligomer again releasing protons [229]. Similarly, these tetramers react with new monomers and oligomers and so on. Furthermore, polymerization primarily occurs at the α-position, but may occur in the β- position as well, resulting in branching and cross-linking of chains. After polymerization, the polymer is in an oxidized state, which means that it carries a

cationic charge. The cationic charges of the polymer are compensated by counter ions carrying anionic charges, in order to maintain charge neutrality [233]. The counter ions are present in the polymerization solution and the morphology, conductivity and electrochemical properties of the polymer are influenced by the choice of counter ions as well as by the solvent and polymerization method [89, 227, 233-238].

Processing of polypyrrole is difficult unlike the conventional thermoplastic and thermoset polymers using methods such as melt processing and casting. It is insoluble in common solvents and decomposes before reaching its melting temperature. Several attempts were carried out in order to improve the processability of polypyrrole using various polymer matrices such as rubber [90], polyamides [91], polyolefins [92], polyesters [93]. Recently there has been growing interest in utilizing the cellulosic materials as a flexible substrate for improving the PPy processability [89].

CHAPTER 3

Cellulose nanocrystal films – Effect of electrolyte and lignin addition on self-assembly, optical, and mechanical properties

3.1 Introduction

A common challenge in engineering new nanocellulose-KL based materials is incompatibility between hydrophilic cellulose and hydrophobic KL. At normal pH and in the absence of chemical additives it is not possible to prepare uniform and homogenous nanocellulose-KL nanocomposite films. It was noticed that nonderivatized cellulose-lignin films could be formed using green solvents such as ionic liquids, but this approach is not economical due to high cost of solvent [239]. Other approaches using some hazardous organic solvents such as dimethyl sulfoxide (DMSO)/water and dioxane/water did not produce homogenous films [240]. In order to compatibilize CNC and lignin, several attempts were carried out through covalent bond formation [241, 242]. Sadeghifar et al [241] have produced flexible cellulose/lignin UV-blocking films containing low amounts of covalently bonded lignin. In this procedure, azide modified cellulose microcrystals dissolved in dimethylacetamide/lithium chloride (DMAc/LiCl) were reacted with propargylated KL to produce 0.5, 1, and 2 wt.% lignin containing materials. Cellulose films were then prepared by regeneration in acetone. Cellulose film containing 2% lignin showed around 100% absorption of UV-B (280−320 nm) and majority of UV-A (320−400 nm). The obtained films were uniform, but the procedure required use of organic solvents and long preparation times. Another approach reported in literature for covalent bond formation between cellulose nanocrystal and lignin was using Fenton's reagent (H_2O_2 and $FeSO_4$) as an initiator [242]. This approach increased covalent and noncovalent bonds between both polymers and contributed to the increase in the water resistance of coated films on quartz slides and in water retention in self-supported

films as a hydrogel-film. However, this approach is prone to CNC degradation and extent of lignin grafting onto CNC is unknown. Natural UV-absorbent coatings prepared from CNC and DHP or organosolv lignin by simple evaporation of the colloidal blended mixture has also been reported [240]. These materials were in the form of thin films and are transparent on glass or quartz slides with variable anti-reflective or UV absorbent properties, depending on the process used. In these materials, lignin and CNC are interacted through noncovalent and electrostatic forces [240, 243]. However, homogeneity and hydrophobicity of these materials were not reported.

In this research simple, novel, and green approach is designed to produce transparent, homogeneous CNC-KL based UV protection films through optimal addition of electrolytes. First, effect of electrolytes with various sizes (CsCl, NaCl), valences (NaCl, $CaCl_2$, $AlCl_3$), pH (NaCl, NaOH) on CNC self-assembly, structural, optical, and mechanical properties was studied. CNC films with maximum transparency and mechanical properties were prepared through optimized electrolyte addition. Further, homogeneous, transparent, UV protecting CNC/KL films were prepared by incorporation of KL in aqueous alkaline CNC dispersion and casting the mixture. The CNC/KL films were characterized for their morphological, optical, and thermal properties. KL was also modified using acetylation and peroxide oxidation methods in order to tune its optical properties. Modified KL was introduced into CNC suspension and resultant nanocomposites were compared for %UV blocking and transparency with the commercial organic UV absorber (4-ABA) containing films. This work shows for the first time that CNC aqueous suspensions with and without containing lignin could be tuned through the addition of electrolyte to produce transparent and homogenous films, providing a facile approach in engineering CNC/lignin transparent, UV-protection nanocomposite films.

3.2 Experimental method

3.2.1 Materials

CNC, purchased from the University of Maine Process Development Center, was manufactured at U.S. Forest Service's Cellulose Nanomaterials Pilot Plant at the Forest Products Laboratory, Madison, WI, USA. The sodium form CNC were obtained as an aqueous gel (11.5-12.5 wt.%), with crystal dimension specifications in the range of 5-20 nm for width and 150-200 nm for length. Some of the literature values are in agreement with these reported dimensions [244-246]. Reid et al have reported aspect ratio of this CNC to be ~19 with an average length of 134±52 nm and width 7±2 nm [245]. KL was provided by our industry partner and this softwood kraft lignin contains 95 wt.% lignin with impurities mainly as residual sugars, sulfur and ash. NaOH pellets, Sodium chloride (NaCl), Cesium chloride (CsCl), Calcium chloride ($CaCl_2$), Aluminum chloride ($AlCl_3$), Anhydrous Pyridine, Acetic Anhydride were obtained from TCI chemicals with ultra-purity. H_2O_2 (35%) solution was purchased from the VWR Chemicals.

3.2.2 Methods

3.2.2.1 Kraft lignin modification

Peroxide oxidation of KL

Kraft lignin was treated with hydrogen peroxide to improve its water solubility and reduce the color. Hydrogen peroxide oxidation of kraft lignin was carried out based on the optimized procedures reported previously [247]. Briefly, KL was solubilized in aqueous medium by adding NaOH and maintaining pH above 10.5. After complete solubilization of KL, required quantity of H_2O_2 was added based on the amount of KL. Concentrations of H_2O_2 added based on KL weight are from 50 to 1000 wt.%. After this addition pH was adjusted to 12.5 and the oxidation was carried out in at 75 ^oC for 2.5 hrs. Reaction mixture was then neutralized and deionized using dialysis

membrane for one week. Lignin powder sample was obtained by further freeze drying. Peroxide bleached KL using H_2O_2 concentrations of 50 wt.%, 150 wt.%, 200 wt.%, 400 wt.%, 600 wt.%, and 1000 wt.% were denoted as PB-KL50, PB-KL100, PB-KL150, PBKL200, PBKL400, PBKL600, PBKL1000, respectively.

Acetylation of KL

The purpose of lignin acetylation was to replace lignin hydroxyl groups with acetyl groups in order to reduce the dark lignin color which is partly caused by chromophores arising from phenolic hydroxyl groups such as quinone and quinonemethides. 1 gm of KL was dissolved in a mixture of pyridine (10 mL) and acetic anhydride (10 mL), and stirred at room temperature for 72 hours [248, 249]. The reaction mixture was then added dropwise into a 500 mL of ice-water to precipitate the acetylated lignin. Subsequently followed by filtration and repeated washing with ice-water and ethanol.

3.2.2.2 Film preparation

CNC films were prepared by mixing 1 gm CNC in 60 ml of deionized water (DI) water with or without addition of electrolytes. Electrolyte concentrations are reported in milli moles per gram (mmol/g) of CNC. CNC/KL films were prepared by suspending 1 gm of CNC in 30 ml of DI water which was mixed for 30 minutes using magnetic stirrer. Separately, required quantity of KL was mixed in a 30 ml of DI water with an addition of 0.875 mmol/g NaOH based on CNC weight. The aqueous alkaline lignin solution was mixed for 30 minutes in order to completely dissolve all the lignin without having any large visible aggregates. CNC suspension and lignin solution were then mixed for another 30 minutes to get the uniform mixture of the CNC/KL. This mixture was then casted on a polystyrene petri dishes and dried at room temperature in a fume hood for 48 hours to

obtain the uniform, transparent CNC/KL films. For peroxide bleached KL samples, same procedure was used with addition of 0.68 mmol/g NaCl instead of NaOH.

CNC/Acetylated KL (Ac-KL) films were also prepared using 0.68 mmol/g NaCl addition. However, in this case Ac-KL was solubilized in 30 ml of dioxane and CNC is suspended in 30 ml of DI water, before mixing these mixtures together. These films were dried on a Teflon molds in fume hood for 48 hours. Lignin concentration wherever mentioned throughout this study are wt.% based on the total weight of 1 gm of CNC instead of mixture weight. This was used for convenience as each film is prepared from 1 gm of CNC.

3.2.2.3 Characterizations

UV-vis spectroscopy

Transmission spectra of the aqueous lignin solutions and CNC/lignin films were carried out using a Thermo Scientific Genesys 10S UV−vis spectrometer in the wavelength range of 200−800 nm. Transmittance at the wavelength of 550 nm was used as a measure of film transparency. Extinction coefficient ($\mathcal{E}_\lambda$) of the lignin samples were calculated using Beer-Lambert equation as follows:

$$\mathcal{E}_\lambda = \frac{A_\lambda}{C \,.d} \qquad 3.1$$

Where $\mathcal{E}_\lambda$ (wt.%$^{-1}$cm^{-1}) is an extinction coefficient measured using absorbance A_λ, which is a maximum peak absorbance at wavelength (λ =255 nm). d is the path length for the incident light which is 1 cm in this case and C (wt.%) is the concentration of lignin solution. The percentage blocking for UV-A (320−400 nm) and UV-B (280−320 nm) was calculated by following equations: [250]

$$\text{UV A blocking (\%)} = 100 - \frac{\int_{320}^{400} T(\lambda)\, d\lambda}{\int_{320}^{400} d\lambda} \qquad 3.2$$

$$\text{UV B blocking (\%)} = 100 - \frac{\int_{280}^{320} T(\lambda)\, d\lambda}{\int_{280}^{320} d\lambda} \qquad 3.3$$

Fourier Transform Infrared Spectroscopy

Fourier transform infrared (FTIR) spectra of the lignin samples were measured on a Nicolet 6700 FTIR spectrometer by Thermo Scientific. A total of 64 cumulative scans in absorption mode were taken, with a resolution of 1 cm^{-1} in the frequency range 4000−600 cm^{-1}.

Atomic Force Microscopy (AFM)

AFM images of CNC/lignin films were performed under ambient conditions on a commercial AFM (Pacific Nanotechnology Nano-R AFM, Pacific Nanotechnology, Santa Clara, CA) in non-contact mode using aluminum AFM tips with resonant frequencies in the range of 150–210 kHz and force constants in the range of 4.5–14 N/m (MikroMasch, Wilsonville, OR). Images are collected at a scan rates of 0.5 Hz or 1Hz depending on the image size, with resolution of 256×256 data points. The RMS roughness of films was obtained from 10 μm×10 μm AFM scans.

Scanning Electron Microscopy (SEM)

SEM images of CNC and CNC/lignin films were taken using a JEOL (Tokyo, Japan) 7000-F Field Emission Scanning Electron Microscope. Films were sputter-coated with gold before taking images.

Optical Microscopy

Cross-polarized images of CNC and CNC/lignin films were taken using a Nikon (Melville, NY) Eclipse 80i Microscope with an LU Plan Fluor 4×/0.13NA Nikon objective lens and a Nikon DS-Ri2 Microscope Camera. Each film was placed between the cross-polarizers and images were taken in direction oriented at 0° and 45° to the polarization axis.

Zeta potential and particle size measurement

The dynamic light scattering (DLS, Zeta sizer Nano ZS, Malvern instrument) was used to determine the zeta potential and CNC particle size in aqueous suspension as a function of electrolyte concentrations. Dilute CNC suspensions of 1.64 wt.% with various electrolyte concentrations were prepared by magnetically stirring the suspension mixture for 2 hours. All measurements were carried out at 25 °C with at least three experiments for each sample.

Contact angle measurement

Static contact angle of the films was measured on a Ramé-Hart model 200 automated goniometer, using DROPimage standard software provided by Ramé-Hart. Measured contact angle was an average of 3 readings obtained for the water droplets, the measurement error is ±2^{o}.

Thickness testing

The thickness of the films was measured using the thickness tester from Testing Machine Inc. Reported thickness values were an average of at least 15 measurements along the film diameter.

X-Ray Diffraction (XRD)

XRD characterization of samples was acquired with a Bruker diffractometer under an acceleration voltage of 40 kV and a current of 40 mA at room temperature. The diffraction signals were

recorded in the 2θ range of 10−40° at a 5° min^{-1} scan rate. The crystallinity of CNC films is calculated using the following equation:

$$X_{c-XRD} = \frac{A_C}{A_C + A_a} \times 100 \qquad 3.4$$

Where A_a is experimental integrated intensity of amorphous phase and A_c is experimental integrated intensity of crystalline phase.

Thermal analysis

Thermogravimetric analysis (TGA) was performed on a TGA Q500 (TA instruments) under nitrogen at a rate of 10 °C min^{-1} from room temperature to 800 °C, with 20 minutes isothermal step at 120 °C to ensure the removal of residual moisture.

3.3 Results and discussions

3.3.1 Structural and morphological characterization of CNC films

CNC forms stable aqueous suspensions due to presence of negative sulfate half ester groups on their surface introduced during sulfuric acid hydrolysis. These suspensions exhibit the liquid crystalline phase behaviour with increase in its concentration orienting themselves randomly at dilute concentrations followed by intermediate biphasic to finally resulting in chiral nematic phase. The CNC used in this study has Na^+ counter ions which typically shows isotropic phase (3 wt.%) to biphasic (4 wt.% to 9 wt.%) and then to fully chiral nematic phase (10 wt.% or above). [251]. CNC films were prepared by casting the aqueous colloidal suspension of 1.64 wt.% and drying it at room temperature. As shown in Fig.3.1(a), dried CNC film showed iridescent colors. This iridescence is caused by the retention of chiral nematic ordering of CNC upon drying [49, 54, 252, 253]. The structural features of CNC rod self-assembly can be observed from the SEM images taken across slanted cross section of the film as shown in Fig. 3.1(b) and 3.1 (c). The chiral

nematically arranged CNC rods across the film thickness can be clearly observed. The different locally nematic layers of CNC are oriented in various directions, giving rise to overall helical chiral nematic self-assembly.

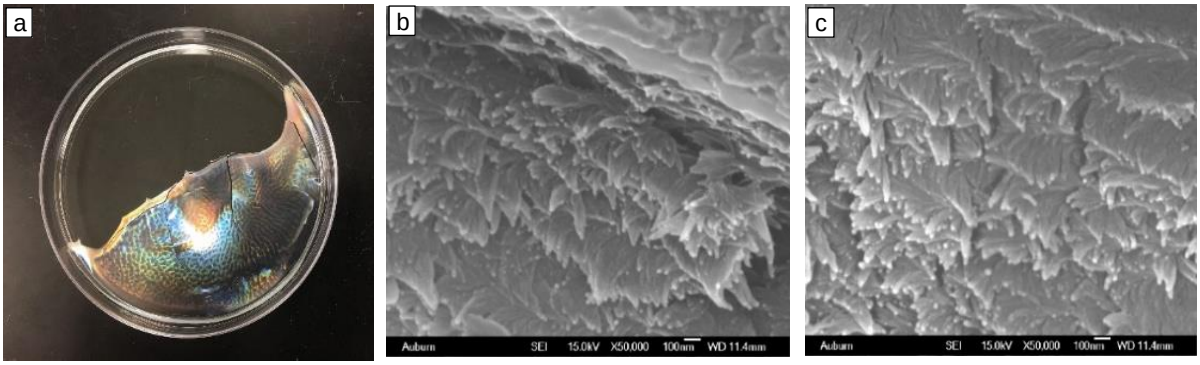

Fig. 3.1 (a) Dried CNC film, (b) and (c) SEM images of CNC film cross section.

As shown in Fig. 3.2 (a), with addition of electrolytes (NaCl, CsCl, NaOH, $CaCl_2$, $AlCl_3$) to CNC suspension in certain concentration range, chiral nematic ordering of CNC in dried film completely disappeared and produced highly transparent film. Although the effect electrolytes and pH on the aqueous phase behavior of the CNC suspensions and gels have been studied for the various inorganic salts [46, 48, 254-256], their effect on CNC film self-assembly and optical properties has not been focussed. Most studies involved the effect of small electrolyte concentrations on zeta potential, particle size, pitch length, alignment and phase formation in aqueous CNC suspensions [46-49]. We have observed that the addition of electrolytes to CNC suspension resulted in highly transparent films. This, to the authors knowledge, is the first attempt to show the effect of electrolytes addition on the CNC film transparency. The presence positive counter ions such as Na^+, Cs^+, Ca^{2+} and Al^{3+} hinders the chiral interaction between the CNC rods [257, 258], this resulted in transparent films. It also helped in forming uniform films reducing the

shrinkage during drying[258]. As shown in Fig.3.2 (a), CNC film containing electrolytes formed uniform film throughout the petri dish while pure CNC film shrank upon drying and produced an iridescent film of uneven thickness (Fig.3.1 (a)). Shrinkage in the pure CNC film is caused by the hydrogen bonding between hydroxyl groups on the surface of CNC [259]. Addition of electrolytes introduced the positive counterions, which reduced the hydrogen bonding between the hydroxyl groups.

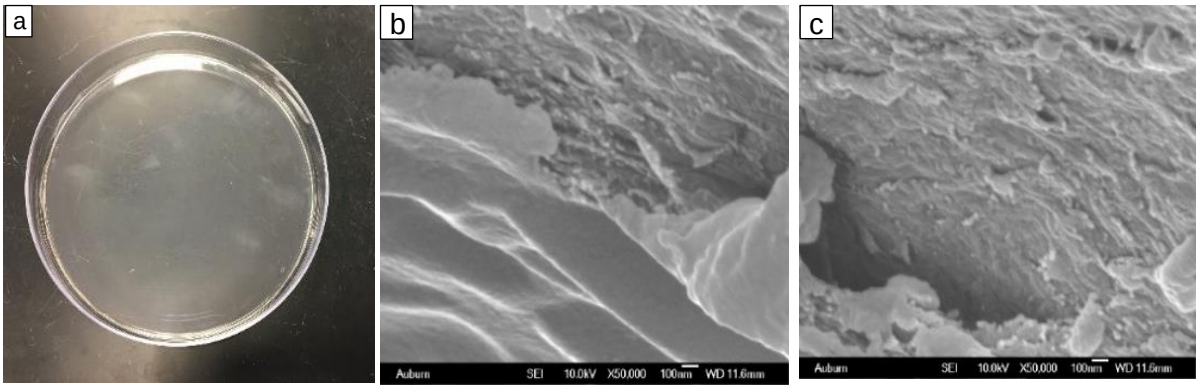

Fig.3.2. (a) Dried CNC film with electrolyte (NaOH), (b) and (c) Cross sectional SEM images of CNC (NaOH) films.

3.3.2 Effect of electrolyte on CNC film optical properties

To enhance the scope of CNC films in applications requiring high transparency, it is desirable to understand the effect of various concentrations of electrolytes on optical properties of CNC film. Since addition of electrolyte influences the film transparency, its concentration in suspension needs to be optimized in order to get the maximum transparency in the film. For this purpose, 1.64 wt.% aqueous CNC suspensions with various electrolyte additions ranging from 0.25 to 5 mmol/g electrolyte were used to prepare the films. As shown in Fig.3.3, addition of electrolyte influenced the size and the zeta potential of the CNC particles in suspension. It was clearly observed that zeta potential and average particle size of CNC slightly increased upto certain electrolyte concentration;

however, drastic changes in these parameters were observed at higher concentrations. The average particle size of CNC only slightly increased with addition of monovalent electrolytes such as CsCl, NaCl, NaOH. For CsCl addition particle size is slightly higher than NaCl and NaOH which may be due to more efficient negative charge screening by bigger sized Cs^+ counter ions than Na^+. Suspensions with $CaCl_2$ and $AlCl_3$ addition showed more prominent effect on the particle size increase. This is due to higher ionic strength of these multivalent ionic suspensions resulting in higher screening of electrostatic repulsion between the CNC rods at same electrolyte concentration and the cationic bridging [46, 254, 260]. Corresponding change in zeta potential of CNC can be observed in Fig. 3.4, for $CaCl_2$ and $AlCl_3$ zeta potential reduced below -20 mV which caused drastic particle size increase as shown in Fig. 3.3 (b). For $AlCl_3$ containing CNC suspensions the particle size increase was drastic in the beginning upto electrolyte concentration of 0.5 mmol/g, after which the increase was gradual. The initial drastic increase may be due to the combined effect of CNC electrostatic repulsion screening by Al^{3+} ions as well as cationic bridging. While at higher concentration of $AlCl_3$ (above 0.5 mmol/g), the zeta potential of CNC turned positive which could have stabilizing effect on CNC due to the electrostatic repulsive interaction. Therefore, the competing factors such electrostatic repulsion, electrostatic attraction screening and cationic bridging may have resulted in the gradual increase in CNC particle size. In case of $CaCl_2$ containing CNC suspensions, the particle size was much higher than monovalent electrolyte containing suspensions; however, unlike $AlCl_3$ it has not shown drastic increment in particle size upto electrolyte concentration of 0.5 mmol/g. This could be due to lower degree of charge screening and bridging by Ca^{2+} compared to Al^{3+} ions, as a result the CNC zeta potential at maximum $CaCl_2$ concentration was still negative.

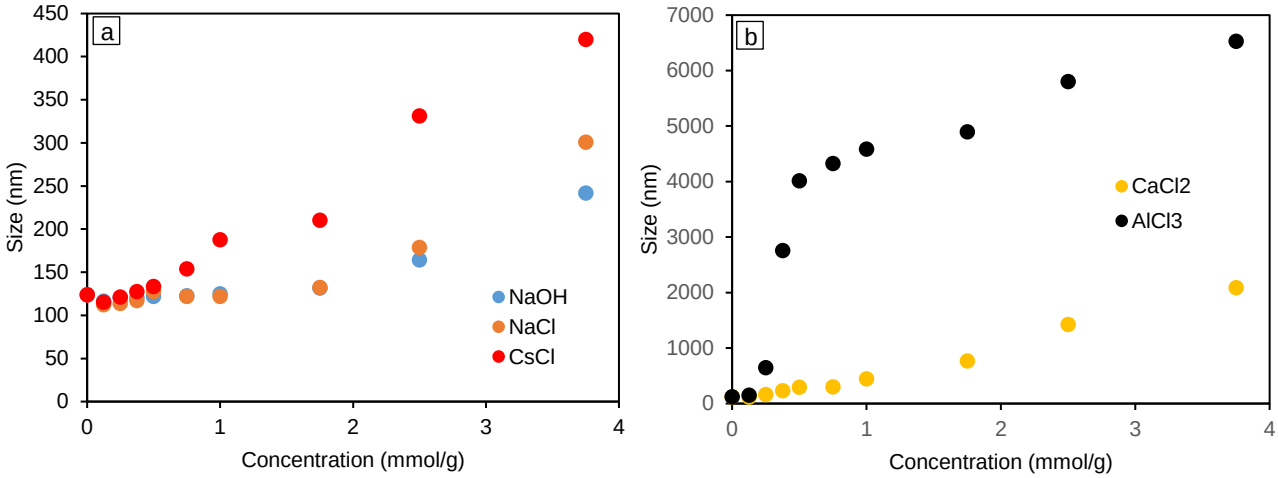

Fig 3.3. Effect electrolyte concentration (a) CsCl, NaCl, NaOH (b) $CaCl_2$ and $AlCl_3$ on CNC particle size in 1.64 wt.% suspension.

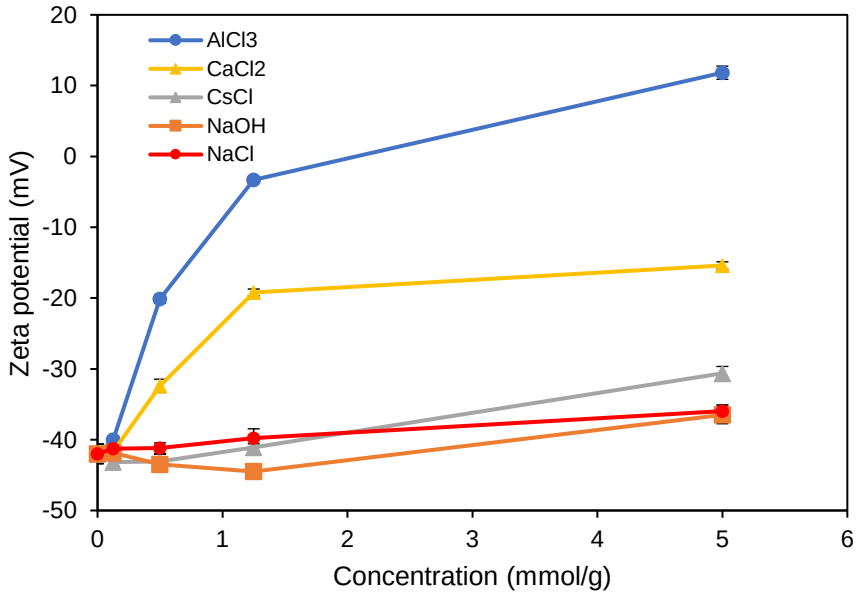

Fig 3.4. Effect of electrolyte addition on zeta potential of CNC in 1.64 wt.% aqueous CNC suspension.

Fig.3.5 shows the transmission spectra of the films prepared from suspensions with various electrolyte types and concentrations. Pure iridescent CNC film showed characteristic reflectance behaviour which is marked by dip in their transmission spectra [49, 55, 118]. At lower electrolyte concentrations the chiral nematic self-assembly in these films is retained. At certain electrolyte concentration the increase in double layer of CNC obscures the chiral morphology by making the effective rods straight and smooth which results in loss of iridescence as shown in Fig.3.2(a). This transition concentration to turn films from chiral nematic to nematic was lower for multivalent electrolytes compared to monovalent electrolytes. Transition occurred in concentration range of 0.09 to 0.135 mmol/g for $CaCl_2$ and 0.037 to 0.075 mmol/g for $AlCl_3$, whereas for NaCl, NaOH and CsCl, it was between 0.34 to 0.43 mmol/g, 0.375 to 0.5 mmol/g, and 0.327 to 0.356 mmol/g, respectively. In these CNC films high electrolyte concentration resulted in elimination of chiral nematic structure which led to increase in film transparency. For similar monovalent electrolytes such as NaCl and CsCl, the difference in transition concentration results from their different counter ion size. Smaller sized ions would require higher concentration to increase to electrical double layer for eliminating the chiral interaction between the CNC rods. Moreover, complex effects such as ions specificity can facilitate such behaviour [261, 262]. It was shown that the sulfate group interaction with monovalent salts followed hoffmeister series, where greater affinity between the soft cations Cs^+ and sulfate groups was observed compared to hard cations like Na^+ [46, 262]. This has resulted in lower aggregation concentration for CsCl in CNC suspension [46]. Similarly, in this case sulfate group containing CNC seem to have greater affinity with Cs^+ compared Na^+ thereby eliminating chiral nematic interaction between CNC at lower transition concentration.

At concentrations higher than the transition concentrations the negative charge on the CNC surface is completely screened by increase in double layer thereby reducing the absolute zeta potential. When the absolute value of zeta potential is less than 30 mV, the van der Waals force

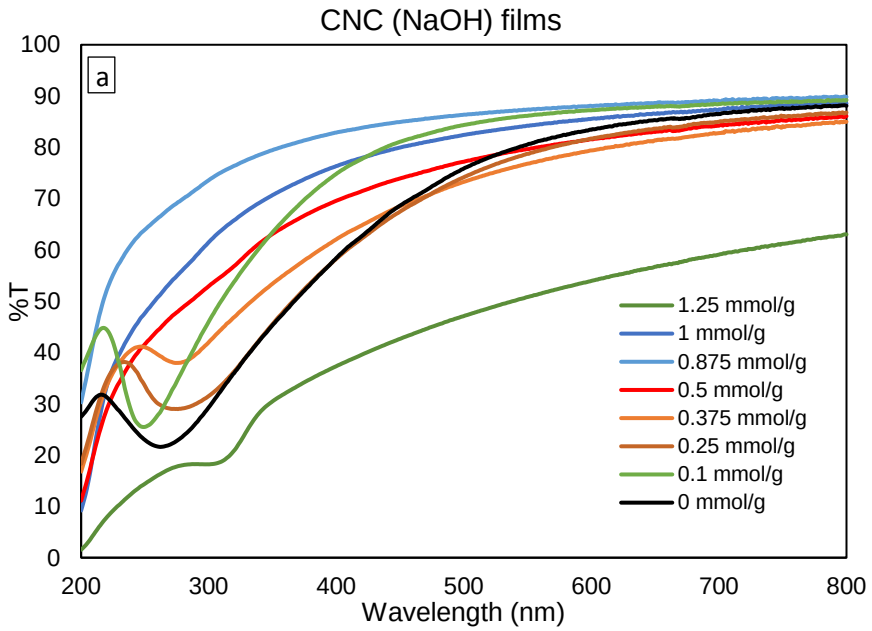

dominates the electrostatic repulsion and thus charged particles tend to aggregate causing drastic increase in particle size as shown in Fig. 3.3 and Fig.3.4 [254].

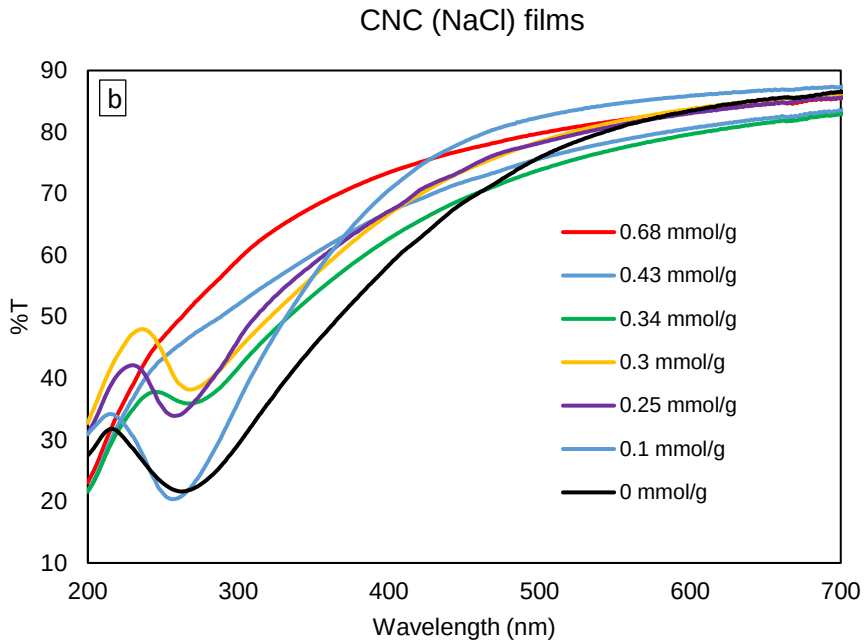
CNC (NaCl) films
b
%T
Wavelength (nm)
0.68 mmol/g
0.43 mmol/g
0.34 mmol/g
0.3 mmol/g
0.25 mmol/g
0.1 mmol/g
0 mmol/g

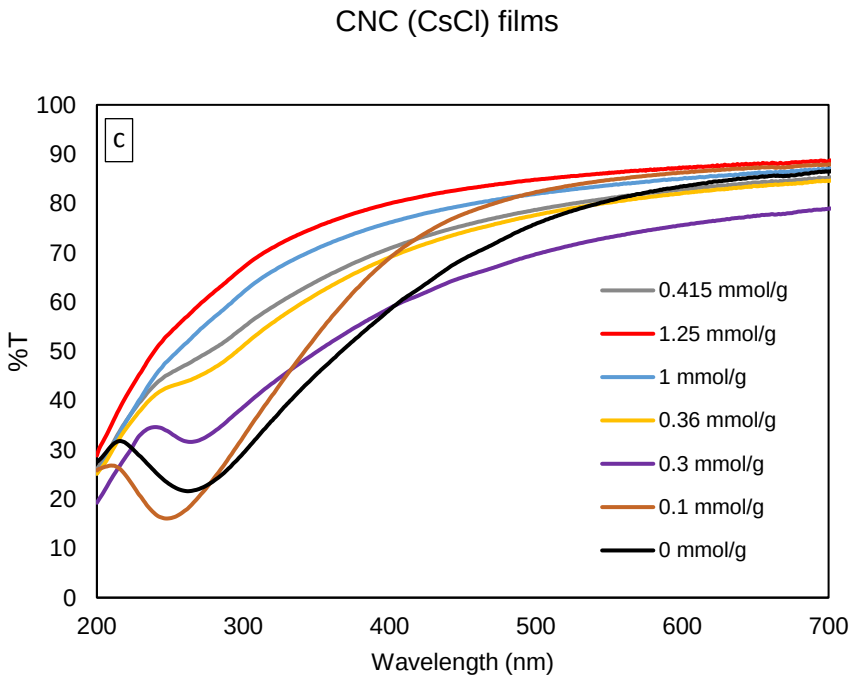
CNC (CsCl) films
c
%T
Wavelength (nm)
0.415 mmol/g
1.25 mmol/g
1 mmol/g
0.36 mmol/g
0.3 mmol/g
0.1 mmol/g
0 mmol/g

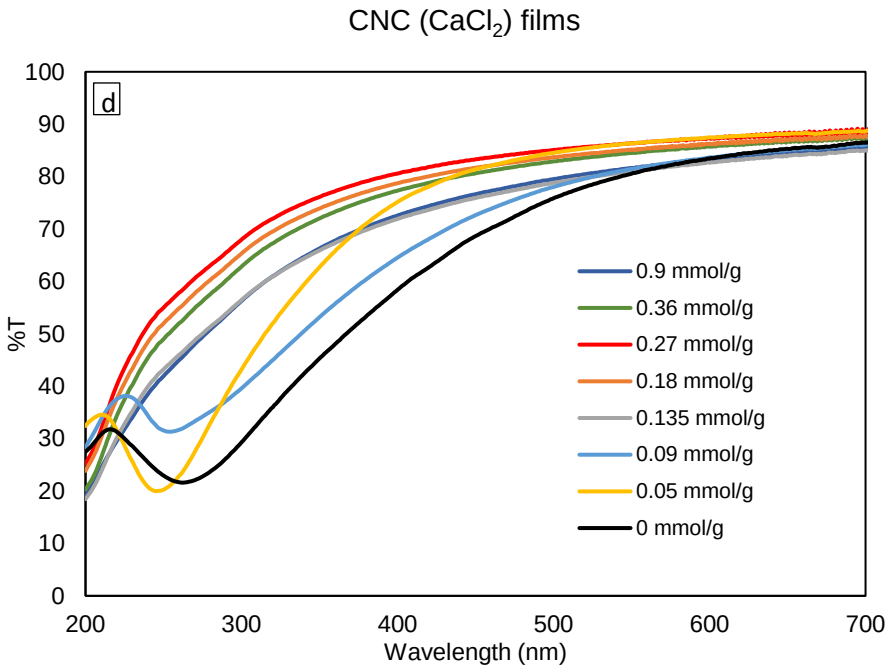

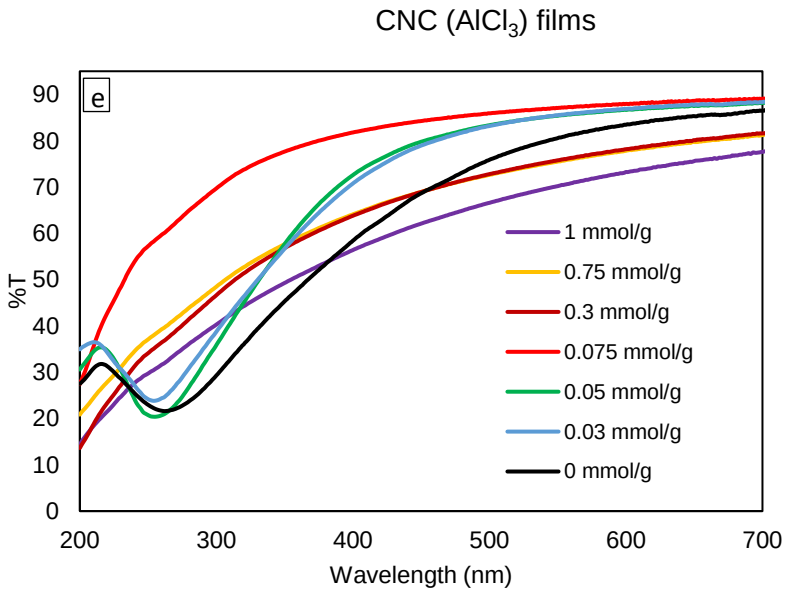

Fig.3.5. Transmission spectra of CNC films with various electrolyte concentrations (a) NaOH (b) NaCl (c) CsCl (d) $CaCl_2$ (e) $AlCl_3$.

As shown in Fig.3.6(c) to Fig.3.6(f), for films obtained using NaOH addition it was observed that the concentration range of 0.375 mmol/g to 0.875 mmol/g looked completely transparent; however, their transmittance has increased within this range (Fig.3.5(a)). Similar trend was observed for the CNC films prepared using other electrolytes. This may have resulted from the increase in nematic domains with electrolyte addition. More nematic domains can increase global alignment of CNC rods in film thereby reducing the variation in refractive index across the film thickness. This in turn will increase the visible light transmittance by lowering the dispersive losses in the film [263]. Detailed explanation is given in section 3.3.4.2 using cross polarized optical microscopy images of these films. The increased CNC particle size at higher NaOH concentrations caused more scattering of incident light reducing the transparency of resulting films. At higher concentration of electrolyte addition film transmittance was reduced (Fig. 3.5(a)) in accordance with the increased CNC particle size (Fig. 3.3(a)) resulting in hazy films (Fig.3.6 (g), Fig.3.6(h), Fig.3.6(i)). Similar morphology of CNC films was observed at higher concentrations using other electrolytes.

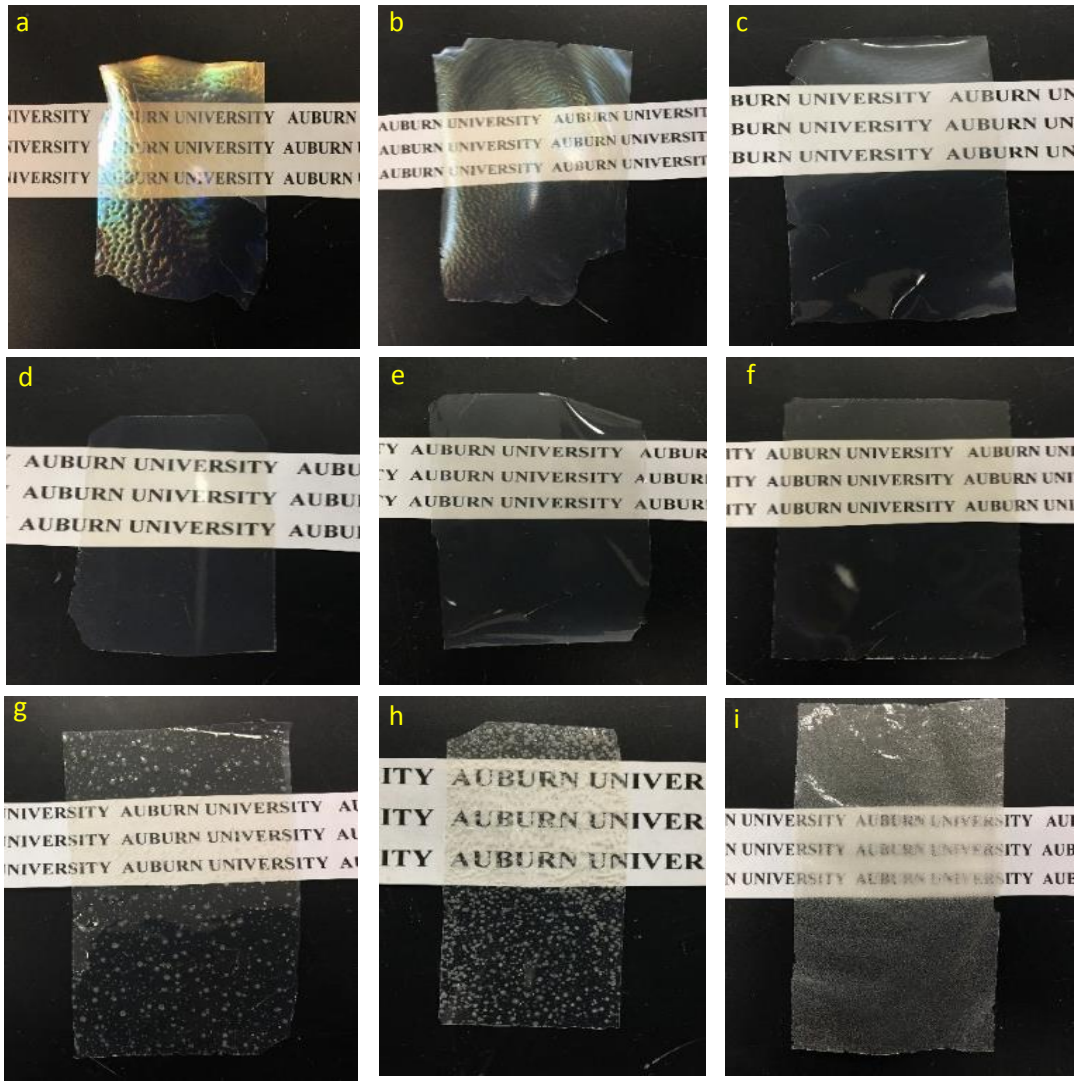

Fig.3.6. CNC films at various NaOH concentrations (a) 0.125 mmol/g (b) 0.25 mmol/g (c) 0.375 mmol/g (d) 0.5 mmol/g (e) 0.75 mmol/g (f) 0.875 mmol/g (g) 1.75 mmol/g (h) 2.5 mmol/g (i) 3.75 mmol/g.

At higher electrolyte concentrations, it was observed that monovalent electrolyte containing films showed very low transparency as electrolyte precipitated at higher concentration (Fig.3.7). Whereas for $CaCl_2$ and $AlCl_3$ containing films transparency reduced due to aggregation; however, films were more transparent compared to monovalent electrolyte containing films. For $AlCl_3$ containing films no precipitation was observed, whereas for $CaCl_2$ slight precipitation could

be seen. This may be due to the stronger interaction between the counterions ($Ca^{2+,}$ Al^{3+}) and negative sulfate ester group. Interestingly, for monovalent electrolytes with 1.5 mmol/g concentration, CsCl containing films did not show precipitation unlike NaCl and NaOH (Fig.3.8), which may be due to stronger specific interaction of Cs^{+} counter ions with the negative sulfate groups compared to Na^{+} as discussed previously. Interaction between these counterions and sulfate ester groups has also influenced the crystallinity of CNC (see section 3.3.5).

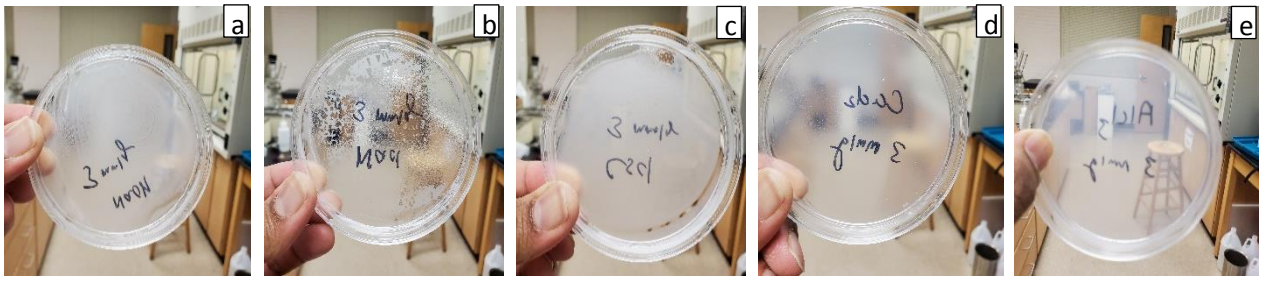

Fig.3.7. Images showing the transparency of the CNC films containing electrolytes (a) NaOH (b) NaCl (c) CsCl (d) $CaCl_2$ (e) $AlCl_3$ at 3 mmol/g concentration.

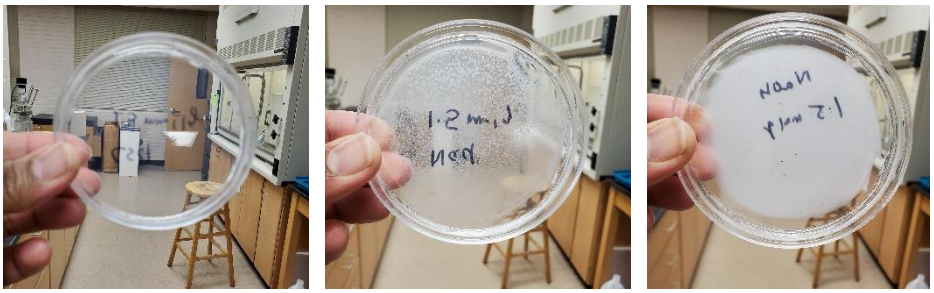

Fig.3.8. Images showing the transparency of the CNC films containing electrolytes (left) CsCl (middle) NaCl (right) NaOH at 1.5 mmol/g concentration.

3.3.3. Theoretical estimation of CNC twist parameter

Chiral nematic self-assembly in CNC film is a multistage process where the CNC phase changes with increase in concentration from isotropic (<3 wt.%) to biphasic (3 to 9 wt.%) to chiral nematic (>9 wt.%). At higher concentration (>10 wt.%) kinetic arrest sets in due to formation of gel phase which restricts further change in CNC self-assembly [251, 264]. For this sodium form of CNC, the chiral nematic to gel phase transition (g_c) is reported to be ~12 wt.% CNC concentration [265]; however, this has reduced in presence of electrolyte in the CNC suspension [260, 266]. Fig. 3.9 shows the CNC phase diagram for the NaCl containing CNC suspension. The initial concentration of CNC used for the preparation of films in this study was 1.64 wt.% which is in isotropic liquid phase, while the concentration of NaCl in this suspension corresponding to the transition concentration was ~6.42 mM. The arrow shown in Fig.3.9 follows the drying path during the film formation for this sample which gives liquid to gel transition at ~5.53 wt.% for this suspension.

It was shown according to Stroobants - Lekkerkerker - Odijk (SLO) theory that the effect of electrostatic interactions on the liquid crystal phase transition in suspensions of rod like polyelectrolyte can be characterized by the effective diameter and twisting action of these rods [267]. Effective diameter (D_e) of these rods is a function of debye length (λ_D), which in turn depend on the ionic strength (I) of solution. The debye length, effective diameter, and twist parameter (h) of rod like polyelectrolyte in suspension can be given as:

$$\lambda_D = \left(\frac{2\,e^2 I}{\varepsilon\varepsilon_0 K_B T}\right)^{-1/2} \qquad 3.5$$

Where $I = \frac{1}{2}\sum_{i=1}^{n}(c_i z_i^2)$

$$D_{eff} = D + 5.54\lambda_D$$

$$h = \frac{\lambda_D}{D_{eff}} \qquad 3.6$$

Where, *e* is charge of electron, ε is relative permittivity of water, ε_0 is vacuum permittivity, T is temperature of suspension, K_B is Boltzmann constant, *c* is concentration of counter ions in electrolyte, *z* is valency of counterions in electrolyte and D is diameter of the polyelectrolyte rods. Using this theory for CNC rods at maximum CNC suspension concentration of 5.53 wt.%, parameters such as $D_{eff,}\ I, \lambda_D, h$ are theoretically calculated as function of NaCl electrolyte concentrations ranging from 0 to 5 mmol/g which is close to its transition concentration. Fig. 3.10 shows these calculated parameters ($D_{eff,}\ I, \lambda_D, h$) as function of NaCl concentration. D_{eff} and twist parameter (*h)* has continuously reduced with increase NaCl concentration. The significant reduction in the twist parameter (*h)* of polyelectrolytes has been shown to promote the nematic phase over the chiral nematic phase [267]. This nematic phase formation is discussed in more detail in section 3.3.3.2. CNC twist parameter (*h)* drastically reduced and the chiral nematic to nematic transition occurred at *h* ~0.0955.

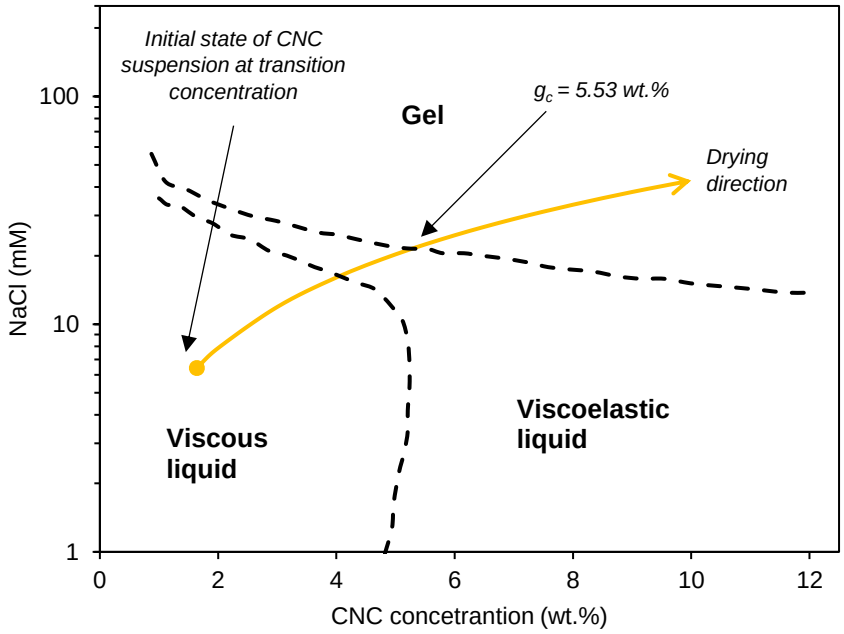

Fig.3.9. CNC aqueous suspension phase diagram in presence of NaCl [266].

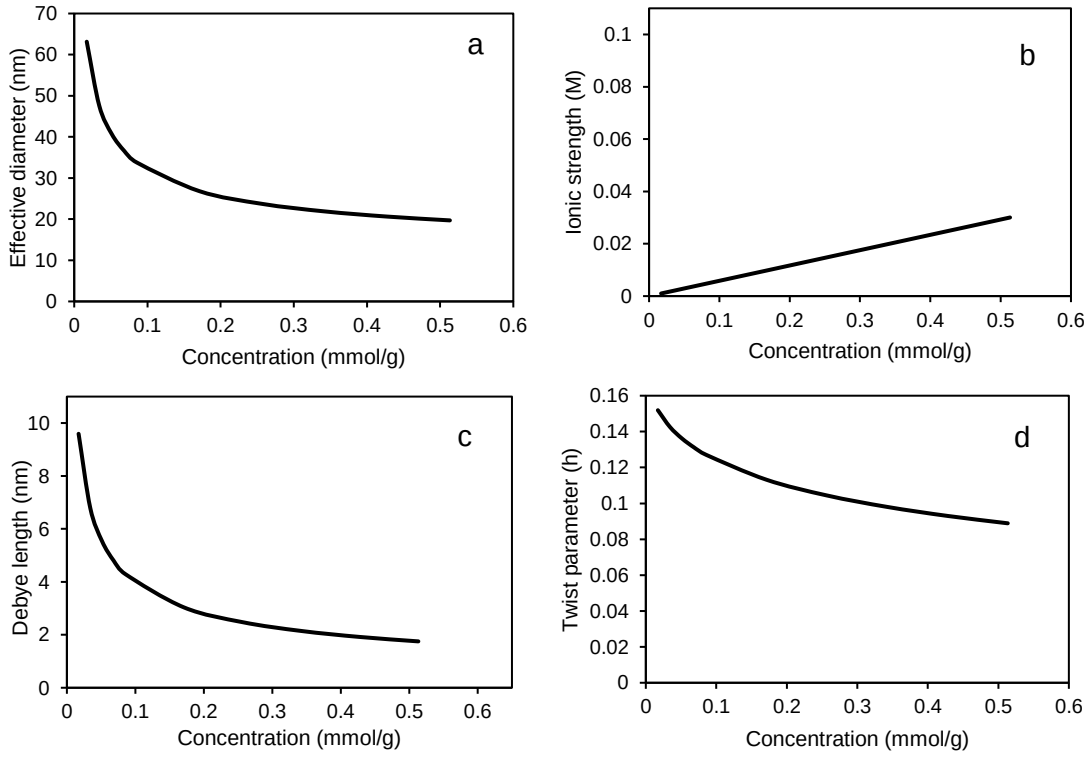

Fig.3.10. Calculated a) Effective diameter b) Ionic strength c) Debye length and d) Twist parameter for cellulose nanocrystals as a function of NaCl concentration.

3.3.4 Effect of electrolyte on self-assembly of CNC

3.3.4.1 Effect of electrolyte on CNC pitch

One complete helix within this helical chiral nematic order in CNC film corresponds to a pitch. The pitch of the chiral nematic CNC film can be estimated using wavelength corresponding to reflectance peak maxima as described in section 2.1. Indirect comparison of the pitch was carried out by comparing the transmittance peak minima (λ_{min}) of CNC films with various electrolyte concentrations upto transition concentration for each electrolyte type.

As shown in Fig.3.11 it was observed that λ_{min} reduced with small addition of electrolyte and increased at further electrolyte addition. This results from the corresponding reduction and then increase in the pitch of the CNC film. The decrease in pitch at lower electrolyte concentration is due to compression of the electrical double layer of CNC which causes reduction in effective diameter of the CNC rods. This increases the electrostatic interaction by increasing chiral twist power and hence the pitch of CNC film is reduced. Similar behaviour has been reported by Araki and Kuga[47], Hirai et al [268]and Dong et al.[114]. The electrolyte concentration corresponding to this pitch minima reduced with increase in counter ion valency. As higher charge in Al^{3+} and Ca^{2+} can significantly influence the electrical double layer compared to monovalent counter ions. Also, among monovalent counter ions CsCl concentration was lower than NaCl which may be due to higher affinity between the Cs^{+} and sulfate groups compared to Na^{+}. At higher electrolyte concentration pitch increased, which may be due to presence of more counter ions intercalating into CNC layers within the chiral nematically assembled CNC helix thereby reducing the chiral interaction.

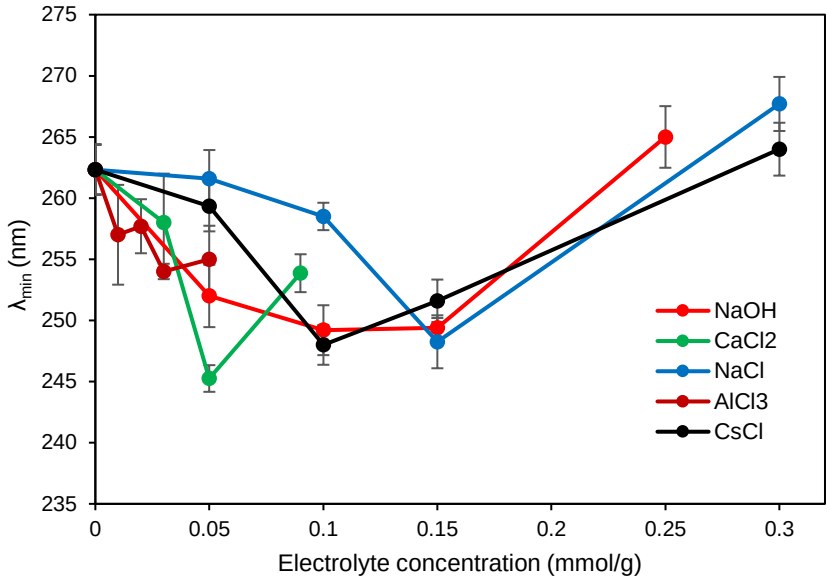

Fig.3.11. Effect of electrolyte concentration on λ_{min} of CNC film

3.3.4.2 Cross polarized optical microscopy of CNC films

As discussed previously, the transparency of the CNC film depends on the self-assembly of CNC rods. The CNC rods in chiral nematic films are helically oriented across the thickness of the film which exhibits various colors owing to circular polarization of the incident light [50], whereas for films with fully nematic arrangement of rods, a linear polarization of incident light is achieved [263]. Fig.3.12 shows the transmitted cross polarized optical microscopy images of CNC and electrolyte containing CNC films. These images were taken at two different orientations of the films which are 45° apart from each other. The transmitted light images of CNC films at these two positions showed clear contrast. The overall image appeared dark at 0° position with respect to either polarizer or analyzer, while strong birefringence occurred when turned to 45° position. This indicated that there is some degree of alignment of CNC rods within the film which can be

attributed to the nematic arrangements induced in transition regime concentration. As shown before, the pitch of CNC showed increasing trend as the concentration of electrolyte is increased. This increase in pitch indicates the decrease in angular dependence of electrostatic interaction between CNC rods and resulting twist. This mobility constraint favoured the formation of nematic domains in these CNC films. Similar results were also reported in literature for CNC suspensions containing NaCl [269, 270]. Nematic ordering of such CNC domains give rise to some degree of overall CNC alignment in the dried films.

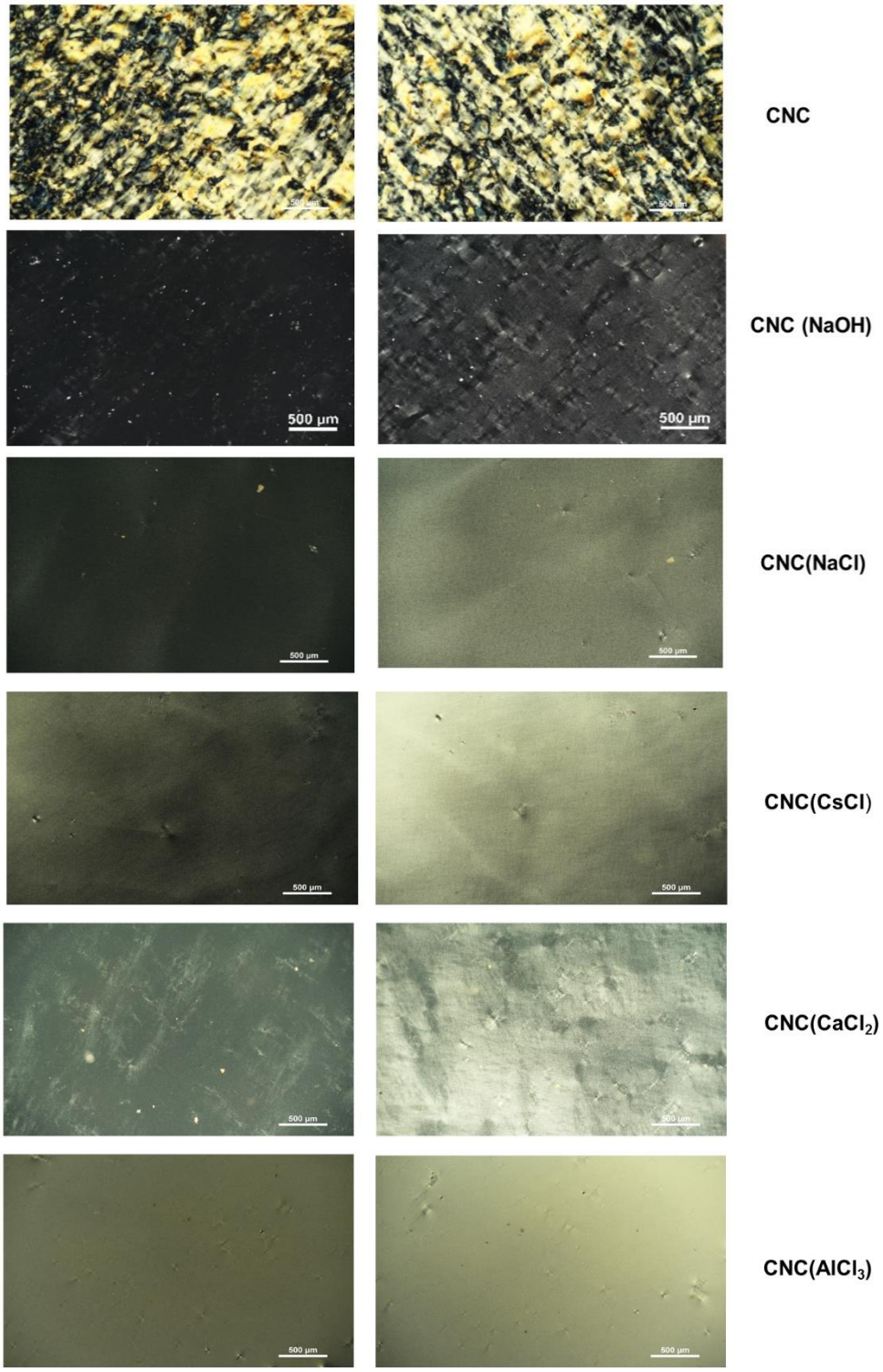

Fig.3.12 Cross polarized optical microscopy images of CNC films containing various electrolytes at transition concentration (First column – film position at 0° orientation to polarizer, Second column - film position at 45° orientation to polarizer).

In order to further understand the effect of counter ions on chiral nematic behavior, dialysis of as received CNC was carried out for 12 days in order to remove the counter ions. The as received CNC from University of Maine has mainly Na^+ counter ions. The conductivity of this dialyzed CNC suspension (3 wt.%) reduced to 112 μs/cm from its initial conductivity of 255 μs/cm. This sample was then used to cast the CNC film using 1.64 wt.% initial concentration and compared with as received CNC film using transmission spectra, zeta potential and cross polarized optical microscopy.

Dialyzed CNC had zeta potential of -44 (±1.2) mV which was slightly higher than the zeta potential of as received CNC -42 (±1.3) mV. Interestingly, dried film obtained from the dialyzed CNC resulted in transparent film without any iridescence. The transmission spectra of this film did not show any peak corresponding to characteristic chiral nematic reflectance (Fig.3.13 (b)). The cross polarized optical microscopy images of dialyzed CNC film in Fig.3.14 did not show characteristic fingerprint texture of chiral nematic self-assembly as observed for as received CNC in Fig.3.12. However, more uniform domains of different colors were observed. This observation was similar to the CNC film dried under orbital mixing where helical ordering was strongly distorted resulting in disappearance of reflection peak [271]. In this case, the removal of most of counterions (H^+ and Na^+) during dialysis could increase the effective diameter of CNC rods due to the repulsion by surface charges extending to long-range (Fig.3.15), this may have resulted in distortion of helical ordering and loss of reflectance peak. It was also observed that the visible light transmittance of this film was lower than the transparent CNC film obtained using optimum electrolyte additions as discussed in previous section. The reduced transparency of this film would be due to more scattering of visible light resulting from the distorted chiral nematic domains.

Compared to dialyzed CNC film, the CNC film prepared using optimum electrolyte concentration had more uniform refractive index because of presence of nematic domains.

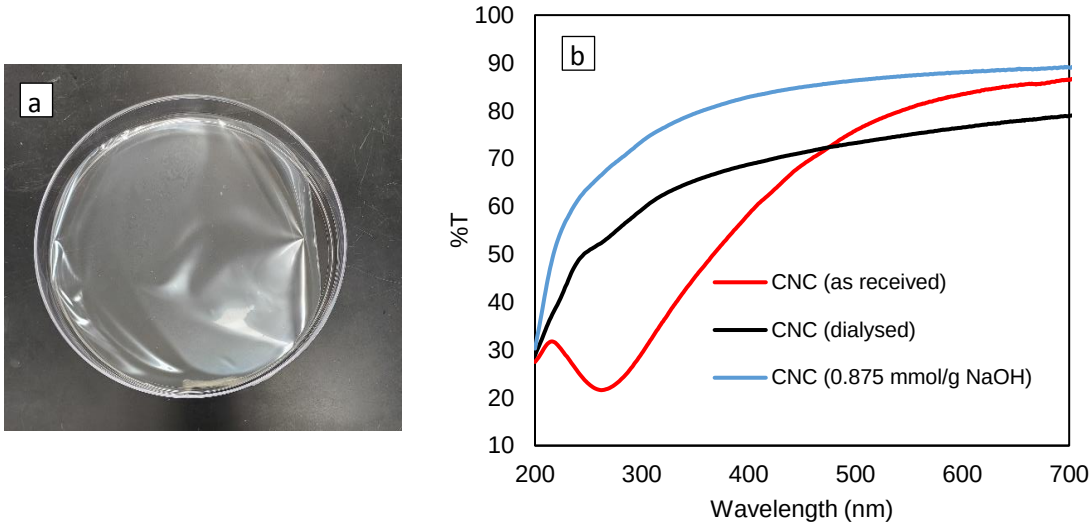

Fig.3.13. (a) Dried dialyzed CNC film (b) Transmission spectra comparison of different CNC samples.

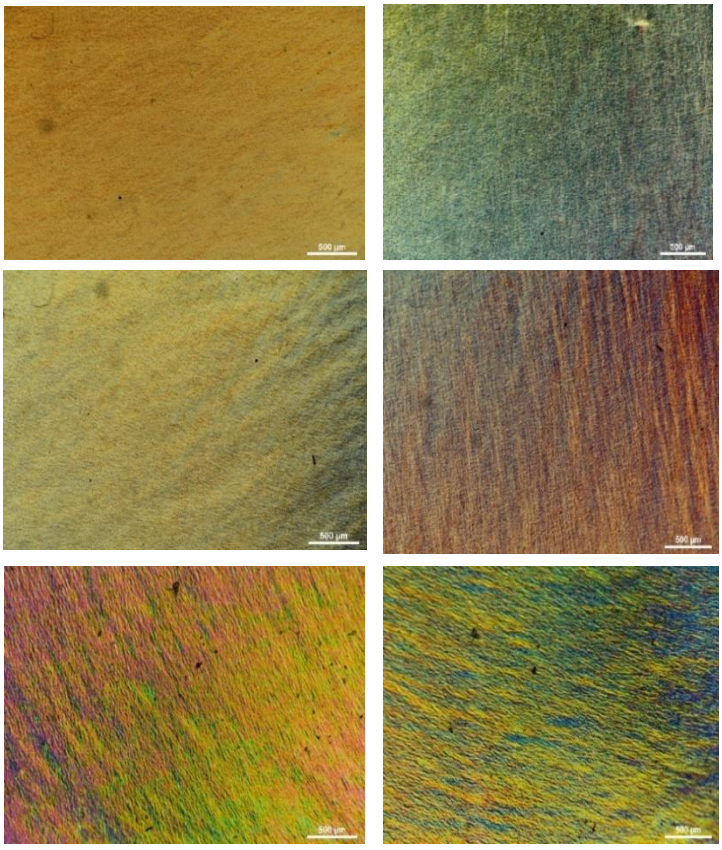

Fig. 3.14. Cross polarized reflected images of the dialyzed CNC films (First column – film position at 0° orientation to polarizer, Second column - film position at 45° orientation to polarizer).

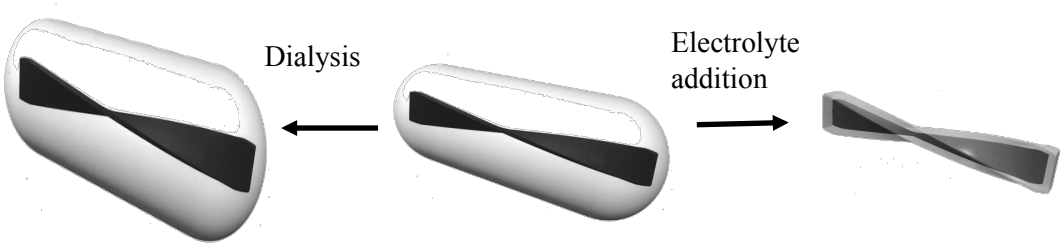

Fig. 3.15. Schematic representation of CNC rods showing influence of dialysis and electrolyte addition on effective diameter.

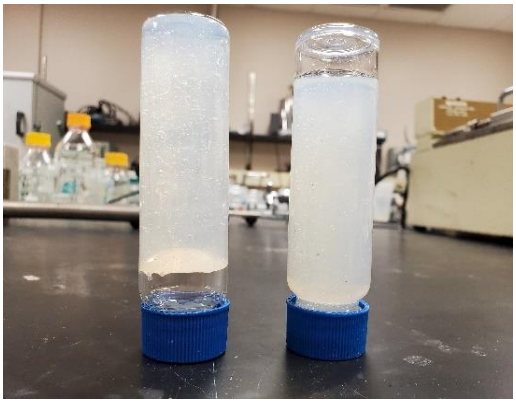

Fig.3.16. 5 wt.% aqueous samples of dialyzed CNC (left) and as received CNC (right).

Also, interesting phase behavior was observed when the 5 wt.% suspensions of dialyzed CNC and as received CNC were compared. Typically, sodium form of CNC shows isotropic phase for concentration upto 3 wt.%, biphasic in 4 to 9 wt.% range and gel concentration above 10 wt.%.[251, 272]. However, the 5 wt.% concentration of dialyzed CNC already turned into highly viscous gel phase as shown in Fig.3.16. This may be due to increased effective diameter and electroviscous effect of charged rods leading to formation of gel at lower suspension concentration [255, 269, 270, 273, 274]. It has been reported that presence of charge on CNC has significant influence on the viscosity of their aqueous suspensions. Sabet et al [275] reported much lower viscosity for non-charged cellulose nanocrystals produced from hydrochloric acid hydrolysis compared to sulfonated CNC.

3.3.5 Effect of electrolyte on CNC crystallinity

XRD patterns of CNC films with various electrolyte concentrations are shown in Fig.3.17. Pure CNC films showed characteristic XRD peaks at around $2\theta = 15.1°$, 16.9° and 22.9° corresponding to the cellulose I structure with reflection planes of (1-10), (110), and (200), respectively [276, 277]. It was observed that these peaks were present in all the CNC films containing electrolytes

concentrations upto 1.25 mmol/g suggesting that the crystal structure of cellulose I was not essentially altered in presence of electrolytes. Presence of electrolyte ions in CNC bulk decreased diffraction intensity of crystalline plane of CNC thereby reducing overall crystallinity of films. Similar observation is reported by Dai et al. [278] for CNC films containing copper chloride. The reduction in crystallinity was higher for CsCl containing films followed by $CaCl_2$, $AlCl_3$ and other monovalent electrolytes with increase in electrolyte concentration (Fig.3.18). This suggests that the large sized counterions have prominent effect on reducing the crystallinity of CNC film. Effect of NaCl on the structure of CNC in films was mentioned previously by Pan et al [49] where salt addition only slightly decreased crystallinity. NaOH containing films, cellulose I to cellulose II structural transformation did not occur for electrolyte concentration upto1.25 mmol/g [279].

In order to actually study the effect of electrolyte on crystallinity of CNC rods. CNC films containing 1.25 mmol/g electrolytes were prepared. These films were again redispersed and dialyzed to remove the electrolytes for 2 weeks. The remaining suspension was again casted to prepare the CNC films. These films were then characterized for XRD and their crystallinity was compared with the films without dialysis and control CNC film. The crystallinity of samples increased for monovalent electrolyte containing samples after dialysis due to removal of counter ions which interfered with diffraction intensity of CNC crystalline planes. For $CaCl_2$ and $AlCl_3$ containing films crystallinity did not improve after dialysis. Compared to control CNC sample, dialyzed CNC films containing monovalent electrolytes showed only slight or no reduction in crystallinity; while in case of $CaCl_2$ and $AlCl_3$ counterparts, significant reduction in crystallinity was observed (Fig.3.19). This may have resulted from the presence of Ca^{2+} and Al^{+3} counter ions on CNC surface due to their strong interaction with the negative sulfate ester groups. Moreover, the low conductivity of their dialyzed suspensions and inability to redisperse upon ultrasonication

further suggested that the Ca^{2+} and Al^{+3} counter ions are strongly interacting with the negative sulfate groups thereby screening the electrostatic repulsion between the CNC rods. On the other hand, monovalent electrolyte treated CNC samples could be easily redispersed by stirring their aqueous suspensions for only one hour (Fig.3.20). Overall, the crystallinity study using XRD showed its limitation in accurately estimating the CNC crystallinity in presence of counter ions.

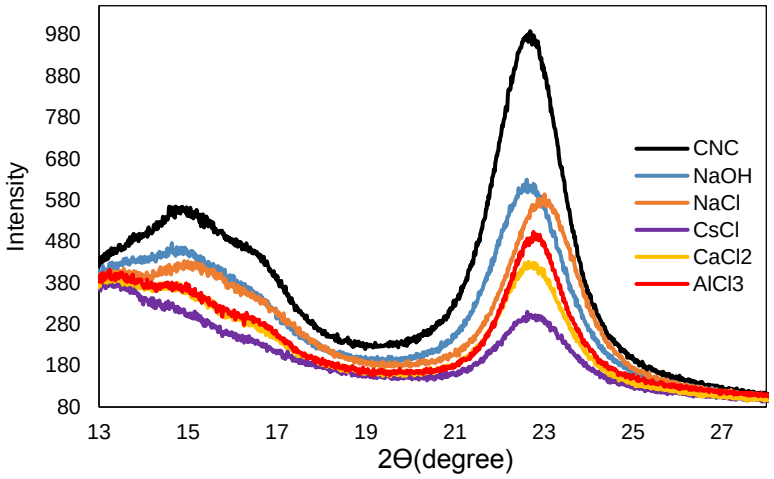

Fig.3.17. XRD plots for pure CNC films and CNC films containing 1.25 mmol/g of various electrolytes.

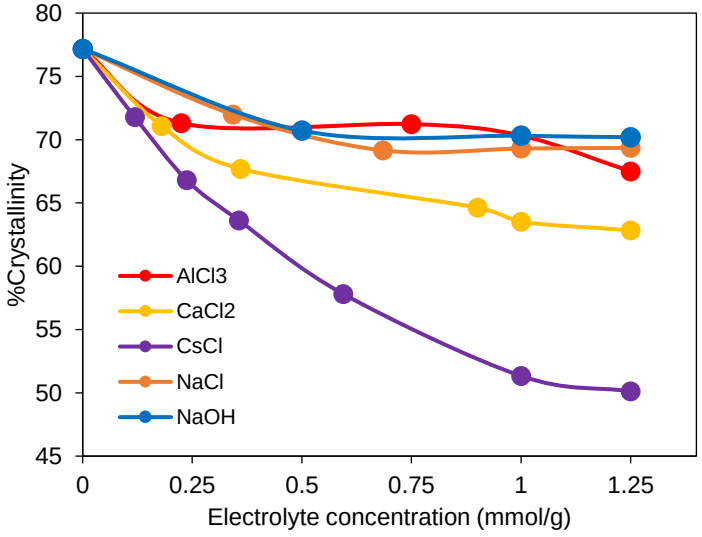

Fig.3.18. Crystallinity of CNC films containing electrolytes at different concentrations.

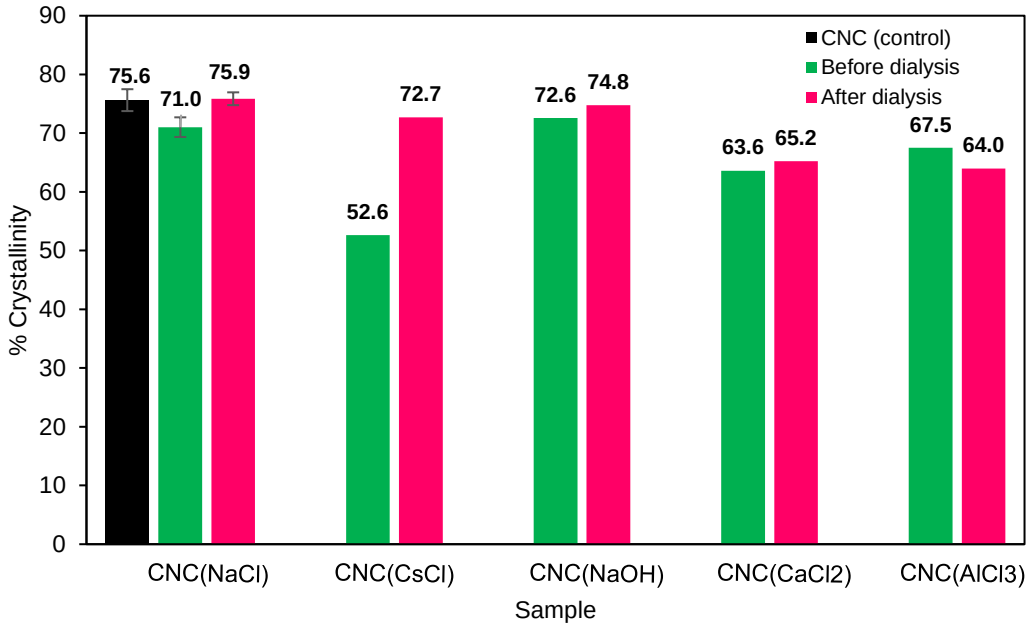

Fig.3.19. Crystallinity of CNC film samples added with 1.25 mmol/g electrolyte before and after dialysis.

Fig.3.20. Dialyzed and redispersed samples after treating with CsCl, NaCl, NaOH, $CaCl_2$ and $AlCl_3$ (from left to right).

3.3.6 Cellulose nanocrystal-kraft lignin nanocomposite films

In order to design the biodegradable, transparent, UV protection films, kraft lignin was incorporated into these CNC suspensions. The KL addition to the alkaline aqueous CNC suspensions produced transparent and homogeneous films of CNC/KL as shown in Fig. 3.21(d). As discussed before NaOH addition eliminated the iridescence in CNC film and produced highly transparent film. Moreover, the addition of NaOH also helped in uniformly dispersing KL in suspension producing the homogenous CNC/KL films. Such uniformity resulted due to alkaline conditions, where pKa of aromatic hydroxyl lignin group is achieved. Deprotonation of this hydroxyl group produced the phenolate anion, thus stabilizing the lignin molecules in aqueous suspensions through electrostatic repulsions. Uniform dispersion of lignin in aqueous suspension is also retained in the dried films, thereby producing highly homogenous CNC/KL films similar to that of lignin grafted CNC films [242]. Based on the maximum optical transmittance and ability to completely solubilize the largest concentration of KL used in this study, 0.875 mmol/g NaOH concentration was chosen to prepare CNC/KL films.

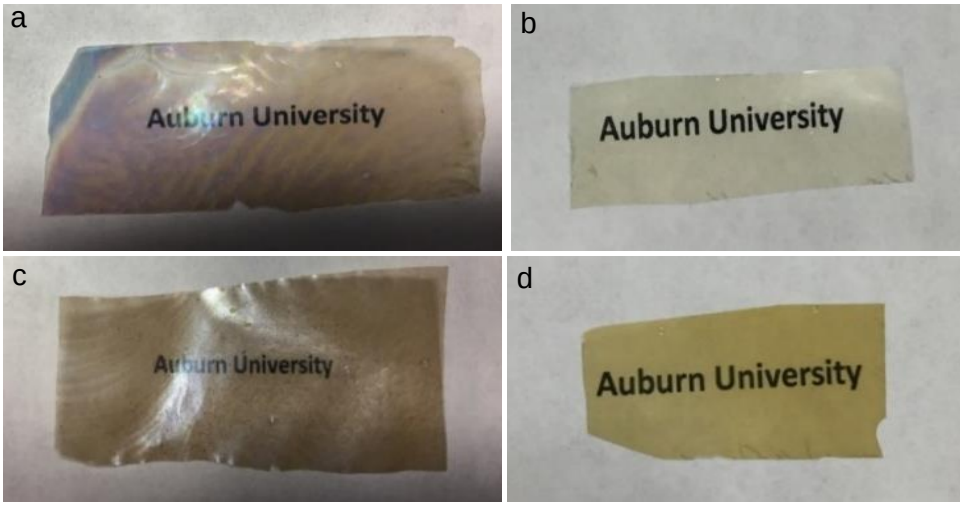

Fig.3.21. Images of (a) Pure CNC film (b) CNC film with 0.875 mmol/g NaOH addition (c) CNC/KL (2 wt.%) (d) CNC/KL (2 wt.%) with 0.875 mmol/g NaOH addition.

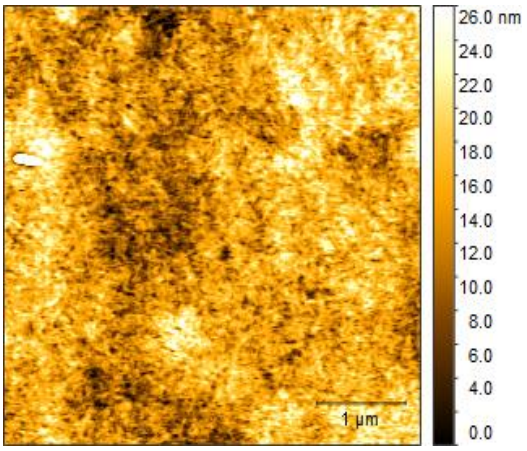

Fig.3.22. Topographical AFM images of CNC/KL (10 wt.%) films using alkaline aqueous mixtures.

The RMS roughness of the CNC/KL films was also measured using AFM. The average RMS roughness values were 7.3±1.3 nm and 12.9±1.4 nm for CNC and CNC/KL (10 wt.%) respectively. Topographical AFM images of the 10 wt.% CNC/KL film (Fig.3.22) showed homogeneity of lignin dispersion in the CNC matrix. Also, the SEM images of their cross-section in Fig.3.23 shows the uniform distribution of lignin particles across the film thickness. The thickness of the CNC/KL films increased linearly with the increase in lignin concentration (Fig.3.24), The average thickness of CNC film was 46.3 µm which has increased upto 67 µm upon 10 wt.% KL addition.

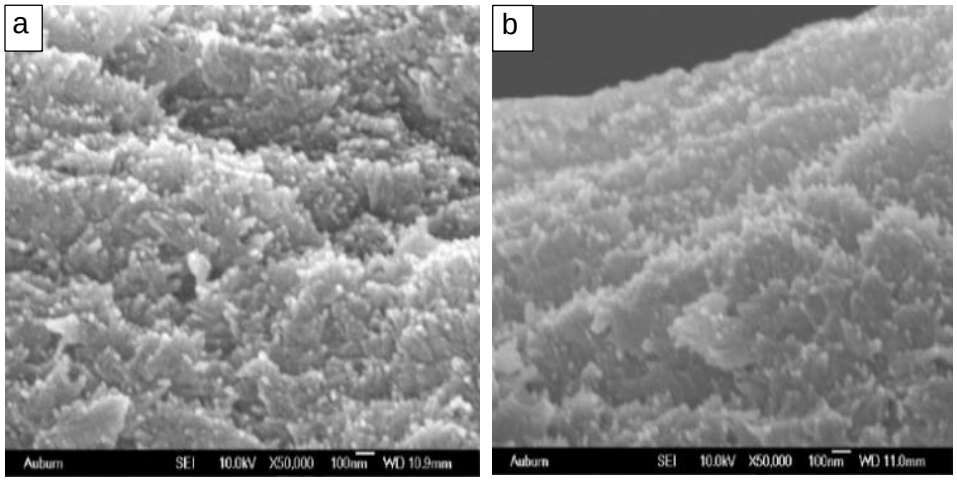

Fig. 3.23. Scanning electron microscopy images of the CNC/KL (10 wt.%) films.

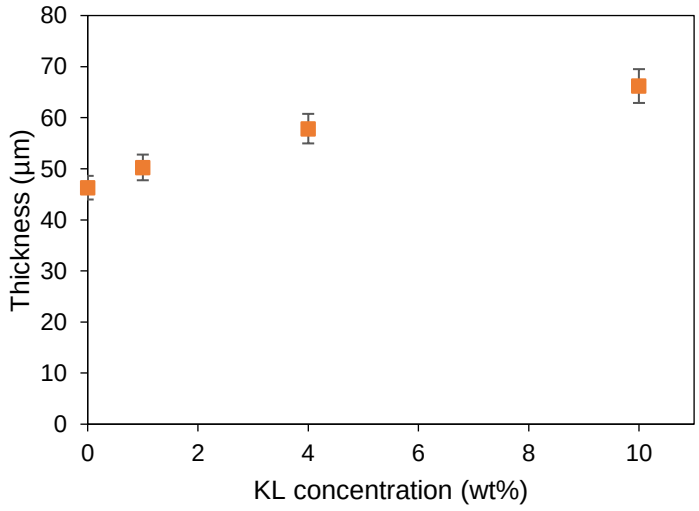

Fig.3.24. Thickness of the nanocomposite films with various lignin concentrations.

3.3.7 Optical properties of cellulose nanocrystal-kraft lignin films

Lignin has the ability to absorb the UV light due to its phenolic structure. UV blocking properties of CNC/KL films were characterized through its UV transmission spectra after incorporating the lignin at various concentrations. The UV−vis transmittance of the films was measured in the wavelength range of 200−800 nm, as shown in Fig.3.25. Transmission spectra includes all the normal incident light on the films exposed perpendicular to the light source excluding the absorbed and scattered light.

The CNC films showed a higher transmittance in the UV and visible regions, maximum transmittance for this film was upto 90%. The homogenous lignin containing films exhibited high transmittance in the visible spectrum and high absorption in the UV spectrum. As shown in Fig.3.25, CNC/KL films with 1 wt.% lignin contents, completely blocked UV-C (200 nm-280 nm) spectrum. Increasing lignin concentration to 4 wt.% completely blocked the UV-C and partially blocked the UV-B (280 nm - 320 nm). Whereas, at 10 wt.% lignin concentration total UV protection was obtained in the both films blocking UV-C, UV-B, and UV-A (320 nm-400 nm) spectrum. The UV protection behaviour and visible light transparency is similar to the covalently bonded microcrystalline cellulose/KL films prepared and reported by Sadeghifar et al[241]. However, the transparency of these films was lower compared to that of the CNC/organosolv lignin films, which have a lower thickness, reported by Hambardzumyan et al[240]. Since UV protection stability of films will determine their service life; the transmission spectra of films before and after exposure to UV light was compared for their UV blocking performance. for 2 hours. As shown in Fig.3.26, the transmission spectra for CNC and CNC/KL films did not change after UV exposure showing UV stability of the films.

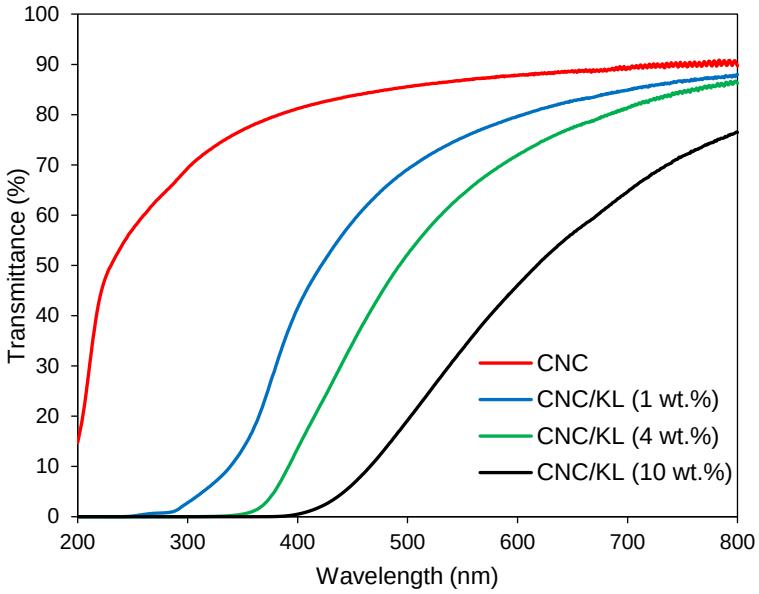

Fig. 3.25. UV-vis transmission spectra of CNC and CNC/KL films with various lignin concentrations.

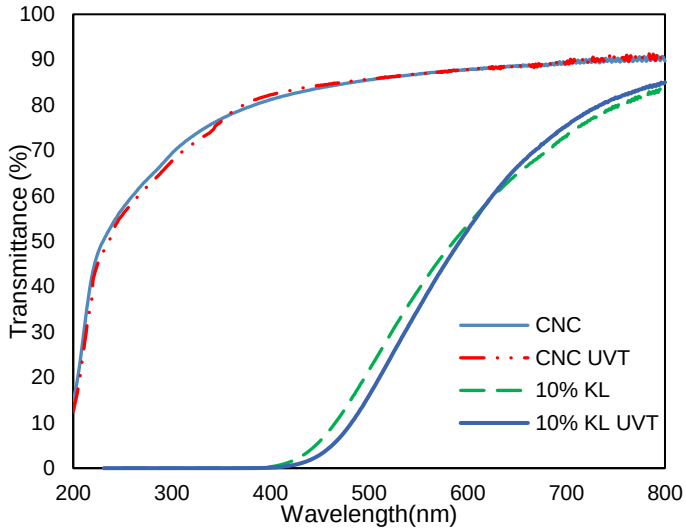

Fig.3.26. UV-Vis transmittance of CNC and CNC/KL (10%) films before and after UV (254 nm) exposure for 2 hours (UVT refers to UV Treated).

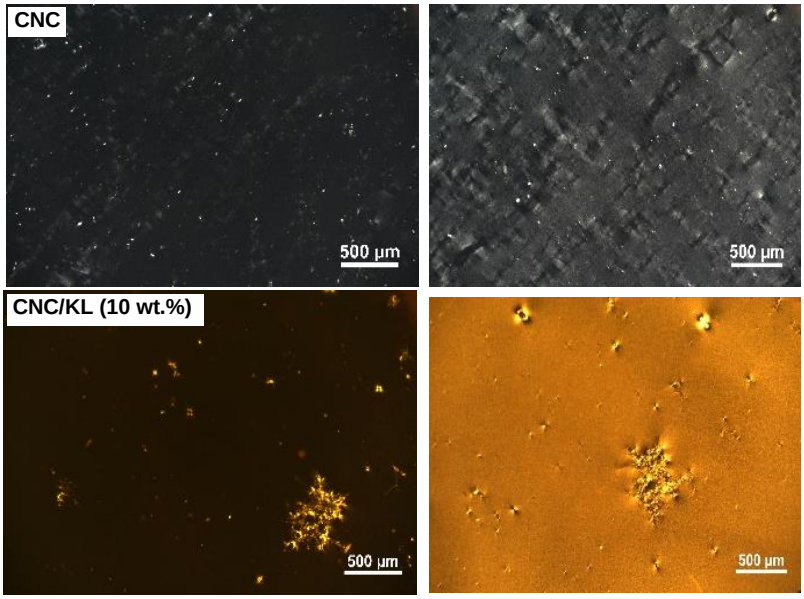

Fig.3.27. Cross polarized reflected images of the CNC (0.875 mmol NaOH) and CNC/KL films (First column – film position at 0° orientation to polarizer, Second column- film position at 45° orientation to polarizer).

Fig.3.27 shows the cross polarized optical microscopy images of CNC and CNC/KL films. It was observed that incorporation of KL did not hinder the NaOH induced self-assembly of CNC. Further optimization of CNC/KL films alignment under shear could improve the applicability of these nanocomposite films as polarizing and UV blocking films. Such films can be used as potential bio-based film material for the applications such as sunglasses, contact lenses, windows etc., where visible light polarization along with UV blocking properties are desired.

3.3.8 Kraft lignin color reduction through acetylation and oxidative treatments

Lignin in its natural form mostly occurs as light colored acetylated lignin in hardwoods [280]. However, it is transformed into the dark brown colored material during its isolation during pulping processes. In spite of many efforts, the isolation of totally unaltered native lignin is still a challenge [281, 282]. The kraft lignin exhibits UV blocking properties; however, it also absorbs the visible light due to colored chromophores induced during the kraft pulping processes. The dark brown

color of this lignin restricts its potential utilization as structural material or functional nanofiller in engineering plastics and nanocomposites. In order to improve the scope of optical applications of CNC/KL films, it is desirable to reduce the lignin color and improve the visible light transmission. Several methods are discussed in literature related to lignin color reduction [280, 283-286]. however, in some cases severe degradation of lignin aromatic structure lead to reduction in UV absorption properties, also the use of hazardous organic solvents render them unattractive to use for large scale applications [283, 287]. In this study we have used green approach using aqueous based hydrogen peroxide bleaching of KL and also compared their optical properties with acetylated KL which is commonly reported approach in literature for lignin color reduction [280, 288, 289].

Acetylation of KL replaces its phenolic hydroxyl groups with the acetyl groups. This prevents the excessive conjugation with benzene rings thus reducing the formation of quinone and quinone methide like chromophores resulting in light colored lignin [280]. However, acetylated lignin is water insoluble which limits its aqueous solvent based processing. KL acetylation was carried in presence of acetic anhydride and pyridine. Degree of acetylation of the lignin samples was qualitatively determined from their FTIR spectra performed before and after acetylation as shown in Fig.3.28. For Ac-KL samples, a stretching vibrational band of the hydroxyl groups between 3200 and 3400 cm^{-1} is eliminated showing complete acetylation of the hydroxyl groups. Also, the C=O stretching vibrational absorptions for phenolic and aliphatic acetyls could be observed in Ac-KL at 1760 cm^{-1} and 1740 cm^{-1}, respectively.

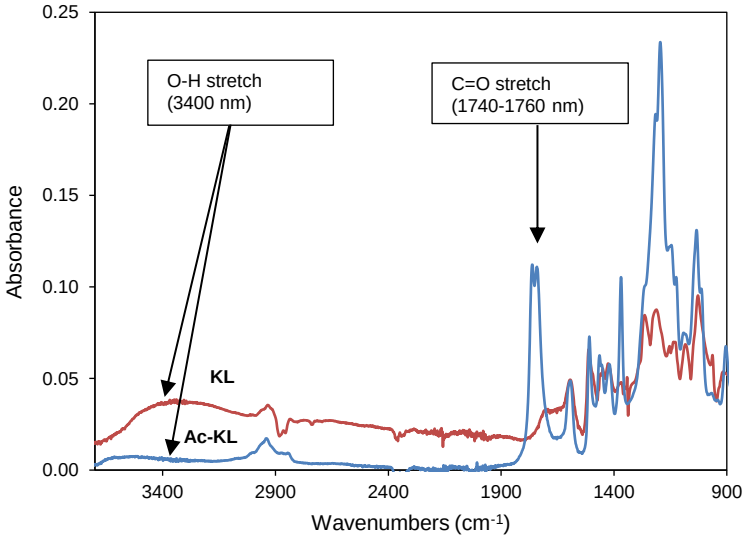

Fig.3.28. FTIR spectra comparison of KL and Ac-KL.

Fig.3.29 shows the change in color obtained after the acetylation of KL, the dark brown color of KL has significantly reduced to the light brown color. 0.1 wt.% solutions of KL and Ac-KL were prepared using 1:1 (v/v) dioxane/water solutions. Fig.3.30 shows the transmission spectra of the 0.1 wt.% solutions of these lignin samples. It was observed that due to lignin color reduction, the visible light transmission at 550 nm is enhanced by 160 % for KL lignin samples. The UV blocking properties of the lignin are only slightly affected due to the acetylation, Ac-KL can still block the UV light upto 375 nm compared to 400 nm obtained for KL.

The extinction coefficient values for the lignin samples listed in Table 3.1 also shows slight reduction after the acetylation. The UV absorption properties of lignin are mostly retained due to the retention of its aromatic structure after acetylation. Fig.3.31 (a) and Fig.3.31 (b) show the effect of lignin acetylation on the transparency and transmission spectra of CNC/lignin films, respectively. The visible light transmittance of 10 wt.% CNC/Ac-KL film at 550 nm is enhanced

by 67% compared to 10 wt.% CNC/KL film, without significantly affecting the UV blocking properties.

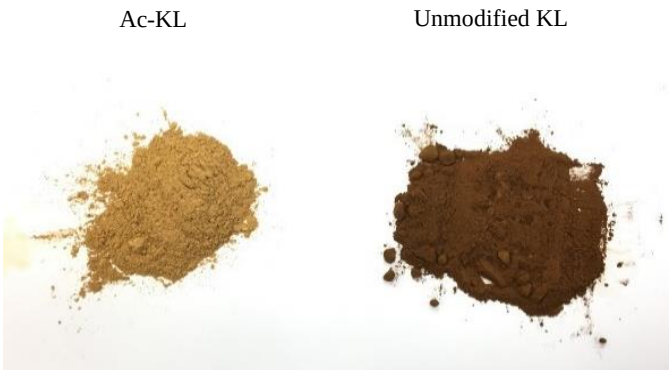

Fig. 3.29. Kraft lignin samples before and after acetylation.

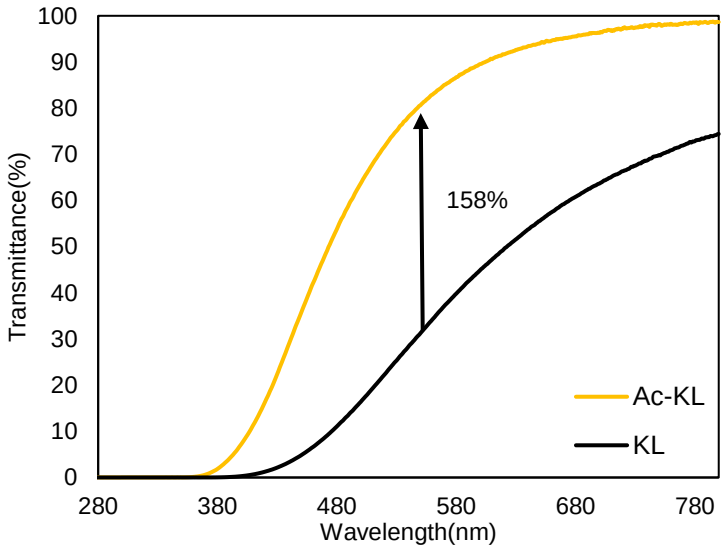

Fig.3.30. Transmission spectra showing the increase in transparency for 0.1 wt.% solution of KL and Ac-KL in dioxane/water (0.5/0.5 v/v) before and after peroxide bleaching.

Table 3.1. Extinction coefficient values for various lignin samples.

Sample	Extinction coefficient at 255 nm ($wt.\%^{-1}\ cm^{-1}$)
KL	223.8
Ac-KL	214.4

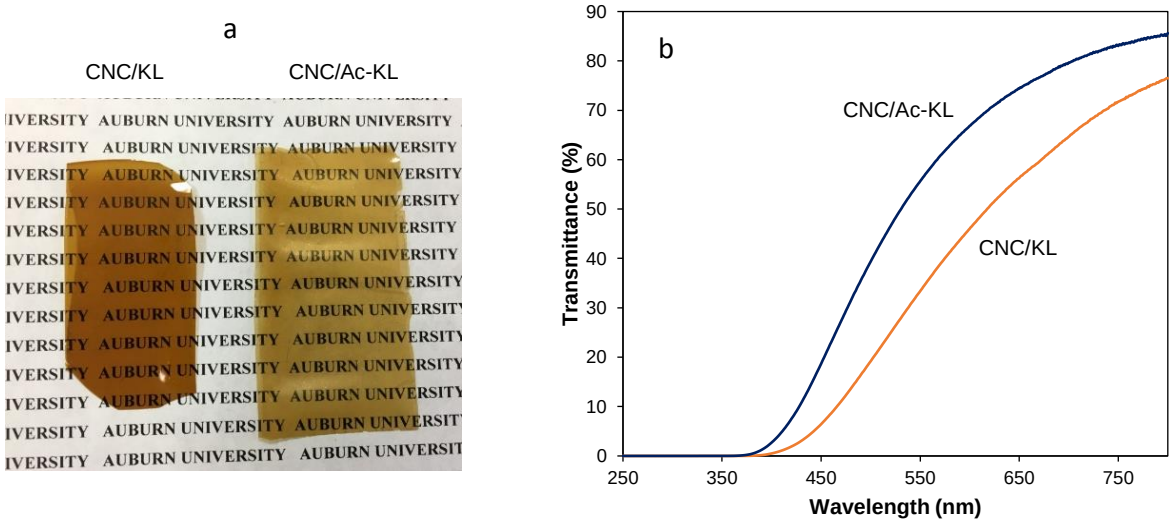

Fig. 3.31. (a) CNC/KL (10 wt.%) and CNC/Ac-KL (10 wt.%) films (b) Transmission spectra of comparison for CNC/KL (10 wt.%) and CNC/Ac-KL (10 wt.%).

In another approach for lignin color reduction, oxidative treatment of KL was carried out using hydrogen peroxide. For efficient bleaching of KL, the optimized processing conditions in terms pH, time and temperature based on studies by Wenming and Barnett et al [247, 290] were used. However, in this study the peroxide concentration was varied to study its effect of H_2O_2 charge on KL optical properties. Bleaching was carried out by varying the H_2O_2/KL weight ratio from 0.5 to 10 at pH of 12, and temperature of 75 ^oC for 2.5 hours. Peroxide bleaching is considered as mostly lignin retaining bleaching with less lignin structure degradation compared to other more

harsher bleaching treatments. Color reduction during peroxide bleaching of lignin is attributed to the oxidation of existing chromophores to colorless bodies [291].

Analysing the IR spectra of peroxide oxidized KL (Fig.3.32), it is observed that bands representing the bond stretching vibrations of the aromatic rings became weaker due to oxidative degradation. The characteristic bands of the aromatics at 1125 cm^{-1}(aromatic C-H in plane deformation), 1426 cm^{-1} (aromatic skeletal vibration combined with C-H deformation), 1512 cm^{-1} (asymmetric aryl ring stretching) and 1595 cm^{-1}(symmetric aryl ring stretching) have lower intensity compared to KL and also shifted to lower wavenumbers**.** The carbonyl peak in KL at 1702 cm^{-1} represent carbonyl, carboxyl or quinones [292, 293]. This peak has vanished after the peroxide oxidation which may be due to oxidation of colored chromophores during bleaching.

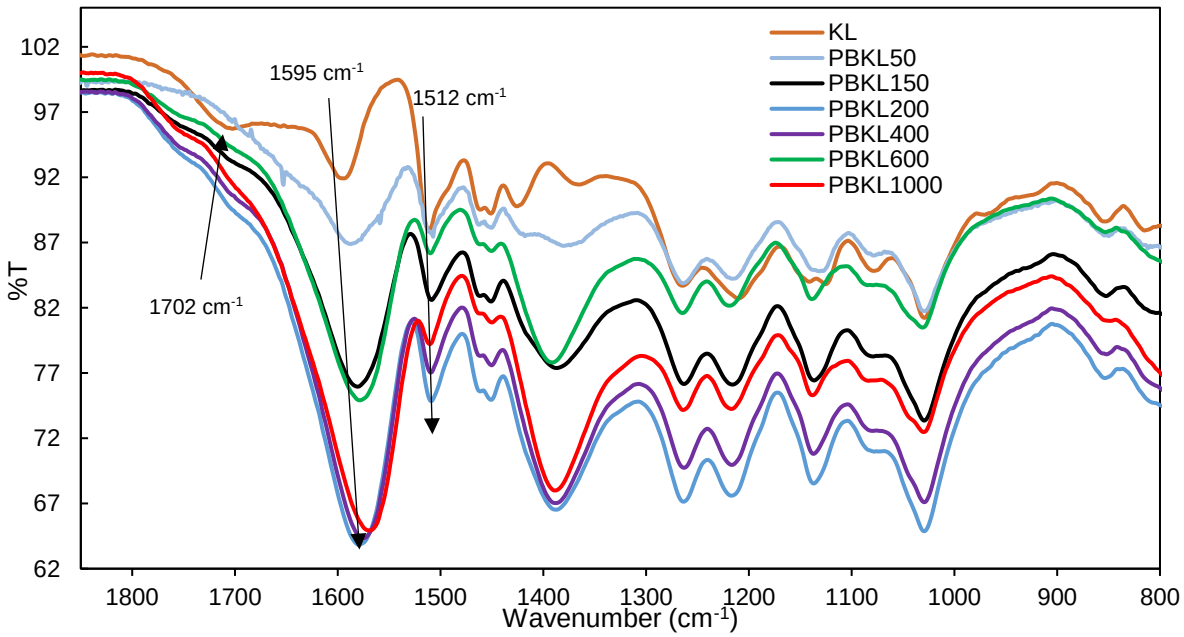

Fig.3.32. FTIR spectra of KL and peroxide bleached KL samples.

It was observed that increase in peroxide charge improved the color reduction. As shown in the Fig.3.33, 0.1 wt.% PB-KL1000 solution looked more transparent compared to 0.1 wt.% KL. Fig.3.34 shows % transmittance at 550 nm improved drastically upto 150% H_2O_2 charge after which transmittance improved only slightly. At the same time UV blocking properties of KL showed reverse trend, where reduction in % UV blocking at 400 nm was observed. H_2O_2 charge of 150% seems to be reasonably optimized peroxide concentration in terms of transparency and UV blocking properties of bleached KL and was used to prepare the nanocomposite films.

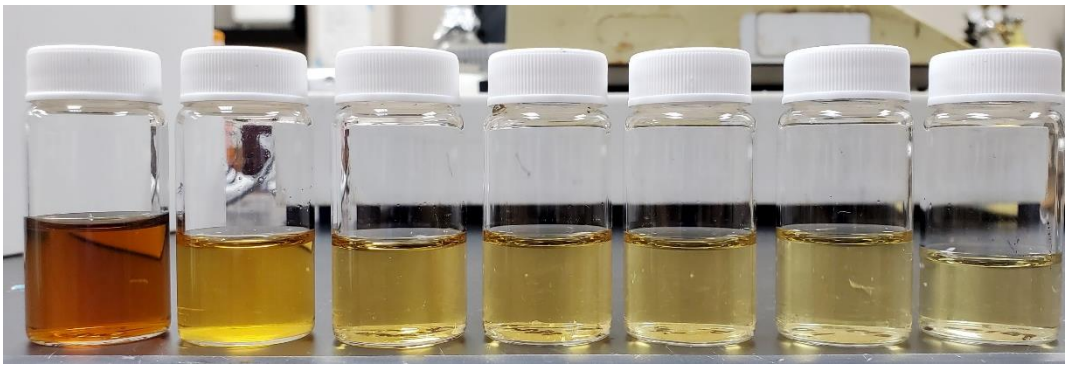

Fig.3.33. 0.1 wt.% peroxide bleached samples (from left to right) KL, PBKL50, PBKL150, PBKL200 PBKL400, PBKL600, PBKL1000.

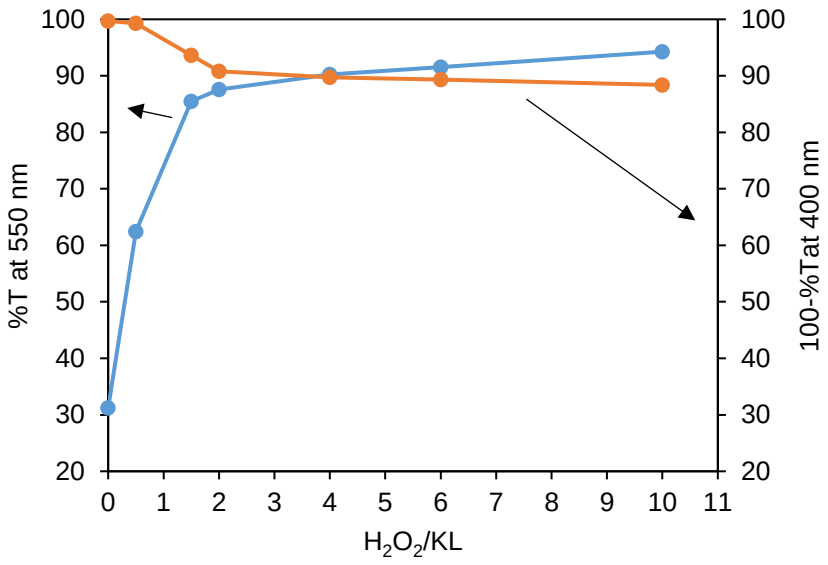

Fig.3.34. Effect of H_2O_2/KL ratio on %T at 550 nm and %UV blocking at 400 nm of 0.1 wt.% bleached lignin solutions.

Table 3.2. Effect of H_2O_2 concentration on lignin optical properties. (%T550 nm and %UV blocking at 400 nm obtained for 0.1 wt.% lignin solution and extinction coefficient obtained using absorbance at 255 nm).

H_2O_2 Conc. (wt%)	H_2O_2/KL	%T at 550 nm	% UV blocking at 400 nm	Extinction coefficient at 255 nm (wt.%$^{-1}$ cm^{-1})
0	0	31.2	99.7	223.8
50	0.5	62.5	99.3	206
150	1.5	85.5	93.7	187.3
200	2	87.6	90.8	185
400	4	90.3	89.8	175.2
600	6	91.6	89.4	157.3
1000	10	94.3	88.4	148.9

Fig.3.35 compares the transmission spectra of modified KL based nanocomposite films with 4-ABA which is commercially used water-soluble UV-absorbent. CNC/PBKL150 (10 wt.%) has significantly improved the transparency of nanocomposite films by ~97% compared to CNC/KL (10 wt.%), while for CNC/Ac-KL (10 wt.%) transparency improved by 66.5%. In both cases almost complete UV blocking was achieved, this showed the effectiveness of peroxide

treatment approach over acetylation. Moreover, unlike acetylation peroxide treatment is faster and do not require hazardous organic solvents.

It is observed that the CNC/PBKL150 (4%) film has shown similar transparency as that of the CNC/4-ABA (10 wt.%), with improved UV-blocking properties in UV-A spectrum (315-400 nm). CNC/4-ABA (10 wt.%) blocked of 54.3% of UV-A (315-400 nm) spectrum of light, whereas CNC/PBKL150 (4%) could block 87.5% of UV-A spectrum. Both samples showed complete blocking of UV-B (280-315 nm) spectrum. This suggests that the PBKL has promising potential as UV absorbent to be used as an alternative for the commercially used organic UV absorbers. The utilization of this water soluble, light colored modified KL can also be extended as functional nanofiller in other hydrophilic transparent polymeric matrices.

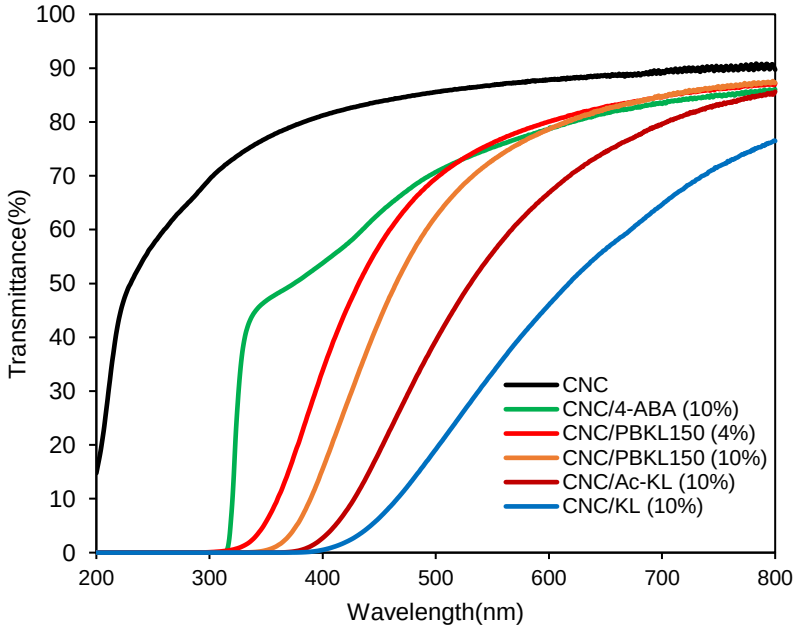

Fig. 3.35. Transmission spectra of CNC, CNC/4-ABA, and CNC/lignin nanocomposite films (0.68 mmol/g NaCl added to films).

Table 3.3. %UV A, %UV B, %UV blocking at 400 nm and %T at 400 nm for CNC and CNC nanocomposites.

Sample	%UV A blocking	%UV B blocking	%T at 550 nm	% UV blocking at 400 nm
CNC	19.9	26.6	86.8	18.8
CNC/KL (10 wt.%)	99.9	100.0	33.4	99.5
CNC/4-ABA (10 wt.%)	54.3	99.5	75.3	46.2
CNC/PB-KL150 (4 wt.%)	87.5	99.9	76.1	66.2
CNC/PB-KL150 (10 wt.%)	99.3	100.0	65.6	95.3
CNC/Ac-KL (10 wt.%)	99.6	100.0	55.6	97.3

Fig.3.36 presents the quantitative comparison of transparency and UV-shielding properties of the lignin based transparent nanocomposites reported in the literature. The CNC/PBKL150 composites in this study are among the nanocomposites with superior performance in terms of transparency and UV blocking at 400 nm. CNC/lignin nanocomposites in this study are more attractive than other nanocomposites because of their biodegradability, nontoxicity, and abundance. Morphological characterizations of CNC/Ac-KL (10 wt.%) and CNC/PB-KL150 (10%) carried out using SEM showed also showed uniform and homogenous lignin distribution across their film thickness (Fig.3.37).

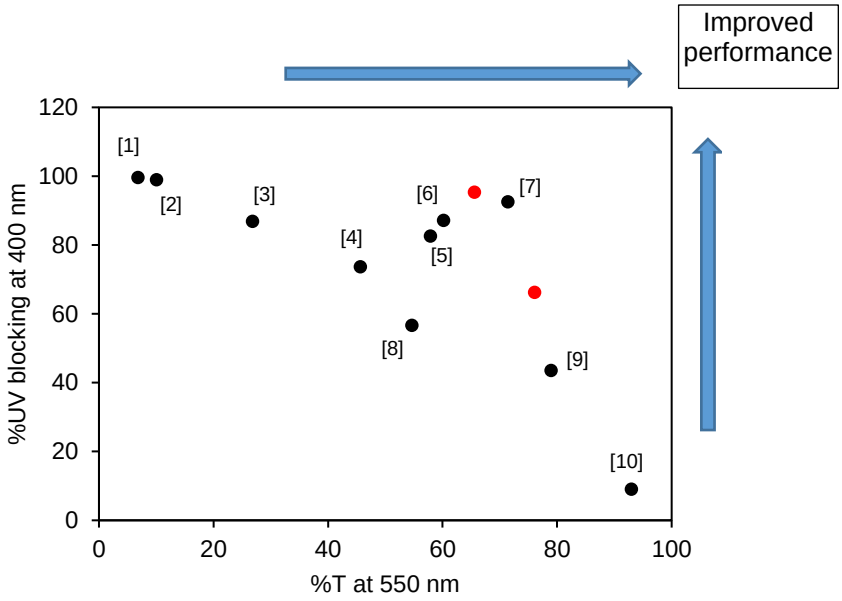

Fig.3.36. Comparison of transparency and UV blocking at 400 nm CNC/PBKL150 with lignin based transparent nanocomposites in literature. Red dots correspond to this study (1- [73], 2-[294], 3-[295], 4-[296], 5-[241], 6-[297], 7-[298], 8-[295] , 9-[240] , 10-[73]).

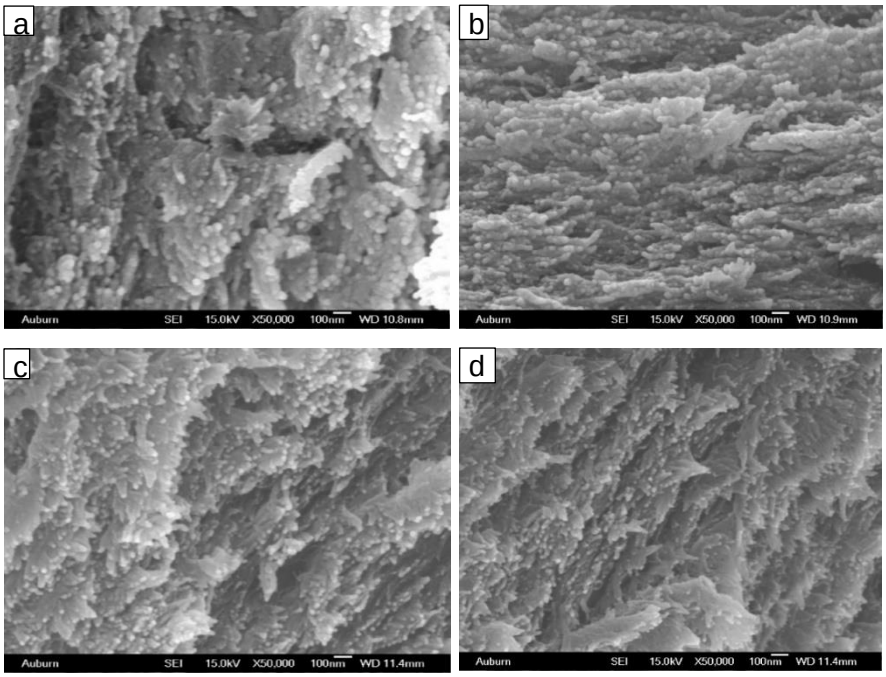

Fig.3.37. Scanning electron microscopy images of the CNC/lignin film cross sections showing the lignin dispersibility in 10 wt.% CNC/PBKL150 (a) and (b), 10 wt.% CNC/Ac-KL (c) and (d).

3.3.9 Effect of electrolyte and lignin on CNC film mechanical properties

CNC iridescent films show brittle and stiff behaviour due to rigid CNC rods and lack of energy dissipation phase in the film. Pure CNC films showed the tensile strength of 65.8±16.1 MPa, because of its brittle nature its stress−strain curve shows only initial elastic deformation region without any plastic deformations (Fig.3.38 and Fig.3.39). For CNC films containing electrolytes, electrolyte addition in certain concentration range showed improvement in tensile strength. This may be due to the generation of more ionic bonding between the negatively charged sulfate ester groups of CNC and positive counter ions in electrolyte, which are stronger compared to the hydrogen bonding interactions [299]. Previously, effect of counter ions on the mechanical properties of CNC/CMC nanocomposite films and TEMPO-CNF films were studied. In both cases improved strength properties were reported when the counter ions such as Na^+, Cu^{2+}, Fe^{3+}, Li^+, Cs^+ were introduced during the film preparation [300-303].

It was observed that upto 50-55% improvement in tensile strength of CNC film was observed at certain optimal concentration range of electrolyte addition. This improved film strength could be due to the increase in ionic bonds between the negatively charged sulfate ester groups and positively charged counter ions. However, at higher concentration of electrolytes the disruption of hydrogen bonding interaction between the CNC rods resulted in deterioration of film strength. In this case the multivalent electrolytes resulted in larger deterioration in tensile strength of CNC film compared to monovalent electrolytes for the concentrations upto 1.25 mmol/g. Interestingly, tensile strength of NaOH containing film did not deteriorate unlike other electrolytes. This could be due to hydroxyl counter ions interaction with nanocrystals. It was also observed that this optimal electrolyte concentration was lower for multivalent electrolytes ($CaCl_2$ and $AlCl_3$) compared to monovalent electrolytes (NaCl, CsCl, NaOH) suggesting larger ionic bonding

interaction between CNC and multivalent electrolytes for given concentration. Elongation at break of CNC film was slightly increased with addition of electrolytes (Fig.3.39 (b)), showing small dissipation of energy in presence of electrolytes. Presence of lignin had negative impact on mechanical properties of electrolyte containing CNC film. 10 % CNC/KL with 1 mmol/g addition of NaOH showed tensile strength and strain % similar to pure CNC film. KL incorporation affected the ionic and hydrogen bonding interactions in the CNC (1 mmol/g NaOH) film.

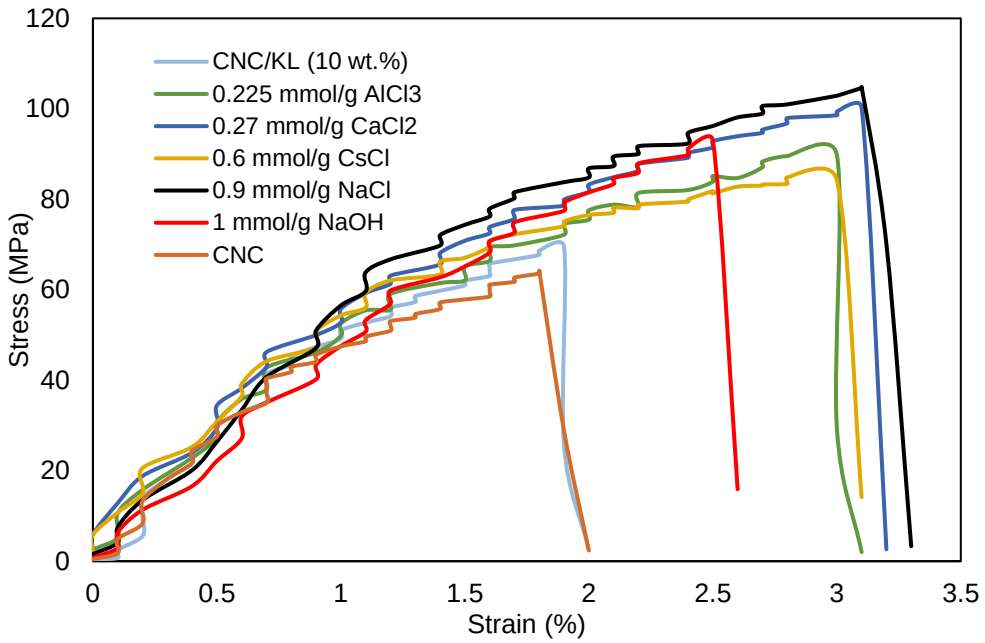

Fig.3.38. Stress vs strain% curve of CNC films containing various electrolytes (optimal concentration) and 10% KL.

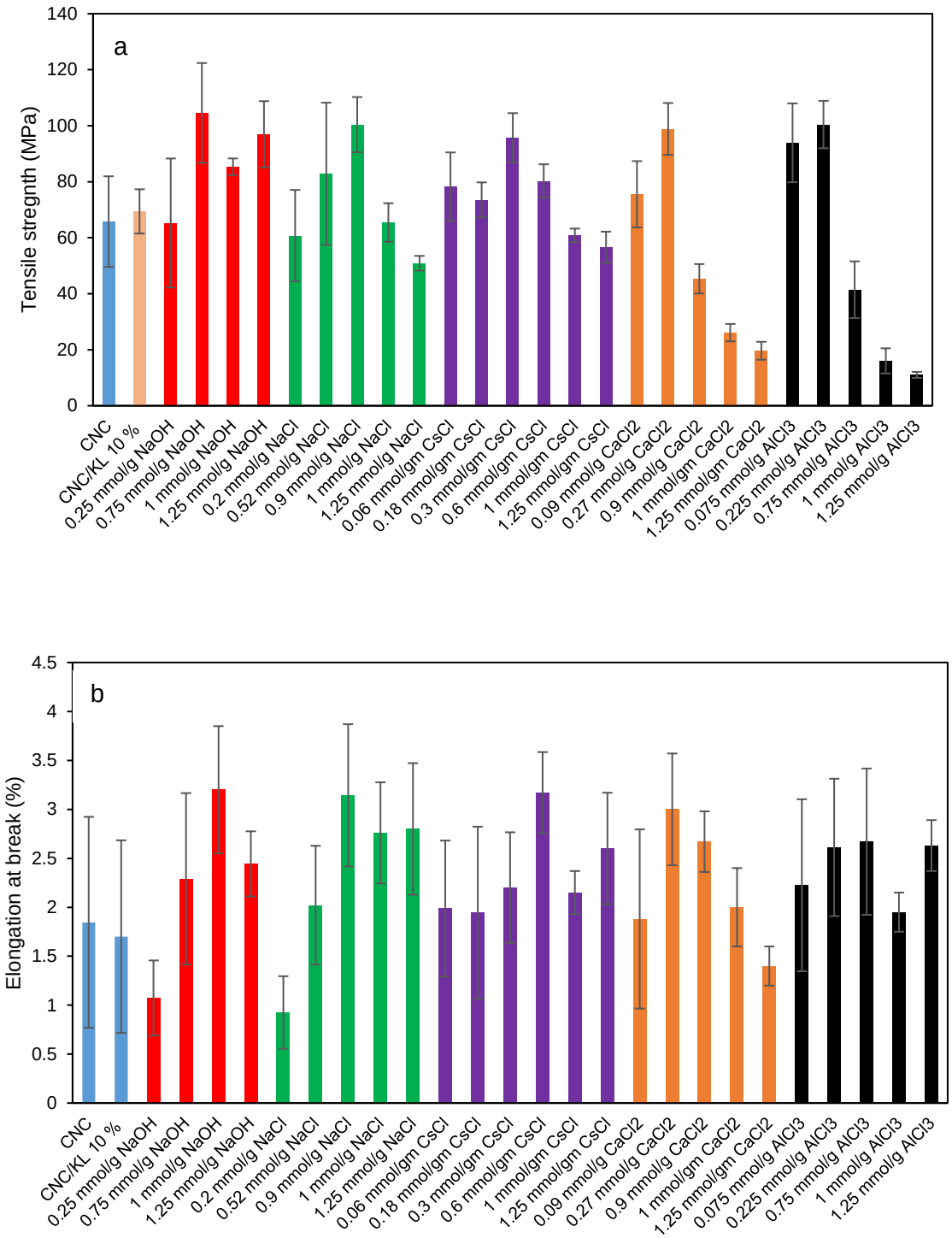

Fig.3.39. (a) Tensile strength and (b) Strain% of CNC films containing electrolytes with various concentrations.

3.3.10 Effect of lignin on CNC surface properties

Owing to its aromatic structure and the fewer hydroxyl groups compared to CNC, lignin is generally considered relatively more hydrophobic than CNC. However, no appreciable change in hydrophobicity was observed upon addition of 10 wt.% KL to CNC as static contact angle did not increase significantly for the CNC/KL films. Average static contact angles measured for 10 wt.% CNC/KL and neat CNC samples were in the range of 43±2º (Fig.3.40). However, it was observed that for KL containing CNC films the contact angle was more stable than that of neat CNC films. Within first hundred seconds the contact angle of 10 wt.% KL containing films CNC/KL reduced to 38°. Whereas, for CNC films contact angle rapidly reduced to 25°. In case of CNC films, hydrophillic hydroxyl groups are easily available for the water molecules. The water droplet spreads easily on the surface thereby rapidly reducing the contact angle. For CNC/KL samples, penetration into the films was reduced by the uniformly dispersed hydrophobic KL network surrounding the cellulose nanocrystals in the matrix. Unexpectedly similar initial contact angle of CNC and CNC/KL films may be due to low concentration of lignin present on the surface of the film.

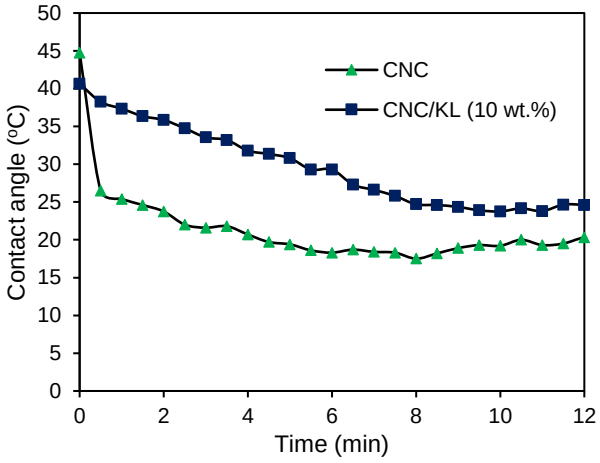

Fig.3.40. Contact angle measurements for CNC and CNC/lignin samples as a function of time.

3.3.11 Effect of lignin on CNC film thermal stability

Thermal decomposition of CNC and CNC/lignin films were studied using thermogravimetric analysis in an inert nitrogen medium. Decomposition behaviour in terms of weight % vs temperature and derivative weight % vs temperature (DTG plot) are shown in shown Fig.3.41(a) and 3.16(b), respectively. DTG plot shows large peaks between temperature range 300 °C to 330 °C which largely corresponds to pyrolysis of cellulose chains resulting from depolymerization, dehydration, and decomposition of glycosyl units [304, 305]. Similar thermal behaviour was obtained for the NaOH treated sulfonated CNC [306]. Smaller peaks between 180°C-190°C for all the samples corresponds to sulfate group decomposition, whereas peaks around 230 °C observed in case of CNC/KL would be due to presence of impurities induced in KL during kraft processing.

Thermal stability of the CNC films is enhanced upon incorporation of the KL. Fig.3.41(a) showed more weight loss at any given temperature for the CNC films compared to lignin containing films. Peak temperature (T1) from DTG plot corresponding to CNC pyrolysis has shifted to higher temperature upon lignin addition. T1 for neat CNC films is 307 °C, which has increased to 312 °C for 10 wt.% CNC/KL. Presence of the phenolic OH groups within the lignin structure and the aromatic char originating from the lignin at elevated temperature are responsible for the thermal stability characteristics of the lignin incorporated in polymer matrix [307-310]. The increased thermal stability of the nanocomposite films makes lignin-based films a promising candidate for applications in severe environmental conditions.

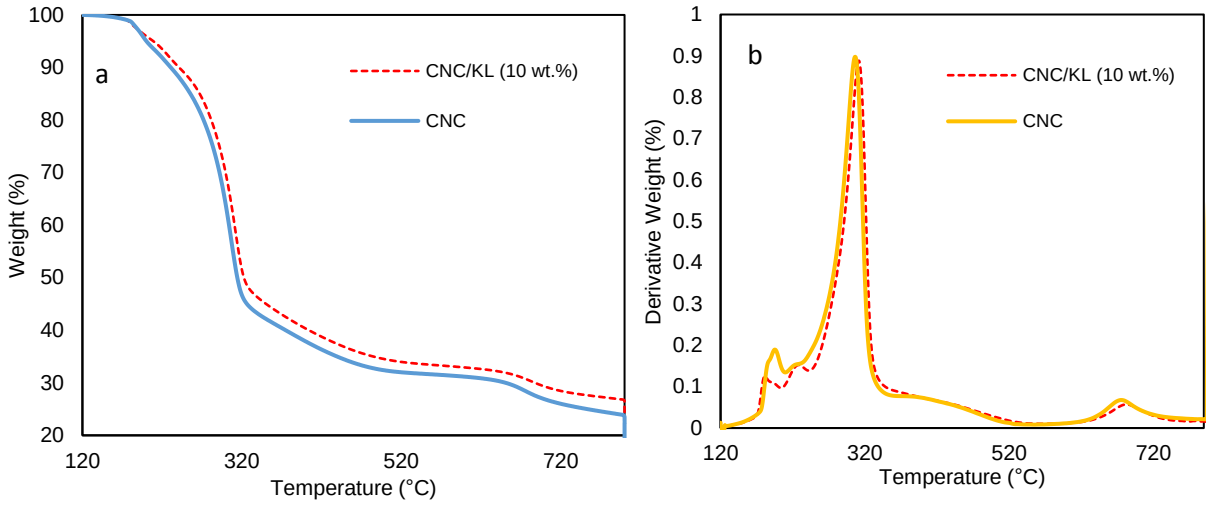

Fig.3.41. Thermogravimetric analysis for CNC and CNC/KL films (a) Weight % vs Temperature (b) Temperature derivative weight % vs Temperature.

3.4 Conclusions

The effect of electrolyte and lignin addition on CNC self-assembly, optical, mechanical, thermal and surface properties was studied. Electrolytes used in this study were CsCl, NaCl, NaOH, $CaCl_2$, $AlCl_3$ which vary in their size, pH and valences. The electrolyte concentrations in the range of 0 to 5 mmol/g were added to CNC suspension and self-assembled films were fabricated by casting and evaporation at ambient conditions. The chiral nematic self-assembly of CNC was fine-tuned by controlling the interaction between the CNC by the addition of electrolytes. The results demonstrated for the first time that CNC aqueous suspensions could be tuned through the optimal addition of electrolytes to produce highly transparent, homogenous, nematic films. CNC particle size increased and transparency reduced at higher concentrations of electrolytes due to aggregation. CNC particle size increased with valency as expected, however, for monovalent electrolytes CsCl addition showed higher particle size than NaCl and NaOH for a given

concentration which may be due to greater affinity between the soft cations Cs^+ and sulfate groups compared to hard cations like Na^+. Concentration of electrolyte for chiral nematic to nematic transition in self-assembled films was dependent on the type of electrolyte. Notably, for large size and higher valency of counter ion lower transition concentration was needed. Theoretically calculated twist factor corresponding to chiral nematic to nematic transition using NaCl was found to be ~0.0955. Effect of electrolyte addition on CNC pitch was evident from the decrease in λ_{min} which may be due to reduction in effective diameter of charged CNC rods. XRD results showed that the %crystallinity of pure CNC only slightly reduced with monovalent electrolytes treatment while for $CaCl_2$ and $AlCl_3$ treated CNC, reduction in crystallinity may be due presence of Ca^{2+} and Al^{3+} on CNC surface due to their strong interaction with negatively charged sulfate groups. Optimal addition of electrolytes also improved the tensile strength (upto 60%) and % strain (upto 170%) of CNC film. This may be due to the presence of ionic interaction between the sulfate ester groups of CNC and positively charged counter ions of electrolyte thereby improving the stress transfer between the rods.

Also, a facile, green approach to design CNC and lignin based transparent and homogenous UV protection films is presented. Besides improving the CNC film transparency, NaOH addition also enhanced uniform dispersion of KL in the CNC/KL nanocomposites. CNC/KL with 10 wt.% lignin concentration provided complete UV blocking. The UV protection behaviour of these films was stable under UV irradiation. In order to improve CNC/KL nanocomposite film transparency in addition to their UV blocking properties; acetylation and hydrogen peroxide bleaching of KL was carried out. It was observed that for peroxide bleached KL, color reduction was significant upto H_2O_2/KL ratio of 1.5 during bleaching after which the color reduction became very gradual. Incorporation of 10 wt.% Ac-KL into CNC films increased $\%T_{550\,nm}$ by 67% compared to 10 wt.%

KL, whereas for 10 wt.% addition of PB-KL150, $\%T_{550\ nm}$ increased by 100%. In both films %UV blocking did not change significantly compared to 10 wt.% CNC/KL films. PBKL150 was compared with 4-ABA, which is a commercially available water-soluble UV absorbent. PBKL150 showed superior UV blocking properties and similar $\%T_{550\ nm}$ at lower loading in CNC film compared to 4-ABA. Presence of lignin also improved thermal stability and reduced water absorption properties of CNC film. Overall, CNC/lignin nanocomposites has promising potential to be a biodegradable, low cost alternative as a coating/film material with high transparency and UV blocking functionality in applications such as automobile windshields, building windows, multilayer food packaging and UV sensitive polymers.

CHAPTER 4

Flexible, transparent, UV protecting, water resistant nanocomposite films based on polyvinyl alcohol and Kraft lignin grafted cellulose nanofibers

4.1 Introduction

In order to develop strong, flexible, transparent, UV protection films based on KL and nanocellulose, PVA was used as a polymeric matrix. This approach enables facile processing of multifunctional nanocomposites compared to synthetic approaches. In this study, TCNF was produced from PMS using combination of TEMPO oxidation and microfluidization. Also, KL was modified using ED as aminating agent to obtain AKL. Further, multifunctional modified CNF (TKL) was synthesized using amidation strategy to conjugate AKL onto TCNF. This modification strategy was simple and used aqueous medium for reaction unlike some other synthetic approaches used in the literature [216, 217, 311, 312]. Further treatment of TKL was carried out using hydrogen peroxide bleaching to reduce lignin color and retain the transparency of PVA in nanocomposite films. PVA nanocomposites were fabricated by casting the aqueous mixture of these modified nanofibers and PVA. The nanocomposites were characterized for their morphological, thermal, mechanical, barrier, and optical properties. Incorporation of modified nanofibers into PVA is expected to prevent lignin leaching unlike KL when exposed to aqueous environment after heat treatment. Moreover, it is expected to reduce UV absorbent migration issue in nanocomposite films as observed in case of inorganic and organic UV absorbers, which hindered their usage in certain applications [313-315]. Moreover, the interactions of PVA with carboxyl and hydroxyl functionality of modified nanofibers and presence lignin are expected to improve the mechanical and thermal properties of the final nanocomposites.

4.2 Experimental

4.2.1 Materials

PVA (98-99% hydrolyzed, M_n=100,000) was purchased from BeanTown Chemical. The never-dried PMS with the moisture content of 75.6 ± 0.5 % was obtained from a pulp and paper mill in Alabama. Formaldehyde (HCHO) and Ethylene diamine (ED) were purchased from Macron Fine Chemicals. Reagents 1-Ethyl-3-(3-(dimethylaminopropyl) carbodiimide (EDC), N-hydroxy succinimide (NHS) were purchased from TCI America, Kraft lignin (KL) (M_n=5000) was obtained from FPInnovations, Pointe Claire, Montreal, Canada. Hydrogen peroxide (H_2O_2, 35%) solution was purchased from the VWR Chemicals. 2,2,6,6-tetramethylpiperidine-1-oxylradical (TEMPO, 98%), sodium bromide (NaBr, 99%), sodium hypochlorite (NaClO, 15%) were purchased from Sigma-Aldrich.

4.2.2 TEMPO CNF Preparation

The TEMPO oxidation of paper mill sludge was performed following the previously reported procedure with slight modification [316]. Briefly, 10 g (dry weight) of sludge was suspended in 1 L of DI water containing TEMPO (0.16 g/L) and sodium bromide (1 g/L) by vigorously mechanical stirring overnight. The TEMPO oxidation was initiated by dropwise adding 75 mL of 10% NaClO solution at room temperature. Meanwhile, the pH of the mixture was maintained at around 10.5 by adding 0.5 M NaOH aqueous solution until no additional NaOH needed. Then, 800 mL of ethanol was added into the mixture to quench the reaction. After that, the mixture was vacuum filtered to remove the liquid. The resultant solid was washed with DI water by continually filtration for several times. Afterwards, the obtained cellulosic solid was diluted with DI water at a consistency of 0.5 wt.%. Finally, the cellulosic solid suspension was passed through a

microfluidizer (M-110EH, Microfluidics Corp., USA) at 160 MPa for 2 times, and gel-like TEMPO CNF (TCNF) was obtained.

4.2.3 Amination of kraft lignin

The amination of KL was carried out under alkaline condition using Mannich reaction by following the procedure optimized by Wang et al. [317]. 5 g KL was firstly dissolved in alkaline aqueous solution (pH- 12) by adding NaOH and stirring the solution for about 30 min. Then, the amination reagents ED and HCHO were added into the above solution in quantities 4.5 gm and 3 ml, respectively. This mixture is ultrasonicated for 30 min and was heated in a water bath at temperature of 75 ^{o}C with refluxing and stirring for 3 h. Afterward, the reaction mixture was dialyzed using the dialysis tubing with a molecular weight cut-off of 1000 Da. Finally, the aminated KL (AKL) aqueous mixture was obtained.

4.2.4 Synthesis of modified TCNF

AKL grafting on TCNF was carried using amidation reaction procedure followed by Le Gars et al [318]. Briefly, 5 gm TCNF aqueous suspension was mixed with the aqueous mixture of EDC and NHS with their molar ratios $4N_{COOH}$: N_{EDC}: $N_{NHS,}$ where N_{COOH}, N_{EDC}, and N_{NHS} represent the molar amounts of carboxylic groups in TCNF, EDC, and NHS, respectively. Reagents were added as first EDC followed by NHS and the mixture was mixed for 15 min, after that pH was maintained between 8-8.5 by adding 0.5 M NaOH solution. 5 gm AKL in suspension form was added to the above mixture. This reaction was carried out for 72 hrs by maintaining pH between 8-8.5 with intermittent additions of NaOH or HCl. After 72 h, the reaction mixture was centrifuged 3 times with DI water dilutions each time. The suspension of the KL grafted TCNF (TKL) was then dialysed (molecular weight cut-off 1000Da) against distilled water for at least 1 week to ensure removal of unreacted reactants and reagents.

4.2.5 Peroxide bleaching of TKL

Hydrogen peroxide bleaching of TKL was carried out to improve the transparency of these modified nanofibers. PBTKL100 and PBTKL400 samples were produced from peroxide bleaching of TKL by using H_2O_2/KL ratios of 1 and 4, respectively. The treatment was carried out at 75 ºC for 2 hours at the pH of 12 which were optimized conditions reported in literature [247, 290].

4.2.6 Fabrication of PVA nanocomposites

PVA nanocomposite films were fabricated using casting method. The PVA (5 wt %) was first dissolved in deionized water at 90 °C, this solution was used to prepare nanocomposites films of 1 gm PVA basis. PVA/TKL, PVA/PBTKL100 and PVA/PBTKL400 nanocomposite aqueous mixtures were prepared by mixing aqueous suspension of PVA and modified nanofibers to obtain final concentrations of 1%, 2%, 5%, 10% based on 1 g PVA. Also, these concentrations were based on TCNF content in modified nanofibers. These mixtures were then casted on a polystyrene Petri dish and allowed to dry at room temperature. These films were further dried in oven at 60 °C for 24 hrs.

4.2.7 Characterizations

Tensile testing

Tensile testing was performed using TAPPI standard methods (TAPPI T494 and TAPPI T456). Testing was performed on the sample film of dimension (length) 100 mm × (width) 15 mm using PARAM XLW (EC) Auto Tensile Tester from Labthink. Cross head speed was set at 25 mm/min. All the samples were conditioned at 50% relative humidity and 23 °C for 24 h before testing.

Water vapor barrier properties of film

Water vapor transmission rate (WVTR) was measured using PERME W3/130 water vapor tester from Labthink for circular samples of 2.54 cm diameter cut from nanocomposite samples. Tests were performed at temperature of 23 ^{o}C and 50% relative humidity.

UV-vis spectroscopy

Transmission spectra of PVA nanocomposite films were carried out using a Thermo Scientific Genesys 10S UV−vis spectrometer in the wavelength range of 200−800 nm. Transmittance at the wavelength of 550 nm was used as a measure of film transparency. The absorption spectra were obtained for AKL and TKL samples in aqueous medium to obtain calibration curves and estimate lignin concentration in TKL, PBTKL100 and PBTKL400. The percentage blocking for UV-A (320 −400 nm) and UV-B (280−320 nm) was calculated by following equations: [250]

$$\text{UV A blocking } (\%) = 100 - \frac{\int_{320}^{400} T(\lambda)\, d\lambda}{\int_{320}^{400} d\lambda} \qquad 4.1$$

$$\text{UV B blocking } (\%) = 100 - \frac{\int_{280}^{320} T(\lambda)\, d\lambda}{\int_{280}^{320} d\lambda} \qquad 4.2$$

Film water resistance and lignin leaching test

Nanocomposite films of dimension 5 cm × 5 cm were cut and immersed in 100 ml DI water in a beaker. Then this aqueous sample was mixed for 24 hours. UV-vis absorption spectra of water from this beaker was carried out after 24 hours to detect the leached lignin in water.

Carboxyl content measurement

The carboxyl content of TCNF before and after conjugation of AKL was determined by conductometric titration using Metrohm auto titrator consisting of an 856 Conductivity module connected to the main module (888 Titrando) coupled with TiamoTM 194 2.5 software. The titration was carried out with 1.5 g samples which were pretreated with 0.1 N HCl for one hour followed by its filtration until the effluent water conductivity was less than 5 μScm^{-1}. The sample was mixed with a 0.001 N NaCl (250 ml) and 0.10 N HCl solution (1.5 ml), stirred and titrated with 0.05 N NaOH in an atmosphere of nitrogen. The amount of weak acid (carboxyl) groups was calculated as described in the standard method by Katz et al [319].

Fourier Transform Infrared Spectroscopy

Fourier transform infrared (FTIR) spectra of the samples were measured on a Nicolet 6700 FTIR spectrometer by Thermo Scientific. A total of 64 cumulative scans in absorption mode were taken, with a resolution of 1 cm^{-1} in the frequency range 4000−600 cm^{-1}.

Scanning Electron Microscopy (SEM)

SEM images of PVA and PVA nanocomposite film cross section were taken using a JEOL (Tokyo, Japan) 7000-F Field Emission Scanning Electron Microscope. Films were sputter-coated with gold before taking images.

X-Ray Diffraction (XRD)

XRD characterization of samples was acquired with a Bruker diffractometer under an acceleration voltage of 40 kV and a current of 40 mA at room temperature. The diffraction signals were recorded in the 2θ range of 10−40° at a 5° min^{-1} scan rate. The crystallinity of PVA nanocomposite films is calculated using the following equation:

$$X_{c-XRD} = \frac{A_C}{A_C + A_a} \times 100 \qquad 4.3$$

Where A_a is experimental integrated intensity of amorphous phase and A_c is experimental integrated intensity of crystalline phase.

Thermal Properties

Melting and crystallization temperatures of PVA and PVA nanocomposite films were measured on a TA Instruments (New Castle, DE) Q500 Differential Scanning Calorimeter (DSC) at a scan rate of 10 °C/min over a temperature range of 20 to 235 °C, using aluminum pans with lids. A heat-cool-heat cycle was performed to ensure the melting of all crystallites and to remove thermal history. The cycle consisted of the following steps: 1) heating at 10 °C/min to 235 °C followed by a 5 min. hold, 2) cooling at 10 °C/min to 20 °C with 5 min. hold, 3) heating at 10 °C/min to 235 °C. The heat-cool-heat cycle. The crystallinity of nanocomposite films from DSC ($X_{c\text{-}DSC}$) was calculated using the equation: $X_{c\text{-}DSC} = \Delta H_m/\Delta H_0$, where ΔH_m is melting enthalpy from DSC curve, ΔH_0 is the enthalpy of pure PVA crystal (138.6 J/g) [320].

Thermal stability was characterized using a TA Instruments (New Castle, DE) Q500 Thermal Gravimetric Analyzer (TGA). All TGA tests occurred under a constant nitrogen balance protection with a flow rate of 40 cm^3/min and a sample gas (nitrogen) flow rate of 60 cm^3/min. Samples were heated with ramp rate of 10 °C/min to 120 °C. They were then held isothermally at 120°C to ensure residual moisture removal. Samples were again ramped to 800 °C at 10 °C/min followed by an isothermal hold for 20 minutes. A sample size of ~15 mg was used for every TGA test to avoid any potential deviations in heat flow or accuracy associated with sample size.

4.3 Results and discussion

4.3.1 Structural and morphological characterization

FTIR

Fig.4.1(a) compares the FT-IR spectra of KL and AKL. Both KL and AKL showed characteristic lignin peaks in the region 1200-1600 cm^{-1} corresponding to aromatic ring structure indicating retention of lignin skeleton after amination. The peaks at 2928 cm^{-1} and 2840 cm^{-1} originate from the C-H asymmetrical and symmetrical stretching vibrations in methylene structures, respectively [321-323]. These peaks are prominent in AKL due to successful amination using ED. The peaks at 1463 cm^{-1} and 832 cm^{-1} derived from C-H bending and out-of-plane deform vibrations, respectively [323]. In the aromatic structures, the peak at 1592 cm^{-1} is attributed to the aromatic skeletal stretching, and the peaks at 1260 cm^{-1} and 1220 cm^{-1} are assigned to the guaiacyl and syringyl structure, respectively, [317, 324-326] suggesting that the skeleton structure of lignin was not destroyed during amination. The new peak at 1655 cm^{-1} arises from the N–H bending vibration of $–NH_2$, and the peak at 1495 cm^{-1} was assigned to the C–N bending vibration [317]. Fig.4.1(b) compares the FT-IR spectra of the TCNF and TKL. TCNF displayed an obvious peak at 1600 cm^{-1} which is assigned to the carboxyl groups introduced by the TEMPO-mediated oxidation of primary C6 hydroxyl groups on CNF surface [327]. The grafting of AKL onto TCNF surface was confirmed by FT-IR. The typical peaks for amide bonds were observed at 1640 cm^{-1} (amide I band, C=O stretching) and 1542 cm^{-1} (amide II band, combined N–H deformation and C–N stretching)[328-330]. Also, the carboxylic C=O peak (1600 cm^{-1}) is observed in TKL corresponding to the unreacted carboxylic groups.

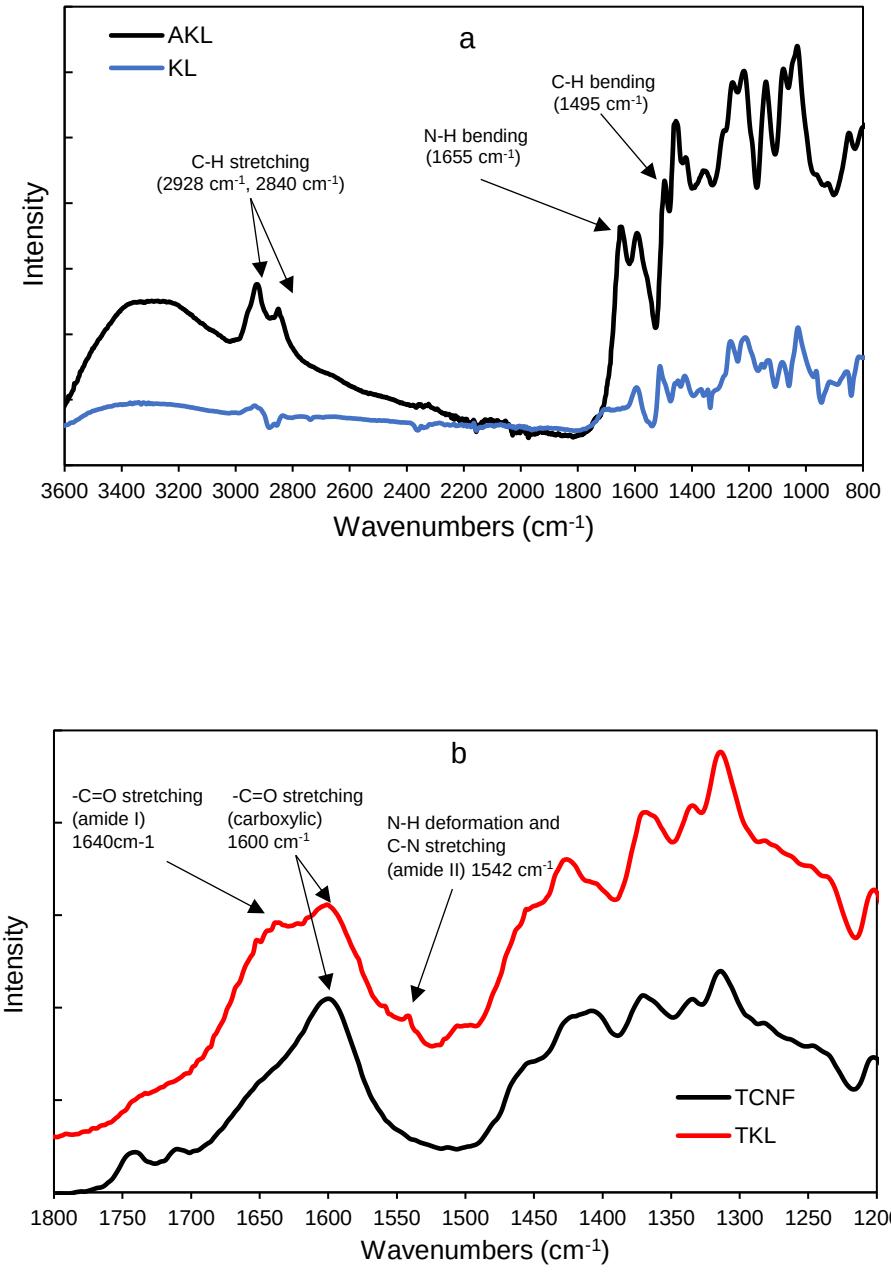

Fig.4.1. FTIR spectra of the (a) KL and AKL (b) TCNF and TKL

Carboxyl and lignin content estimation

As shown in Fig.4.2, TEMPO-oxidation of paper mill sludge resulted in successful preparation of TCNF with high carboxyl content (~2.1 mmol/g). It has been reported that TEMPO oxidation also removes most of the residual hemicelluloses and uniform carboxyl distribution is obtained due even penetration of reactants. The carboxyl contents of TCNF after grafting of KL is reduced by ~31% due to the coupling of the AKL to the surface carboxyl groups during the reaction, indicating significant degree of conversion of amidation reaction.

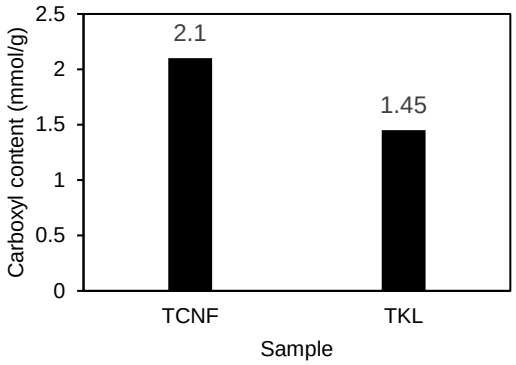

Fig.4.2. Carboxyl content of nanofibers before and after KL grafting as estimated by conductometric titration.

Fig.4.3. shows the 0.1 wt.% aqueous suspensions of TKL, PBTKL100 and PBTKL400. Lignin contents of these samples were estimated using UV vis spectroscopy. First, the calibration curves were obtained for the similarly treated AKL samples (AKL, PBAKL100, PBAKL400) by plotting the absorbance (at 253 nm) vs concentration plot. Their extinction coefficients (slope calibration curve) were then used to estimate the lignin content in these modified nanofiber samples by using the absorbance (at 253 nm) of known concentration. Hydrogen peroxide bleaching is a lignin retaining bleaching technique and relatively higher lignin retention is expected after this treatment (Table 4.2).

Table 4.1. Lignin content in modified TCNF samples.

Sample	%Lignin content
TKL	47.2 (1.7)
PBTKL100	43.5 (1.2)
PBTKL400	41 (0.9)

Fig.4.3. 0.1 wt.% suspensions of nanofibers (from right to left) TCNF, TKL, PBTKL100, PBTKL400.

XRD

XRD was performed to analyze the impact of the incorporation of modified nanofibers on the crystalline structure of the PVA films. Fig.4.4 shows the XRD plots of pure PVA and PVA/PBTKL400 nanocomposite films with nanofiber concentrations of 2, 5, and 10 wt.%. The pure PVA film showed diffraction peak around 19.50^{o} assigned to the strong interaction of intermolecular and intramolecular hydrogen bonding between the PVA chains [331, 332]. The XRD plots of the PVA/PBTKL400 nanocomposite films showed a superposition of two portions, indicating the interaction between modified PBTKL400 and PVA matrix [333, 334]. A weak peak around 22.6° can be observed with increase in PBTKL400 concentration is assigned to the (200) plane of cellulose I. %Crystallinity of PVA nanocomposites decreased with increase in PBTKL400

concentration (Table 4.1). This shows that presence of nanofibers interfered with the crystallization behaviour of PVA. Similar trend was also observed from their DSC analysis in section 4.3.2.

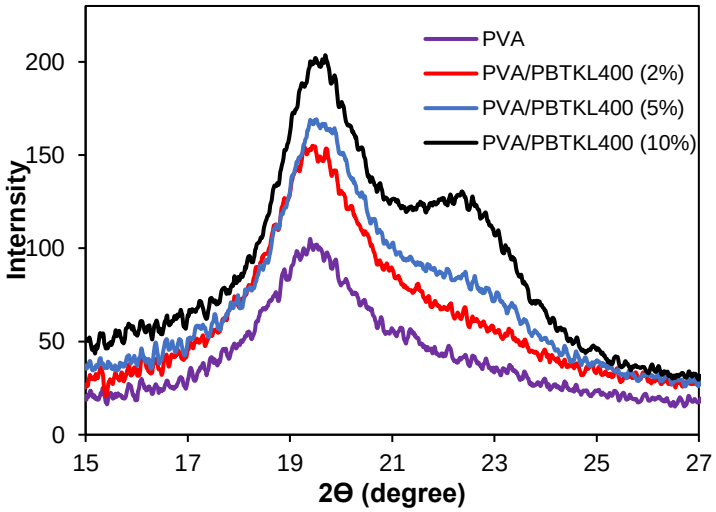

Fig 4.4. XRD plots for PVA and PVA/PBTKL400 nanocomposites.

Table 4.2. % Crystallinity of PVA and PVA/PBTKL400 nanocomposites.

Sample	%Crystallinity
PVA	47.9
PVA/PBTK400(2%)	42.3
PVA/PBTK400(5%)	38
PVA/PBTK400(10%)	35.9

SEM

SEM images of the cross sections of PVA and PVA nanocomposite films were obtained to observe the nanofiber dispersion in PVA matrix. Pure PVA exhibited a uniform and smooth cross section (Fig.4.5) whereas PVA/PBTKL400 (5%) showed rougher cross section with nanofibers protruding

out of the surface. It can be observed these nanofibers are randomly oriented and has uniform distribution across the film cross section without any agglomeration and clusters indicating good interaction with PVA matrix.

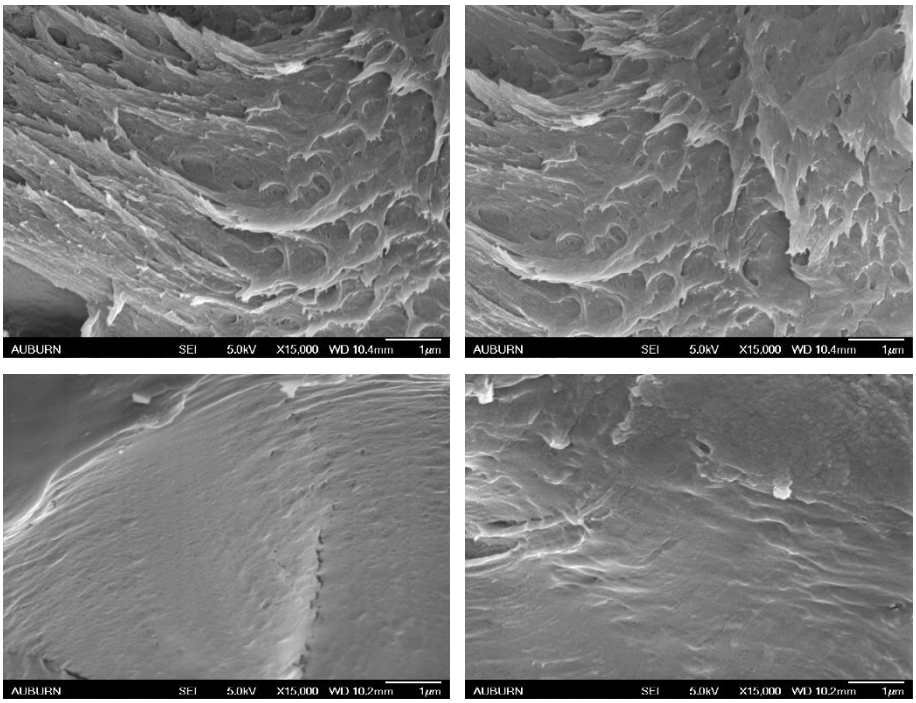

Fig.4.5. SEM images cross sections of (a) and (b) PVA/PBTKL (5%), (c) and (d) PVA

4.3.2 Thermal Properties

The DSC curves for the PVA and PVA nanocomposites are shown in Fig.4.6. The glass transition temperature (T_g) of the nanocomposite films was higher than that of pure PVA film. The T_g of PVA increased from 71 °C to 73.8 °C for 2% addition of PBTKL400 whereas for 5% addition, the T_g increased upto 75 °C. This result can be explained by the strong interactions between PBTKL400 and PVA matrix, which restricts the mobility of the motion of PVA chain segments, leading to the improved T_g of PVA [335, 336]. Also, it was observed that T_m of the nanocomposites

reduced compared to PVA. This reduction in T_m and the increased T_g with single glass transition peak suggested compatibility between the PBTKL400 and PVA matrix [337]. PVA/PBTKL400 (5%) nanocomposite films exhibited a ~4 °C decrease in cold crystallization temperature (T_C) compared to pure PVA, showing the influence of PBTKL400 on the crystallization behavior of PVA matrix.

Table 4.3. Thermal properties and crystallinity of PVA and PVA nanocomposite films.

Sample	T_g	T_m	T_c	dH_m(J/g)	%Crystallinity
PVA	71	220	196.1	52.07	37.6
PVA/PBTKL400 (2%)	73.8	216.32	195.6	43.52	31.4
PVA/PBTKL400 (5%)	75	215.8	192.4	34.09	24.6

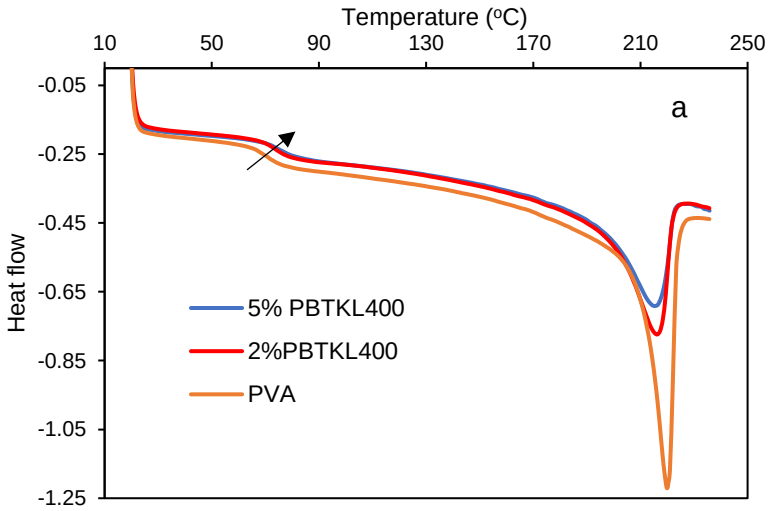

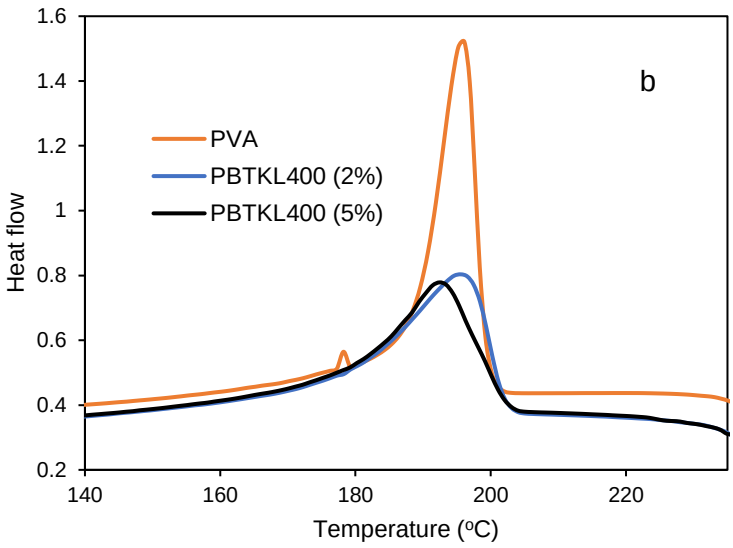

Fig. 4.6. DSC thermograms for PVA and PVA nanocomposite samples showing (a) Glass transition and melting peaks (b) crystallization peaks.

The thermal stability and degradation behavior are crucial for the processing and end applications of PVA nanocomposite films. The TGA and DTG plots in Fig.4.7 shows mainly two degradation stages for the PVA and PVA nanocomposite samples. The first major weight loss occurred in the temperature range from 200 to 400 °C associated with the decomposition of the side chains of PVA. The maximum weight loss temperature (T_{max}) of the second degradation process for the PVA/PBTKL400 nanocomposite films were higher than those for pure PVA. Incorporation of 5% PBTKL improved the T_{max} to 326°C from 317°C for pure PVA, while for 2% PBTKL, T_{max} improved to 320 °C. The results indicated that the incorporation of PBTKL had a positive effect on the thermal stability of the nanocomposites. The improved thermal stability of the PVA/PBTKL400 has resulted from the lignin present in the PBTKL400, which is expected to improve thermal stability due to presence of stable aromatic units and the covalent linkages between the CNF and lignin [283, 338]. Moreover, due to the compatibility between PVA and PBTKL400, PVA chains could get stabilized at the PBTKL400 and PVA interphase resulting in

reduced transport of their decomposition products thereby increasing the T_{max} [339-341]. It was also reported that the crystallinity of CNF can also contribute to the thermal stability in the nanocomposite [342]. The second weight loss at 400 to 600 °C resulted from the decomposition of the PVA backbone.

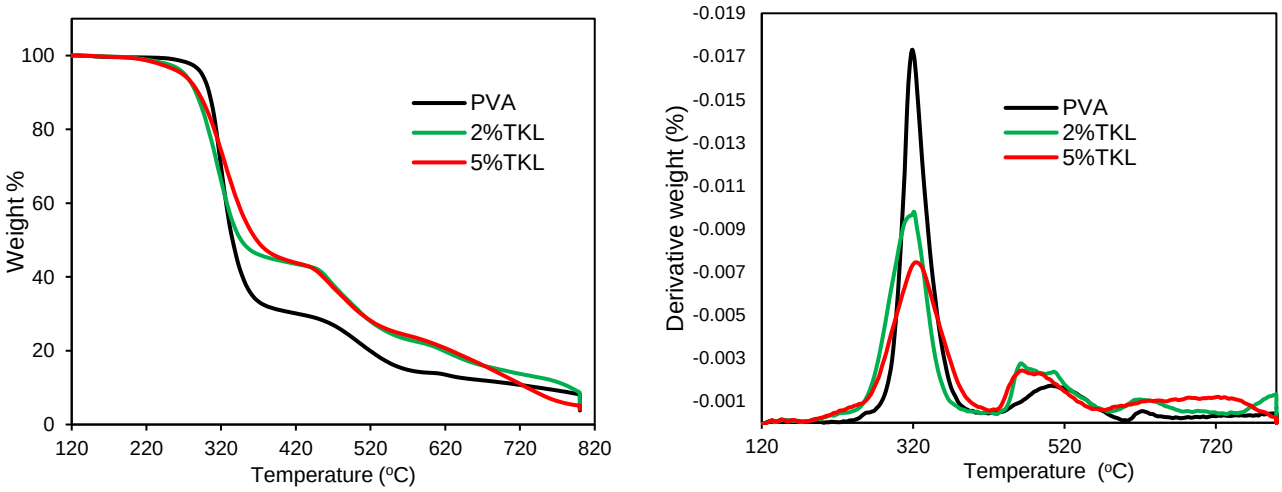

Fig.4.7. TGA plots for PVA and PVA nanocomposites (a) Weight% vs Temperature (b) Derivative weight % vs Temperature.

4.3.3 Mechanical properties

The tensile strength, Young's modulus, elongation at break and toughness properties of the PVA nanocomposite films are reported in Fig.4.9. The mechanical properties, especially the tensile strength and flexibility, are significant for the application of packaging films. The nanocomposite samples with nanofiber content of 2% and 5% improved tensile strength of nanocomposites compared to pure PVA. While at 10 wt.% addition of nanofiber drastic reduction in strength was observed. In contrast, the elongation at break only decreased with increase in concentration of nanofibers and Young's modulus showed increasing trend upto 10 wt.% addition of nanofibers. It has been observed that cellulose nanofibers incorporation in polymer matrix usually increased tensile strength, Young's modulus and has negatively impacted the elasticity [343]. This impact

on stiffness of nanocomposite can be attributed to percolated network of nanofibers in polymer matrix interacting with polymer through hydrogen bonding and other intermolecular interactions [344]. For 5 wt.% nanofiber concentration, PVA/PBTKL400 showed maximum improvement in tensile strength compared to PBTKL and PBTKL100 containing samples. This may be due to establishment of more hydrogen bonded network between nanofibers and PVA as carboxyl content in PBTKL400 is expected to be higher after peroxide oxidation compared to PBTKL100 and PBTKL. PVA/PBTKL400 showed tensile strength and young's modulus of 134 MPa and 3.05 GPa, respectively. Which were 1.25 and 1.2 times higher than those of pure PVA film. Toughness of PVA slightly reduced upto 5 wt.% addition of nanofiber after which drastic reduction was observed due to increased brittleness of the nanocomposite samples as shown in Fig.4.8.

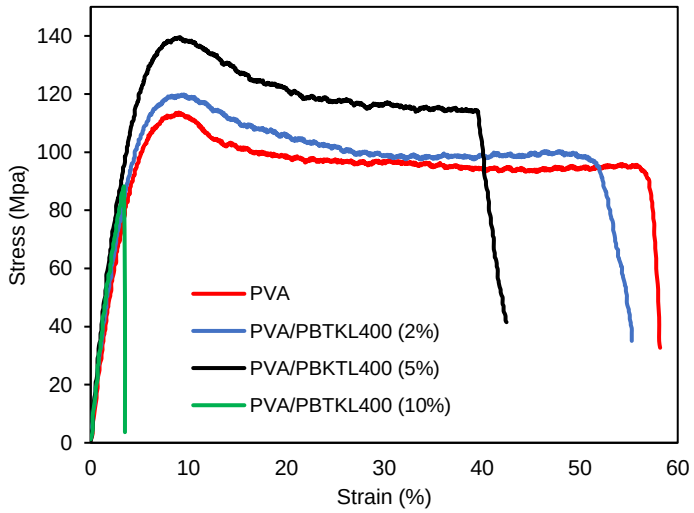

Fig.4.8. Stress vs (%) Strain plot of the PVA and PVA/PBTKL400 nanocomposite samples.

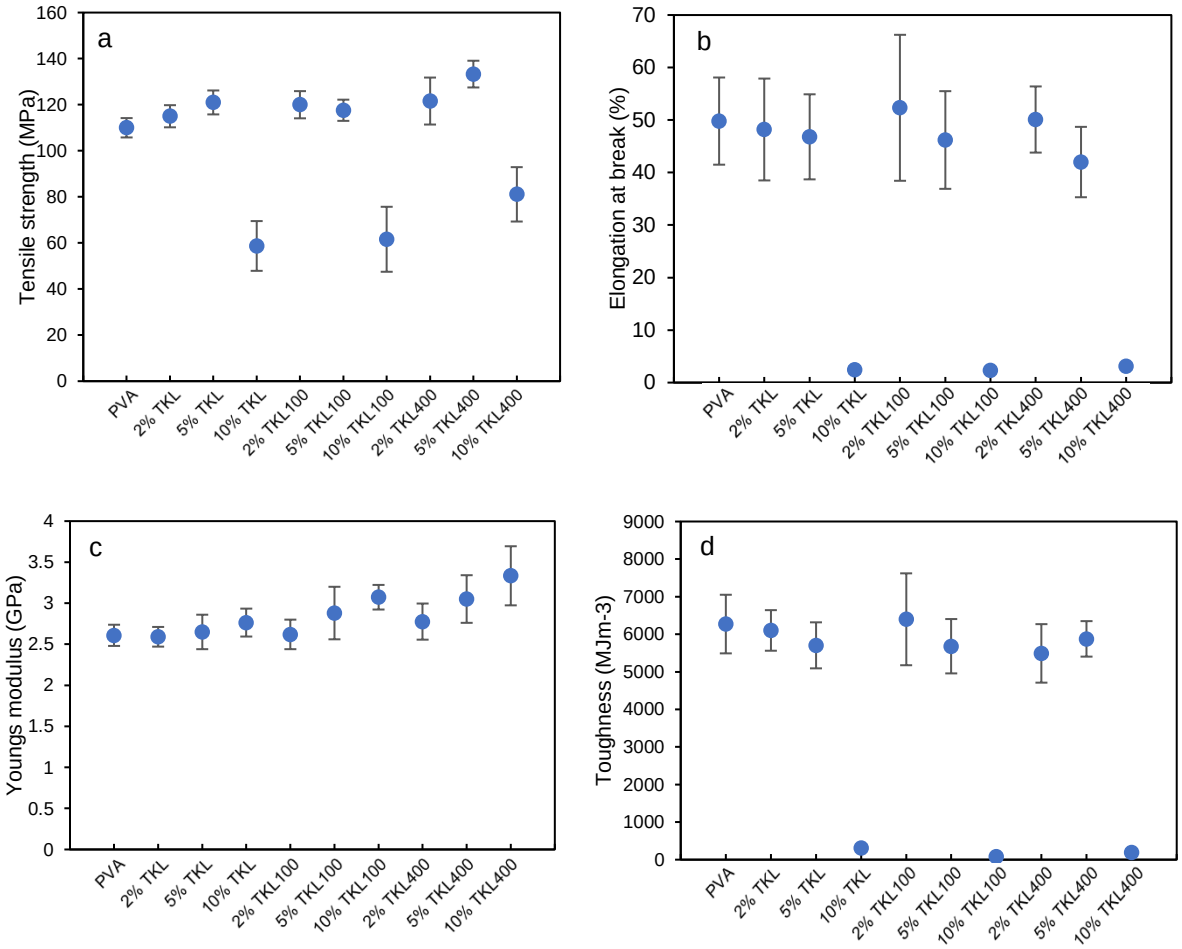

Fig.4.9. Mechanical properties of PVA and PVA nanocomposites (a) Tensile strength (b) Elongation at break (c) Young's modulus and (d) Toughness.

4.3.4 Water vapor barrier properties

Water vapor barrier properties of PVA and PVA nanocomposites were characterized in terms water vapor transmission rate (WVTR) and water vapor permeability (WVP). It was observed that the WVTR and WVP of the PVA did not improve with the addition of PBTKL400. Tukey test carried out to compare the barrier properties of nanocomposites with pure PVA showed no significant difference ($P>0.05$).

The WVP of polymer is governed by water vapor's solubility (S) and diffusion coefficient (D) in that polymer matrix and is given as follows [345].

$$WVP = SD$$

Therefore, it was expected that the crystalline structure in PBTKL400 would provide tortuous pathway for the water vapor diffusion across the film thereby reducing the diffusion coefficient of PVA matrix with increase in their concentration [346]. Also, the presence of lignin in PBTKL400 could contribute towards reducing WVP since relatively hydrophobic lignin can negatively impact the solubility of water vapors in the film [347]. However, the results from this study showed that the reduction in crystallinity of PVA with addition of PBTKL400 (as shown from XRD and DSC) may have predominantly governed the diffusion of water vapors. The reduction in crystallinity of PVA gave rise to increase in diffusion coefficient as more amorphous regions in PVA enabled easy water vapor diffusion through the film. Therefore, incorporation of PBTKL400 overall did not have any impact on the water vapor barrier properties of PVA.

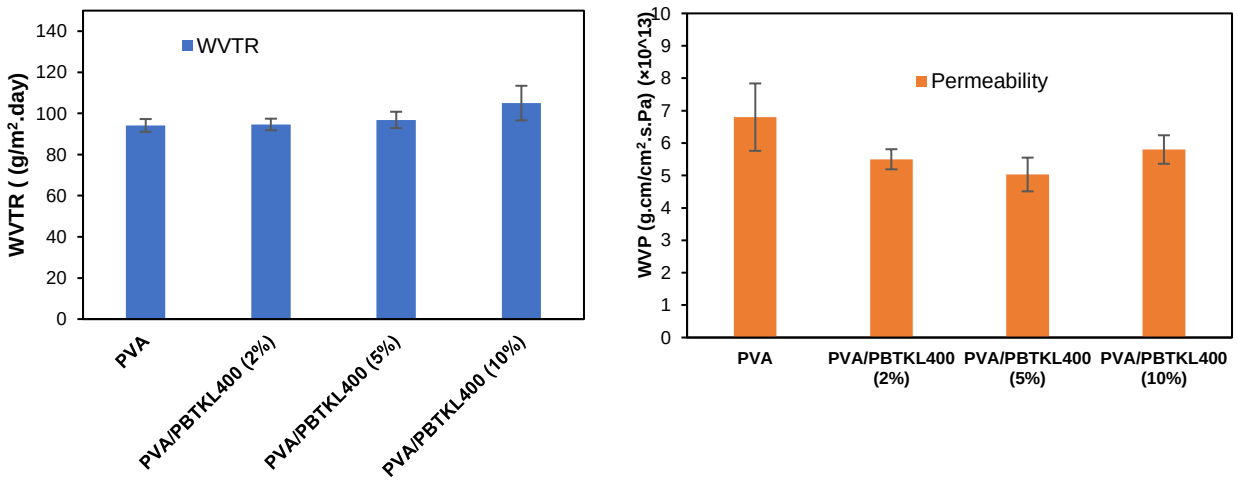

Fig.4.10. WVTR and WVP of PVA and PVA/PBTKL400 samples.

4.3.5 Water resistance and lignin leaching test

In order to improve the applicability of these transparent, UV blocking nanocomposite films in aqueous environment, their water solubility and lignin leaching need to be prevented. For this purpose heat treatment of the nanocomposite films was carried out by keeping films in oven at 150 ^{o}C for 1.5 hour. This treatment improved water resistance of these nanocomposite films through physical cross-linking of the PVA chains. Stability of the nanocomposite films in aqueous medium was characterized by monitoring the structural stability of nanocomposites samples kept under mixing in glass beaker with aqueous medium for 24 hours. As shown in Fig.4.11(a) and 4.11 (c), the structural stability of these films was maintained after this treatment, showing water resistance of the nanocomposite films. Also, the water from this container is tested for any lignin leaching by characterizing them using UV-vis absorption spectra. As shown Fig.4.11(b), the heat treated PVA/PBTKL400 did not show any absorption peak for lignin, whereas for control PVA/PBAKL400 nanocomposite sample lignin absorption peak was observed showing the lignin leaching in aqueous medium. Therefore, the current approach of grafting KL onto TCNF followed by heat treatment of their PVA nanocomposite films presents simple and efficient approach to develop the transparent, UV blocking nanocomposite films which can withstand aqueous environment without losing its functionality.

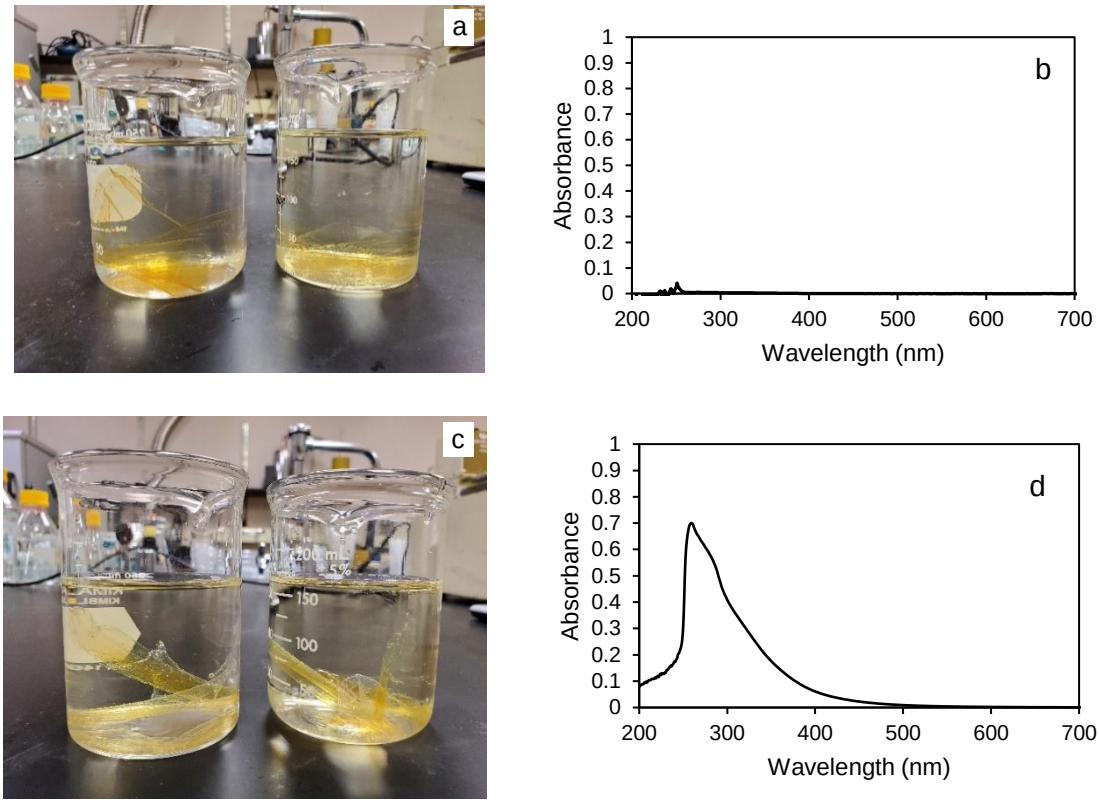

Fig.4.11. Images showing water resistance and lignin leaching of (a) PVA/PBTKL400 (5wt.%), (c) PVA/PBAKL400 (5wt.%); Absorption spectra of aqueous sample containing (b) heat treated PVA/PBTKL400 (5 wt.%), (d) PVA/PBAKL400 (5 wt.%).

4.3.6 Optical properties

High transparency and strong UV absorption are desired properties for films to be used as packaging material in various applications such food packaging, polymer coatings, medicine [348-352]. The UV–vis spectra of PVA and PVA nanocomposite films were obtained to determine their transparency and UV shielding properties. As shown in Fig.4.12, PVA/PBTKL400 (5%) appeared more transparent and light yellow compared to PVA/PBTKL100 (5%) and PVA/TKL (5%) due to bleaching action of hydrogen peroxide treatment to remove the chromophores in lignin. Fig.4.13 compares the transmission spectra of the PVA and PVA/PBTKL400 nanocomposites with concentrations of 1 wt.%, 2 wt.%, 5 wt.%, 10 wt.%. Pure PVA showed high transmittance for both

UV and visible spectrum of light due to lack of UV absorbing functionality. It was observed that with 1 wt.% addition of PBTKL400 most of UV-C spectrum (200-280 nm) of light is blocked while for 2 wt.% addition of PBTKL400, UV-C (200-280 nm) and UV-B spectrum (280 nm-315 nm) are completely blocked. For PVA/ PBTKL400 (10%) almost all the UV spectrum of light is blocked. At this concentration of PBTKL400 more than 85% of the original PVA matrix transparency is still maintained. This modified CNF because of its smaller nanofiber size compared to other CNF types and reduction in chromophores of KL upon peroxide oxidation resulted in superior UV shielding and transparency for PVA nanocomposites.

Fig.4.12. Films samples of PVA and PVA nanocomposites (from right to left) PVA, PVA/PBTKL400 (5%), PVA/PBTKL100 (5%) and PVA/TKL (5%).

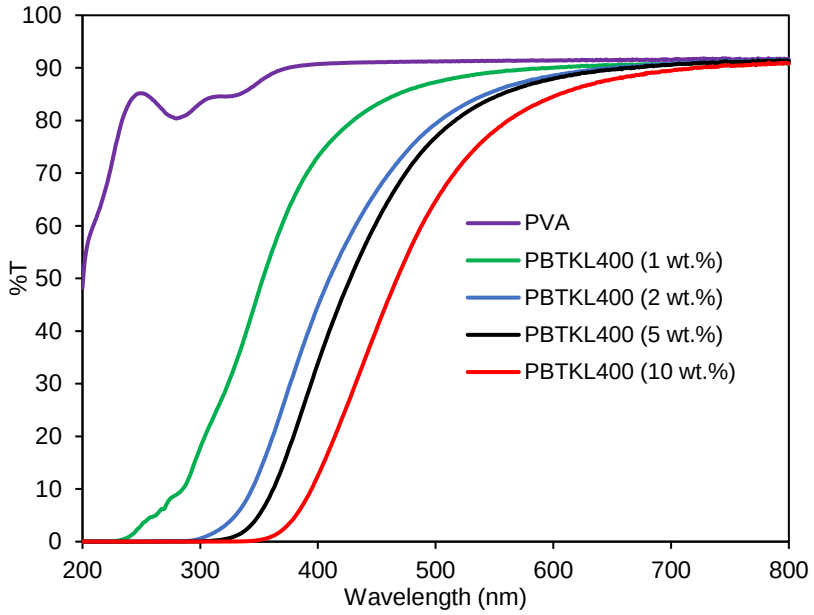

Fig.4.13. Transmission spectra of PVA and PVA/PBTKL400 nanocomposite films.

Table 4.4 represents the % UV B, %UV A shielding, %UV blocking at 400 nm and %T at 550 nm for the PVA nanocomposites prepared from the 1%, 2%, 5%, 10% concentrations of TKL, PBTKL100, PBTKL400 samples. Fig.4.14 summarizes %UV shielding at 400 nm and transparency (%T at 550 nm) of lignin based transparent, UV blocking nanocomposites in literature. PVA/modified CNF nanocomposites in this study showed superior performance in terms of transparency and UV blocking properties.

Table 4.4. %UV blocking and %T of PVA and PVA nanocomposite films.

Sample	%UV A blocking	%UV B blocking	%UV blocking at 400 nm	%T at 550 nm
PVA	11.9	17.1	9.3	91.4
PVA/TKL(1%)	64.0	94.5	40.1	88.0
PVA/TKL(2%)	79.3	99.1	55.2	84.6
PVA/TKL(5%)	96.5	100.0	85.8	72.2
PVA/TKL(10%)	100.0	98.9	99.0	55.6
PVA/PBTKL100(1%)	47.1	82.3	28.9	87.3
PVA/PBTKL100(2%)	75.4	98.4	50.7	86.3
PVA/PBTKL100(5%)	94.3	100.0	81.8	77.2
PVA/PBTKL100(10%)	99.9	100.0	97.1	61.1
PVA/PBTKL400(1%)	46.6	78.5	26.8	89.2
PVA/PBTKL400(2%)	65.8	94.1	44.0	85.6
PVA/PBTKL400(5%)	88.0	99.9	66.1	84.4
PVA/PBTKL400(10%)	97.2	100.0	87.5	78.1

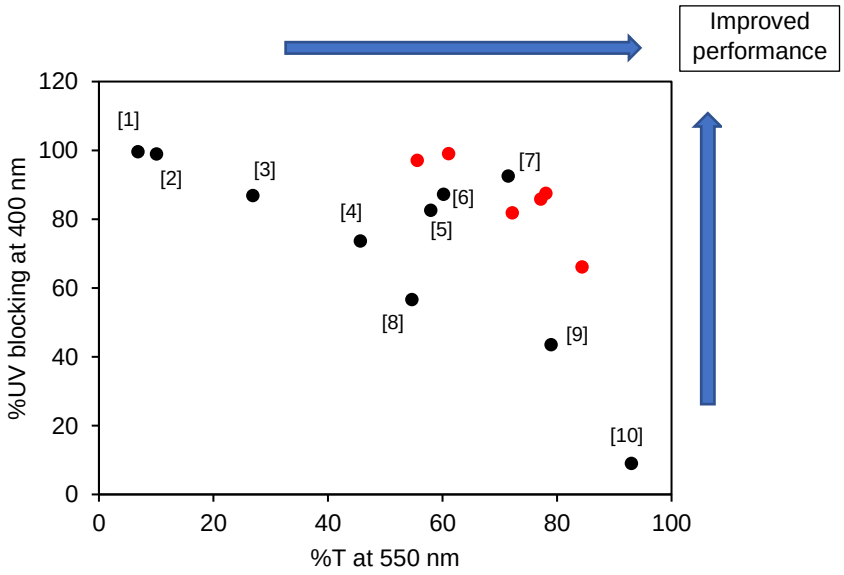

Fig.4.14. Comparison of transparency and UV blocking at 400 nm of PVA nanocomposites with 5 wt.% and 10 wt.% concentrations of PBTKL400, PBTKL100 and TKL with lignin based transparent nanocomposites in literature. Red dots correspond to samples in this study. (1- [73], 2-[294], 3-[295], 4-[296], 5-[241], 6-[297], 7-[298], 8-[295] , 9-[240] , 10-[73]).

The modified nanofibers developed in the present work shows its potential as biobased, multifunctional, modified CNF which can retain most of the transparency of polymeric matrices

and can impart structural strength, UV blocking functionality and thermal stability. These nanocomposites can be used applications such as healthcare, polymer coatings, food packaging, windshields, and transparent windows.

4.5 Conclusions

This study demonstrated a new route to utilize a kraft pulping waste, paper mill sludge (PMS) and a byproduct, kraft lignin, to synthesize modified CNF. TCNF and AKL were first synthesized using simple modification strategies such as TEMPO oxidation and amination of PMS and KL, respectively. Modified CNF (TKL) was produced by conjugating AKL with TCNF using amidation strategy. TKL has lignin content of about 47%, which reduced to 43.5% and 41% for PBTKL100 and PBTKL400, respectively, after a hydrogen peroxide treatment These hydrogen peroxide treated TKL samples showed improved transparency with minimal lignin loss. These modified nanofibers were then used to fabricate PVA based nanocomposite films. The compatibility of modified nanofibers with PVA matrix was observed from their uniform dispersion in PVA matrix and improved T_g of their resultant nanocomposites. PBTKL400 showed its potential as a multifunctional nanomaterial which improved UV absorption properties, thermal stability and retained high transparency of PVA matrix. 5 wt.% addition of PBTKL400 to PVA seems to be an optimized concentration to improve thermal, mechanical properties along with high transparency and UV blocking properties. Tensile strength and young's modulus of PVA/PBTKL400 (5%) increased by1.25 and 1.2 times, respectively, compared to pure PVA film. Also, it has retained more than 92% of pure PVA transparency with complete UV B screening and 88 % of UV A screening. This was among the best performance in terms of transparency and UV blocking properties compared lignin based transparent nanocomposites studied in literature.

Thermal treatment of the PVA nanocomposites improved water resistance to the films in aqueous environment and prevented leaching of lignin due to grafting of lignin on nanofiber. Moreover, the barrier properties (WVP and WVTR) of PVA were retained in the nanocomposite films which may be due to the counterbalancing effect of increase in crystalline domains of PBTKL400 and reduction of PVA crystallinity on diffusion of water vapors. Thermal properties such as T_g and $T_{d\ max}$ of this samples was increased by 4 ^oC and 9 ^oC, respectively. This fully biobased modified CNF has potential to be used with hydrophilic polymeric matrices for the utilization in applications such as transparent UV protecting coatings and films in healthcare, food and UV sensitive materials packaging, optical lenses and optoelectronics that require high visible light transparency, strong UV blocking properties and mechanical strength.

CHAPTER 5

Standardization of preparation procedure for uniform cellulose nanopapers

5.1 Introduction

Fast preparation of large, smooth and uniform cellulose nanopapers is important in order to facilitate their development for potential applications. There are several preparation procedures for cellulose nanopapers described in the literature. These procedures mainly include filtration of cellulose nanofiber suspension followed by oven drying [150, 155] or hot pressing [155, 353], and air/oven drying of the cellulose nanofiber suspension (suspension casting) [106, 354-357]. Cast-coating of cellulose nanofibers on surface modified polymeric supports followed by oven drying and hot pressing was also reported [358]. The preparation time for these nanopapers ranges from few hours to days. Suspension casting is the most time-consuming method and results in an uneven wrinkled nanopapers. Drying rate plays key role in uniformity of the nanopaper; slower drying provides low moisture concentration gradients and can reduce the wrinkling problem to some extent [148]. Nanopaper preparation using filtration of suspension through conventional metal wire sieves is not feasible due to significant loss of MFC through the sieve [148]. A range of different filter media have been utilized including hydrophilic polytetrafluroethylene membrane with pore size 0.1 µm [162], Millipore filter membrane with a pore size 0.65 µm [150], polyamide filter cloth of 235 mesh along with filter paper (no mention of pore size) [162], cellulose ester filter membrane of 0.65 µm pore size [148], woven filter fabrics with pore sizes 55, 109 or 150 µm [151]. Although nanofiber loss was reduced, problems associated with nanopaper removal from the filter media [148] and longer preparation time were reported [150]. Several attempts were performed to reduce the preparation time by modifying the filtration and drying steps. These efforts involve application of vacuum [148, 149, 359] and over pressure during filtration [360], hot

pressing for drying [360] and use of polyelectrolytes for filtration aid [361]. Drainage time has reduced to few minutes from hours, also the drying time were reported to be few minutes/hours instead of days. Lowest drainage time up to 3 minutes and with 94% nanofiber retention was possible by applying vacuum of 25 MPa through a 125 µm woven copper wire mesh filter media [359].

These different methodologies so far have improved the uniformity of nanopapers and reduced the processing time. However, it is difficult to compare the results obtained for CNF nanopapers in the literature due to significant variations in preparation methodologies in terms of type of procedure, filter media and equipment used etc. In this study we have attempted to standardize the nanopaper making procedure, in doing so we have modified the TAPPI standard method (T-205) which is a well-established handsheet preparation method for physical testing of pulps using british handsheet maker [362]. Although some studies mentioned the use of similar british handsheet maker [170, 359, 361, 363] ; however, no efforts were made to systematically optimize/modify the standard paper handsheet making procedure for nanopaper preparation.

Modifications to the standard TAPPI method (T-205) helps in producing uniform, wrinkle free nanopapers within a practical time frame of few hours. The new standardized procedure will enable the comparison of nanopaper physical properties between the studies by eliminating the variations associated with the different preparation methodologies.

5.2 Experimental method

5.2.1 Materials

Cellulose nanofibers used in this study were obtained in a gel form from University of Maine. (Lot no-U31, grade-91% fines). Grade 2 Qualitative Filter Paper Standard Grade, circle, 185 mm from Whatman^{TM}, Nylon-polyester filter bag fabric of 75 µm size.

5.2.2 Fibrillation of CNF

Fibrillation of as received CNF, when applied, was carried using the microfluidizer M-110EH-30 from Microfluidics. The CNF was diluted to 2 wt.% before introducing to the microfluidizer, such dilution of nanofibers reduced the clogging of the channels. 2 passes of CNF was carried out to obtain relatively more homogeneous CNF which is referred as CNF2P throughout this literature.

5.2.3 Nanopaper preparation

Nanopapers were prepared using the automatic british handsheet maker. The CNF was diluted to aqueous suspensions (1 litre, 2 litre or 7 litre) based on total weight of 1.2 grams of fibers per nanopaper (basis weight of 60 g/m^2). The mixture was magnetically stirred for 2 hours before introducing it to handsheet maker to allow for uniform distribution of fibers in suspension. The filter paper of 8 µm pore size was used above the metal screen in order to reduce the CNF loss. Also, an additional layer of filter fabric cloth was used above the filter paper for easy removal of filtered nanopapers. The CNF suspension was then slowly poured into the handsheet maker followed by stirring using perforated stirrer, moving up and down 5 to 6 times, keeping the perforated disc beneath the level of the liquid. After pausing for few seconds, when the surface of liquid became almost motionless, drain of the machine was fully and rapidly opened to allow water drainage through the film and filter paper under suction from the water leg at the bottom of the metal screen.

After filtration the drained nanopaper was pressed using the couch roll five times by placing a layer of Nylon-polyester filter bag fabric, 2 pieces of blotting papers and a couch plate on top. This initial pressing removed the significant amount of residual water from the gel like nanopaper. The resultant nanopaper was removed from the handsheet maker metal screen by removing the couch plate, wet blotting papers from top but keeping the fabric cloths intact. It was

then kept on a couch plate with couple of blotting papers on the top and pressed in a cold press at a pressure of 345 kPa (50 psig) for 2 minutes. Same procedure was repeated by flipping over nanopaper and replacing the blotting papers. Most of the water was removed from the cellulose nanopaper after this step. The pressing in contact with the metal plate increased the smoothness of the surface. Finally, the pressed nanopaper along with both fabric cloths was placed on a couch plate and inserted between two drying rings, assembled in such a way that nanopaper is uppermost and in contact with the rubber seat of the drying ring above it. Heavy weight was placed on top of the stack of rings to dry the nanopaper in stretched position which reduces the fiber shrinkage. These nanopapers were allowed to become fully dried at room temperature in front of the fan in a constant humidity room which usually takes 2-3 hours. The nanopapers were stored at conditions of 23 ˚C and 50% relative humidity before testing them for physical properties.

5.2.4 Characterizations

Nanopapers were characterized for their physical properties such as tensile strength, burst strength, folding endurance, tear strength and water vapor barrier properties. These physical properties were obtained as an average of the 5 different nanopaper samples. CNF fiber dimensions were measured using a combination of SEM and sedimentation experiments.

SEM images of CNF were taken using a JEOL (Tokyo, Japan) 7000-F Field Emission Scanning Electron Microscope, to measure the diameter of nanofibers. Images were acquired at magnification levels ranging between 7000-50000 to precisely measure the nanofibers of various dimensions using Image J software.

Tensile testing was performed on the nanopaper strips of dimension (length)100 mm × (width) 12 mm using PARAM XLW (EC) Auto Tensile Tester from Labthink. Cross head speed was set at 25 mm/min. Tensile index which is tensile strength divided by the basis weight was

reported to account for variations in nanopaper basis weight that could skew the tensile strength results.

Burst strength was determined using BURST-O-MATIC from Lorentzen and Wettre. Water vapor transmission rate (WVTR) was measured using PERME W3/130 water vapor tester from Labthink for circular samples of 2.6 cm diameter cut from nanopaper. Tests were performed at temperature of 23 ˚C and 50% relative humidity. Tear strength was measured using Tearing Tester from Lorentzen and Wettre. Thickness of nanopaper was measured using thickness tester from Testing Machine Inc. Folding endurance was measured using MIT Folding Endurance Tester from Tinus Olsen Testing Machine Company.

5.2.5 Aspect ratio determination

We have adopted the sedimentation method to determine CNF aspect ratios [151, 364]. In this method, sedimentation height was measured for CNF and CNF2P suspensions with different initial concentrations (C_o). 5 samples of 100 mL of nanofiber suspensions at 5 different concentrations (C_o) were mixed using magnetic stirrer in beaker for 2 hours, these uniform suspensions were then poured into 100 mL graduated glass cylinders. The fibers were then allowed to settle over several days. The height of sediment (h_s) was observed every day until it becomes steady. After about 30 days the height of sediment (h_s) was stable. All settling measurements were performed in a refrigerator to avoid the loss of water which might change the concentration of these suspensions. Initial concentrations (C_o) were plotted against ratio of h_s/ C_o and fitted as quadratic equation. The linear term of the fitted equation gives the gel concentration (g_c). Using the linear relationship between the gel concentration estimated from sedimentation method and the experimentally measured length of fibers, which is given as $g_c = {33\ w}/{l_f^2}$ where w is the fiber coarseness (mass per unit length) and l_f is the fiber length [364]. Assuming the density of the cellulose nanofibers,

ρ to be 1,500 kg/ m^3, and using equation for coarseness as $w = (\pi/4)\, D^2\, \rho$, the aspect ratio, A, is given as follows

$$\frac{1}{A^2} = \frac{D^2}{l_f^2} = \frac{4g_c}{33\pi\rho} \qquad 5.1$$

Assumptions for the above equation also include treating fibers as simple cylinders with uniform cross-sections, with the density same as density of the cell wall material [151]. Applying this method to the CNF sample used in this study, we obtained an aspect ratio of 100 which is in agreement with those reported in the literature [151, 365].

5.3 Results and discussion

In this study we have attempted to standardize the nanopaper making procedure by modifying TAPPI standard method (T-205) for forming handsheets for physical testing of pulp. T-205 is widely used to for physical testing of pulps using british handsheet maker (TAPPI 2000). Modified TAPPI standard procedure for nanopaper preparation was compared with some fast and uniform nanopaper preparation methodologies from literature.

The fiber diameters were determined from the SEM images taken at different magnifications ranging from 7000 to 50000. Fig.5.1 shows the SEM images for CNF and CNF2P at the magnifications of 15000 and 1500. Table 5.1 shows the average diameters, average aspect ratios and average lengths of CNF and CNF2P calculated from the combination of sedimentation experiment and the SEM images. The average diameter, length and aspect ratio for the CNF2P is lower than CNF due to defibrillation and applied shear during microfluidization (Table 5.1). As seen from the Fig. 5.1, number of small diameter fibers have increased after this treatment. Diameter distribution of these fibers depicted in Fig.5.2 shows narrower diameter distribution for CNF2P than CNF. The aspect ratio estimated for CNF and CNF2P using sedimentation experiment

is 100 and 90 respectively, which is representative of fibers with range of dimensions. Average fiber lengths determined using the calculated aspect ratios are 7.4 µm and 4.9 µm for CNF and CNF2P, respectively. These lengths are smaller than pore size of filter paper (8 µm); however, fiber entanglement increases the effective size of the fiber during the filtration which leads to maximum fiber retention. 100% retention of fibers was observed for both CNF and CNF2P nanopapers prepared in this study.

Table 5.1. Aspect ratio, average diameter, and average length of nanofibers calculated by fitting the linear term in equation 1.

Sample	Aspect ratio	Average diameter (nm)	Average length (µm)
CNF	100	74	7.4
CNF2P	90	54	4.9

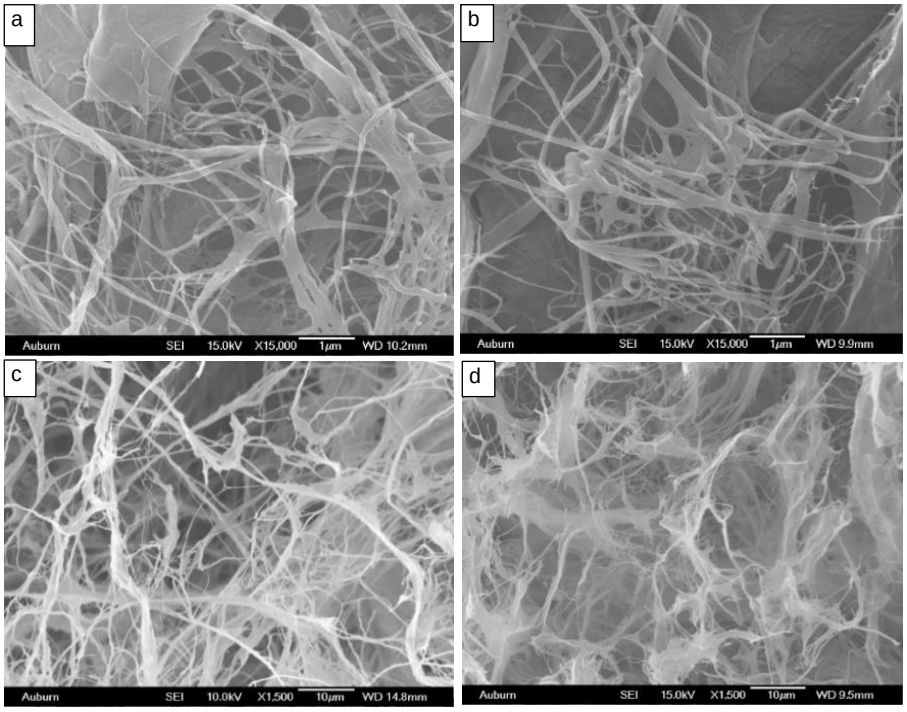

Fig 5.1. Scanning election micrographs of nanofibers (a) and (c) CNF (b) and (d) CNF2P.

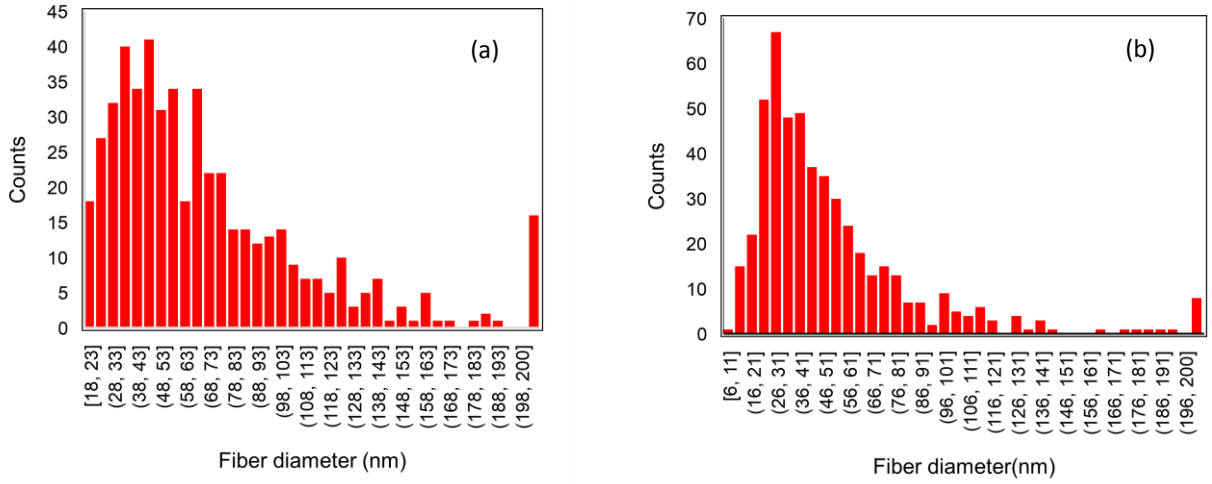

Fig 5.2. Distribution of nanofiber diameters (a) CNF (b) CNF2P.

One of the main concerns for preparation of nanopapers using filtration is the impractically longer drainage time and subsequently the total preparation time. Current literature values for drainage time ranges from few minutes to few hours [106, 148-150, 359, 360]. Drainage time depends upon the nanofiber suspension volume, nanofiber gel pore volume, pore size, thickness of the gel formed on filter medium and the pore size of the filter medium. While employing the modified procedure, the efforts were made to reduce the drainage time of standard TAPPI method for nanopaper preparation. In the TAPPI standard method, 7 liters of aqueous suspension was used to prepare the pulp handsheets; however, it was impractical to use such dilutions for nanofibers as the drainage time was almost 2 hours as listed in Table 5.2. Hence, we evaluated if the volume of nanofiber suspension can be reduced to a lower volume to reduce drainage time. As listed in the Table 5.2 the drainage time has drastically reduced from ~2 hrs to 27 minutes and 12 minutes for 2 liter and 1liter CNF suspension volume respectively. The minimum drainage time of 12 minutes obtained in this case was comparable to some literature values [151] and even lower than some

others [148, 155]. The nanofiber suspension volume was not reduced below 1 liter, since certain liquid level is required to uniformly distribute fibers using perforated stirrer used in this method. Lowest drainage time (3 minutes) so far was reported by Varanasi et al for making nanopapers of diameter 159 mm with a basis weight of 56.4 gm/m^2 [359]. In their case high concentration (0.6 wt.%) aqueous suspension of nanofibers with an average diameter of 53 nm on a 125 µm woven copper wire was used by applying the vacuum of 25 MPa. The resultant cellulose nanopapers had 94% nanofiber retention. However, in our case, it was not possible to produce desired uniform nanopaper on metal screen due to difficulties in its removal from screen surface and tendency of nanofibers to stick to the blotting paper in subsequent steps. Owing to these difficulties, a layered structure of nylon-polyester filter fabric (75 µm) and filter paper (8 µm pore size) was used above the metal screen which resolved these issues. Moreover, it also prevented the fiber loss, producing ~100% fiber retention and helped in preventing fiber shrinkage during drying.

Table 5.2. Mechanical and barrier properties of nanopapers (standard deviations are indicated in bracket).

Sample	Burst Index (kN/g)	Folding Endurance	Tear Index (mN.m^2/g)	WVTR (g/m^2.day)	Tensile Index (kN/kg)	Drainage Time (min)	Thickness (mm)
7 liter	9.20(0.6)	3.80(0.09)	3.01(0.06)	125(20)	86.03(8.3)	118(6.1)	0.13(0.01)
1 liter	9.95(0.7)	3.60(0.16)	2.87(0.08)	115(3.8)	93.30(8)	12(0.6)	0.11(0.01)
2 liter	8.89(0.8)	3.53(0.05)	2.84(0.11)	123(5.6)	94.90(4.9)	27(3.2)	0.11(0.01)
2P (1liter)	9.07(0.7)	3.67(0.2)	2.72(0.09)	132(26)	94.5(4.8)	33(1.1)	0.15(0.01)
2P (2liter)	9.67(1.2)	3.41(0.17)	2.79(0.14)	132(26)	101.01(2.4)	77(1.5)	0.16(0.01)

Physical properties of nanopapers prepared using various volumes and CNF samples are listed in Table 5.2. Mechanical and barrier properties listed are characterized using TAPPI standard of T220 “Physical Testing of Pulp Handsheets” [366]. Tukey statistical test was performed using Minitab statistical software to see if there is any effect on the properties of the cellulose nanopapers

prepared from the various CNF suspension volumes and different degree of CNF fibrillation. Tukey method considers all possible pairwise differences of means at the same time. The P value obtained from this test helps in identifying the significant difference between the different set of cellulose nanopaper samples. As shown in the Table 5.3, the P values of statistical comparison between 7 liter and 1 liter as well as 7 liter and 2 liter nanopaper samples are higher than 0.05 for all the properties characterized showing no significant differences in physical properties. Thus, drainage time could be reduced by lowering the CNF suspension volume without affecting the cellulose nanopaper properties. To evaluate the effect of CNF fibrillation on physical properties, similar comparison was also carried out between the CNF and CNF2P nanopapers prepared from same initial suspension volume of 2 liter. CNF with only 2 pass fibrillation was used since for higher passes drainage time was increased to few hours which was impractical for this study. Although an average diameter, length and aspect ratio was reduced after fibrillation, it was not enough to achieve any significant difference in the physical properties of the nanopapers as the P values obtained from Tukey test were higher than 0.05 for all the properties tested. Stelte et al [4] have reported an increase in strength and stiffness of CNF films with increased number of passes in the homogenizer; however, the number of passes in their case were higher and ranged between 5-150, with an initial fiber diameter of 20-30 μm.

Table 5.3. P values obtained from Tukey statistical test for comparison among different sample groups (0- CNF 7 litre, 1-CNF 1 litre, 2-CNF 2 litre, 3-CNF2P 1 litre, 4-CNF2P 2 litre).

Difference of samples	Property				
	Burst Index	Folding Endurance	Tear Index	WVTR	Tensile Index
0 and 1	0.497	0.225	0.401	0.963	0.369
0 and 2	0.969	0.057	0.229	1	0.242
1 and 3	0.283	0.956	0.264	0.797	0.998
2 and 4	0.522	0.678	0.954	0.982	0.588

Although the physical properties of nanopaper depend upon the raw material from which nanofibers are produced and the type of method used for their production, the tensile index of the nanopapers prepared in this study is comparable to the several reported values in literature. Similar values were reported in some cases such as 94.2 kNm/kg by Varanasi et al [359] using microfibrillated cellulose and 105 kN m/kg by Spence et al. [367] using bleached softwood nanofiber, also the lower values were reported by Stelte et al [4] and Jonoobi et al. [368] as 77.3 and 62.8 kN m/kg, respectively. However, nanopapers are weaker compared to the values reported by several authors where the tensile index ranged from 126 to 159 kN m/kg [148, 150, 162, 369]. WVTR for nanopapers ranged between 115 to 130 g/m^2.day, these values are difficult to compare to the literature values due to variation in the thickness and test conditions such as temperature and humidity. However, values obtained in this study correlate with the various thickness dependent WVTR values measured at similar conditions [370-372]. Burst Index, Tear strength and Folding endurance of CNF nanopapers has not been reported in literature but are only listed for papers where CNF was used as an additive. Standard deviations in the measured physical properties were lower than 10% of their average values (Table 5.2), these values were also very consistent between

the samples. However, in case of WVTR, the standard deviations were higher and ranged from 3% to 20% of the average WVTR values. These large variations in WVTR may be associated with the sample preparation and its mounting in the WVTR tester. Most of the literature values of standard deviation in tensile strength for nanopapers and papers were also found to be below 10% of their average reported values [137, 148-150, 152, 156, 171, 360, 373].

Drying is a crucial step in nanopaper preparation since uneven drying can induce stresses in nanofiber leading to distorted and wrinkled nanopapers as shown in Fig. 5.3(a). Issue of poor mechanical properties resulted from drying induced distortion of nanopapers during preparation has not been discussed in literature. Only few studies evaluated the effect of drying restraint on the mechanical properties of CNF films [148, 152]. Baez et al. [152] have shown that the fully restrained CNF films has superior mechanical properties than partially restrained films due to reduction in stress concentrations. Sehaqui et al [148] have reported that restrained drying of microfibrillated cellulose wet film using a vacuum sheet drier had superior mechanical performance than films prepared from other means such as oven drying or hot pressing. Restricted drying of nanopaper carried out in this study produced flat, wrinkle free and undistorted nanopapers as shown in Figure 5.3(b). Support provided by a layer of couch plate and nylon polyester fabrics restricted the out of plane distortion of nanofibers whereas the contact of nanopaper with rubber seat of drying rings restricted in-plane shrinkage of nanofibers. Consequently, such a standardized drying restraint approach would reduce the physical property data scatter between the studies.

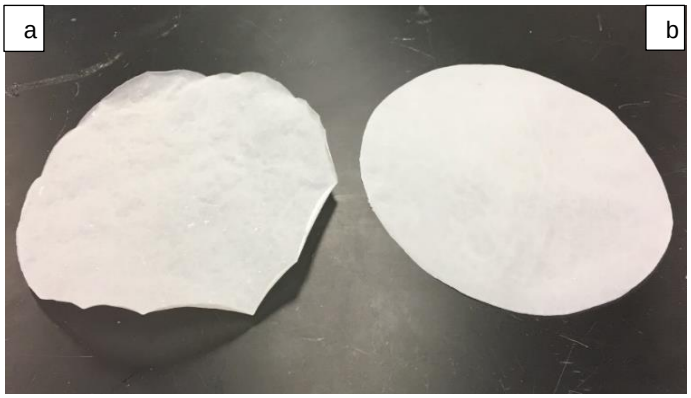

Fig 5.3. Dried nanopapers using (a) unrestricted drying between nylon polyester fabrics and without drying rings (b) restricted drying between nylon polyester fabrics with drying rings.

5.4 Conclusions

TAPPI standard method of preparation of pulp handsheets is systematically modified/optimized to prepare uniform and wrinkle free cellulose nanopapers within a practical time frame of few hours. The properties of the resultant cellulose nanopapers were comparable to the literature values. The new standardized procedure would enable the comparison of nanopaper physical properties between the studies by eliminating the variations associated with the different preparation methodologies.

CHAPTER 6

Synthesis and characterization of cellulose nanofiber and polypyrrole based nanocomposite films with improved physical and electrical properties for electromagnetic shielding applications

6.1 Introduction

Rapidly growing the electronic industry demands for shielding enclosures for protecting the devices from the electromagnetic interference (EMI) [79, 80]. As incoming electromagnetic radiation can affect the device functionality and integrity, the emitted radiations from the certain devices also need to be controlled to comply government standards [82]. Various conducting materials have been utilized for EMI shielding nanocomposite films such as metals, carbon nanotubes, carbon black, carbon fibres, graphene platelets. However, their utilization was not promising due to the requirement of higher loading for certain shielding effect, higher cost and poor mechanical properties as result of higher loading. There vary few attempts to utilize the conducting polymer and cellulose nanofiber based flexible conducting films for EMI shielding applications. This study is focused on developing flexible, strong CNF-PPy based films for EMI shielding applications.

In this research, we have prepared flexible, strong, and highly conducting nanopaper through *in-situ* polymerization of PPy on CNP (cellulose nanopaper) and PVA coated CNP. The proposed method showed improved conductivity and mechanical properties over the widely used approach in which nanocomposite films are prepared from in situ polymerized nanofibers. PPy/PVA-CNF nanocomposites prepared in this study provided highest conductivity, dry and wet tensile strength and EMI shielding effectiveness due to its smooth and uniform PPy coating and

low porosity. Physical and electrical properties of this nanocomposite film are superior to most of the cellulose-PPy based reported values in literature.

6.2 Experimental method

6.2.1 Materials

CNF used in this study was obtained in a gel form from University of Maine (Lot no-U31, grade-91% fines). Pyrrole was purchased from sigma Aldrich. Anhydrous $FeCl_3$ was purchased from Spectrum chemical. High molecular weight PVA (98-99% hydrolyzed, M_n = 150000) was obtained from Beantown chemical. Hydrochloric acid (HCl) was purchased from Macron Fine Chemicals.

6.2.2 CNP preparation

CNP was prepared using the standardized CNP preparation protocol (Fig.6.1) we have established previously [374]. PVA coated CNP (PVA-CNP) were prepared by using a doctor blade coater. Coating of CNP was carried out using aqueous PVA solution (10 wt.%) followed by drying the film in an oven at 70 °C for 12 hours, similar treatment was carried out on the other side. The dried films were further heat treated in an oven at 150 °C for 1.5 hours in order to physically cross-link the PVA coating.

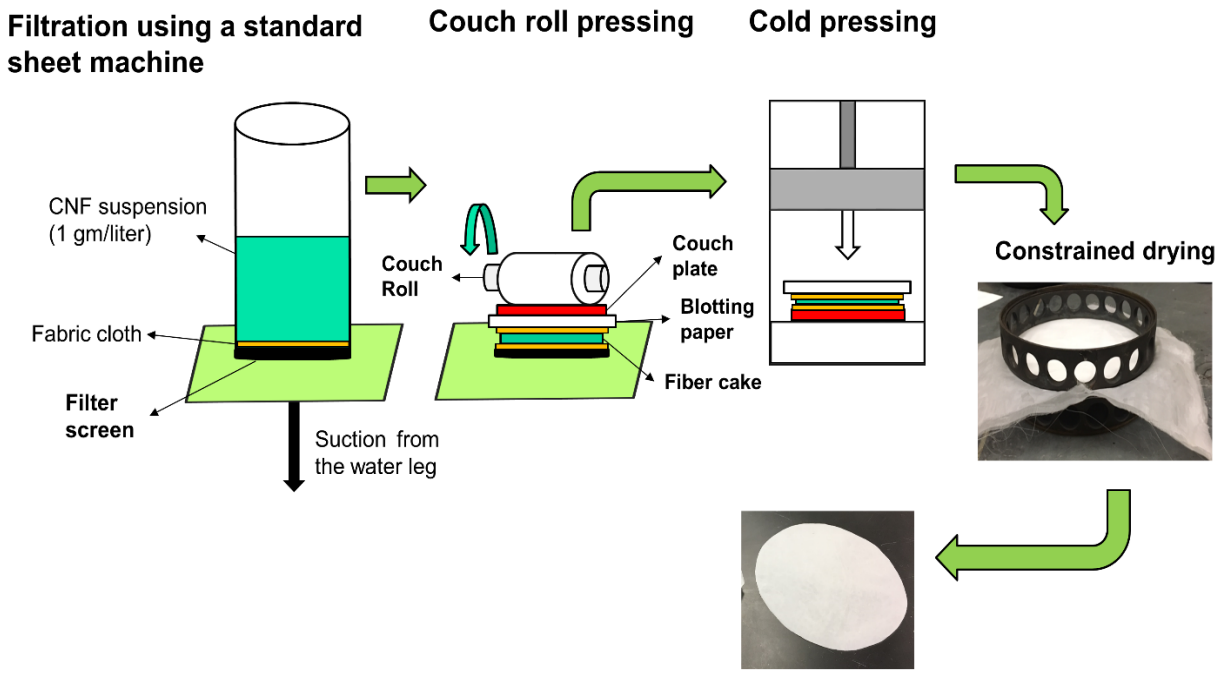

Fig.6.1. CNP preparation using a standard sheet machine.

6.2.3 Preparation of nanocomposite films

The PPy and CNF based nanocomposite films were prepared using 3 different approaches (Fig.6.2). In first approach, nanofibers were first coated with PPy followed by nanopaper preparation. The method used by Lay et al. [375] for *in-situ* polymerization of nanofibers was used. 1 g of CNF were dispersed in 1L aqueous suspension. Separately, 1.05 mL of pyrrrole was dissolved in 150 mL of 0.5 M HCl by magnetically stirring the mixture for 5 min. The pyrrole solution was then added into the above CNF suspension, and the mixture was stirred for 10 min. 6.05 g of anhydrous $FeCl_3$ in 150 mL of 0.5 HCl solution was added drop wise into the mixture to initiate the polymerization. This final mixture was stirred at room temperature for 1.5 hours. After the reaction, the PPy coated CNF mixture was first washed by filtration. This was followed by

washing of the PPy coated nanofibers using 500 mL of 0.5 M HCl, 500 mL of 0.1 M NaCl, and distilled water. Washing with DI water was complete when the filtrate did not show any increase in conductivity due to presence of residual inorganics. Finally, the PPy coated CNF aqueous suspension was mixed rigorously using magnetic stirring for 2 hours to ensure the uniform suspension. This suspension was then used for preparation of PPy-CNF nanopaper using standardized protocol described in previous section. The nanopapers prepared using this method are designated as ISF.

In second approach nanocomposite films were prepared by *in-situ* polymerization of PPy on CNP and denoted as PPy/CNP. For this 1.05 mL of pyrrole was mixed in 100 mL of water for 10 minutes. CNP was then introduced into this mixture in order to carry out the surface wetting of the CNP with concentrated pyrrole solution. The container containing this mixture was covered with the plastic film to avoid evaporation loss of pyrrole during mixing. This mixture was gently mixed for 10 min using orbital mixer to allow pyrrole monomer contact with the CNP surface. Then, 6.05 g of $FeCl_3$ in 200 mL of 0.5 M HCl solution was added dropwise to this CNP containing pyrrole mixture. The container was again covered with the plastic film after complete addition of $FeCl_3$. The reaction was continued for 1.5 hours, halfway flipping the nanopaper to ensure its good contact with reaction mixture on both sides. After the reaction PPy coated nanopaper was first washed under DI water stream to get rid of loosely bound precipitated PPy on the surface. This was followed by washing of the film using 500 mL of 0.5 M HCl, 500 mL of 0.1 M NaCl, and distilled water using filtration set up. Film washing using DI water was complete when the filtrate conductivity did not change suggesting complete removal of residual inorganics remaining in the film. This film was then further processed by cold pressing in presence of blotting papers on both sides. The couch plate was placed underneath this sample during the cold pressing on both sides

with replacement of blotting papers each time. This processing helped in removal of most of the water from the film and increased the film surface smoothness. The nanocomposite film was then dried in a constrained manner as mentioned in standardized procedure [374]. In third approach, the preparation method was same as the second approach; however, PVA-CNP was used as a substrate to obtain the nanocomposite films denoted as PPy/PVA-CNP.

6.2.4 Characterizations

Scanning electron microscopy

SEM images of film samples were taken using a JEOL (Tokyo, Japan) 7000-F Field Emission Scanning Electron Microscope, to study the morphology of the nanofibers and film surface. Samples were sputter-coated with gold before taking images.

Tensile testing

Tensile testing was performed using TAPPI standard methods (TAPPI T494 and TAPPI T456). Testing was performed on the sample film of dimension (length) 100 mm × (width) 15 mm using PARAM XLW (EC) Auto Tensile Tester from Labthink. Cross head speed was set at 25 mm/min. All the samples were conditioned at 50% relative humidity and 23 °C for 24 h before testing.

Conductivity measurement

The electric conductivity of nanopaper samples was measured on square samples (2 × 2 cm) using a linear 4 probe measurement setup connected to Agilent Technologies 34980A multifunctional switch/measure unit. The tests were carried out at the ambient atmospheric conditions. Five specimens were measured for each sample to achieve an average value. The measured resistance in Ohm was converted to conductivity (S/cm) using the equation:

$$\rho = \frac{1}{R.t} \qquad 6.1$$

Where R is resistance in Ohm and t is specimen thickness in centimeter.

Fourier transform infrared (FTIR) spectroscopy

Fourier transform infrared (FTIR) spectra of the samples were measured on a Nicolet 6700 FTIR spectrometer by Thermo Scientific. A total of 64 cumulative scans in transmission mode were taken, with a resolution of 1 cm^{-1} in the frequency range 4000−600 cm^{-1}.

Contact angle measurement

Static contact angle of the films was measured on a Ramé-Hart model 200 automated goniometer, using DROPimage standard software provided by Ramé-Hart. Measured contact angle was an average of 5 readings obtained for the water droplets, the measurement error is $\pm 2^{o}$.

Electromagnetic shielding

The SE of the samples were tested with a Keysight N55222B network analyzer. This device was connected to WR-90 which is an X-band waveguide (8–12 GHz). The network analyzer was carefully calibrated with the length of waveguide in place between ports 1 and 2. A piece of the sample was placed inside the waveguide then a two port S-parameter measurement was completed to calculate the SE values. This test was conducted on 5 specimens of each sample to mitigate any potential error.

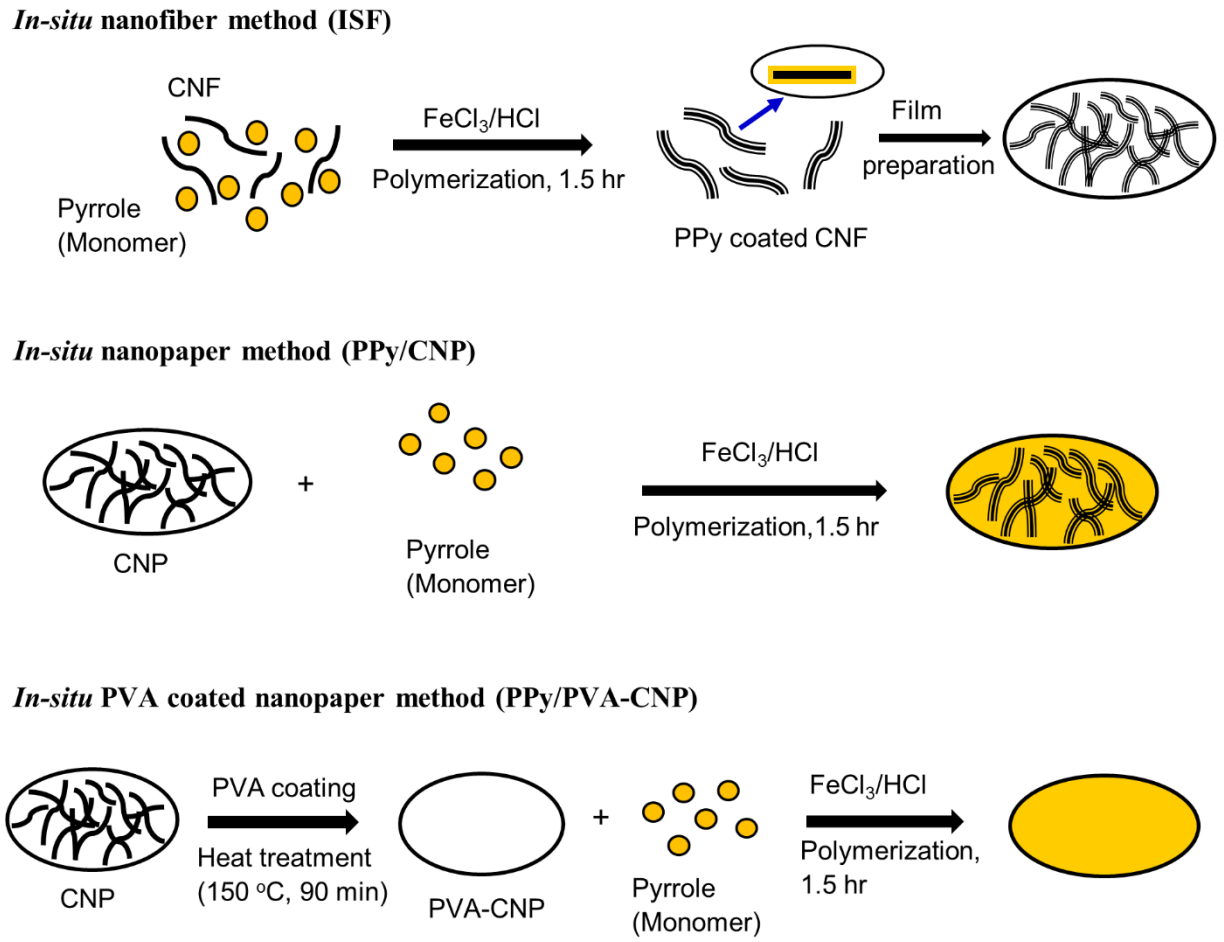

Fig.6.2. Preparation methodologies of CNF-PPy based conducting nanocomposite films.

6.3 Results and Discussion

6.3.1 Morphology

Fig.6.3 (a) depicts the CNP surface showing compact and entangled nanofiber network due to large internanofiber hydrogen bonding interactions. The ISF nanocomposite film surface in Fig.6.3 (b) also showed entangled nanofiber network; however, it has loosely packed nanofibers displaying porous surface morphology. In this case the nanofiber diameter increased due to uniform PPy coating on its surface. PPy interacts with CNF through the hydrogen bonding interaction between

N–H of the pyrrole ring and O–H of the cellulose moiety. Presence of PPy reduced the internanofiber hydrogen bonding in ISF resulting in lower film density (Table 6.1).

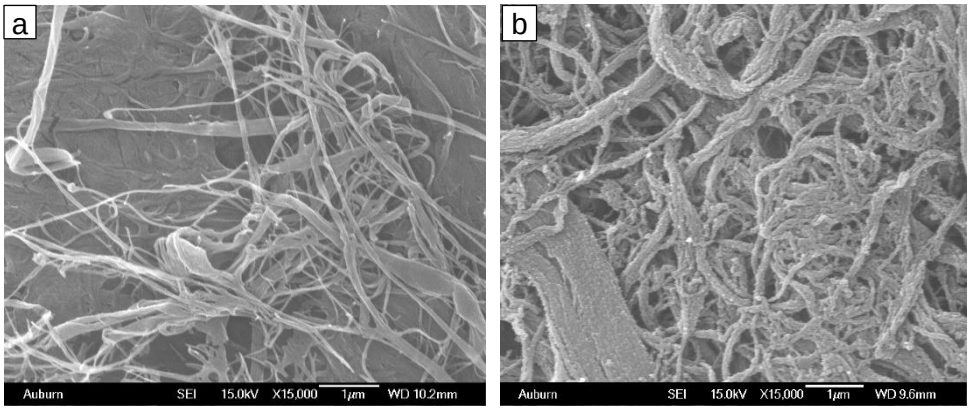

Fig.6.3. Surface morphology of the films (a) CNP (b) ISF.

Although the same reaction conditions of temperature, time and reactant ratios (CNF/Pyrrole and CNF/$FeCl_3$) were used for preparation of ISF, PPy/CNP and PPy/PVA-CNP, their SEM images revealed distinct surface morphology (Fig.6.4). Overall, it can be observed that PPy/CNP and PPy/PVA-CNP has smoother and compact surface morphology compared to ISF nanocomposite films. ISF showed a rough and porous surface (Fig.6.4 (a,b,c)), while uniform deposition of PPy on the CNP resulted in a compact yet uneven surface in PPy/CNP (Fig.6.4 (d,e,f)). Highly uniform and compact PPy coating was obtained in case PPy/PVA-CNP as shown in Fig.6.4 (g,h,i). In pyrrole polymerization, nucleation begin in aqueous pyrrole monomer solution which generates oligomers containing the initiators. During *in-situ* polymerization in presence of CNP and PVA-CNP these oligomers gets physically adsorbed onto nanopaper surface through the hydrogen bonding. The further reaction then mainly take place on the surface of these oligomer adsorbed surface than in aqueous reaction mixture since the oxidation potential of these adsorbed dimers and oligomers are lower than the pyrrole in the reaction bulk phase [376, 377]. Since both

CNF and PVA can interact with pyrrole oligomers/dimers through hydrogen bonding, the difference in surface morphology of PPy coating in PPy/CNP and PPy/PVA-CNP is related to their surface smoothness. In PPy/PVA-CNP, PPy interacts with evenly distributed high molecular weight PVA chains, while in PPy/CNP it interacts with relatively uneven surface of much larger nanofibers compared to PVA chains. The molecular distribution of individual polymer chains results in more uniform PPy coating formation on PVA coated surface [378-380]. *In-situ* polymerized nanocomposite films exhibited better flexibility than ISF nanocomposite films (Fig.6.5). PPy/CNP and PPy/PVA-CNP are strong enough to withstand the bending as well as twisting stresses; however, ISF film was stable only under bending and could not retain its shape upon twisting.

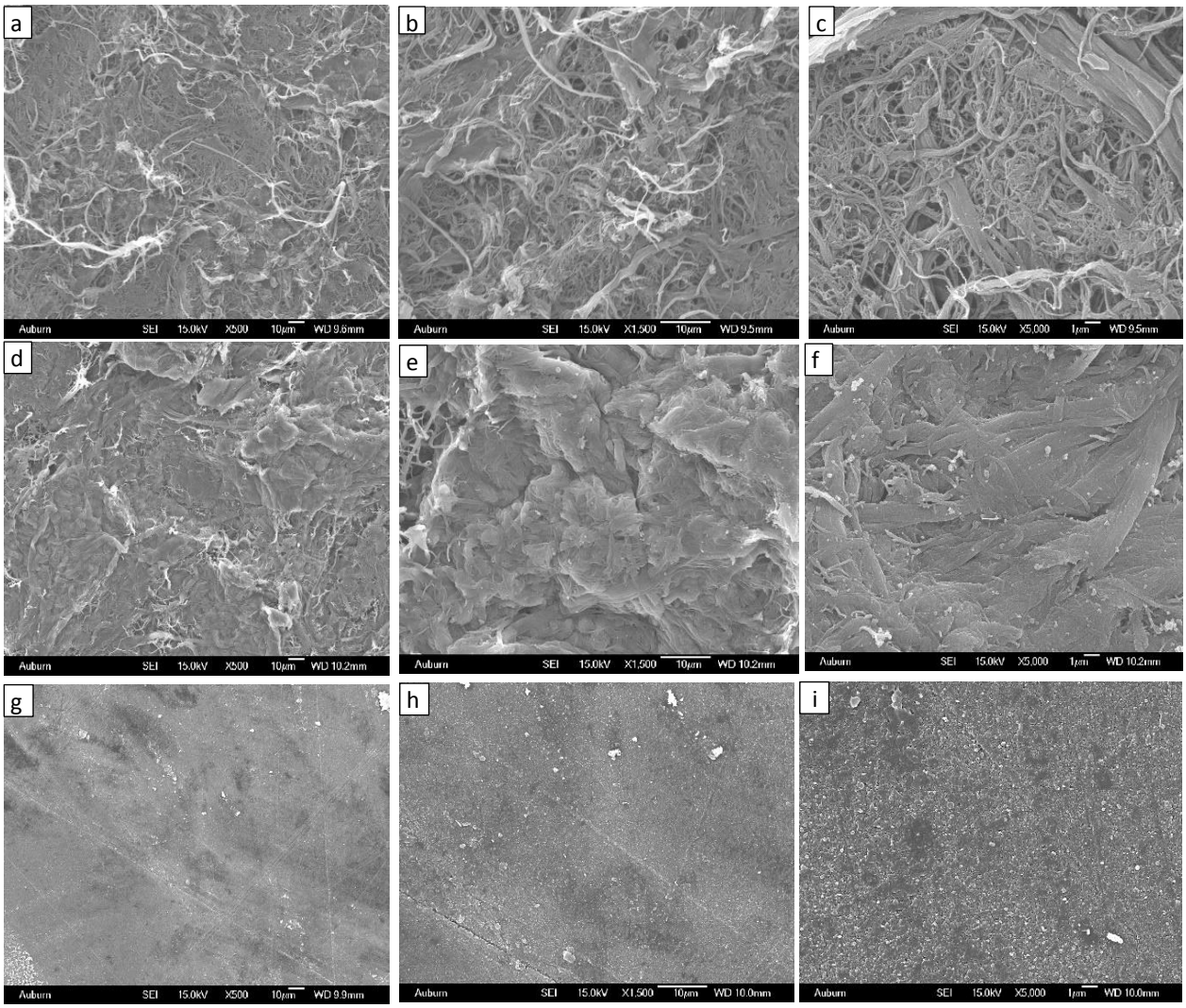

Fig.6.4. Scanning election micrographs of nanopaper samples: ISF (a,b,c), PPy/CNP (d,e,f), PPy/PVA-CNP (g,h,i).

Table 6.1. Cellulose nanopaper and nanocomposite film's average weight and densities.

Sample	Thickness (μm)	Average weight of sample (gm)	Density (kg/m^3)
CNP	75 (2.1)	1.10 (0.03)	901.0 (16)[a]
ISF	217 (8.8)	2.15 (0.05)	607.3 (15.1)
PPy/CNP	128.4 (2.9)	1.67(0.03)	796.8 (7.9)
PPy/PVA-CNP	138.4 (4.5)	2.61 (0.06)	1158.7 (22)

[a]values in parenthesis are standard deviations

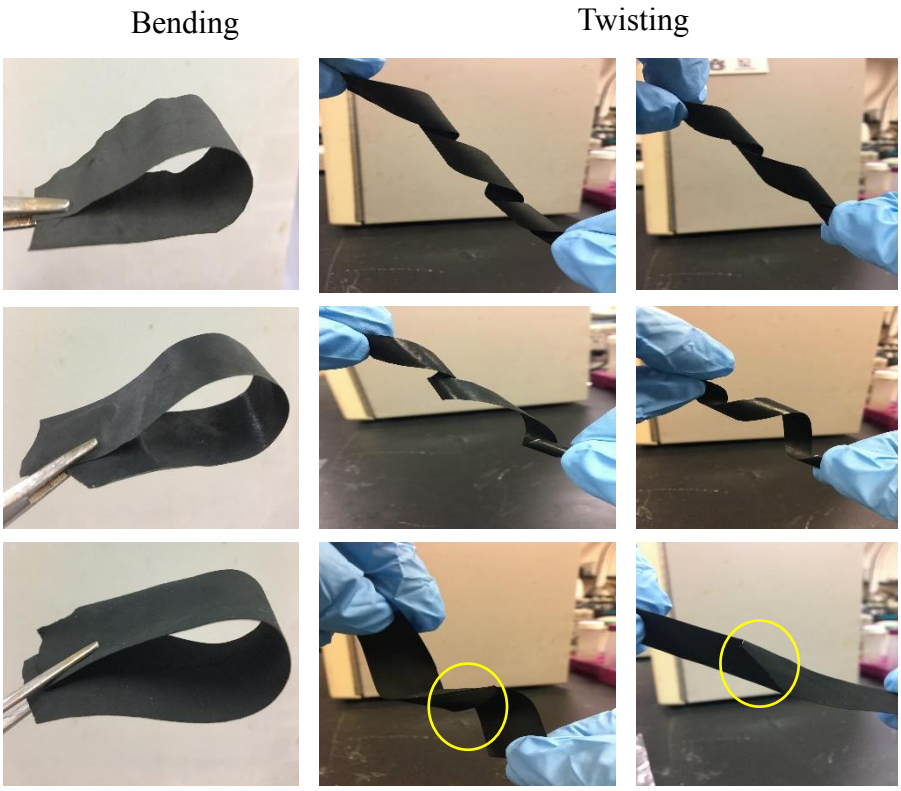

Fig.6.5. Images showing the flexibility of the PPy-CNF nanocomposite films. Row 1 (PPy/CNP), Row 2 (PPy/PVA-CNP), Row 3 (ISF). Broken portions of twisted ISF samples are marked by circle.

6.3.2 FTIR spectroscopy

Fig. 6.6(a) shows FTIR spectra of heat-treated and untreated PVA-CNP films. Peaks at 3100–3500 cm^{-1} are attributed to –OH stretching vibration of the hydrogen bonds of the water molecules and the intensity of this peak increases with the increase in water content [381]. It was observed that heat-treated samples had lower peak intensity, which can be related to the lower water content due to the higher crystallinity. For heat treated PVA-CNP, an increase in absorption peak at around 1140 cm^{-1} was observed corresponding to the C–C stretching mode; this peak is related to the crystallinity of the PVA [320, 382]. Untreated samples showed a very weak peak at around 1140

cm^{-1} while the intensity of this peak increased after heat treatment showing an increase in degree of crystallinity of PVA after heat treatment [383]. Increase in crystallinity of PVA imparted water resistance to the PVA coating during polymerization.

Fig.6.6 (b) shows the FTIR spectra for the control CNP and CNF-PPy nanocomposite films. For control CNP sample three major bands were observed, which includes the large hydroxyl group band at around 3350 cm^{-1}, C-H carbohydrate stretching band at 2900 cm^{-1}, and a sharp band corresponding to characteristic pyranose C-O-C stretching present in CNF carbohydrate ring structure at around 1050 cm^{-1}. All PPy-CNF nanocomposite films showed characteristic PPy peaks at around 1550 cm^{-1} and 1450 cm^{-1} corresponding to C-C and C-N stretching in pyrrole ring, respectively [97, 98]. For ISF nanocomposite film, these characteristic PPy peaks are prominent, while for PPy/CNP and PPy/PVA-CNP these peaks have weakened in intensity due to lower PPy content in these samples. Presence of PVA in PPy/PVA-CNP may also have weakening effect on these peak intensities. Hydroxyl peak of CNF was also absent in these nanocomposite films.

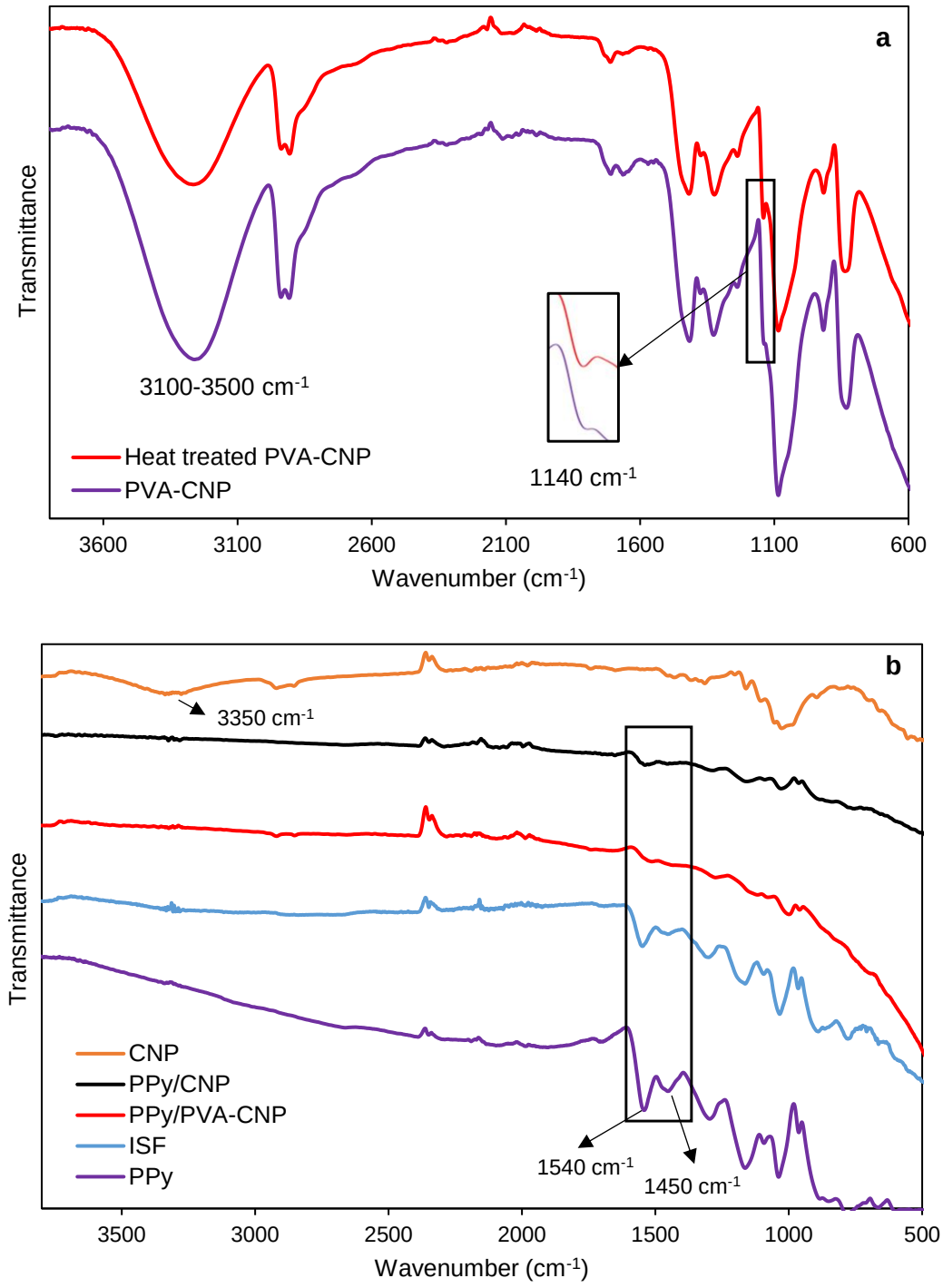

Fig.6.6. FTIR spectra of (a) heat treated and untreated PVA-CNP (b) CNP, PPy and CNF-PPy based nanocomposite films.

6.3.3 Conductivity

Table 6.2 shows that the PPy/CNP and PPy/PVA-CNP prepared using same reactant concentrations, reactant ratios and solvent volume (1.3 liters) as that of ISF resulted in about an order of magnitude lower conductivity than ISF. This was likely caused by low PPy retention on the CNP surface which resulted from the poor interaction of pyrrole monomers and oligomers with CNP surface hydroxyl groups. Most of the PPy formed during the reaction was lost as a precipitate in reaction medium. In order to improve the interaction of PPy monomers/oligomers with CNP surface hydroxyl groups, pyrrole concentration was increased without changing the CNF quantity and reactant ratios ($FeCl_3$/CNF and pyrrole/CNF). This is carried out by reducing the volume of water (up to 0.3 liters) used for solubilizing pyrrole but still ensuring complete immersion of CNP during the reaction. The improved interaction of pyrrole monomers and oligomers with the CNP surface hydroxyl groups resulted in an increased retention of PPy in PPy/CNP and PPy/PVA-CNP as seen from their percentage of weight gained after the reaction. Consequently, significant increase in their conductivity was observed (Table 6.2).

Table 6.2. Conductivity and % PPy gain in nanocomposite films prepared using different methods.

Solvent volume (L)	Sample	Conductivity (S/cm)	% PPy weight gain
1.3	ISF	0.26 (0.05)[a]	95 (3.2)
	PPy/CNP	0.02 (0.006)	10.4 (2.1)
	PPy/PVA-CNP	0.06 (0.009)	5.3 (1.3)
0.3	PPy/CNP	4.3 (0.2)	51.4 (1.8)
	PPy/PVA-CNP	8.4 (0.7)	48.2 (1.5)

[a]values in parenthesis are standard deviations

As shown in Table 6.2, percentage of weight gained due to formation of PPy after the reaction was highest for the ISF nanocomposite films as there was no PPy loss during its preparation. For PPy/CNP and PPy/PVA-CNP prepared using 0.3 liter solvent volume, almost half

of the PPy is lost through its precipitation in the reaction media. Interestingly, ISF did not have higher conductivity than the PPy/CNP and PPy/PVA-CNP despite having more PPy content. This may be due to high film porosity in ISF as shown in Fig.6.3(b) impeding the conduction of electrons. Among the *in-situ* polymerized nanopaper samples, PPy/PVA-CNP has shown higher conductivity than the PPy/CNP despite having similar PPy retention. Smoother and more uniform PPy coating is likely responsible for this improved conductivity in PPy/PVA-CNP [384]. Physically cross-linked PVA coating in PPy/PVA-CNP provided a smooth surface for interaction with pyrrole monomers and oligomers through hydrogen bonding thereby providing a continuous and compact network of PPy. Moreover, it is possible that the good conducting state of PPy can be maintained in PPy/PVA-CNP than in PPy/CNP because of a possible weaker interaction of PPy with cross-linked PVA surface compared to CNF surface in PPy/CNP. A similar observation was reported for PPy/cellulose nanocomposite films where cross-linked cellulose surface resulted in higher conductivity than pure cellulose surface [385]. Fig.6.7 shows the conductivity measurements of the nanocomposite films in different configurations.

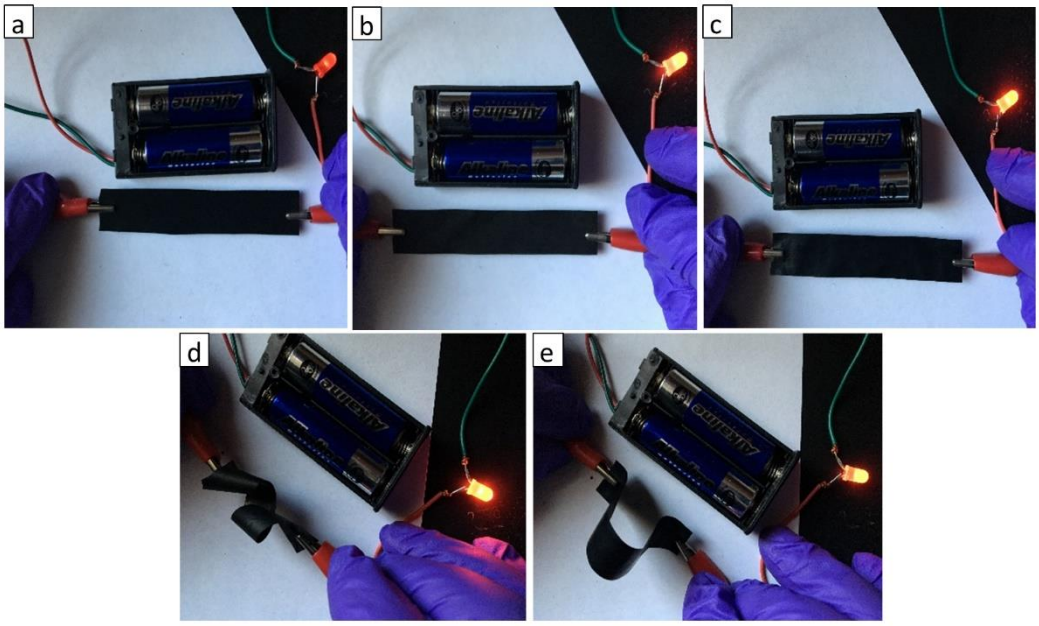

Fig.6.7. Images showing conductivity of (a) ISF (b) PPy/CNP (c) PPy/PVA-CNP (d) PPy/PVA-CNP (twisted) (e) PPy/PVA-CNP (bend).

6.3.4 Mechanical properties

Due to poor mechanical strength and difficulty in processing of PPy based films, it is desirable to utilize the flexible substrates like cellulose nanofibers. However, most attempts to prepare the PPy and CNF based conducting nanocomposite films in the literature are based on the *in-situ* polymerization of pyrrole onto nanofibers to obtain the conducting polymer coated nanofibers followed by film preparation using these nanofibers. However, the main drawback of this approach is loss of mechanical strength owing to reduction in hydrogen bonding between the nanofibers. Fig.6.8 compares the tensile strength of the CNP prepared using the standardized method as discussed in chapter 5 with the CNP prepared using casting method. It was observed that CNP prepared using standardized method resulted in tensile strength of 91.7 (±5.9) MPa compared to 81.9 (±6) MPa for casted CNP. The increased strength of CNP from standardized method may be

due to their higher density and in-plane orientation of nanofibers compared to casted CNP [148]. Unlike casting approach standardized method resulted in compact nanopaper formation due to couch roll pressing and cold pressing steps. This standardized CNP was used for nanocomposite preparation using *in-situ* nanopaper method.

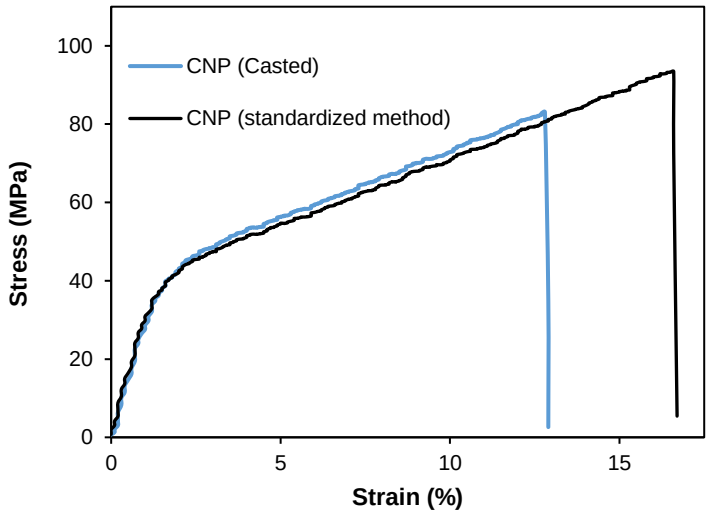

Fig.6.8. Stress vs Strain (%) plot for CNP using casting and standardized method.

Fig. 6.9 (a) shows the stress vs strain plots for the pure CNP and nanocomposite films. ISF showed poor mechanical properties due to reduction in hydrogen bonding interaction between the PPy coated nanofibers. Tensile strength of 7.6 MPa was obtained for ISF which was significantly lower compared to pure CNP tensile strength of 91.7 MPa. Van der Waal interaction between the PPy coated CNF in ISF was poor compared to hydrogen bonding interaction among CNFs in CNP. This has also resulted in increase in porosity of the ISF than CNP as shown in Fig.6.3(b). Unlike ISF nanocomposite films, internanofiber hydrogen bonding interaction was retained in PPy/CNP and PPy/PVA-CNP thus facilitating the higher tensile strength of these nanocomposite films. PPy/CNP films had tensile strength of 88.6 MPa which is similar to the tensile strength of CNP. For PPy/PVA-CNP tensile strength was higher compared to PPy/CNP. The improvement in tensile

strength resulted from the reduced porosity of the film due to impregnation of PVA into CNP during coating process. Moreover, reduction in moisture absorption of the film resulted from increased crystallinity of PVA coating can also contribute to the increase in strength. Elongation at break has reduced in case of PPy/PVA-CNP due to higher stiffness of physically cross-linked PVA coating. PPy/CNP showed higher elongation at break than PPy/PVA-CNP.

The nanocomposite films were also characterized for their wet strength, which is carried out by soaking the films in water for 1 hour prior to its tensile testing (Fig.6.9(b)). Tensile strength and elongation at break decreased for all the nanocomposite films. However, the degree of tensile strength retention was higher for PPy/PVA-CNP than PPy/CNP. Absorption of water has significantly reduced the hydrogen bonding interaction between the nanofibers in PPy/CNP, while in case of PPy/PVA-CNP, high crystallinity of heat treated PVA coating reduced the water absorption thereby minimizing the strength reduction. Higher elongation at break for PPy/PVA-CNP compared to PPy/CNP is due to higher extensibility of the physically cross-linked PVA coating upon absorption of water. ISF has poor wet strength due to high absorption of water in its porous structure.

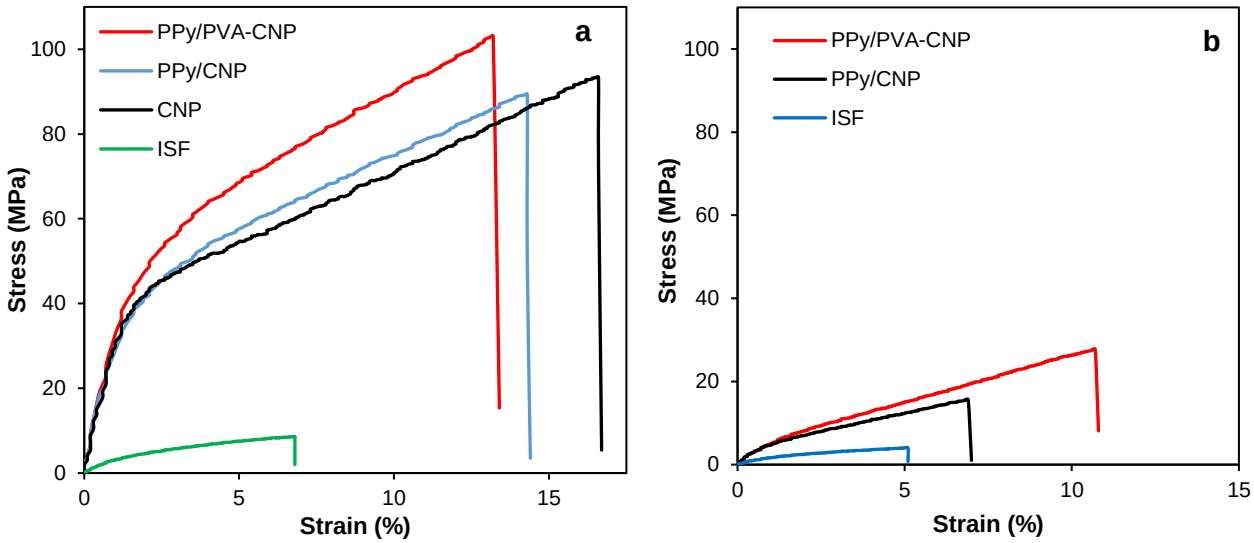

Fig.6.9. Stress vs Strain (%) plot for (a) CNF and CNF-PPy nanocomposite films (b) wet CNF and CNF-PPy nanocomposite films.

Table 6.3. Mechanical properties of CNF and CNF-PPy nanocomposite films.

	Tensile strength (MPa)		Strain (%)		
Sample	**Dry**	**Wet**	**Dry**	**Wet**	**Thickness (μm)**
CNP	91.7 (5.9)[a]	N/A	16.1 (1.4)	N/A	75 (2.1)
ISF	7.6 (0.2)	4 (1.7)	5.8 (0.8)	2.1 (0.3)	217 (8.8)
PPy/CNP	88.6 (5.8)	16 (4.5)	13.4 (1.9)	6.6 (1.4)	128.4 (2.9)
PPy/PVA- CNP	103.8 (5.9)	27.4 (2.2)	11.9 (1.7)	9.4 (1.1)	138.4 (4.5)

[a]values in parenthesis are standard deviations

Compared to most of the studies in literature, the current study showed superior tensile strength and conductivity for CNF and conducting polymer based nanocomposite films (Fig.6.10). This is due to the advantages offered by the current approach such as retention of internanofiber hydrogen bonding, higher nanopaper density, minimal direct exposure of nanofibers with $FeCl_3$ or HCl and uniform PPy coating formation. The *in-situ* polymerization of CNP in aqueous medium

in this study resulted in significantly higher conductivity compared to other *in-situ* vapor phase polymerization [98, 386] and *in-situ* nanofiber polymerization [387] approaches due to high PPy retention on nanopaper surface and uniform PPy coating formation. Amount of PPy deposited on CNP surface in this case in ~25 gm/m^2 which was significantly higher compared to 9.8 gm/m^2 obtained during vapor phase polymerization [98]. Also, unlike vapor phase method the current approach minimizes the direct interaction of nanofibers with the oxidant and acid dopant which can have negative impact on strength properties of the CNP. This approach can largely retain or enhance the tensile strength of CNP in nanocomposite films. High tensile strength reported by Chen et al. [98] resulted from different type of nanocellulose (regenerated cellulose) used in their study as a substrate for the preparation of PPy based nanocomposite films, where the substrate has very high tensile strength compared to CNF used in our study.

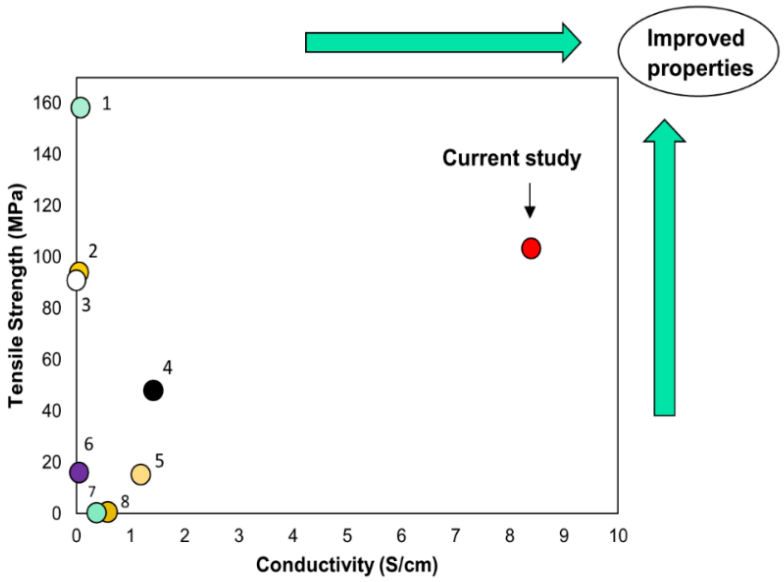

Fig.6.10. Comparison of the cellulose based conducting nanocomposite films based on their maximum reported conductivity and tensile strength. (1-[98], 2-[388], 3-[102], 4-[101], 5-[100], 6-[384], 7-[99], 8-[389]).

6.3.5 Water resistance and surface wettability

Applicability of CNF-PPy based nanocomposite films would be improved if these films can withstand the aqueous environment. Although PPy is water resistant, hydrophilic nature of CNF affects the structural stability of these films in aqueous medium. Stability of the composite films in aqueous medium was characterized by monitoring their structural stability. Films samples of size 3 cm× 3 cm were cut and were kept under rigorous mixing in water for 7 days. It was observed that ISF nanocomposite film completely disintegrated into large fragments, while PPy/CNP and PPy/PVA-CNP retained their original shape without dissociation of any PPy from surface (Fig.6.11). The enhanced water stability of these films is due to the presence of relatively hydrophobic, uniform, and compact PPy coating.

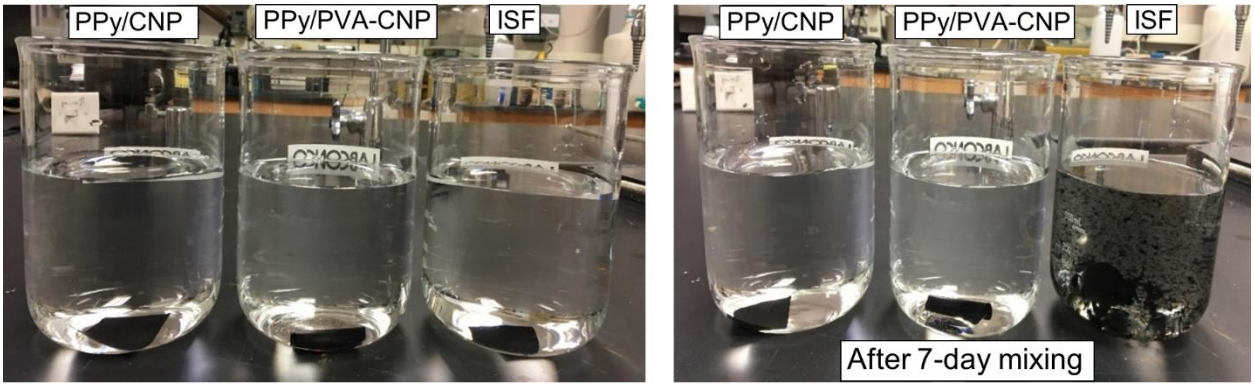

Fig.6.11. Images showing water stability of the nanocomposite films before and after 7-day mixing.

Surface wettability of the nanocomposite films was characterized using the water contact angle measurements (Table 6.4). The control CNP showed lower contact angle of 65^{o} due to hydrophilic nature of CNF. For heat treated PVA-CNP the contact angle increased up to 77^{o} as increase in crystallinity of PVA coating reduced the surface hydrophilicity. Due to presence of compact and relatively hydrophobic PPy coating, contact angle for PPy/CNP and PPy/PVA-CNP

has increased to 92^{o} and 93^{o}, respectively. For ISF nanocomposite film the contact angle drastically reduced to 20^{o} due its highly porous surface morphology.

Table 6.4. Water contact angle measurement of the films.

Sample	Contact angle (deg)
CNP	65 (3.1)[a]
PVA-CNP (heat treated)	77 (1.5)
ISF	20 (0.5)
PPy/CNP	92 (2.2)
PPy/PVA-CNP	93 (2.6)

[a]values in parenthesis are standard deviations

6.3.6 EMI shielding properties of films

The EMI shielding properties of the films were characterized. Electromagnetic interference (EMI) can be defined as conducted or radiated electromagnetic signal that interferes with the operation of other electronic devices [390]. When an electromagnetic wave encounters a material surface it can either be reflected, absorbed, or transmitted. EMI shielding can be carried out by reflection or absorption of the electromagnetic signal. The efficacy of the EMI shielding is often characterized as shielding effectiveness (SE) measured in the logarithmic unit of decibels (dB). Total shielding effectiveness SE_{total} is a summation of three different shielding mechanisms and is given as follows

$$SE_{total}\ (dB) = SE_A + SE_R + SE_{MR}$$

where SE_A represents the absorption loss of the wave through attenuation in the medium, SE_R represents the shielding by reflection in the medium, and SE_{MR} represents the additional effects due to multiple reflections and absorption in the medium [82].

The SE of the nanocomposite films were measured and recorded in X-band microwave region (8–12 GHz). As shown in Fig.6.12(a), the control samples of CNP and PVA-CNP have SE values near zero as these films had very low conductivity and therefore transmit most of the electromagnetic energy. The ISF sample had a SE value of around -10.6 dB, while the PPy/CNP and PPy/PVA-CNP films exhibited a higher shielding effectiveness of -21 dB and -23 dB, respectively. Poor SE of ISF was due to a lower conductivity and higher porosity of this film; while the superior SE of the PPy/PVA-CNP can be attributed to its higher conductivity and greater density which reduced the radiation transparent empty voids. The shielding effectiveness values of these films are directly related to their conductivity and showed absorption and resistive dissipation to be main mechanism for the EMI shielding (Fig.6.12(b)). EMI shielding properties of these films were superior when compared to the previous studies based on conducting polymer and cellulose based flexible nanocomposite films (Fig.6.13). Shielding effectiveness of PPy/PVA-CNP in this study is higher than the reported literature values of cellulose and conducting polymer based nanocomposite films of given thickness (Table 6.5). These films can have applicability as flexible, low cost and light weight alternative of EMI shielding material for electronic devices such as desktop computers and laptops where SE upto 20 dB is desired [80, 391, 392].

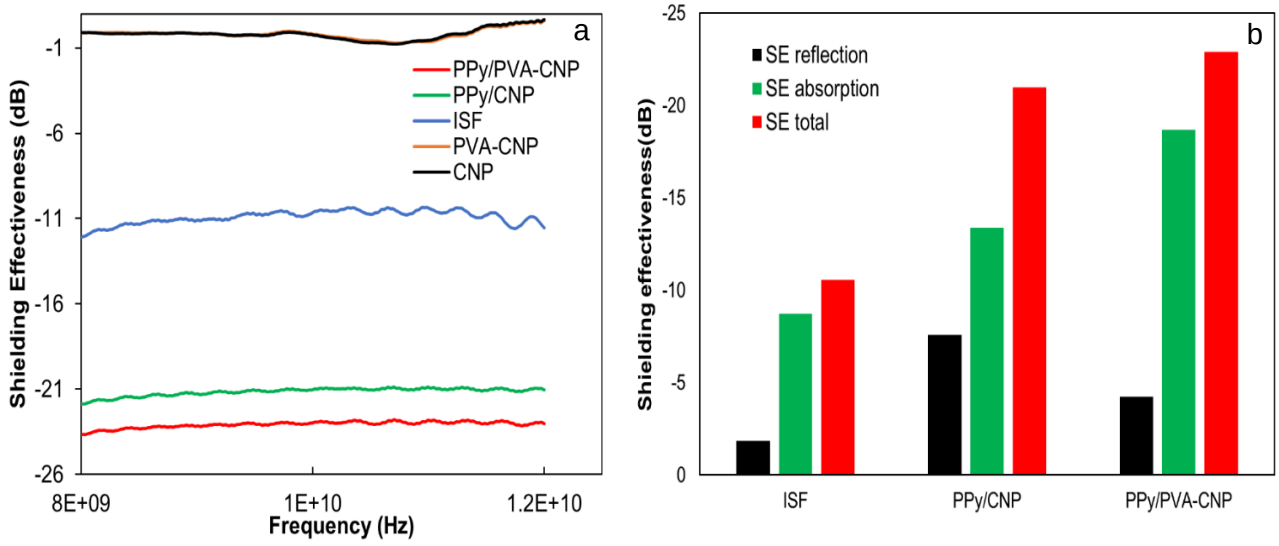

Fig.6.12. (a) Electromagnetic shielding effectiveness plot for CNP and CNF-PPy nanocomposite films (b) Shielding effectiveness of the nanocomposite films at 10 GHz.

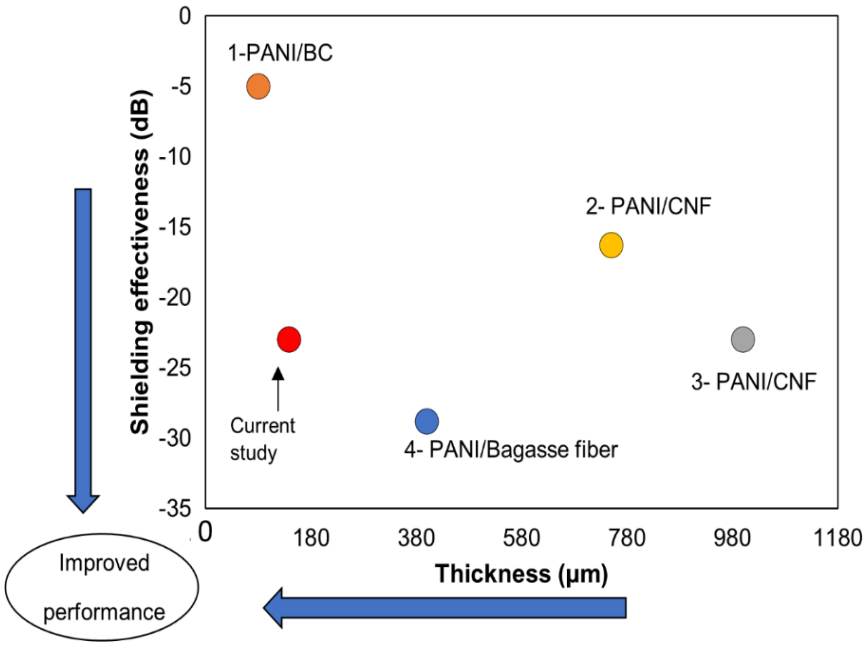

Fig.6.13. EMI shielding performance comparison for cellulose and conducting polymer based nanocomposite films.(1-[384], 2 and 3 - [88], 4-[393]).

Table 6.5. Comparison of EMI shielding effectiveness of conducting polymer and cellulose based nanocomposite films.

Material	Conductivity (S/cm)	Thickness (μm)	Shielding effectiveness (dB)	Reference
PPy/PVA-CNP	8.4	138.4	-23	Current study
PANI/Bacterial cellulose	0.038	80	-5	[384]
PANI/CNF	0.314	1000	-23	[88]
PANI/CNF	0.314	750	-16.3	[88]
PANI/Bagasse fiber	2	400	-28.8	[393]

In good conductors, the magnetic field lags the electric field by 45 degrees, therefore there is a large decrease in propagation velocity and wavelength leading to a rapid attenuation as the electromagnetic wave propagates through them [394]. The distance where the field strength has reduced to e^{-1} or ~37% is known as the penetration depth, and in good conductors it is referred to as the skin depth [391]. It can be mathematically calculated with the following equation:

$$\text{Skin depth } (\delta) = \frac{1}{\sqrt{\pi f \mu \sigma}} = -8.68 \frac{t}{SE_A} \qquad 6.2$$

Where f is frequency, σ is conductivity, μ is permeability and t is thickness of the sample. Skin depths for ISF, PPy/CNP and PPy/PVA-CNP are 228.7 μm, 83.2 μm and 64.3 μm, respectively. Skin depth is smaller in PPy/PVA-CNP and PPy/CNP due to uniform and compact PPy coating in these films which provides higher and uniform conductivity allowing for greater attenuation with thinner substrates than other flexible coatings presented in literature. This promising EMI shielding effectiveness of the PPy/PVA-CNP enhances their applicability as a flexible, strong, EMI shielding coating in various electronic devices.

6.3.7 Thermal properties

Fig.6.14 shows the thermogravimetric weight% vs temperature plots for the CNF and PPy based nanocomposites. The data is plotted after the 20 minutes equilibrium step at 120 °C to ensure the moisture removal from the sample. Pure CNF nanopaper has drastic degradation between the 280 °C to 370 °C, with residual weight% upto 20% at 800 °C. This degradation behavior is typical for the cellulose pyrolysis involving the formation of various anhydro-monosaccharides such as levoglucosan, 1,6-anhydro-β-D-glucopyranose, also carbon dioxide and char [395]. While pure PPy has gradual degradation from 180 °C to 800 °C with residual weight % of about 60%, which shows the superior high temperature thermal stability of the PPy than CNF. The derivative weight% vs temperature plot in Fig.6.15 is more sensitive to weight loss, the difference in rate of degradation of CNF and PPy can be marked by their peak intensity. A single sharp peak was observed for the CNF with maximum degradation temperature of around 336.5 ^{o}C, while PPy has two degradation peaks between the temperature range of 105-315 ^{o}C and 315-600 ^{o}C corresponding to loss of dopant ion and polymer backbone degradation, respectively [396]. The maximum degradation temperature for these degradation steps are 264 ^{o}C and 482 ^{o}C, respectively.

Among the PPy-CNF based nanocomposite films, ISF nanopapers showed more stability compared to others due to higher retention of PPy on the nanopaper surface. PPy/CNF has similar degradation behavior as ISF nanopapers with reduced thermal stability due to lower PPy concentration in the film. For PPy/PVA-CNF samples the thermal stability was slightly higher than the CNF/PPy samples upto 240 ^{o}C which may be due to presence of cross-linked high molecular weight PVA. The residual weight % for the PPy/PVA-CNF sample was lower than that of PPy/CNF and ISF samples because of the complete degradation of PVA happens at around 500 ^{o}C.

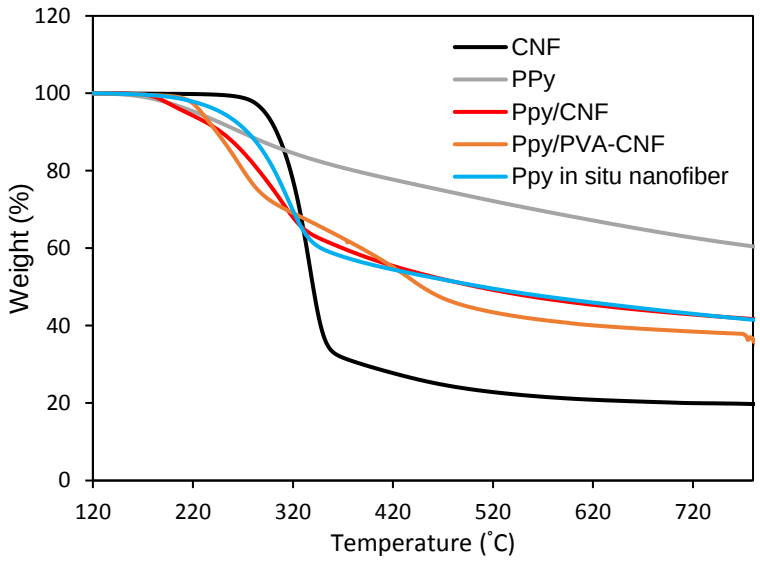

Fig.6.14. TGA curves of CNF, PPy and nanocomposite films.

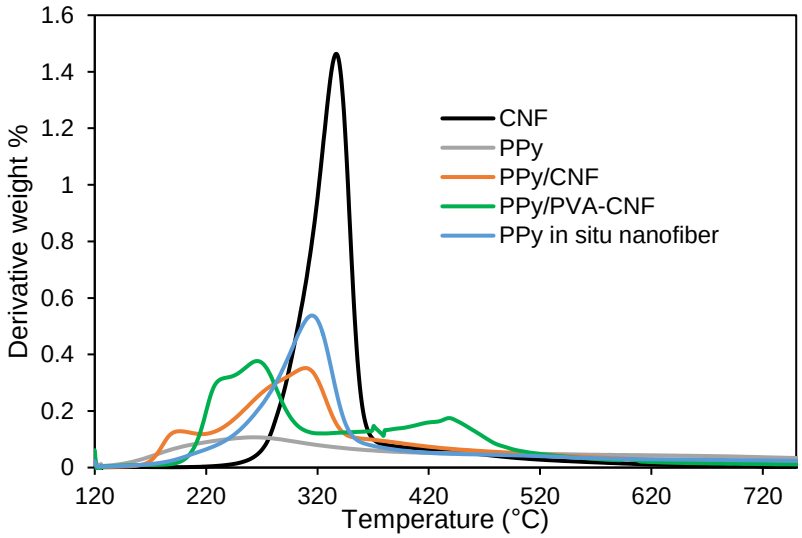

Fig.6.15. Derivative weight loss plots for the CNF, PPy and nanocomposite samples.

6.4 Conclusions

Newly developed PPy-CNF based nanocomposite films in this study showed superior physical and electrical properties compared to the widely used ISF approach. The nanocomposite films were prepared by *in-situ* polymerization of PPy onto CNP (PPy/CNP) and PVA coated CNP (PPy/PVA-CNP). FTIR characterization confirmed the structure of these films. SEM images of these film surfaces revealed distinct morphology of PPy coating. PPy/CNP and PPy/PVA-CNP showed more uniform and compact PPy coating compared to ISF which exhibited rough and porous structures. PVA coated CNP improved uniformity of PPy coating in PPy/PVA-CNP compared to PPy/CNP. This has resulted in significant improvement in the conductivity and water resistance of PPy/PVA-CNP. Tensile strength of CNP was retained in PPy/CNP and PPy/PVA-CNP compared to ISF where reduction in internanofiber hydrogen bonding drastically reduced its tensile strength. Presence of physically cross-linked PVA and reduced film porosity has further improved the tensile strength of PPy/PVA-CNP. It has conductivity of 8.4 S/cm, tensile strength of 103.8 MPa, wet strength of 27.4 MPa, and EMI shielding effectiveness of -23 dB for a film thickness of 138.4 μm. The tensile strength and SE of PPy/PVA-CNP in this study is so far the maximum reported value for a conducting polymer and CNF based nanocomposite film of this thickness. We believe that the current approach would enable the scalable preparation of PPy-CNF based flexible conducting nanocomposite films with superior physical and electrical properties. These low cost biobased conducting nanocomposite films can have potential applications in EMI shielding films, antistatic and anticorrosive coatings, sensors, flexible electrodes, and tissue engineering scaffolds.

CHAPTER 7

Conclusions and future work

This dissertation established the valorization of lignocellulosic nanomaterials CNC, CNF and KL through design, synthesis, and processing of their functional nanocomposites. Simple, novel, and green approach was designed to produce transparent, homogeneous CNC-KL based UV protection films through optimal addition of electrolytes. First, the effect of electrolytes with the different valences, sizes and pH was studied on self-assembly, optical, and mechanical properties of CNC films. At optimal addition of electrolytes chiral nematic self-assembly was eliminated giving highly transparent, nematic films as confirmed from their cross polarized optical microscopy, which demonstrated for the first time that the CNC suspension can be tuned through addition of electrolytes to produce transparent, homogenous CNC films. Also, the tensile strength of CNC film improved with an optimum addition of electrolytes which may be due to the ionic bonding interaction between the positive counter ions and negative sulfate ester groups. At higher electrolyte concentration, the screening of electrostatic repulsion between CNC rods caused aggregation which reduced the transparency of CNC film. For multivalent electrolytes stronger interaction of positive counter ions with negative sulfate ester groups of CNC prevented their precipitation at higher concentration unlike monovalent electrolyte counter ions. Further, CNC/KL based transparent, UV protection films were designed by incorporating KL and using NaOH as an additive. Besides screening the chiral interaction, NaOH could also solubilize KL in CNC suspension through deprotonation of phenolic groups in KL resulting in their uniform dispersion in CNC films. In order to improve the transparency of CNC/KL films, KL was further modified by acetylation or oxidative hydrogen peroxide bleaching treatment. Bleaching treatment was optimized to tune KL optical properties for achieving high transparency and UV blocking in

CNC/KL nanocomposite films. CNC and peroxide bleached KL nanocomposites showed superior performance in terms of UV blocking and transparency compared to 4-amino benzoic acid (4-ABA), a commercial organic UV absorbent and most of the lignin based transparent, UV blocking nanocomposites in literature. Overall, these CNC/KL nanocomposites has promising potential to be a biodegradable, low-cost alternative as a coating material with high transparency and UV blocking functionality in applications such as automobile windshields, building windows, UV sensitive polymer coatings, and transparent multilayer packaging materials.

Scope of the nanocellulose and KL was further expanded by synthesizing multifunctional nanocomposites using KL, CNF, and PVA. In order to address the issue of dark brown kraft lignin color and its possible migration and leaching in nanocomposite films, modified CNF was synthesized by grafting KL onto carboxylated CNF via amidation reaction and further treatment with hydrogen peroxide to reduce the lignin color. The modified CNF exhibited thermodynamic compatibility with the PVA matrix. This was qualitatively observed from their uniform dispersion in PVA matrix without formation of large aggregates, while the quantitative confirmation was obtained from improved T_g of the modified CNF and PVA nanocomposites. These nanocomposites were UV blocking and transparent, with high flexibility, mechanical strength, and thermal stability. Also, the addition of modified CNF may have the counterbalancing effect on permeability of water vapors in nanocomposite films. The increase in modified CNF provided more crystalline regions in nanocomposites which could reduce the diffusion and solubility of water vapors in nanocomposite films; however, it has also reduced the crystallinity of PVA matrix contributing to increase in diffusion. As an overall result the water vapor barrier properties of PVA were retained in these nanocomposites. Heat treatment of these nanocomposites rendered them water resistance and prevented lignin leaching. PVA and modified CNF nanocomposites also showed superior

performance in terms of transparency and UV blocking properties compared to most lignin based transparent and UV blocking nanocomposites reported in literature. These multifunctional nanocomposites using biobased nanofiller can be used as transparent, UV protecting films in applications such as healthcare, food and UV sensitive materials packaging, optical lenses, and optoelectronics where high flexibility, strength, and water resistance are desired. The use of this fully biobased modified CNF can be further extended to other hydrophilic polymer matrices to introduce multifunctionality.

Standard CNP preparation procedure based on papermaking like process was developed. This method enabled uniform and fast preparation of CNP which can be used as a standard for comparing the physical properties of CNF from various sources and processes. The CNP prepared using this procedure has superior physical properties compared to CNP obtained from casting approach. CNP prepared using this standardized method was developed as a flexible and biodegradable substrate for synthesizing the polypyrrole based conducting nanocomposite films with improved physical and electrical properties. A new approach based on *in-situ* CNP polymerization was developed, which allowed the PPy nanocomposite processing without need for its compatibilization unlike nanocomposite blends. PPy interacted with CNP and physically cross linked PVA coated CNP (PVA-CNP) through hydrogen bonding interaction. Highly smooth PVA coating resulted in much uniform PPy deposition and higher density which caused maximum electronic conductivity, tensile strengths (dry and wet) and water stability compared to widely used *in-situ* nanofiber polymerization approach in literature. The applicability of these nanocomposite films in EMI shielding applications was shown. PPy/PVA-CNP exhibited higher shielding effectiveness (SE) compared to nanocomposites produced using *in-situ* nanofiber polymerization approach. The tensile strength and SE of PPy/PVA-CNP in this study is so far the maximum

reported value for a conducting polymer and CNF based nanocomposite film of this thickness. These nanocomposites have applicability as new functional materials for flexible EMI shielding, antistatic and anticorrosive coatings in electronic devices.

Overall, this research showed that the kraft pulp and paper industry biomass derived lignocellulosic nanomaterials (CNC, CNF, and KL) has potential to be developed into value added materials. Inherent optical, thermal, and mechanical properties of these biobased nanomaterials can be synergistically utilized to design, process, and synthesize functional polymer nanocomposites. These efforts can provide a new platform for the economically and environmentally feasible utilization of lignocellulosic biomass produced from pulp & paper industry and biorefineries, contributing to the sustainability of these industries.

Future study can focus on realizing the potential of the CNC/KL nanocomposites as coating material for applications such as building windows, multilayer packaging applications. The adhesion of the optimized CNC/KL coating formulations in gel form on glass and various polymeric substrates can be explored. Moreover, the standard prolonged UV weathering tests [397] can be performed to assess the performance of KL and peroxide bleached KL as an UV absorbent. Also, more insights into effect of surface charge and electrolyte on self-assembly and rheological properties of CNC can be obtained from rheological characterizations of dialyzed CNC, as received CNC and CNC containing electrolytes. Moreover, it would be interesting to see the role of surface charge and electrolyte counter ions in unwinding the chiral nematic self-assembly and promoting the alignment of CNC rods under mechanical shear. The order parameter can be estimated for these sheared films using facile UV-vis spectrophotometer-based birefringence method developed by Choudhary et al.[263]. The highly aligned CNC films with incorporation of KL can have potential applications as UV blocking and polarizing films.

Functional applications of CNC films containing NaOH below its transition concentration can be further extended as humidity and acid vapor sensor by introducing hydrophilic polymeric additive such as PVA. Addition of PVA can improve the moisture absorption, it can also provide water resistance to the CNC films by simple heat treatment induced physical cross-linking. Improved moisture absorption by this film will result in increase in CNC pitch and corresponding shift in reflectance peak wavelength. This response at various relative humidity can be used for designing humidity sensors. Also, the presence NaOH in CNC film facilitates similar response when exposed to acid vapors such as HCl or H_2SO_4. These vapors upon interaction with NaOH can release water thereby causing shift in reflectance peak wavelength. Hence a simple, novel, and robust acid vapor and humidity sensor could be designed.

References

1. Sudesh, K. and T. Iwata, *Sustainability of biobased and biodegradable plastics.* CLEAN–Soil, Air, Water, 2008. **36**(5-6): p. 433-442.
2. Shen, L., J. Haufe, and M.K. Patel, *Product overview and market projection of emerging bio-based plastics PRO-BIP 2009.* Report for European polysaccharide network of excellence (EPNOE) and European bioplastics, 2009. **243**.
3. Bastioli, C., *Handbook of biodegradable polymers*. 2005: iSmithers Rapra Publishing.
4. Stelte, W. and A.R. Sanadi, *Preparation and characterization of cellulose nanofibers from two commercial hardwood and softwood pulps.* Industrial & Engineering Chemistry Research, 2009. **48**(24): p. 11211-11219.
5. Du, H., et al., *Sustainable preparation and characterization of thermally stable and functional cellulose nanocrystals and nanofibrils via formic acid hydrolysis.* Journal of Bioresources and Bioproducts, 2017. **2**(1): p. 10-15.
6. Kang, L., W. Wang, and Y.Y. Lee, *Bioconversion of kraft paper mill sludges to ethanol by SSF and SSCF.* Applied biochemistry and biotechnology, 2010. **161**(1-8): p. 53-66.
7. Guan, W., et al., *Acetone–butanol–ethanol production from Kraft paper mill sludge by simultaneous saccharification and fermentation.* Bioresource Technology, 2016. **200**: p. 713-721.
8. Karthikeyan, K. and S. Balasubramanian, *Studies on the characterization and possibilities of reutilization of solid wastes from a waste paper based paper industry.* Global Journal of Environmental Research, 2010. **4**(1): p. 18-22.
9. Wang, W., L. Kang, and Y.Y. Lee, *Production of cellulase from kraft paper mill sludge by Trichoderma reesei rut C-30.* Applied biochemistry and biotechnology, 2010. **161**(1): p. 382-394.
10. Marquardt, W., et al., *The biorenewables opportunity-toward next generation process and product systems.* AIChE journal, 2010. **56**(9): p. 2228-2235.
11. Tran, H. and E.K. Vakkilainnen, *The kraft chemical recovery process.* Tappi Kraft Pulping Short Course, 2008: p. 1-8.
12. Lora, J.H. and W.G. Glasser, *Recent industrial applications of lignin: a sustainable alternative to nonrenewable materials.* Journal of Polymers and the Environment, 2002. **10**(1-2): p. 39-48.
13. Dehne, L., et al., *Influence of lignin source and esterification on properties of lignin-polyethylene blends.* Industrial Crops and Products, 2016. **86**: p. 320-328.
14. Pucciariello, R., et al., *Lignin/poly (ε-caprolactone) blends with tuneable mechanical properties prepared by high energy ball-milling.* Journal of Polymers and the Environment, 2010. **18**(3): p. 326-334.
15. Parit, M. and Z. Jiang, *Towards lignin derived thermoplastic polymers.* International journal of biological macromolecules, 2020.
16. Ting, W.W., C.D. Vest, and R. Sontheimer, *Practical and experimental consideration of sun protection in dermatology.* International journal of dermatology, 2003. **42**(7): p. 505-513.
17. Brash, D.E., *Sunlight and the onset of skin cancer.* Trends in genetics, 1997. **13**(10): p. 410-414.
18. Singh, R., N.S. Tomer, and S.V. Bhadraiah, *Photo-oxidation studies on polyurethane coating: effect of additives on yellowing of polyurethane.* Polymer Degradation and Stability, 2001. **73**(3): p. 443-446.
19. Auclair, N., et al., *Improvement of photoprotection of wood coatings by using inorganic nanoparticles as ultraviolet absorbers.* Forest Products Journal, 2011. **61**(1): p. 20-27.
20. Yang, R., et al., *Degradation products formed during UV exposure of polyethylene–ZnO nano-composites.* Polymer Degradation and Stability, 2010. **95**(9): p. 1533-1541.
21. Nowicki, M., et al., *Nanoscale mechanical properties of polymers irradiated by UV.* Polymer, 2003. **44**(21): p. 6599-6606.

22. Demir, M.M., et al., *Optical properties of composites of PMMA and surface-modified zincite nanoparticles.* Macromolecules, 2007. **40**(4): p. 1089-1100.
23. Liou, G.-S., et al., *Highly flexible and optical transparent 6F-PI/TiO 2 optical hybrid films with tunable refractive index and excellent thermal stability.* Journal of Materials Chemistry, 2010. **20**(3): p. 531-536.
24. Mazzocchetti, L., E. Cortecchia, and M. Scandola, *Organic− Inorganic Hybrids as Transparent Coatings for UV and X-ray Shielding.* ACS applied materials & interfaces, 2009. **1**(3): p. 726-734.
25. Koziej, D., et al., *Nonaqueous TiO2 nanoparticle synthesis: a versatile basis for the fabrication of self-supporting, transparent, and UV-absorbing composite films.* ACS applied materials & interfaces, 2009. **1**(5): p. 1097-1104.
26. Druffel, T., et al., *Polymer nanocomposite thin film mirror for the infrared region.* small, 2008. **4**(4): p. 459-461.
27. FALKEHAG, S.I., J. MARTON, and E. ADLER, *Chromophores in kraft lignin*. 1966, ACS Publications.
28. Lin, S.Y. and C.W. Dence, *Methods in lignin chemistry*. 2012: Springer Science & Business Media.
29. Barsberg, S., T. Elder, and C. Felby, *Lignin− Quinone Interactions: Implications for Optical Properties of Lignin.* Chemistry of materials, 2003. **15**(3): p. 649-655.
30. Vallejo, J.J., M. Mesa, and C. Gallardo, *Evaluation of the avobenzone photostability in solvents used in cosmetic formulations.* Vitae, 2011. **18**(1): p. 63-71.
31. Butt, S. and T. Christensen, *Toxicity and phototoxicity of chemical sun filters.* Radiation protection dosimetry, 2000. **91**(1-3): p. 283-286.
32. Díaz-Cruz, M.S., M. Llorca, and D. Barceló, *Organic UV filters and their photodegradates, metabolites and disinfection by-products in the aquatic environment.* TrAC Trends in Analytical Chemistry, 2008. **27**(10): p. 873-887.
33. Teo, C.H. and F. Rahman, *Degradation and protection of polyaniline from exposure toáultraviolet radiation.* Applied Physics A, 2010. **99**(1): p. 311-316.
34. Tu, Y., et al., *Transparent and flexible thin films of ZnO-polystyrene nanocomposite for UV-shielding applications.* Journal of Materials Chemistry, 2010. **20**(8): p. 1594-1599.
35. Xiong, H.-M., X. Zhao, and J.-S. Chen, *New polymer− inorganic nanocomposites: PEO− ZnO and PEO− ZnO− LiClO4 films.* The Journal of Physical Chemistry B, 2001. **105**(42): p. 10169-10174.
36. Silvestre, C. and S. Cimmino, *Ecosustainable polymer nanomaterials for food packaging: innovative solutions, characterization needs, safety and environmental issues*. 2013: CRC Press.
37. Moon, R.J., et al., *Cellulose nanomaterials review: structure, properties and nanocomposites.* Chemical Society Reviews, 2011. **40**(7): p. 3941-3994.
38. Fortunati, E., et al., *Binary PVA bio-nanocomposites containing cellulose nanocrystals extracted from different natural sources: Part I.* Carbohydrate polymers, 2013. **97**(2): p. 825-836.
39. Brinchi, L., et al., *Production of nanocrystalline cellulose from lignocellulosic biomass: technology and applications.* Carbohydrate polymers, 2013. **94**(1): p. 154-169.
40. Podsiadlo, P., et al., *Molecularly engineered nanocomposites: layer-by-layer assembly of cellulose nanocrystals.* Biomacromolecules, 2005. **6**(6): p. 2914-2918.
41. Podsiadlo, P., et al., *Layer-by-layer assembled films of cellulose nanowires with antireflective properties.* Langmuir, 2007. **23**(15): p. 7901-7906.
42. Xing, Q., S.R. Eadula, and Y.M. Lvov, *Cellulose fiber− enzyme composites fabricated through layer-by-layer nanoassembly.* Biomacromolecules, 2007. **8**(6): p. 1987-1991.
43. Prathapan, R., et al., *Surface engineering of transparent cellulose nanocrystal coatings for biomedical applications.* ACS Applied Bio Materials, 2018. **1**(3): p. 728-737.
44. Klemm, D., et al. *Nanocellulose materials–different cellulose, different functionality*. in *Macromolecular symposia*. 2009. Wiley Online Library.

45. Ruan, D., Q. Huang, and L. Zhang, *Structure and properties of CdS/regenerated cellulose nanocomposites.* Macromolecular Materials and Engineering, 2005. **290**(10): p. 1017-1024.
46. Phan-Xuan, T., et al., *Aggregation behavior of aqueous cellulose nanocrystals: the effect of inorganic salts.* Cellulose, 2016. **23**(6): p. 3653-3663.
47. Araki, J. and S. Kuga, *Effect of trace electrolyte on liquid crystal type of cellulose microcrystals.* Langmuir, 2001. **17**(15): p. 4493-4496.
48. Prathapan, R., et al., *Modulating the zeta potential of cellulose nanocrystals using salts and surfactants.* Colloids and Surfaces A: Physicochemical and Engineering Aspects, 2016. **509**: p. 11-18.
49. Pan, J., W. Hamad, and S.K. Straus, *Parameters affecting the chiral nematic phase of nanocrystalline cellulose films.* Macromolecules, 2010. **43**(8): p. 3851-3858.
50. Lagerwall, J.P., et al., *Cellulose nanocrystal-based materials: from liquid crystal self-assembly and glass formation to multifunctional thin films.* NPG Asia Materials, 2014. **6**(1): p. e80.
51. Revol, J.-F., D.L. Godbout, and D.G. Gray, *Solidified liquid crystals of cellulose with optically variable properties*, 1997, Google Patents.
52. Finkelmann, H., et al., *Tunable mirrorless lasing in cholesteric liquid crystalline elastomers.* Advanced Materials, 2001. **13**(14): p. 1069-1072.
53. Palffy-Muhoray, P., et al., *Photonics and lasing in liquid crystal materials.* Philosophical Transactions of the Royal Society of London A: Mathematical, Physical and Engineering Sciences, 2006. **364**(1847): p. 2747-2761.
54. Liu, D., et al., *Structure–color mechanism of iridescent cellulose nanocrystal films.* RSC Advances, 2014. **4**(74): p. 39322-39331.
55. Beck, S., J. Bouchard, and R. Berry, *Controlling the reflection wavelength of iridescent solid films of nanocrystalline cellulose.* Biomacromolecules, 2010. **12**(1): p. 167-172.
56. Bardet, R., N. Belgacem, and J. Bras, *Flexibility and color monitoring of cellulose nanocrystal iridescent solid films using anionic or neutral polymers.* ACS applied materials & interfaces, 2015. **7**(7): p. 4010-4018.
57. Yao, K., et al., *Flexible and responsive chiral nematic cellulose nanocrystal/poly (ethylene glycol) composite films with uniform and tunable structural color.* Advanced Materials, 2017. **29**(28): p. 1701323.
58. Gu, M., et al., *Cellulose nanocrystal/poly (ethylene glycol) composite as an iridescent coating on polymer substrates: Structure-color and interface adhesion.* ACS applied materials & interfaces, 2016. **8**(47): p. 32565-32573.
59. Reising, A.B., R.J. Moon, and J.P. Youngblood, *Effect of particle alignment on mechanical properties of neat cellulose nanocrystal films.* 2012.
60. Halima, N.B., *Poly (vinyl alcohol): review of its promising applications and insights into biodegradation.* RSC Advances, 2016. **6**(46): p. 39823-39832.
61. Kumar, R., et al., *Fabrication and characterization of polyvinyl-alcohol-based thin-film optical waveguides.* Optical Engineering, 2004. **43**(9): p. 2134-2143.
62. Shoji, S., et al., *Optical polarizer made of uniaxially aligned short single-wall carbon nanotubes embedded in a polymer film.* Physical Review B, 2008. **77**(15): p. 153407.
63. Couture, J.J., *Polarization holographic characterization of organic azo dyes/PVA films for real time applications.* Applied optics, 1991. **30**(20): p. 2858-2866.
64. Stokes, N.L., et al., *Spectrally selective coatings of gold nanorods on architectural glass.* Journal of Nanoparticle Research, 2010. **12**(8): p. 2821-2830.
65. Gyenes, T., et al., *Electrically adjustable thermotropic windows based on polymer gels.* Polymers for advanced technologies, 2003. **14**(11-12): p. 757-762.

66. Kim, J.-K., B. Choi, and J. Jin, *Transparent, water-stable, cellulose nanofiber-based packaging film with a low oxygen permeability.* Carbohydrate polymers, 2020. **249**: p. 116823.
67. Kim, T., et al., *Crab-on-a-tree: all biorenewable, optical and radio frequency transparent barrier nanocoating for food packaging.* ACS nano, 2019. **13**(4): p. 3796-3805.
68. Gaume, J., et al., *Optimization of PVA clay nanocomposite for ultra-barrier multilayer encapsulation of organic solar cells.* Solar Energy Materials and Solar Cells, 2012. **99**: p. 240-249.
69. Mestdagh, F., et al., *Protective influence of several packaging materials on light oxidation of milk.* Journal of Dairy Science, 2005. **88**(2): p. 499-510.
70. Kubo, S. and J.F. Kadla, *The formation of strong intermolecular interactions in immiscible blends of poly (vinyl alcohol)(PVA) and lignin.* Biomacromolecules, 2003. **4**(3): p. 561-567.
71. Ciemniecki, S.L. and W.G. Glasser, *Multiphase materials with lignin: 2. Blends of hydroxypropyl lignin with poly (vinyl alcohol).* Polymer, 1988. **29**(6): p. 1030-1036.
72. Nair, S.S., et al., *High shear homogenization of lignin to nanolignin and thermal stability of Nanolignin-Polyvinyl alcohol blends.* ChemSusChem, 2014. **7**(12): p. 3513-3520.
73. Xiong, F., et al., *Transparent nanocomposite films of lignin nanospheres and poly (vinyl alcohol) for UV-absorbing.* Industrial & Engineering Chemistry Research, 2018.
74. Sirviö, J.A., et al., *UV-absorbing cellulose nanocrystals as functional reinforcing fillers in polymer nanocomposite films.* Journal of Materials Chemistry A, 2016. **4**(17): p. 6368-6375.
75. Zhang, Z., et al., *Cinnamate-Functionalized Cellulose Nanocrystals as UV-Shielding Nanofillers in Sunscreen and Transparent Polymer Films.* Advanced Sustainable Systems, 2019: p. 1800156.
76. Sirviö, J.A. and M. Visanko, *Highly Transparent Nanocomposites Based on Poly (vinyl alcohol) and Sulfated UV-Absorbing Wood Nanofibers.* Biomacromolecules, 2019.
77. Yang, M., et al., *Preparation of lignin containing cellulose nanofibers and its application in PVA nanocomposite films.* International journal of biological macromolecules, 2020. **158**: p. 1259-1267.
78. Liu, C., et al., *Production of lignin-containing cellulose nanofibers using deep eutectic solvents for UV-absorbing polymer reinforcement.* Carbohydrate polymers, 2020. **246**: p. 116548.
79. Wu, J. and D. Chung, *Increasing the electromagnetic interference shielding effectiveness of carbon fiber polymer–matrix composite by using activated carbon fibers.* Carbon, 2002. **40**(3): p. 445-447.
80. Markham, D., *Shielding: quantifying the shielding requirements for portable electronic design and providing new solutions by using a combination of materials and design.* Materials & Design, 1999. **21**(1): p. 45-50.
81. Wang, Y. and X. Jing, *Intrinsically conducting polymers for electromagnetic interference shielding.* Polymers for advanced technologies, 2005. **16**(4): p. 344-351.
82. Paul, C.R., *Introduction to electromagnetic compatibility*. Vol. 184. 2006: John Wiley & Sons.
83. Bagwell, R.M., J.M. McManaman, and R.C. Wetherhold, *Short shaped copper fibers in an epoxy matrix: their role in a multifunctional composite.* Composites Science and Technology, 2006. **66**(3-4): p. 522-530.
84. Osawa, Z. and K. Kobayashi, *Thermal stability of shielding effectiveness of electromagnetic interference of composites.* Journal of materials science, 1987. **22**(12): p. 4381-4387.
85. Li, N., et al., *Electromagnetic interference (EMI) shielding of single-walled carbon nanotube epoxy composites.* Nano Letters, 2006. **6**(6): p. 1141-1145.
86. Das, N., et al., *Electromagnetic interference shielding effectiveness of carbon black and carbon fibre filled EVA and NR based composites.* Composites Part A: Applied Science and Manufacturing, 2000. **31**(10): p. 1069-1081.
87. Yan, D.-X., et al., *Efficient electromagnetic interference shielding of lightweight graphene/polystyrene composite.* Journal of Materials Chemistry, 2012. **22**(36): p. 18772-18774.

88. Gopakumar, D.A., et al., *Cellulose nanofiber-based polyaniline flexible papers as sustainable microwave absorbers in the X-band.* ACS applied materials & interfaces, 2018. **10**(23): p. 20032-20043.
89. Sasso, C., et al., *Polypyrrole and polypyrrole/wood-derived materials conducting composites: a review.* BioResources, 2011. **6**(3).
90. Tjahyono, A.P., K.C. Aw, and J. Travas-Sejdic, *A novel polypyrrole and natural rubber based flexible large strain sensor.* Sensors and Actuators B: Chemical, 2012. **166**: p. 426-437.
91. Granato, F., et al., *Composite polyamide 6/polypyrrole conductive nanofibers.* Macromolecular rapid communications, 2009. **30**(6): p. 453-458.
92. Mravčáková, M., et al., *Poly (propylene)/montmorillonite/polypyrrole composites: structure and conductivity.* Polymers for advanced technologies, 2006. **17**(9-10): p. 715-726.
93. Yildiz, Z., I. Usta, and A. Gungor, *Electrical properties and electromagnetic shielding effectiveness of polyester yarns with polypyrrole deposition.* Textile Research Journal, 2012. **82**(20): p. 2137-2148.
94. Babu, K.F., et al., *One pot synthesis of polypyrrole silver nanocomposite on cotton fabrics for multifunctional property.* Carbohydrate polymers, 2012. **90**(4): p. 1557-1563.
95. Ding, Q., et al., *Nanocellulose-mediated electroconductive self-healing hydrogels with high strength, plasticity, viscoelasticity, stretchability, and biocompatibility toward multifunctional applications.* ACS applied materials & interfaces, 2018. **10**(33): p. 27987-28002.
96. Zhang, L., et al., *Recent progress on nanostructured conducting polymers and composites: synthesis, application and future aspects.* Science China Materials, 2018. **61**(3): p. 303-352.
97. Tang, L., et al., *Flexible conductive polypyrrole nanocomposite membranes based on bacterial cellulose with amphiphobicity.* Carbohydrate polymers, 2015. **117**: p. 230-235.
98. Chen, J., et al., *Highly thermostable, flexible, and conductive films prepared from cellulose, graphite, and polypyrrole nanoparticles.* ACS applied materials & interfaces, 2015. **7**(28): p. 15641-15648.
99. Lay, M., et al., *Strong and electrically conductive nanopaper from cellulose nanofibers and polypyrrole.* Carbohydrate polymers, 2016. **152**: p. 361-369.
100. Sasso, C., et al., *Highly conducting polypyrrole/cellulose nanocomposite films with enhanced mechanical properties.* Macromolecular Materials and Engineering, 2010. **295**(10): p. 934-941.
101. Fei, G., et al., *Fabrication of Bacterial Cellulose/Polyaniline Nanocomposite Paper with Excellent Conductivity, Strength, and Flexibility.* ACS Sustainable Chemistry & Engineering, 2019. **7**(9): p. 8215-8225.
102. Bober, P., et al., *Biocomposites of nanofibrillated cellulose, polypyrrole, and silver nanoparticles with electroconductive and antimicrobial properties.* Biomacromolecules, 2014. **15**(10): p. 3655-3663.
103. Klemm, D., et al., *Cellulose: fascinating biopolymer and sustainable raw material.* Angewandte Chemie International Edition, 2005. **44**(22): p. 3358-3393.
104. John, M.J. and S. Thomas, *Biofibres and biocomposites.* Carbohydrate polymers, 2008. **71**(3): p. 343-364.
105. Andresen, M., et al., *Properties and characterization of hydrophobized microfibrillated cellulose.* Cellulose, 2006. **13**(6): p. 665-677.
106. Dufresne, A., J.-Y. Cavaille, and M.R. Vignon, *Mechanical behavior of sheets prepared from sugar beet cellulose microfibrils.* Journal of Applied Polymer Science, 1997. **64**(6): p. 1185-1194.
107. Stenstad, P., et al., *Chemical surface modifications of microfibrillated cellulose.* Cellulose, 2008. **15**(1): p. 35-45.

108. Azizi Samir, M.A.S., F. Alloin, and A. Dufresne, *Review of recent research into cellulosic whiskers, their properties and their application in nanocomposite field.* Biomacromolecules, 2005. **6**(2): p. 612-626.
109. Håkansson, H. and P. Ahlgren, *Acid hydrolysis of some industrial pulps: effect of hydrolysis conditions and raw material.* Cellulose, 2005. **12**(2): p. 177-183.
110. Bondeson, D., A. Mathew, and K. Oksman, *Optimization of the isolation of nanocrystals from microcrystalline cellulose by acid hydrolysis.* Cellulose, 2006. **13**(2): p. 171.
111. Elazzouzi-Hafraoui, S., et al., *The shape and size distribution of crystalline nanoparticles prepared by acid hydrolysis of native cellulose.* Biomacromolecules, 2007. **9**(1): p. 57-65.
112. Marchessault, R., F. Morehead, and N. Walter, *Liquid crystal systems from fibrillar polysaccharides.* Nature, 1959. **184**(4686): p. 632.
113. Revol, J.-F., et al., *Helicoidal self-ordering of cellulose microfibrils in aqueous suspension.* International journal of biological macromolecules, 1992. **14**(3): p. 170-172.
114. Dong, X.M., et al., *Effects of ionic strength on the isotropic− chiral nematic phase transition of suspensions of cellulose crystallites.* Langmuir, 1996. **12**(8): p. 2076-2082.
115. Dong, X.M., *Chiral Nematic Ordered Suspensions of Cellulose Microcrystallites*. 1999: McGill University.
116. Revol, J.-F., et al., *Chiral nematic suspensions of cellulose crystallites; phase separation and magnetic field orientation.* Liquid Crystals, 1994. **16**(1): p. 127-134.
117. Orts, W., et al., *Enhanced ordering of liquid crystalline suspensions of cellulose microfibrils: A small angle neutron scattering study.* Macromolecules, 1998. **31**(17): p. 5717-5725.
118. Revol, J.-F., L. Godbout, and D. Gray, *Solid self-assembled films of cellulose with chiral nematic order and optically variable properties.* Journal of pulp and paper science, 1998. **24**(5): p. 146-149.
119. Straley, J.P., *Theory of piezoelectricity in nematic liquid crystals, and of the cholesteric ordering.* Physical review A, 1976. **14**(5): p. 1835.
120. Abitbol, T., et al., *Surface charge influence on the phase separation and viscosity of cellulose nanocrystals.* Langmuir, 2018. **34**(13): p. 3925-3933.
121. Zhao, G., et al., *Fabrication and characterization of photonic cellulose nanocrystal films with structural colors covering full visible light.* Journal of Materials Science, 2020. **55**(20): p. 8756-8767.
122. Zhu, B., et al., *Supramolecular engineering of hierarchically self-assembled, bioinspired, cholesteric nanocomposites formed by cellulose nanocrystals and polymers.* ACS applied materials & interfaces, 2016. **8**(17): p. 11031-11040.
123. Klemm, D., et al., *Nanocelluloses: a new family of nature-based materials.* Angewandte Chemie International Edition, 2011. **50**(24): p. 5438-5466.
124. Lagerwall, J.P. and G. Scalia, *A new era for liquid crystal research: applications of liquid crystals in soft matter nano-, bio-and microtechnology.* Current Applied Physics, 2012. **12**(6): p. 1387-1412.
125. Parit, M., et al., *Transparent and homogenous cellulose nanocrystal/lignin UV-protection films.* ACS Omega, 2018. **3**(9): p. 10679-10691.
126. Roman, M. and W.T. Winter, *Cellulose nanocrystals for thermoplastic reinforcement: effect of filler surface chemistry on composite properties*. 2006, ACS Publications.
127. Dufresne, A., *Cellulose nanomaterial reinforced polymer nanocomposites.* Current Opinion in Colloid & Interface Science, 2017. **29**: p. 1-8.
128. Ilyas, R., et al., *Nanocrystalline cellulose as reinforcement for polymeric matrix nanocomposites and its potential applications: a review.* Current Analytical Chemistry, 2018. **14**(3): p. 203-225.
129. Parit, M., *Thermoplastic polymer nanocomposites.* 2016.
130. Hodgkinson, I.J., et al., *Spacerless circular-polarization spectral-hole filters using chiral sculptured thin films: theory and experiment.* Optics Communications, 2000. **184**(1-4): p. 57-66.

131. Bi, Q., et al., *An electrochemical sensor based on cellulose nanocrystal for the enantioselective discrimination of chiral amino acids.* Analytical biochemistry, 2016. **508**: p. 50-57.
132. Kafy, A., et al., *Cellulose nanocrystal/graphene oxide composite film as humidity sensor.* Sensors and Actuators A: Physical, 2016. **247**: p. 221-226.
133. Yang, X., et al., *Cellulose nanocrystal aerogels as universal 3D lightweight substrates for supercapacitor materials.* Advanced Materials, 2015. **27**(40): p. 6104-6109.
134. Herrick, F.W., et al. *Microfibrillated cellulose: morphology and accessibility*. in *J. Appl. Polym. Sci.: Appl. Polym. Symp.;(United States)*. 1983. ITT Rayonier Inc., Shelton, WA.
135. Nakagaito, A. and H. Yano, *The effect of morphological changes from pulp fiber towards nano-scale fibrillated cellulose on the mechanical properties of high-strength plant fiber based composites.* Applied Physics A, 2004. **78**(4): p. 547-552.
136. Turbak, A.F., F.W. Snyder, and K.R. Sandberg. *Microfibrillated cellulose, a new cellulose product: properties, uses, and commercial potential*. in *J. Appl. Polym. Sci.: Appl. Polym. Symp.;(United States)*. 1983. ITT Rayonier Inc., Shelton, WA.
137. Spence, K.L., et al., *A comparative study of energy consumption and physical properties of microfibrillated cellulose produced by different processing methods.* Cellulose, 2011. **18**(4): p. 1097-1111.
138. Zhu, J.Y., R. Sabo, and X. Luo, *Integrated production of nano-fibrillated cellulose and cellulosic biofuel (ethanol) by enzymatic fractionation of wood fibers.* Green Chemistry, 2011. **13**(5): p. 1339-1344.
139. Zimmermann, T., N. Bordeanu, and E. Strub, *Properties of nanofibrillated cellulose from different raw materials and its reinforcement potential.* Carbohydrate polymers, 2010. **79**(4): p. 1086-1093.
140. Du, H., et al., *Sustainable valorization of paper mill sludge into cellulose nanofibrils and cellulose nanopaper.* Journal of Hazardous Materials, 2020. **400**: p. 123106.
141. Wang, Q., et al., *Morphological development of cellulose fibrils of a bleached eucalyptus pulp by mechanical fibrillation.* Cellulose, 2012. **19**(5): p. 1631-1643.
142. Chen, W., et al., *Individualization of cellulose nanofibers from wood using high-intensity ultrasonication combined with chemical pretreatments.* Carbohydrate polymers, 2011. **83**(4): p. 1804-1811.
143. Cheng, Q., S. Wang, and T.G. Rials, *Poly (vinyl alcohol) nanocomposites reinforced with cellulose fibrils isolated by high intensity ultrasonication.* Composites Part A: Applied Science and Manufacturing, 2009. **40**(2): p. 218-224.
144. Tonoli, G., et al., *Cellulose micro/nanofibres from Eucalyptus kraft pulp: preparation and properties.* Carbohydrate polymers, 2012. **89**(1): p. 80-88.
145. Alemdar, A. and M. Sain, *Biocomposites from wheat straw nanofibers: morphology, thermal and mechanical properties.* Composites Science and Technology, 2008. **68**(2): p. 557-565.
146. Chakraborty, A., M. Sain, and M. Kortschot, *Cellulose microfibrils: A novel method of preparation using high shear refining and cryocrushing.* Holzforschung, 2005. **59**(1): p. 102-107.
147. Wang, B., M. Sain, and K. Oksman, *Study of structural morphology of hemp fiber from the micro to the nanoscale.* Applied Composite Materials, 2007. **14**(2): p. 89.
148. Sehaqui, H., et al., *Fast preparation procedure for large, flat cellulose and cellulose/inorganic nanopaper structures.* Biomacromolecules, 2010. **11**(9): p. 2195-2198.
149. Sehaqui, H., et al., *Cellulose nanofiber orientation in nanopaper and nanocomposites by cold drawing.* ACS applied materials & interfaces, 2012. **4**(2): p. 1043-1049.
150. Henriksson, M., et al., *Cellulose nanopaper structures of high toughness.* Biomacromolecules, 2008. **9**(6): p. 1579-1585.
151. Zhang, L., et al., *Effect of cellulose nanofiber dimensions on sheet forming through filtration.* Cellulose, 2012. **19**(2): p. 561-574.

152. Baez, C., J. Considine, and R. Rowlands, *Influence of drying restraint on physical and mechanical properties of nanofibrillated cellulose films.* Cellulose, 2014. **21**(1): p. 347-356.
153. Siró, I. and D. Plackett, *Microfibrillated cellulose and new nanocomposite materials: a review.* Cellulose, 2010. **17**(3): p. 459-494.
154. Berglund, L.A. and T. Peijs, *Cellulose biocomposites—from bulk moldings to nanostructured systems.* MRS bulletin, 2010. **35**(3): p. 201-207.
155. Nogi, M., et al., *Optically transparent nanofiber paper.* Advanced Materials, 2009. **21**(16): p. 1595-1598.
156. Kumar, V., et al., *Comparison of nano-and microfibrillated cellulose films.* Cellulose, 2014. **21**(5): p. 3443-3456.
157. Nogi, M., et al., *High thermal stability of optical transparency in cellulose nanofiber paper.* Applied Physics Letters, 2013. **102**(18): p. 181911.
158. Olsson, R.T., et al., *Making flexible magnetic aerogels and stiff magnetic nanopaper using cellulose nanofibrils as templates.* Nature Nanotechnology, 2010. **5**(8): p. 584-588.
159. Liu, A., et al., *Clay nanopaper with tough cellulose nanofiber matrix for fire retardancy and gas barrier functions.* Biomacromolecules, 2011. **12**(3): p. 633-641.
160. Eichhorn, S.J., et al., *current international research into cellulose nanofibres and nanocomposites.* Journal of materials science, 2010. **45**(1): p. 1.
161. Miao, C., et al., *Superior crack initiation and growth characteristics of cellulose nanopapers.* Cellulose, 2020. **27**(6): p. 3181-3195.
162. Syverud, K. and P. Stenius, *Strength and barrier properties of MFC films.* Cellulose, 2009. **16**(1): p. 75.
163. Edgar, C.D. and D.G. Gray, *Smooth model cellulose I surfaces from nanocrystal suspensions.* Cellulose, 2003. **10**(4): p. 299-306.
164. Zhu, H., et al., *Transparent paper: fabrications, properties, and device applications.* Energy & Environmental Science, 2014. **7**(1): p. 269-287.
165. Gao, K., et al., *Cellulose nanofibers/reduced graphene oxide flexible transparent conductive paper.* Carbohydrate polymers, 2013. **97**(1): p. 243-251.
166. Parit, M., et al., *Polypyrrole and cellulose nanofiber based composite films with improved physical and electrical properties for electromagnetic shielding applications.* Carbohydrate polymers, 2020. **240**: p. 116304.
167. Liu, F., et al., *Nafion/PTFE composite membranes for fuel cell applications.* Journal of Membrane Science, 2003. **212**(1): p. 213-223.
168. Johnson, J., A. Ghosh, and J. Lannutti, *Microstructure-property relationships in a tissue-engineering scaffold.* Journal of Applied Polymer Science, 2007. **104**(5): p. 2919-2927.
169. Ye, S.H., et al., *Antifouling blood purification membrane composed of cellulose acetate and phospholipid polymer.* Biomaterials, 2003. **24**(23): p. 4143-4152.
170. Varanasi, S., Z.-X. Low, and W. Batchelor, *Cellulose nanofibre composite membranes–Biodegradable and recyclable UF membranes.* Chemical Engineering Journal, 2015. **265**: p. 138-146.
171. Balea, A., et al., *Effect of Bleached Eucalyptus and Pine Cellulose Nanofibers on the Physico-Mechanical Properties of Cartonboard.* BioResources, 2016. **11**(4): p. 8123-8138.
172. Strassberger, Z., S. Tanase, and G. Rothenberg, *The pros and cons of lignin valorisation in an integrated biorefinery.* RSC Advances, 2014. **4**(48): p. 25310-25318.
173. Gordobil, O., et al., *Kraft lignin as filler in PLA to improve ductility and thermal properties.* Industrial Crops and Products, 2015. **72**: p. 46-53.
174. Yang, W., et al., *Synergic effect of cellulose and lignin nanostructures in PLA based systems for food antibacterial packaging.* European Polymer Journal, 2016. **79**: p. 1-12.

175. Chen, F., et al., *Physical properties of lignin-based polypropylene blends.* Polymer composites, 2011. **32**(7): p. 1019-1025.
176. Toriz, G., F. Denes, and R. Young, *Lignin-polypropylene composites. Part 1: Composites from unmodified lignin and polypropylene.* Polymer composites, 2002. **23**(5): p. 806-813.
177. Alexy, P., B. Košıková, and G. Podstránska, *The effect of blending lignin with polyethylene and polypropylene on physical properties.* Polymer, 2000. **41**(13): p. 4901-4908.
178. Luo, F., et al., *Effects of compatibilizers on the mechanical properties of low density polyethylene/lignin blends.* Chinese Journal of Polymer Science, 2009. **27**(06): p. 833-842.
179. Sadeghifar, H. and D.S. Argyropoulos, *Macroscopic Behavior of Kraft Lignin Fractions: Melt Stability Considerations for Lignin–Polyethylene Blends.* ACS Sustainable Chemistry & Engineering, 2016. **4**(10): p. 5160-5166.
180. Diop, A., et al., *Study of lignin dispersion in low-density polyethylene.* Journal of Thermoplastic Composite Materials, 2015. **28**(12): p. 1662-1674.
181. Xu, G., et al., *Fabrication and properties of alkaline lignin/poly (vinyl alcohol) blend membranes.* BioResources, 2013. **8**(2): p. 2510-2520.
182. Kubo, S. and J.F. Kadla, *Kraft lignin/poly (ethylene oxide) blends: effect of lignin structure on miscibility and hydrogen bonding.* Journal of Applied Polymer Science, 2005. **98**(3): p. 1437-1444.
183. Kadla, J.F. and S. Kubo, *Miscibility and hydrogen bonding in blends of poly (ethylene oxide) and kraft lignin.* Macromolecules, 2003. **36**(20): p. 7803-7811.
184. Atifi, S., C. Miao, and W.Y. Hamad, *Surface modification of lignin for applications in polypropylene blends.* Journal of Applied Polymer Science, 2017. **134**(29).
185. Maldhure, A.V., J. Ekhe, and E. Deenadayalan, *Mechanical properties of polypropylene blended with esterified and alkylated lignin.* Journal of Applied Polymer Science, 2012. **125**(3): p. 1701-1712.
186. Laurichesse, S. and L. Avérous, *Synthesis, thermal properties, rheological and mechanical behaviors of lignins-grafted-poly (ε-caprolactone).* Polymer, 2013. **54**(15): p. 3882-3890.
187. Zhang, Y., et al., *Renewable High-Performance Polyurethane Bioplastics Derived from Lignin–Poly (ε-caprolactone).* ACS Sustainable Chemistry & Engineering, 2017. **5**(5): p. 4276-4284.
188. Liu, X., et al., *Preparation and characterization of Lignin-graft-poly (ε-caprolactone) copolymers based on lignocellulosic butanol residue*. International journal of biological macromolecules, 2015. **81**: p. 521-529.
189. Chung, Y.-L., et al., *A renewable lignin–lactide copolymer and application in biobased composites.* ACS Sustainable Chemistry & Engineering, 2013. **1**(10): p. 1231-1238.
190. Zong, E., et al., *Combination of lignin and l-lactide towards grafted copolymers from lignocellulosic butanol residue.* International journal of biological macromolecules, 2016. **86**: p. 80-88.
191. Kim, S.J., et al., *Synthesis and characterization of kraft lignin-graft-polylactide copolymers.* Wood science and technology, 2016. **50**(6): p. 1293-1304.
192. Chung, H., A. Al-Khouja, and N.R. Washburn, *Lignin-Based Graft Copolymers via ATRP and Click Chemistry*, in *Green Polymer Chemistry: Biocatalysis and Materials II*. 2013, ACS Publications. p. 373-391.
193. Han, Y., et al., *Renewable polymers from lignin via copper-free thermal click chemistry.* Polymer, 2016. **83**: p. 92-100.
194. Saito, T., et al., *Development of lignin-based polyurethane thermoplastics.* RSC Advances, 2013. **3**(44): p. 21832-21840.
195. *Fisher Solve Data Base Fisher International 2014*.
196. Smook, G.A., *Handbook for pulp & and paper technologists*. 2002: Angus Wilde Publ.
197. Chakar, F.S. and A.J. Ragauskas, *Review of current and future softwood kraft lignin process chemistry.* Industrial Crops and Products, 2004. **20**(2): p. 131-141.

198. *Sven A. Rydholm, Pulping Processes, Interscience Publishers, New York, 1965*.
199. Alen, R., et al., *Chemical Pulping Part 1, Fibre Chemistry and Technology*. Vol. 6. 2011: Paper Engineers' Association/Paperi ja Puu Oy; Helsinki.
200. *Biermann's Handbook of Pulp and Paper: Volume 1: Raw Material and Pulp Making 3rd Edition*.
201. Ranby, B.G., *Aqueous colloidal solutions of cellulose micelles*, 1949, MUNKSGAARD INT PUBL LTD 35 NORRE SOGADE, PO BOX 2148, DK-1016 COPENHAGEN …. p. 649-650.
202. Dong, X.M., J.-F. Revol, and D.G. Gray, *Effect of microcrystallite preparation conditions on the formation of colloid crystals of cellulose.* Cellulose, 1998. **5**(1): p. 19-32.
203. Wang, Q., et al., *Approaching zero cellulose loss in cellulose nanocrystal (CNC) production: recovery and characterization of cellulosic solid residues (CSR) and CNC.* Cellulose, 2012. **19**(6): p. 2033-2047.
204. Sunasee, R. and U. Hemraz, *Synthetic strategies for the fabrication of cationic surface-modified cellulose nanocrystals.* Fibers, 2018. **6**(1): p. 15.
205. De Nooy, A.E., A.C. Besemer, and H. van Bekkum, *Highly selective nitroxyl radical-mediated oxidation of primary alcohol groups in water-soluble glucans.* Carbohydrate research, 1995. **269**(1): p. 89-98.
206. de Nooy, A.E., A.C. Besemer, and H. van Bekkum, *Selective oxidation of primary alcohols mediated by nitroxyl radical in aqueous solution. Kinetics and mechanism.* Tetrahedron, 1995. **51**(29): p. 8023-8032.
207. De Nooy, A.E., A.C. Besemer, and H. van Bekkum, *On the use of stable organic nitroxyl radicals for the oxidation of primary and secondary alcohols.* Synthesis, 1996. **1996**(10): p. 1153-1176.
208. Isogai, A., T. Saito, and H. Fukuzumi, *TEMPO-oxidized cellulose nanofibers.* Nanoscale, 2011. **3**(1): p. 71-85.
209. Saito, T., et al., *Homogeneous suspensions of individualized microfibrils from TEMPO-catalyzed oxidation of native cellulose.* Biomacromolecules, 2006. **7**(6): p. 1687-1691.
210. Saito, T., et al., *Cellulose nanofibers prepared by TEMPO-mediated oxidation of native cellulose.* Biomacromolecules, 2007. **8**(8): p. 2485-2491.
211. Shinoda, R., et al., *Relationship between length and degree of polymerization of TEMPO-oxidized cellulose nanofibrils.* Biomacromolecules, 2012. **13**(3): p. 842-849.
212. Wen, Y., et al., *Preparation and characterization of lignin-containing cellulose nanofibril from poplar high-yield pulp via TEMPO-mediated oxidation and homogenization.* ACS Sustainable Chemistry & Engineering, 2019. **7**(6): p. 6131-6139.
213. Isogai, A., *Development of completely dispersed cellulose nanofibers.* Proceedings of the Japan Academy, Series B, 2018. **94**(4): p. 161-179.
214. ; Available from: https://www.microfluidicscorp.com.
215. Iwamoto, S., et al., *Optically transparent composites reinforced with plant fiber-based nanofibers.* Applied Physics A, 2005. **81**(6): p. 1109-1112.
216. Bian, H., et al., *Green and low-cost production of thermally stable and carboxylated cellulose nanocrystals and nanofibrils using highly recyclable dicarboxylic acids.* JoVE (Journal of Visualized Experiments), 2017(119): p. e55079.
217. Bian, H., et al., *Effect of fiber drying on properties of lignin containing cellulose nanocrystals and nanofibrils produced through maleic acid hydrolysis.* Cellulose, 2017. **24**(10): p. 4205-4216.
218. Herrera, M., et al., *Preparation and evaluation of high-lignin content cellulose nanofibrils from eucalyptus pulp.* Cellulose, 2018. **25**(5): p. 3121-3133.
219. Zhang, W., S. Okubayashi, and T. Bechtold, *Fibrillation tendency of cellulosic fibers—Part 3. Effects of alkali pretreatment of lyocell fiber.* Carbohydrate polymers, 2005. **59**(2): p. 173-179.
220. Carlton, W., R. Dence, and Tappi, *Pulp Bleaching: Principles and Practice.[by] Carlton W. Dence, Douglas W. Reeve Editors*. 1996: Tappi.

221. Colodette, J., S. Rothenberg, and C. Dence, *Factors affecting hydrogen peroxide stability in the brightening of mechanical and chemimechanical pulps. I: hydrogen peroxide stability in the absence of stabilizing systems.* Journal of pulp and paper science, 1988. **14**(6): p. J126-J132.
222. Abbot, J. and D.G. Brown, *Stabilization of iron-catalysed hydrogen peroxide decomposition by magnesium.* Canadian Journal of Chemistry, 1990. **68**(9): p. 1537-1543.
223. Hobbs, G. and J. Abbot, *Peroxide bleaching reactions under alkaline and acidic conditions.* Journal of wood chemistry and technology, 1991. **11**(2): p. 225-246.
224. Abbot, J., et al., *The influence of manganese and magnesium on alkaline peroxide bleaching of radiata pine thermomechanical pulp.* Appita, 1992. **45**(2): p. 109-112.
225. Gerard, M., A. Chaubey, and B. Malhotra, *Application of conducting polymers to biosensors.* Biosensors and bioelectronics, 2002. **17**(5): p. 345-359.
226. Heeger, A.J., E.B. Namdas, and N.S. Sariciftci, *Semiconducting and metallic polymers*. 2010: Oxford Univ. Press.
227. Inzelt, G., *Chemical and electrochemical syntheses of conducting polymers.* Conducting Polymers: A New Era in Electrochemistry, 2008: p. 123-148.
228. Reynolds, J.R. and T.A. Skotheim, *Handbook of Conducting Polymers: Conjugated Polymers: Theory, Synthesis, Properties, and Characterization*. 2007: CRC Press.
229. Heinze, J., B.A. Frontana-Uribe, and S. Ludwigs, *Electrochemistry of Conducting Polymers・ Persistent Models and New Concepts.* Chemical reviews, 2010. **110**(8): p. 4724-4771.
230. Jureviciute, I. and S. Bruckenstein, *Electrochemical activity of chemically deposited polypyrrole films.* Journal of Solid State Electrochemistry, 2003. **7**(9): p. 554-560.
231. Guimard, N.K., N. Gomez, and C.E. Schmidt, *Conducting polymers in biomedical engineering.* Progress in Polymer Science, 2007. **32**(8-9): p. 876-921.
232. Freund, M.S. and B.A. Deore, *Self-doped conducting polymers*. 2007: John Wiley & Sons.
233. Inzelt, G., *Conducting polymers: a new era in electrochemistry*. 2012: Springer Science & Business Media.
234. Wallace, G.G., et al., *Conductive electroactive polymers: intelligent polymer systems*. 2008: CRC press.
235. Ansari, R., *Polypyrrole conducting electroactive polymers: synthesis and stability studies.* Journal of Chemistry, 2006. **3**(4): p. 186-201.
236. Razaq, A., et al., *Influence of the type of oxidant on anion exchange properties of fibrous Cladophora cellulose/polypyrrole composites.* The Journal of Physical Chemistry B, 2008. **113**(2): p. 426-433.
237. Wang, L.-X., X.-G. Li, and Y.-L. Yang, *Preparation, properties and applications of polypyrroles.* Reactive and Functional Polymers, 2001. **47**(2): p. 125-139.
238. Tat'yana, V.V. and O.N. Efimov, *Polypyrrole: a conducting polymer; its synthesis, properties and applications.* Russian chemical reviews, 1997. **66**(5): p. 443.
239. Wu, R.-L., et al., *Green composite films prepared from cellulose, starch and lignin in room-temperature ionic liquid.* Bioresource Technology, 2009. **100**(9): p. 2569-2574.
240. Hambardzumyan, A., et al., *Natural organic UV-absorbent coatings based on cellulose and lignin: designed effects on spectroscopic properties.* Biomacromolecules, 2012. **13**(12): p. 4081-4088.
241. Sadeghifar, H., et al., *Cellulose-Lignin Biodegradable and Flexible UV Protection Film.* ACS Sustainable Chemistry & Engineering, 2016. **5**(1): p. 625-631.
242. Hambardzumyan, A., et al., *Organosolv lignin as natural grafting additive to improve the water resistance of films using cellulose nanocrystals.* Chemical Engineering Journal, 2015. **264**: p. 780-788.

243. Hambardzumyan, A., et al., *Structure and optical properties of plant cell wall bio-inspired materials: Cellulose–lignin multilayer nanocomposites.* Comptes rendus biologies, 2011. **334**(11): p. 839-850.
244. Abitbol, T., E. Kloser, and D.G. Gray, *Estimation of the surface sulfur content of cellulose nanocrystals prepared by sulfuric acid hydrolysis.* Cellulose, 2013. **20**(2): p. 785-794.
245. Reid, M.S., M. Villalobos, and E.D. Cranston, *Benchmarking cellulose nanocrystals: from the laboratory to industrial production.* Langmuir, 2016. **33**(7): p. 1583-1598.
246. Heggset, E.B., G. Chinga-Carrasco, and K. Syverud, *Temperature stability of nanocellulose dispersions.* Carbohydrate polymers, 2017. **157**: p. 114-121.
247. Barnett, C. and W. Glasser. *Bleaching of hydroxypropyl lignin with hydrogen peroxide*. in *ACS Symposium series-American Chemical Society (USA)*. 1989.
248. Cachet, N., et al., *Esterification of organosolv lignin under supercritical conditions.* Industrial Crops and Products, 2014. **58**: p. 287-297.
249. Gilarranz, M.A., et al., *Phenolic OH group estimation by FTIR and UV spectroscopy. Application to organosolv lignins.* Journal of wood chemistry and technology, 2001. **21**(4): p. 387-395.
250. Wang, Y., et al., *A novel UV-shielding and transparent polymer film: when bioinspired dopamine–melanin hollow nanoparticles join polymers.* ACS applied materials & interfaces, 2017. **9**(41): p. 36281-36289.
251. Honorato-Rios, C., et al., *Equilibrium liquid crystal phase diagrams and detection of kinetic arrest in cellulose nanocrystal suspensions.* Frontiers in Materials, 2016. **3**: p. 21.
252. Abitbol, T. and E.D. Cranston, *Chiral nematic self-assembly of cellulose nanocrystals in suspensions and solid films*, in *HANDBOOK OF GREEN MATERIALS: 3 Self-and direct-assembling of bionanomaterials*. 2014. p. 37-56.
253. Picard, G., et al., *Cellulose nanocrystal iridescence: a new model.* Langmuir, 2012. **28**(41): p. 14799-14807.
254. Zhong, L., et al., *Colloidal stability of negatively charged cellulose nanocrystalline in aqueous systems.* Carbohydrate polymers, 2012. **90**(1): p. 644-649.
255. Shafiei-Sabet, S., W. Hamad, and S. Hatzikiriakos, *Ionic strength effects on the microstructure and shear rheology of cellulose nanocrystal suspensions.* Cellulose, 2014. **21**(5): p. 3347-3359.
256. Li, C., et al., *pH dependence of the chirality of nematic cellulose nanocrystals.* Scientific reports, 2019. **9**(1): p. 1-7.
257. Lyubimova, O., et al., *Electric interfacial layer of modified cellulose nanocrystals in aqueous electrolyte solution: predictions by the molecular theory of solvation.* Langmuir, 2015. **31**(25): p. 7106-7116.
258. Gençer, A., et al., *Effect of gelation on the colloidal deposition of cellulose nanocrystal films.* Biomacromolecules, 2018. **19**(8): p. 3233-3243.
259. Gray, D.G. and X. Mu, *Chiral nematic structure of cellulose nanocrystal suspensions and films; polarized light and atomic force microscopy.* Materials, 2015. **8**(11): p. 7873-7888.
260. Chau, M., et al., *Ion-mediated gelation of aqueous suspensions of cellulose nanocrystals.* Biomacromolecules, 2015. **16**(8): p. 2455-2462.
261. Lo Nostro, P. and B.W. Ninham, *Hofmeister phenomena: an update on ion specificity in biology.* Chemical reviews, 2012. **112**(4): p. 2286-2322.
262. Vlachy, N., et al., *Hofmeister series and specific interactions of charged headgroups with aqueous ions.* Advances in colloid and interface science, 2009. **146**(1-2): p. 42-47.
263. Chowdhury, R.A., S.X. Peng, and J. Youngblood, *Improved order parameter (alignment) determination in cellulose nanocrystal (CNC) films by a simple optical birefringence method.* Cellulose, 2017. **24**(5): p. 1957-1970.

264. Mu, X. and D.G. Gray, *Formation of chiral nematic films from cellulose nanocrystal suspensions is a two-stage process.* Langmuir, 2014. **30**(31): p. 9256-9260.
265. Honorato-Rios, C., et al., *Fractionation of cellulose nanocrystals: enhancing liquid crystal ordering without promoting gelation.* NPG asia materials, 2018. **10**(5): p. 455-465.
266. Xu, Y., A.D. Atrens, and J.R. Stokes, *"Liquid, gel and soft glass" phase transitions and rheology of nanocrystalline cellulose suspensions as a function of concentration and salinity.* Soft Matter, 2018. **14**(10): p. 1953-1963.
267. Stroobants, A., H. Lekkerkerker, and T. Odijk, *Effect of electrostatic interaction on the liquid crystal phase transition in solutions of rodlike polyelectrolytes.* Macromolecules, 1986. **19**(8): p. 2232-2238.
268. Hirai, A., et al., *Phase separation behavior in aqueous suspensions of bacterial cellulose nanocrystals prepared by sulfuric acid treatment.* Langmuir, 2009. **25**(1): p. 497-502.
269. Bertsch, P., S. Isabettini, and P. Fischer, *Ion-Induced Hydrogel Formation and Nematic Ordering of Nanocrystalline Cellulose Suspensions.* Biomacromolecules, 2017.
270. Bertsch, P., et al., *Ion-induced formation of nanocrystalline cellulose colloidal glasses containing nematic domains.* Langmuir, 2019. **35**(11): p. 4117-4124.
271. Park, J.H., et al., *Macroscopic control of helix orientation in films dried from cholesteric liquid crystalline cellulose nanocrystal suspensions.* Chemphyschem: a European journal of chemical physics and physical chemistry, 2014. **15**(7): p. 1477-1484.
272. Saha, P., *Optimization of Cellulose Nanocrystal Films for Optical and Micromechanical Applications.* 2018.
273. Wierenga, A.M., A.P. Philipse, and E.M. Reitsma, *Decay of flow birefringence in dispersions of charged colloidal rods: Effect of double-layer interactions.* Langmuir, 1997. **13**(26): p. 6947-6950.
274. Russel, W.B., *Bulk stresses due to deformation of the electrical double layer around a charged sphere.* Journal of Fluid Mechanics, 1978. **85**(4): p. 673-683.
275. Shafiei Sabet, S., *Shear rheology of cellulose nanocrystal (CNC) aqueous suspensions*, 2013, University of British Columbia.
276. Liu, D., et al., *Structure and rheology of nanocrystalline cellulose.* Carbohydrate polymers, 2011. **84**(1): p. 316-322.
277. Wada, M., L. Heux, and J. Sugiyama, *Polymorphism of cellulose I family: reinvestigation of cellulose IVI.* Biomacromolecules, 2004. **5**(4): p. 1385-1391.
278. Dai, S., et al., *Cholesteric film of Cu (II)-doped cellulose nanocrystals for colorimetric sensing of ammonia gas.* Carbohydrate polymers, 2017. **174**: p. 531-539.
279. Yue, Y., *A comparative study of cellulose I and II and fibers and nanocrystals.* 2011.
280. Qian, Y., et al., *Reaction-free lignin whitening via a self-assembly of acetylated lignin.* Industrial & Engineering Chemistry Research, 2014. **53**(24): p. 10024-10028.
281. VVU, S. and D. Argyropoulos, *An Improved Method for lsolating Lignin in High Yield and Purity.* Journal of pulp and paper science, 2003. **29**(7).
282. Ikeda, T., et al., *Studies on the effect of ball milling on lignin structure using a modified DFRC method.* Journal of agricultural and food chemistry, 2002. **50**(1): p. 129-135.
283. Wang, J., et al., *Reduction of lignin color via one-step UV irradiation.* Green Chemistry, 2016. **18**(3): p. 695-699.
284. Dilling, P. and P.T. Sarjeant, *Reduction of lignin color*, 1984, Google Patents.
285. Zhang, H., et al., *Color reduction of sulfonated eucalyptus kraft lignin.* International journal of biological macromolecules, 2017. **97**: p. 201-208.
286. Lin, S.Y., *Process for reduction of lignin color*, 1980, Google Patents.
287. Zhang, H., et al., *A practicable process for lignin color reduction: fractionation of lignin using methanol/water as a solvent.* Green Chemistry, 2017. **19**(21): p. 5152-5162.

288. Zhang, H., et al., *High-value utilization of kraft lignin: Color reduction and evaluation as sunscreen ingredient.* International journal of biological macromolecules, 2019. **133**: p. 86-92.
289. Zhang, H., et al., *Micromorphology influence on the color performance of lignin and its application in guiding the preparation of light-colored lignin sunscreen.* ACS Sustainable Chemistry & Engineering, 2018. **6**(9): p. 12532-12540.
290. He, W., W. Gao, and P. Fatehi, *Oxidation of kraft lignin with hydrogen peroxide and its application as a dispersant for kaolin suspensions.* ACS Sustainable Chemistry & Engineering, 2017. **5**(11): p. 10597-10605.
291. Suess, H.U., *Pulp bleaching today*. 2010: Walter de Gruyter.
292. Sarkanen, K.V. and C.H. Ludwig, *Liguins. Occurrence, formation, structure, and reactions*. 1971.
293. Mancera, A., et al., *Physicochemical characterisation of sugar cane bagasse lignin oxidized by hydrogen peroxide.* Polymer Degradation and Stability, 2010. **95**(4): p. 470-476.
294. Peng, Y., W. Wang, and J. Cao, *Preparation of lignin–clay complexes and its effects on properties and weatherability of wood flour/polypropylene composites.* Industrial & Engineering Chemistry Research, 2016. **55**(36): p. 9657-9666.
295. Wang, H., et al., *A novel lignin/ZnO hybrid nanocomposite with excellent UV-absorption ability and its application in transparent polyurethane coating.* Industrial & Engineering Chemistry Research, 2017. **56**(39): p. 11133-11141.
296. Kaur, R., et al., *Development of agri-biomass based lignin derived zinc oxide nanocomposites as promising UV protectant-cum-antimicrobial agents.* Journal of Materials Chemistry B, 2020. **8**(2): p. 260-269.
297. Mehta, M.J. and A. Kumar, *Ionic liquid stabilized gelatin–lignin films: a potential UV-shielding material with excellent mechanical and antimicrobial properties.* Chem. Eur. J, 2019. **25**: p. 1269-1274.
298. Sirviö, J.A., et al., *Transparent lignin-containing wood nanofiber films with UV-blocking, oxygen barrier, and anti-microbial properties.* Journal of Materials Chemistry A, 2020. **8**(16): p. 7935-7946.
299. Israelachvili, J.N., *Intermolecular and surface forces*. 2011: Academic press.
300. Benítez, A.J. and A. Walther, *Counterion size and nature control structural and mechanical response in cellulose nanofibril nanopapers.* Biomacromolecules, 2017. **18**(5): p. 1642-1653.
301. Wang, B., et al., *Aligned bioinspired cellulose nanocrystal-based nanocomposites with synergetic mechanical properties and improved hygromechanical performance.* ACS applied materials & interfaces, 2015. **7**(8): p. 4595-4607.
302. Shimizu, M., T. Saito, and A. Isogai, *Water-resistant and high oxygen-barrier nanocellulose films with interfibrillar cross-linkages formed through multivalent metal ions.* Journal of Membrane Science, 2016. **500**: p. 1-7.
303. Khanjani, P., et al., *Interaction of divalent cations with carboxylate group in TEMPO-oxidized microfibrillated cellulose systems.* Cellulose, 2019. **26**(8): p. 4841-4851.
304. Roman, M. and W.T. Winter, *Effect of sulfate groups from sulfuric acid hydrolysis on the thermal degradation behavior of bacterial cellulose.* Biomacromolecules, 2004. **5**(5): p. 1671-1677.
305. Martínez-Sanz, M., A. Lopez-Rubio, and J.M. Lagaron, *Optimization of the nanofabrication by acid hydrolysis of bacterial cellulose nanowhiskers.* Carbohydrate polymers, 2011. **85**(1): p. 228-236.
306. Wang, N., E. Ding, and R. Cheng, *Thermal degradation behaviors of spherical cellulose nanocrystals with sulfate groups.* Polymer, 2007. **48**(12): p. 3486-3493.
307. Gerlock, J., A. Kucherov, and C. Smith, *Determination of active HALS in automotive paint systems II: HALS distribution in weathered clearcoat/basecoat paint systems.* Polymer degradation and stability, 2001. **73**(2): p. 201-210.

308. Glasser, W.G., R.A. Northey, and T.P. Schultz, *Lignin: historical, biological, and materials perspectives*. 1999: ACS Publications.
309. González Sánchez, C. and L. Alvarez, *Micromechanics of lignin/polypropylene composites suitable for industrial applications.* Macromolecular Materials and Engineering, 1999. **272**(1): p. 65-70.
310. De Chirico, A., et al., *Flame retardants for polypropylene based on lignin.* Polymer degradation and stability, 2003. **79**(1): p. 139-145.
311. Chen, L., et al., *Highly thermal-stable and functional cellulose nanocrystals and nanofibrils produced using fully recyclable organic acids.* Green Chemistry, 2016. **18**(13): p. 3835-3843.
312. Wang, R., et al., *Tailored and integrated production of carboxylated cellulose nanocrystals (CNC) with nanofibrils (CNF) through maleic acid hydrolysis.* ChemNanoMat, 2017. **3**(5): p. 328-335.
313. Anderson, W. and L. Castle, *Benzophenone in cartonboard packaging materials and the factors that influence its migration into food.* Food Additives & Contaminants, 2003. **20**(6): p. 607-618.
314. Horie, K., H. Ando, and I. Mita, *Photochemistry in polymer solids. 8. Mechanism of photoreaction of benzophenone in poly (vinyl alcohol).* Macromolecules, 1987. **20**(1): p. 54-58.
315. Sanches-Silva, A., et al., *Study of the migration of photoinitiators used in printed food-packaging materials into food simulants.* Journal of agricultural and food chemistry, 2009. **57**(20): p. 9516-9523.
316. Liu, C., et al., *Properties of nanocellulose isolated from corncob residue using sulfuric acid, formic acid, oxidative and mechanical methods.* Carbohydrate polymers, 2016. **151**: p. 716-724.
317. Wang, X., et al., *Ultrasonic-assisted synthesis of aminated lignin by a Mannich reaction and its decolorizing properties for anionic azo-dyes.* RSC Advances, 2014. **4**(53): p. 28156-28164.
318. Le Gars, M., et al., *Amidation of TEMPO-oxidized cellulose nanocrystals using aromatic aminated molecules.* Colloid and Polymer Science, 2020: p. 1-15.
319. Katz, S. and R.P. Beatson, *The determination of strong and weak acidic groups in sulfite pulps.* Svensk papperstidning, 1984. **87**(6): p. 48-53.
320. Mallapragada, S.K. and N.A. Peppas, *Dissolution mechanism of semicrystalline poly (vinyl alcohol) in water.* Journal of Polymer Science Part B: Polymer Physics, 1996. **34**(7): p. 1339-1346.
321. Wang, G. and H. Chen, *Carbohydrate elimination of alkaline-extracted lignin liquor by steam explosion and its methylolation for substitution of phenolic adhesive.* Industrial Crops and Products, 2014. **53**: p. 93-101.
322. Boeriu, C.G., et al., *Characterisation of structure-dependent functional properties of lignin with infrared spectroscopy.* Industrial Crops and Products, 2004. **20**(2): p. 205-218.
323. Qu, L., et al., *Chemical profiling and adulteration screening of Aquilariae Lignum Resinatum by Fourier transform infrared (FT-IR) spectroscopy and two-dimensional correlation infrared (2D-IR) spectroscopy.* Spectrochimica Acta Part A: Molecular and Biomolecular Spectroscopy, 2017. **174**: p. 177-182.
324. Meier, D., et al., *Conversion of technical lignins into slow-release nitrogenous fertilizers by ammoxidation in liquid phase.* Bioresource Technology, 1994. **49**(2): p. 121-128.
325. Lin, L., et al., *Liquefaction mechanism of β-O-4 lignin model compound in the presence of phenol under acid catalysis. Part 2. Reaction behaviour and pathways.* 2001.
326. Matsushita, Y., et al., *Phenolization of hardwood sulfuric acid lignin and comparison of the behavior of the syringyl and guaiacyl units in lignin.* Journal of Wood Science, 2007. **53**(1): p. 67-70.
327. Fujisawa, S., et al., *Preparation and characterization of TEMPO-oxidized cellulose nanofibril films with free carboxyl groups.* Carbohydrate polymers, 2011. **84**(1): p. 579-583.
328. Orelma, H., et al., *Preparation of photoreactive nanocellulosic materials via benzophenone grafting.* RSC Advances, 2016. **6**(88): p. 85100-85106.

329. Johnson, R.K., A. Zink-Sharp, and W.G. Glasser, *Preparation and characterization of hydrophobic derivatives of TEMPO-oxidized nanocelluloses.* Cellulose, 2011. **18**(6): p. 1599-1609.
330. Leung, A.C., et al., *Characteristics and properties of carboxylated cellulose nanocrystals prepared from a novel one-step procedure.* Small, 2011. **7**(3): p. 302-305.
331. Sun, X., et al., *Melt-processed poly (vinyl alcohol) composites filled with microcrystalline cellulose from waste cotton fabrics.* Carbohydrate polymers, 2014. **101**: p. 642-649.
332. Xiao, S., et al., *Poly (vinyl alcohol) films reinforced with nanofibrillated cellulose (NFC) isolated from corn husk by high intensity ultrasonication.* Carbohydrate polymers, 2016. **136**: p. 1027-1034.
333. Hu, N., et al., *Effect of fabrication process on electrical properties of polymer/multi-wall carbon nanotube nanocomposites.* Composites Part A: Applied Science and Manufacturing, 2008. **39**(5): p. 893-903.
334. Qian, X.-F., et al., *The preparation and characterization of PVA/Ag2S nanocomposite.* Materials chemistry and physics, 2001. **68**(1-3): p. 95-97.
335. Yang, W., J.M. Kenny, and D. Puglia, *Structure and properties of biodegradable wheat gluten bionanocomposites containing lignin nanoparticles.* Industrial Crops and Products, 2015. **74**: p. 348-356.
336. Zhang, X., et al., *Biomimetic Supertough and Strong Biodegradable Polymeric Materials with Improved Thermal Properties and Excellent UV-Blocking Performance.* Advanced Functional Materials, 2019. **29**(4): p. 1806912.
337. El-Hadi, A.M., *The effect of additives interaction on the miscibility and crystal structure of two immiscible biodegradable polymers.* Polímeros, 2014. **24**(1): p. 9-16.
338. Kaushik, A. and M. Singh, *Isolation and characterization of cellulose nanofibrils from wheat straw using steam explosion coupled with high shear homogenization.* Carbohydrate research, 2011. **346**(1): p. 76-85.
339. Kashiwagi, T., et al., *Thermal degradation and flammability properties of poly (propylene)/carbon nanotube composites.* Macromolecular rapid communications, 2002. **23**(13): p. 761-765.
340. Peng, Y., et al., *Effects of lignin content on mechanical and thermal properties of polypropylene composites reinforced with micro particles of spray dried cellulose nanofibrils.* ACS Sustainable Chemistry & Engineering, 2018. **6**(8): p. 11078-11086.
341. Parit, M. and V.A. Davis, *Effects of Non-covalent Functionalization and Initial Mixing Methods on SWNT/PP and SWNT/EVOH Composites.* ACS Omega, 2021.
342. Yang, P. and S. Kokot, *Thermal analysis of different cellulosic fabrics.* Journal of Applied Polymer Science, 1996. **60**(8): p. 1137-1146.
343. Liu, D., et al., *Effects of cellulose nanofibrils on the structure and properties on PVA nanocomposites.* Cellulose, 2013. **20**(6): p. 2981-2989.
344. Tarrés, Q., et al., *Lignocellulosic nanofibers from triticale straw: The influence of hemicelluloses and lignin in their production and properties.* Carbohydrate polymers, 2017. **163**: p. 20-27.
345. Ashley, R., *Permeability and Plastics Packaging in Polymer Permeability, edited by J. Comyn*, 1985, Elsevier Applied Science Publishers, London.
346. Shankar, S., J.-W. Rhim, and K. Won, *Preparation of poly (lactide)/lignin/silver nanoparticles composite films with UV light barrier and antibacterial properties.* International journal of biological macromolecules, 2018. **107**: p. 1724-1731.
347. Zhang, X., et al., *High performance PVA/lignin nanocomposite films with excellent water vapor barrier and UV-shielding properties.* International journal of biological macromolecules, 2020. **142**: p. 551-558.
348. Wiles, D. and D. Carlsson, *Photostabilisation mechanisms in polymers: A review.* Polymer Degradation and Stability, 1980. **3**(1): p. 61-72.

349. Simmons, T.J., et al., *Preparation of synthetic wood composites using ionic liquids.* Wood science and technology, 2011. **45**(4): p. 719-733.
350. Han, C., et al., *Transparent epoxy–ZnO/CdS nanocomposites with tunable UV and blue light-shielding capabilities.* Journal of Materials Chemistry C, 2015. **3**(19): p. 5065-5072.
351. Wang, X., S. Zhou, and L. Wu, *Facile encapsulation of SiO 2 on ZnO quantum dots and its application in waterborne UV-shielding polymer coatings.* Journal of Materials Chemistry C, 2013. **1**(45): p. 7547-7553.
352. Li, S., et al., *Durable antibacterial and UV-protective Ag/TiO2@ fabrics for sustainable biomedical application.* International journal of nanomedicine, 2017. **12**: p. 2593.
353. Nakagaito, A.N. and H. Yano, *Novel high-strength biocomposites based on microfibrillated cellulose having nano-order-unit web-like network structure.* Applied Physics A: Materials Science & Processing, 2005. **80**(1): p. 155-159.
354. Taniguchi, T. and K. Okamura, *New films produced from microfibrillated natural fibres.* Polymer International, 1998. **47**(3): p. 291-294.
355. Zimmermann, T., E. Pöhler, and T. Geiger, *Cellulose fibrils for polymer reinforcement.* Advanced engineering materials, 2004. **6**(9): p. 754-761.
356. Chinga-Carrasco, G., et al., *Micro-structural characterisation of homogeneous and layered MFC nano-composites.* Micron, 2013. **44**: p. 331-338.
357. Andresen, M., et al., *Nonleaching antimicrobial films prepared from surface-modified microfibrillated cellulose.* Biomacromolecules, 2007. **8**(7): p. 2149-2155.
358. Salminen, T., U. Hippi, and A. Salminen, *Method for the Preparation of NFC Films on Supports*, 2014, Google Patents.
359. Varanasi, S. and W.J. Batchelor, *Rapid preparation of cellulose nanofibre sheet.* Cellulose, 2013. **20**(1): p. 211-215.
360. Österberg, M., et al., *A fast method to produce strong NFC films as a platform for barrier and functional materials.* ACS applied materials & interfaces, 2013. **5**(11): p. 4640-4647.
361. Raj, P., et al., *Effect of cationic polyacrylamide on the processing and properties of nanocellulose films.* Journal of colloid and interface science, 2015. **447**: p. 113-119.
362. TAPPI, T., *Forming handsheets for physical tests of pulp.* Technical Association of the Pulp and Paper Industry, 2000. **205**.
363. Varanasi, S. and W. Batchelor, *Superior non-woven sheet forming characteristics of low-density cationic polymer-cellulose nanofibre colloids.* Cellulose, 2014. **21**(5): p. 3541-3550.
364. Martinez, D., et al. *Characterizing the mobility of papermaking fibres during sedimentation*. in *Proceedings of the Transactions of 12th fundamental Research Symposium, Oxford*. 2001.
365. Varanasi, S., R. He, and W. Batchelor, *Estimation of cellulose nanofibre aspect ratio from measurements of fibre suspension gel point.* Cellulose, 2013. **20**(4): p. 1885-1896.
366. TAPPI, T.M., *Physical Testing of Pulp Handsheets, TAPPI Press, Atlanta, T 220 om-88.* 1988.
367. Spence, K.L., et al., *The effect of chemical composition on microfibrillar cellulose films from wood pulps: water interactions and physical properties for packaging applications.* Cellulose, 2010. **17**(4): p. 835-848.
368. Jonoobi, M., A.P. Mathew, and K. Oksman, *Producing low-cost cellulose nanofiber from sludge as new source of raw materials.* Industrial Crops and Products, 2012. **40**: p. 232-238.
369. Fukuzumi, H., et al., *Transparent and High Gas Barrier Films of Cellulose Nanofibers Prepared by TEMPO-Mediated Oxidation.* Biomacromolecules, 2009. **10**(1): p. 162-165.
370. Farmahini-Farahani, M., et al., *Cellulose/nanoclay composite films with high water vapor resistance and mechanical strength.* Cellulose, 2015. **22**(6): p. 3941-3953.
371. Bedane, A.H., et al., *Water vapor transport properties of regenerated cellulose and nanofibrillated cellulose films.* Journal of Membrane Science, 2015. **493**: p. 46-57.

372. Rodionova, G., et al., *Surface chemical modification of microfibrillated cellulose: improvement of barrier properties for packaging applications.* Cellulose, 2011. **18**(1): p. 127-134.
373. Vallejos, M.E., et al., *Nanofibrillated cellulose (CNF) from eucalyptus sawdust as a dry strength agent of unrefined eucalyptus handsheets.* Carbohydrate polymers, 2016. **139**: p. 99-105.
374. Parit, M., B. Aksoy, and Z. Jiang, *Towards standardization of laboratory preparation procedure for uniform cellulose nanopapers.* Cellulose, 2018. **25**(5): p. 2915-2924.
375. Lay, M., et al., *Smart nanopaper based on cellulose nanofibers with hybrid PEDOT: PSS/polypyrrole for energy storage devices.* Carbohydrate polymers, 2017. **165**: p. 86-95.
376. Zotti, G., et al., *Well-defined pyrrole oligomers: Electrochemical and UV/vis studies.* Advanced Materials, 1992. **4**(12): p. 798-801.
377. Nicolau, Y. and S. Davied. *Layer-by-layer chemical deposition of conducting polymer thin films. Method and procedure*. in *AIP Conference Proceedings*. 1996. American Institute of Physics.
378. Bideau, B., et al., *Mechanical and antibacterial properties of a nanocellulose-polypyrrole multilayer composite.* Materials Science and Engineering: C, 2016. **69**: p. 977-984.
379. Ojio, T. and S. Miyata, *Highly transparent and conducting polypyrrole–poly (vinyl alcohol) composite films prepared by gas state polymerization.* Polymer Journal, 1986. **18**(1): p. 95-98.
380. Dhawan, S. and D. Trivedi, *Thin conducting polypyrrole film on insulating surface and its applications.* Bulletin of Materials Science, 1993. **16**(5): p. 371-380.
381. Buslov, D., N. Sushko, and O. Tretinnikov, *IR investigation of hydrogen bonds in weakly hydrated films of poly (vinyl alcohol).* Polymer Science Series A, 2011. **53**(12): p. 1121-1127.
382. Wang, Y.L., H. Yang, and Z.L. Xu, *Influence of post-treatments on the properties of porous poly (vinyl alcohol) membranes.* Journal of Applied Polymer Science, 2008. **107**(3): p. 1423-1429.
383. Miraftab, M., A.N. Saifullah, and A. Çay, *Physical stabilisation of electrospun poly (vinyl alcohol) nanofibres: comparative study on methanol and heat-based crosslinking.* Journal of materials science, 2015. **50**(4): p. 1943-1957.
384. Marins, J.A., et al., *Self-supported bacterial cellulose polyaniline conducting membrane as electromagnetic interference shielding material: effect of the oxidizing agent.* Cellulose, 2014. **21**(3): p. 1409-1418.
385. Yin, W., et al., *Conducting composite film based on polypyrrole and crosslinked cellulose.* Journal of Applied Polymer Science, 2001. **80**(9): p. 1368-1373.
386. Qian, X., J. Chen, and X. An, *Polypyrrole-coated conductive paper prepared by vapour-phase deposition method.* Appita Journal: Journal of the Technical Association of the Australian and New Zealand Pulp and Paper Industry, 2010. **63**(2): p. 102.
387. Li, J., et al., *Conductivity decay of cellulose–polypyrrole conductive paper composite prepared by in situ polymerization method.* Carbohydrate polymers, 2010. **82**(2): p. 504-509.
388. Liu, S., et al., *Surface modification of cellulose scaffold with polypyrrole for the fabrication of flexible supercapacitor electrode with enhanced capacitance.* RSC Advances, 2015. **5**(106): p. 87266-87276.
389. Lee, H.-J., et al., *Fabrication and evaluation of bacterial cellulose-polyaniline composites by interfacial polymerization.* Cellulose, 2012. **19**(4): p. 1251-1258.
390. Thomassin, J.-M., et al., *Polymer/carbon based composites as electromagnetic interference (EMI) shielding materials.* Materials Science and Engineering: R: Reports, 2013. **74**(7): p. 211-232.
391. Chung, D., *Electromagnetic interference shielding effectiveness of carbon materials.* Carbon, 2001. **39**(2): p. 279-285.
392. Yang, Y., et al., *Novel carbon nanotube− polystyrene foam composites for electromagnetic interference shielding.* Nano Letters, 2005. **5**(11): p. 2131-2134.

393. Zhang, Y., et al., *A novel polyaniline-coated bagasse fiber composite with core–shell heterostructure provides effective electromagnetic shielding performance.* ACS applied materials & interfaces, 2016. **9**(1): p. 809-818.
394. Wentworth, S.M., *Applied electromagnetics: early transmission lines approach*. 2007: John Wiley & Sons.
395. Lin, Y.-C., et al., *Kinetics and mechanism of cellulose pyrolysis.* The Journal of Physical Chemistry C, 2009. **113**(46): p. 20097-20107.
396. Carrasco, P.M., et al., *Comparison of surface and bulk doping levels in chemical polypyrroles of low, medium and high conductivity.* Surface and Interface Analysis: An International Journal devoted to the development and application of techniques for the analysis of surfaces, interfaces and thin films, 2007. **39**(1): p. 26-32.
397. ASTM, *Standard practice for operating fluorescent ultraviolet (UV) lamp apparatus for exposure of nonmetallic materials.* ASTM G154, 2016: p. 1-12.